A GEOCHEMICAL STUDY OF DIAMONDS FROM CULLINAN DIAMOND MINE, SOUTH AFRICA

KERRYN WHITEHEAD

BSc (Hons) University of Cape Town

Thesis presented for the Degree of

MASTER OF SCIENCE

In the Department of Geological Sciences

Faculty of Science

University of Cape Town

SEPTEMBER 2005

Kerryn Whitehead
September, 2005

Signed by candidate

Signature removed

ACKNOWLEDGEMENTS

I wish to thank Steve Richardson for allowing me the opportunity to undertake this project. Steve has been very supportive and patient during the course of this dissertation. He always made time to assist me when difficulties arose and his knowledge on diamonds has been invaluable to me during this project. John Gurney, my co-supervisor, has also always been willing to offer assistance and support. His knowledge of mantle geology has added greatly to this study.

The majority of funding for this project was made possible by a NRF grant. Thanks to De Beers for providing the peridotitic diamonds for this project and for funding various aspects of this study. Thank you to Fanus Viljoen and my colleagues at the De Beers GeoScience Centre for their input and assistance on various aspects of the project. Thanks too to Judith Milledge for providing the eclogitic diamonds for this project and insight into various aspects of cathodoluminescence and FTIR analyses of diamonds. Howard Bell (Zlotowski's Diamond Cutting Works (Pty) Ltd.) must be thanked for doing an excellent job of polishing some of the diamonds into plates.

A special thank you to Kurt Kaiser and Herb Helmstaedt from Queen's University, Kingston, Canada, for allowing me the opportunity to do stable isotope analyses on the diamonds and to experience a new country.

Thank you to Anton le Roex for his assistance and advice during the course of this project and to Andreas Spath for all of his help and technical support on the electron microprobe and LA ICP-MS at UCT. Thank you to Eva Anckar of the Kimberlite Research Group for her help in obtaining data from the Kimberlite Research Group Database. The cathodoluminescence images were made possible with the help of Miranda Waldon at the Electron Microscope Unit at UCT. Very special thanks must go to Kalle Westerlund and Neil Mc Kenna for all of their patient assistance and technical training during my time at UCT.

Finally thank you to Scott Gray, Tanya le Roex, my family and friends for their love, believing in me and motivating me to continue.

ABSTRACT

The Cullinan kimberlite is a Group I kimberlite and is located in the northeastern region of the Kaapvaal Craton, South Africa. The kimberlite pipe has been dated at 1180 ± 30 Ma and intrudes the Bushveld Igneous Complex (2.05 Ga). This study explores the geochemistry of a suite of one hundred selected diamonds and their associated mineral inclusions. The majority of the diamonds described here are peridotitic (94%) and the remainder are eclogitic. The peridotitic inclusions may be further subdivided into harzburgitic and lherzolitic parageneses. The three major diamond parageneses have been dated previously from Cullinan; the harzburgitic diamonds at ~3.2 Ga, the lherzolitic diamonds at 1.93 Ga and the eclogitic diamonds at 1.15 Ga.

The majority of diamonds are brown (93%), which is associated with plastic deformation. About 40% of the diamonds display physical characteristics indicative of partial resorption that would have occurred in the kimberlite. Half of the diamonds also exhibit growth features. Fourier transform infra-red (FTIR) analysis of the whole stones and diamond plates has shown that approximately half of the suite are Type II (i.e. do not contain significant nitrogen). The rest of the suite have low nitrogen concentrations and show medium to high states of nitrogen aggregation (Type IaAB). The time-averaged mantle residence temperatures calculated for the diamonds show that they fall between the 1180 and 1240 °C isotherms on a plot of nitrogen aggregation versus nitrogen content. Cathodoluminescence images coupled with FTIR analyses have shown evidence of episodic growth of the diamonds and suggest that the harzburgitic paragenesis has possibly recrystallized during the formation of the lherzolitic paragenesis.

Stable isotope analysis of the diamonds yields a range of carbon isotopic compositions from ~ -10 to -1 ‰ for the entire suite. The harzburgitic and lherzolitic diamonds are intermixed across this range and the eclogitic diamonds fall towards the lighter isotopic compositions. A few nitrogen isotopic analyses were obtained and the range was wide, from ~ -24 to +10 ‰. The carbon isotopic values obtained most likely reflect fractionation of carbon isotopes from a globally homogeneous convecting mantle. The wide range of nitrogen isotopes could indicate a primitive nitrogen source or alternatively a large dependence of the fractionation of nitrogen isotopes on the rate and kinetics of diamond growth.

The peridotitic inclusions show linear trends in major element composition between the harzburgitic and lherzolitic inclusions. The minerals recovered from the diamonds were garnet, (rare) clinopyroxene, orthopyroxene and olivine. These inclusions span the range of values observed for diamond inclusions worldwide, from depleted to fertile compositions. Only a few inclusions were liberated from the eclogitic diamonds. The eclogitic garnet and clinopyroxene chemistries are similar to previous values obtained for Cullinan. The rare earth element (REE) patterns obtained, using a laser ablation ICP-MS, for the peridotitic garnet inclusions indicate that the majority of the inclusions have experienced some degree of melt metasomatism. Estimates of temperatures and pressures of formation have been calculated for the diamonds using various geothermobarometers. The majority of the diamonds have formed over a range of temperatures from ~1050 to 1300 °C. The pressures obtained for the diamond formation are also wide and span a range from ~40 to 77 kbar. The temperatures obtained for these diamonds are higher than those obtained from inclusions in diamonds from surrounding kimberlites. The peridotitic diamonds are shown to have formed episodically in an environment of low nitrogen, under "typical" mantle carbon isotopic compositions. The REE patterns and temperatures of formation suggest that these diamonds formed in the presence of variable amounts of melt.

The harzburgitic paragenesis is suggested to have formed from a depleted harzburgitic source. This source is suggested to be the residual material remaining after extraction of komatiites during the Archean. The lherzolitic paragenesis is likely to have developed as the result of re-fertilization of the depleted harzburgitic source. This may have occurred by infiltration of metasomatic fluids associated with the intrusion of the Bushveld Igneous Complex. The eclogitic diamonds also show "typical" mantle chemistries, carbon isotopic compositions, temperatures of formation and nitrogen aggregation state. This evidence in conjunction with previous work done on the radiogenic isotopes suggests that they have most likely crystallized from a MORB-type mantle, several million years prior to the emplacement of the kimberlite pipe.

TABLE OF CONTENTS

APPENDIX 4

ELECTRON MICROPROBE METHODOLOGY AND ANALYSES FOR INCLUSIONS FROM CULLINAN MINE DIAMONDS

APPENDIX 5

LA ICP-MS METHODOLOGY FOR CULLINAN MINE DIAMONDS

APPENDIX 6

GEOTHERMOBAROMETRY ESTIMATES FOR DIAMOND INCLUSIONS FROM CULLINAN

1. INTRODUCTION

1.1 Diamonds and the cratonic lithosphere

Diamonds containing mineral inclusions are invaluable for study as non-touching mineral inclusions are unable to re-equilibrate and therefore provide information about the crystallization environment of the diamonds. The inclusions also have the potential to give temperatures and pressures of formation of the diamonds. The stable isotope compositions (carbon and nitrogen) of diamond give information about the diamond source regions and about diamond growth. Fourier transform infra-red studies provide information about the residence time and/or temperature that the diamonds experienced in the mantle, as well as growth history when used in conjunction with cathodoluminescence imaging. Combining this information helps to achieve a comprehensive overview of the mantle evolution in the source region of the diamonds and an understanding of how, where and why diamonds form.

Richardson et al. (1984) obtained ancient ages (~3.2 – 3.3 Ga) for sub-calcic garnets liberated from diamonds. The diamonds were brought to the surface by relatively young (~90 Myr) kimberlite hosts. This demonstrated that diamonds are xenocrysts and not cognate with their kimberlite or lamproite host, as previously thought. Experimental work conducted by Kennedy and Kennedy (1976) showed that diamonds are only stable at pressures in excess of 46 kbar. In order for diamonds to have been preserved from the Archean a stable lithosphere must have been in place by this time. Xenoliths hosted in Late Cretaceous kimberlites indicate that the lithosphere extended to depths of 170-190 km beneath the surface (Boyd and Gurney, 1986). The authors also suggest that the Archean root was relatively cool (900 – 1200 °C) based on geothermometry of ancient inclusions in diamond. Finnerty and Boyd (1984) obtained similar temperatures for Late Cretaceous garnet peridotite xenoliths. Temperatures and pressures of equilibration for mineral inclusions in diamonds and xenoliths are consistent with a present day surface heat flow, for the Kaapvaal Craton of ~40 mW/m^2 (Boyd et al., 1985; Pollack and Chapman, 1977). Recent Re-Os isotope studies on peridotitic and eclogitic xenoliths (Carlson et al., 1999; Menzies et al., 1999) show that the lithospheric keel had already reached at least 200 km in the Archean and remained stable at that depth until, at least, the

Cretaceous. This is substantially thicker than the lithosphere in the Proterozoic terrains surrounding the Kaapvaal craton (Jones, 1988).

Diamonds may be divided into two main parageneses, eclogitic and peridotitic, based upon their mineral inclusion chemistry. The mineral chemistry of the inclusions is similar to that of their peridotite and eclogite xenolith hosts, although they tend to be more depleted due to the inert nature of the surrounding diamond (Chapter 6). Studies of mineral inclusions allow a rare glimpse of mantle conditions at the time of diamond formation. A number of mineral inclusion studies suggest that diamonds may form in response to thermal perturbations in the lithosphere (Griffin et al., 1988; 1992; 1993; Sobolev, et al., 1997). Studies of nitrogen aggregation, cathodoluminescence images and geothermobarometry of diamonds and their inclusions indicate that the diamonds may have grown during a decrease in temperature after the heating event (Taylor et al., 1995).

A correlation has been observed between P-wave velocity at depths within the diamond stability field and the composition of diamonds and their syngenetic inclusions (Shirey et al., 2003; Figure 1). The authors found that silicate inclusions from diamonds in the Kaapvaal and Zimbabwe cratons show a regional relationship to the seismic velocity of the lithosphere. Lithosphere that has slower P-wave velocities was observed to correlate with a higher proportion of eclogitic vs. peridotitic silicate inclusions in diamond, a greater incidence of younger Sm-Nd ages of silicate inclusions, a greater proportion of diamonds with lighter C isotopic composition and a lower percentage of low-N diamonds (e.g. Cullinan (formerly Premier), Jwaneng, Orapa, Letlhakane and Jagersfontein mines). The converse holds true for diamonds from a higher velocity mantle (e.g. Wesselton, Bultfontein, Dutoitspan, Finsch, Koffiefontein, Roberts Victor and Venetia mines; Shirey et al., 2003).

The P-wave anomaly (seismically slow mantle) beneath the Cullinan kimberlite has been ascribed to refertilization of the mantle (Griffin et al., 2003; Hoal, 2003). Evidence for this comes from a study of mantle xenoliths from Cullinan that are enriched in Fe and Ti and do not exhibit any signs of potassic metasomatism common in Phanerozoic kimberlites (Hoal, 2003). Further evidence is given in a trace element and geothermobarometry study of garnets (Griffin et al., 2003). These values were used to construct subcontinental lithospheric mantle (SCLM) sections across the Kaapvaal and Zimbabwe cratons. The SCLM for the Cullinan region gives a strongly melt-metasomatised signature. The upwelling of sublithospheric mantle to produce the

Bushveld Igneous Complex is the likely source of the silicate melt available for metasomatism in this region (Griffin et al., 2003; Hoal, 2003).

Diamond formation in the Kaapvaal craton appears to be episodic. The earliest harzburgitic parageneses (~3.3 Ga) is associated with large scale melting of the Archean mantle. A later generation of eclogitic diamonds has been linked to Late Archean (~2.9 Ga) accretionary events of oceanic lithosphere. The formation of lherzolitic and further eclogitic parageneses are believed to be related to the tectonothermal alteration of the continental lithosphere during the Proterozoic (Carlson et al., 2000; Shirey et al., 2003). There is no generally accepted model for the formation of diamonds and their source material. Some of the theories of eclogitic and peridotitic diamond formation will be discussed further in the following sections.

1.1.1 The formation of peridotitic diamonds

The peridotitic diamonds may be further subdivided into harzburgitic and lherzolitic parageneses. The harzburgitic diamonds are more abundant generally than the lherzolitic assemblage (Meyer, 1987). In comparison with peridotite xenoliths, harzburgitic inclusions are more refractory, with higher Cr and Mg-numbers and low Ca (Boyd and Finnerty, 1980; Harte et al., 1980). Harte et al. (1980) suggested that the depleted diamond inclusions could form from a 5% melt of garnet-peridotite in the presence of CO_2, which would remove all Ca-rich solid phases. Boyd and Finnerty (1980) first suggested that diamonds of harzburgitic paragenesis formed in sub-solidus metamorphic or metasomatic processes, as their temperature estimates were lower than the C-H-O solidus for ultramafic rocks.

Following these hypotheses it was proposed that diamonds could form from the graphite produced during sepentinization of hydrated oceanic lithosphere. The serpentinites have depleted characteristics similar to the harzburgitic diamond inclusions and could also give rise to the lherzolite inclusions if some diopside escaped serpentinization (Schulze, 1986). A problem with this hypothesis is that the most serpentinised peridotites have Cr/(Cr+Al) ratios are too low to generate the peridotitic diamond inclusion suite (Kesson and Ringwood, 1989). Haggerty (1986) suggested another hypothesis for harzburgitic diamond formation that the oxidation of CH_4 or the reduction of CO_2 would occur at the lithosphere-asthenosphere boundary, due to the

differences in densities, temperatures and redox conditions. Gaseous cracking would occur at the boundary with the precipitation of carbon and the vapour fractionation of O-H. This carbon is proposed as a possible source of carbon for diamond formation. Another source of carbon proposed by Haggerty (1986) is the dissociation of CH_4 or CO_2 during partial melting, the incompatible carbon remains with the refractory residue during partial melting. Either alternative for the source of carbon requires the growth of diamonds from a solid-state metamorphic growth in a closed environment.

A feature of peridotitic diamonds that was not considered in earlier models was that of the trace element chemistry of their inclusions. Harzburgitic Cr-pyrope inclusions studied by Shimizu and Richardson (1987) display light rare earth element (LREE) enrichment in comparison with the heavy rare earth elements (HREE) and the Ti and Zr concentrations that are considerably lower than fertile lherzolite xenoliths. These data are inconsistent with the inclusions forming in equilibrium with silicate or carbonate liquids. Instead it is suggested that the sub-solidus metasomatism of a residual harzburgite would account for the depleted signature of the magmaphile elements and the subsequent enrichment in the LREE and Cr contents of the garnet inclusions. Kesson and Ringwood (1989) also propose a refractory harzburgitic protolith for harzburgitic diamonds; however they invoke an igneous origin of the diamonds from hydrous slab-derived melts carrying dissolved carbonate which ascended into overlying refractory peridotite. The melts would evolve towards equilibrium with the harzburgite through the precipitation of crystalline phases and hybridisation with peridotitic minerals. Diamond crystallization is believed to occur by the reduction of carbonate under low oxygen fugacity conditions. The precipitation of garnets from the hybrid fluid is argued to provide the LREE enrichment observed by Shimizu and Richardson (1987).

Griffin et al. (1992) and Stachel et al. (2004) also propose a two-stage process of depletion of the harzburgitic protolith followed by metasomatism by a carbonatitic fluid to account for the trace element enrichment of the harzburgitic garnet diamond inclusions. These sub-calcic inclusions yield lower average temperatures than the lherzolitic inclusions. The harzburgitic diamonds that give temperatures less than 1100 °C most likely formed in sub-solidus conditions, even in the presence of C-H-O fluids with a high incompatible trace element content. The hotter diamonds, 1100 – 1300 °C, of which the majority are lherzolitic, most likely formed by silicate melt metasomatism above the solidus temperature of their source rock (~1200 °C at 5 GPa) allowing for melt percolation

along grain boundaries. The protolith for the lherzolitic diamonds is suggested to be refertilized harzburgitic material that formed following the formation of the harzburgitic paragenesis. Stachel and Harris (1997a) favour the hypothesis of variable degrees of partial melting of a previously depleted and later re-enriched common mantle source for both harzburgitic and lherzolitic diamonds. The degree of partial melting for the lherzolitic parageneses is thought to be small, allowing for some clinopyroxene to remain in the residuum and higher in the case of harzburgite causing all the clinopyroxene to be consumed.

1.1.2 The formation of the eclogitic paragenesis

The majority of eclogitic inclusions in diamond are uniformly above 1100 °C (Boyd and Gurney, 1986) and give an average equilibration temperature of ~1250°C (Harris, 1992). They are estimated to form at pressures between 4.5 and 14 GPa (Irifune et al., 1986), although the majority are below 10 GPa (Kesson and Ringwood, 1989). This evidence suggests that eclogitic diamonds crystallized from silicate melts, as the water saturated eclogitic solidus is only 1200°C at 10 GPa (Green, 1982). Eclogitic inclusion chemistries (namely lower Mg-number of garnet and clinopyroxene and higher K contents of clinopyroxene) in comparison with host eclogite are also best explained by crystallization from an initial partial melt formed from the now refractory eclogite (Kesson and Ringwood, 1989). Eclogitic diamonds from Orapa, Botswana show variation in mineral chemistry linked to change in temperature. These variations were explained by Gurney et al. (1985) by closed-system crystal-liquid fractionation processes, implying crystallization from a silicate melt. Griffin et al. (1988) found high concentrations of Pb, U, Rb, Sr and K in eclogitic garnet and clinopyroxene inclusions from Western Australia. They suggest that the diamonds could have only crystallized from fluids, as opposed to melts, due to the disequilibrium in major and/or trace element concentrations between the inclusions in single diamonds.

Many authors have linked the subduction of oceanic lithosphere with the formation of eclogite and eclogitic diamonds. MacGregor and Manton (1986) showed that the highly fractionated oxygen isotopes found in eclogitic xenoliths is consistent with seawater alteration. This suggests that they are metamorphic fragments of oceanic

lithosphere and/or oceanic crust with or without associated sediments (Helmstaedt and Gurney, 1984; Jagoutz et al., 1984; MacGregor and Manton, 1986). Other studies have indicated that oceanic crust can undergo partial melting (Kesson and Ringwood, 1989) or melt incongruently (Rudnick, 1995) and then be underplated onto the lithosphere.

The wide range of carbon isotopic compositions (-34 to +3‰) obtained for eclogitic diamonds is also suggestive of an input of oceanic carbon (Kirkley et al., 1991). Boyd and Pillinger (1994) found that diamonds with low $\delta^{13}C$ ($\delta^{13}C$ –19.4 to –9.5 ‰) tend to be enriched in $\delta^{15}N$ relative to air ($\delta^{15}N$ –3 to +16.4 ‰); the authors attribute this to the subduction of crustal material. The large range of diamond inclusion sulphide isotopes is also indicative of an organic source or possibly due to hydrothermal alteration of mid-ocean ridge basalt (Eldridge et al., 1991). Another possibility to explain the range of sulphur isotopes in diamond inclusions is the subduction of a sedimentary sulphide component into the diamond source regions, with part of the sulphur in the inclusions having been processed through the Archean atmosphere (Farquhar et al., 2002). Cartigny et al. (1998a; 1998b) suggest that fractionation processes can explain the wide range in carbon and nitrogen isotopic compositions obtained for eclogitic diamonds. The bulk of isotopic evidence supports an origin of eclogitic diamonds from subducted material, however.

Kesson and Ringwood (1989) suggest that dehydration of the subducted slab allows aqueous fluids to migrate upwards until they encounter eclogite (formerly basalt) at high enough pressures for partial melting to take place. They propose that the diamonds crystallize in situ from the siliceous melts produced. The source of carbon for the diamonds may come from biogenic carbon contained in subducted sediments, carbonate fluid from the dehydration of serpentine or carbonate minerals from the previous dehydration of the crust. The authors also suggest that these diverse sources are likely to account for the wide range of carbon and nitrogen isotopic compositions obtained from eclogitic diamonds.

The REE pattern of eclogitic garnet and clinopyroxene inclusions in diamonds (Stachel et al.; 2004) is similar to a MORB composition that has experienced moderate degrees of melt extraction (~10%) followed by minor enrichment in LREE. This information coupled with Eu-anomalies observed in eclogitic inclusions is indicative of a subduction origin for eclogitic diamonds. The authors indicate that the high equilibration temperatures of the inclusions suggest that the diamonds form through metasomatic

processes following the emplacement of eclogite in the cratonic lithosphere, as opposed to formation during the subduction of cold slabs.

1.2 Aims of the study

The discussion on formation of diamonds shows that further study is necessary, in particular multi-disciplinary study, to try and solve the questions of diamond formation. For this study a suite of diamonds containing, amongst others, extremely rare lherzolitic clinopyroxene inclusions was made available from Cullinan mine (formerly the Premier mine). It was hoped that this study of the diamonds and their inclusions would shed some light on the unusual nature of the mantle in the region of the Cullinan kimberlite pipe and the formation of the diamonds in this region.

The diamonds were described in terms of their physical characteristics (i.e. colour, crystal form, deformation features) and mineral inclusion content. Fourier transform infra-red analysis of the whole stones was performed in order to identify different diamond populations. This technique was also utilized to establish their time-averaged mantle temperatures based upon their nitrogen contents, aggregation state and age. The age of different diamond populations at Cullinan mine has been previously determined by Richardson et al. (1993). A number of the whole diamonds were polished into plates. The cathodoluminescence images obtained from the plates in conjunction with further detailed Fourier-transform infra-red analysis gave information on the growth histories of the diamonds.

The inclusions were liberated from the diamonds and used to obtain mineral chemistry information on the individual inclusions using an electron microprobe. This gave further evidence on the nature of the mantle in this region and allowed for temperatures and pressures of formation to be calculated. The garnet inclusions were also analysed using a laser ablation ICP-MS (Inductively Coupled Plasma – Mass Spectrometer) in order to obtain information on the trace element concentrations of the inclusions. This was done in order to get an indication of the metasomatic history of the mantle in this region.

The conclusions drawn from these analyses are brought together in the final chapter and an origin for the diamonds and evolution of the mantle in this region is proposed.

2. GEOLOGY

2.1 Regional setting

The Cullinan kimberlite is located in the north-eastern region of the Kaapvaal craton. The name of this mine was changed from the Premier diamond mine to the Cullinan diamond mine in November 2003. It will be referred to as the Cullinan mine in the text, but a point to note is that it is referred to as the Premier mine in many of the references. The craton formed and stabilized between 3.7 and 2.7 Ga (de Wit et al., 1992). The oldest terrains of the craton, the granite-greenstone terrains, formed between ~3.7-3.1 Ga. A lithospheric keel of at least 150 km was developed by 3.3-3.2 Ga (Richardson et al., 1984). These cratonic nuclei may have formed by stacking of light oceanic lithosphere formed after the mid oceanic ridges (MOR's) had sunk below sea level. A second period of continental growth, between 3.1-2.6 Ga, is likely to have formed through intra-continental and continental-margin processes amalgamating the nuclei. Finally major volcano-sedimentary basins in the late Archean led to the final stabilization of the craton (de Wit et al., 1992).

The Cullinan kimberlite intrudes into the Central Terrain of the Kaapvaal Craton, which consists of granitic gneisses and migmatites with granitoid domes (Anhaeusser & Burger, 1982). The Cullinan kimberlite also intrudes into Bushveld Igneous Complex (dated at 2.05 Ga; Tankard et al., 1982). The Cullinan mine lies within the NW-SE oriented band of relatively slow seismic velocities in the Kaapvaal craton mantle lithosphere (James et al., 2001). This band extends from the eastern Bushveld Igneous Complex westward into Botswana (Carlson et al., 2000). The band of lower-velocity mantle is attributed to refertilization, particularly in iron, of the mantle in this region and is likely to be related to the Bushveld igneous event (James et al., 2001; Griffin et al., 2003; Hoal, 2003). Many of the mantle xenoliths studied from Cullinan give Re-Os model ages of ~2.0 Ga, giving further evidence of substantial modification of the mantle in this region during the intrusion of the Bushveld Igneous Complex (Carlson et al., 1999).

2.2 Geological setting of the kimberlite

The Cullinan mine kimberlite is the largest known kimberlite in South Africa and is one of 11 kimberlite pipes in the Cullinan-Rayton area. It is located 37 km east-north-east of Pretoria and is a Group I kimberlite. The intrusion of the pipe has been dated at 1180 ± 30 Ma (Allsopp & Kramers, 1977). This is 870 million years younger than the intrusion of the Bushveld Igneous Complex (2.05 Ga; Tankard et al., 1982) into which the kimberlite intrudes (Figure 2.1).

2.2.1 Country rock

The wall rock to a depth of about 350 m is aphanitic felsite. The felsite has been correlated with the Rooiberg felsites, but the possibility that it is a product of feldspathisation of quartzite rocks of the Waterberg or Pretoria supergroups has not been ruled out (Bartlett, 1998). Below the felsite the pipe intrudes into norite of the Main zone of the Bushveld Igneous Complex until approximately 700 m below the surface. The wall rock below the norite consists of quartzites, shales, sandstones and dolomitic shales of the Transvaal Supergroup (De Beers internal report, unattributed, 1969). Large rafts of Waterberg quartzite and conglomerate were found in the pipe, but the Waterberg sediments have been eroded away at the surface. A layered gabbro sill, approximately 70 m thick with an east-west strike and a dip of 15-20 degrees to the north, cuts through the pipe and country rock. This sill is dated at 1150 Ma (Bartlett, 1998) and was first discovered at its shallowest point of 347 m below the surface. The kimberlite adjacent to the sill is metamorphosed to a distance of at least 15 m.

2.2.2 Kimberlite

The Cullinan pipe had a maximum length of 860 m in the east-west direction and a width of 400m in the north-south direction (Bartlett, 1998). There are a number of kimberlite intrusions and the various types of kimberlite present are described by their predominant matrix colour (Figure 2.2). The most abundant kimberlite is the grey kimberlite; it is a typical tuffisitic kimberlite breccia (TKB) with an inequigranular texture. This kimberlite

contains Waterberg quartzite rafts and fragments and lies in contact with the rim of the pipe everywhere except for the east side of the pipe. The brown kimberlite occupies most of the south-eastern lobe of the pipe and forms a crescentic column. This kimberlite increases in area with depth at the expense of the grey kimberlite and is also a TKB and texturally similar in appearance to the grey kimberlite. The black kimberlite is found in the western section of the mine and it forms a roughly circular column. This kimberlite is transitional between a hypabyssal facies kimberlite and a TKB facies kimberlite. Two types of kimberlite referred to, as pale piebald and dark piebald are carbonatised varieties of the black kimberlite. These facies are located around the carbonatite dykes, the pale piebald lying adjacent to the dykes; this facies has a gradational contact between itself and the dark piebald kimberlite. Black hypabyssal kimberlite occurs below the 615 m-level. Green kimberlite surrounds the black kimberlite. It is texturally and mineralogically similar to the black kimberlite and is believed to be an altered variety of the black kimberlite. The green kimberlite is also found in the eastern section of the mine as two bodies (Bartlett, 1998; De Beers Internal Report, unattributed, 1969).

2.2.3 Sequence of intrusion

It appears as though there were three main intrusive phases. First to intrude was the brown kimberlite; following this was the grey kimberlite. The black kimberlite is interpreted to be the last kimberlite to intrude. The remaining kimberlite types described above are believed to be altered or mixed kimberlites of these earlier intrusions. There was a final intrusion of carbonatite, mostly into the black kimberlite (De Beers Internal Report, unattributed, 1969).

2.2.4 Diamonds

Cullinan diamond mine is renowned for its large gem quality diamonds. It is estimated that 30% of production are gem quality (Bartlett, 1998). Some of the large gems produced from Cullinan include the Cullinan diamond (3106 carat, uncut), Star of Africa (two cut stones of 530.2 and 317.4 carats respectively) and the Centenary diamond (373 carat, cut; De Beers Consolidated Mines internal pamphlet).

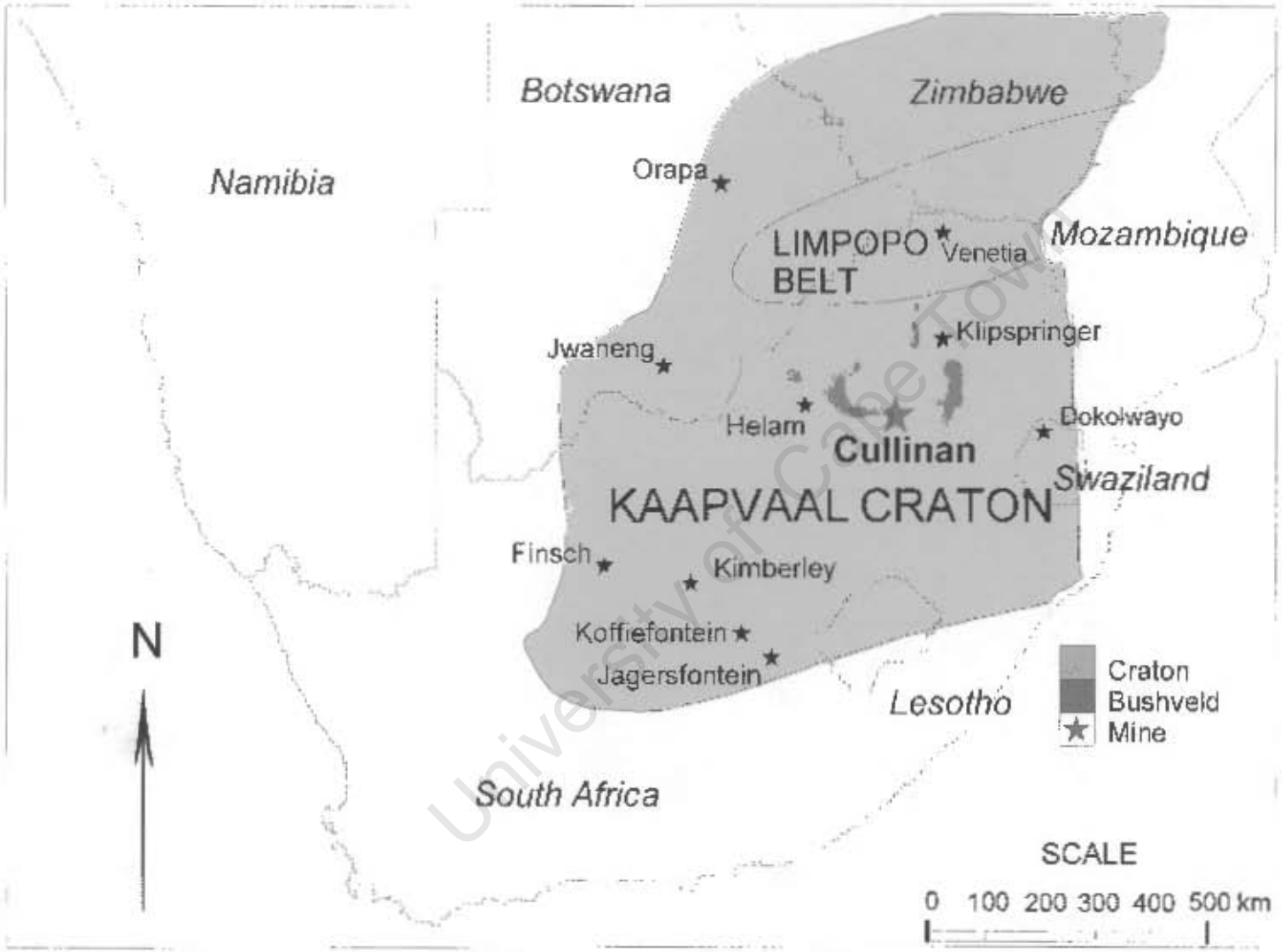

Figure 2.1: A schematic map of South Africa showing the location of various kimberlite pipes, the Bushveld Igneous Complex and the outline of the Kaapvaal and Zimbabwe Cratons. Modified after Westerlund (2000).

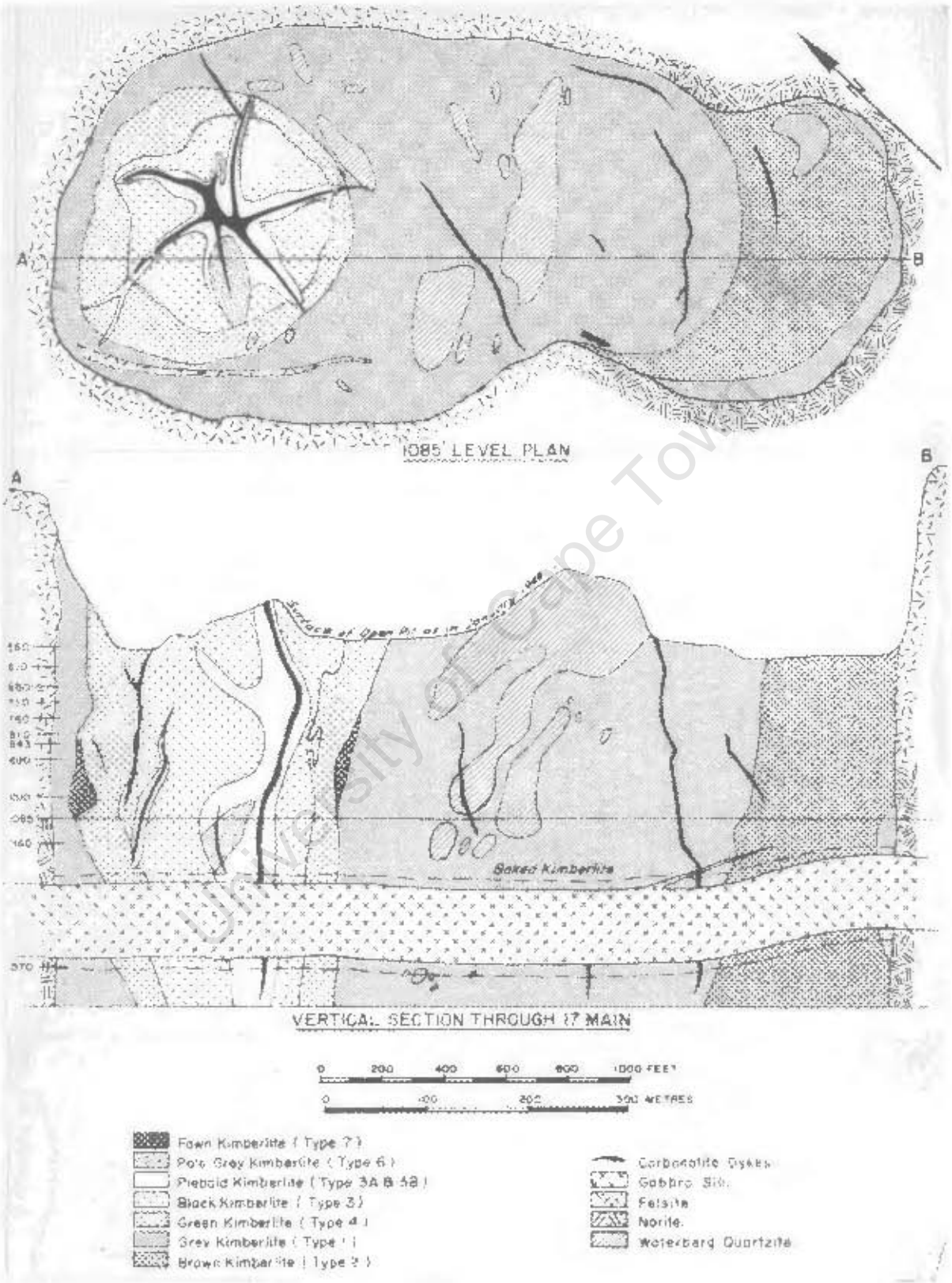

Figure 2.2: Generalized geological plan and section through the Cullinan Mine. After a De Beers Internal Report, unattributed, 1969.

3. PHYSICAL CHARACTERISTICS OF DIAMONDS

3.1 Introduction

The physical characteristics of diamonds are controlled by processes operating during diamond growth and residence in the mantle. Diamonds may further be modified during transport in the kimberlite (Robinson, 1979). Previous studies of diamond characteristics have shown that differences exist between diamonds on an inter-cratonic scale (e.g. Gurney, 1989; Robinson et al., 1989) as well as on a regional scale (Robinson et al., 1989). A detailed study of the suite of Cullinan diamonds was undertaken, firstly, in order to identify whether sub-populations of diamonds exist within this suite. Secondly, to determine what processes were responsible for the various diamond characteristics. This helps to establish the history of the diamonds from their formation to extraction from the kimberlite.

The sequence of events that affect diamonds, as proposed by Robinson (1979), are: crystallization, residence within the upper mantle, plastic deformation, resorption and etching, crystal breakage and further etching. Primary crystal form and in some cases colour is determined by the crystallisation environment, whilst the latter four processes are believed to take place during transport of the diamond to the surface. This indicates that the study of both 'primary' and 'secondary' physical characteristics may yield important information on the environment of diamond formation as well as transport within the kimberlite.

3.2 Nature of the sample

The diamonds that make up the suite for this study were all collected from the Cullinan Diamond mine and provided for study by Steve Richardson, from a collection donated by De Beers (J-982 samples) and from Judith Milledge (M samples). The suite selected consists of 100 whole diamonds. Of these 95 are peridotitic and 5 are eclogitic, based upon mineral inclusion types. The peridotitic diamonds are of the order of 2 mm in diameter and range from 0.033 – 0.125 carats. The eclogitic diamonds range from 0.010 – 0.024 carats. The peridotitic diamonds may be separated into three groups based upon their mineral inclusions.

There are those that contain non-touching, purple Cr-pyrope garnet and green diopside inclusions (Plate 3.1). Others that contain purple, Cr-pyrope garnet (Plate 3.2) and those that contain green diopside (Plate 3.3). The five eclogitic diamonds contain non-touching orange garnet and green omphacite. The sample suite selected contains a large amount of bias as the diamonds were primarily chosen for their mineral inclusions and secondly for their suitability for FTIR study (i.e. flat surfaces). This suite does not therefore quantitatively represent the sub-populations at the Cullinan mine.

Also included in this study to supplement the FTIR analyses and stable isotope work were 19 diamonds (P samples; now broken and kept in separate glass phials) from Cullinan Mine, used in a previous inclusion study by Steve Richardson (Richardson et al., 1993; Kimberlite Research Group (KRG) database). These diamonds had all previously contained garnet inclusions.

Thirteen diamonds were selected from the peridotitic suite and polished into plates parallel to {100} on two sides, in an attempt to investigate their internal chemical variations and growth histories (Section 4.3.1).

3.3 Physical characteristics

A detailed description of physical characteristics of the suite of Cullinan diamonds is presented in Appendix 1. General observations of the diamond suite are presented below.

3.3.1 Colour

The different colours of diamonds are caused by various impurities that absorb light in the visible spectrum (Harris, 1987). The most common colours of diamonds are colourless, yellow and brown (Harris et al., 1975). Other colours noted are green, mauve, pink, orange, blue, grey and black. Of the one hundred diamonds in the suite 93% are brown (Plate 3.4), 6% are colourless (Plate 3.1) and 1% are grey.

The brown colour is believed to be the result of graphite localised along (111) epigenetic glide planes (Urusovskaya and Orlov, 1964), which is suggested to form during plastic deformation of the diamonds in the upper mantle (Harris, 1992). A common surface manifestation of plastic deformation is lamination lines found on resorbed surfaces (Robinson, 1979). The minimum temperature and pressure for graphitisation are 930 °C and 4 GPa, based upon the diamond stability curve (De Vries, 1975; Bundy 1980). This suggests that the majority of samples in this suite have experienced elevated temperatures and plastic deformation. Brown diamonds may be both Type I and Type II (Chapter 4).

Colourless diamonds may either contain very low or abundant nitrogen impurity (Robinson, 1979). It is thought that nitrogen in the colourless diamonds with substantial nitrogen impurity are associated with the submicroscopic platelets, this results in absorption in the ultraviolet region, which does not affect colour (Robinson, 1979). Of the six colourless diamonds in this suite, two contain abundant nitrogen with very strong platelet peaks and four show no nitrogen to very little nitrogen with no platelet peaks (Chapter 4).

The colour of the single grey diamond could be attributed to an abundance of graphite due to internal graphitisation along glide planes. Natural diamonds grown at low temperatures are usually black (Bovenkerk, 1961), which may suggest that low temperatures of crystallization may produce a natural grey diamond (Robinson, 1979). Another more likely possibility is that the diamond contains abundant black submicroscopic inclusions (Robinson, 1979).

3.3.2 Crystal Form

The two primary diamond forms are octahedra and cubes. Octahedra exhibit planar faces, whereas cubes tend to display rough, indented surfaces (Robinson, 1979). Primary crystal forms of diamonds from southern Africa tend to be octahedra and macles (Harris et al., 1975). These primary forms may be resorbed by oxidising agents; this begins at the 4-fold axis of octahedra and at the corners of cubes, resulting in the tetrahexahedroid (TTH) form (Robinson, 1979). Tetrahexahedroids exhibit curved surfaces. A loss of approximately 45% of the mass of the diamond is required to convert an octahedron into a TTH (Robinson, 1979),

as shown in Figure 3.1. Due to the rough nature of the cube form's surfaces it is not possible to accurately estimate the percentage of mass lost when resorbed to form a TTH, although the conversion should involve substantially greater mass loss than an octahedron (Robinson, 1979).

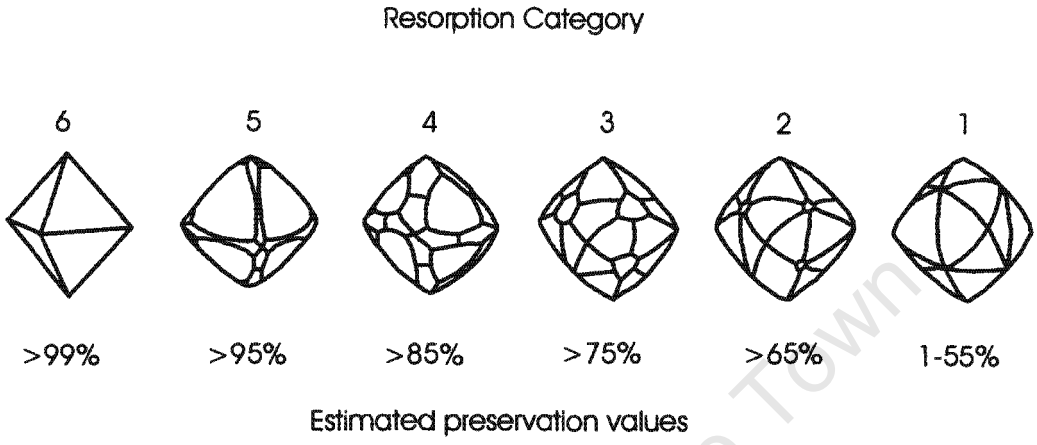

Figure 3.1 The stages of resorption of a perfect octahedron through to the tetrahexahedroid (from Robinson, 1979). The percentage indicates the volume of preservation of the original octahedron.

Diamonds may also occur as aggregates and twins. The most common of the twins is the macle, a contact twin. This form is usually described as a tabular triangular crystal, with two (111) faces divided by a twin plane parallel to the faces (Harris et al., 1975). Aggregates are composed of two or more crystals of any shape; which are joined together along a common edge or face to form a collection of crystals (Harris et al., 1975). In this suite of diamonds all the aggregates occur as octahedral aggregates. Irregular diamonds are those diamonds that do not display any crystal faces and do not fit into any of the previously defined groups. In this suite, the majority of diamonds (45%) have an octahedral form (Plate 3.2), 15% have a TTH form (Plate 3.4), 29% are macles (Plate 3.5), 10% are octahedral aggregates (Plate 3.6) and one is irregular. Of the octahedra and macles, a large percentage (39%) show partial resorption of their surfaces.

3.3.3 Crystal state

Crystal regularity refers to the deviation of a crystal from its regular crystal form (Otter, 1990). The distortion may develop during crystal growth or from preferential resorption in certain directions. Most diamonds of this suite are distorted in some way from a perfect form, either slightly elongated and/or flattened. This departure from crystal regularity has been divided into three categories: A ($x = y = z$), B ($x = y \neq z$) and C ($x >> z$). The majority of crystals (88%) are type B with 8% type A and 4% severely flattened type C crystals. This would suggest that the growth environment for the majority of these diamonds deviated from ideal crystallization conditions.

Chinn (1995) classified the crystal state of diamonds as whole (0% volume loss), chipped (<10% volume loss), broken (10-50% volume loss) and fragment (>50% volume loss). The majority of diamonds in this suite are whole (83%), whereas the remaining 17% are broken. Of these broken diamonds, 12 have fracture surfaces that contain a cubo-octahedral pit, these pits are believed to have contained a mineral inclusion. This fracturing is indicative of differential expansion between the diamond and the mineral inclusion from decompression during the ascent to the surface (Sutton, 1928). These fracture surfaces are commonly etched and resorbed. Only five diamonds show 'fresh' fracture surfaces indicating that they were broken subsequent to etching and resorption; possibly during a brittle deformation event or during crushing processes at the mine.

3.3.4 Surface features

Surface features may be divided into primary and secondary features. Primary features are considered to have developed on the crystal surface prior to their liberation or extraction from a kimberlite (Robinson, 1979). Surface features may also be further divided into those that were caused by the growth of the diamond, those caused by deformation and those attributed to processes of oxidation and dissolution.

3.3.4.1 Features associated with crystal growth

Triangular plates are noted on some octahedral surfaces in this suite. Experimentally plates have been shown to form under conditions favouring rapid nucleation, with each plate having separate nucleation (Wentorf, 1965). It is likely that natural diamonds form in similar conditions. Serrate laminae are the result of the stacking of triangular plates on the octahedral surface (Robinson, 1979). These features are associated with diamonds enclosed within xenoliths (Otter, 1990) and are termed xenolithic features. In this suite 47% of the diamonds show triangular plates and/or serrate laminae.

3.3.4.2 Features associated with deformation

On resorbed crystals lamination lines are common, these are best seen near four-fold axial corners (Robinson, 1979). These lines are closely spaced and run parallel to cleavage planes of the diamond. They are a result of plastic slip (Harris, 1992), which occurs at temperatures in excess of 1000 °C at 30 kbar or at lower temperatures with higher pressures (De Vries, 1975). Lamination lines are visible on 33% of the diamonds in this suite; all of the diamonds are brown except one colourless TTH.

3.3.4.3 Features associated with oxidation and etching

The predominant surface feature, of this type, on 26% of the diamonds from this suite is negatively oriented triangular pits (trigons). Trigons have been shown to develop through etching of the diamond. A negatively oriented triangular etch pit has an opposite orientation to the octahedral face, whereas a positively oriented triangular pit has the same orientation as the octahedral face. It is thought that steam and wet carbon dioxide gas are likely etchants, when temperatures are in excess of 950°C (Robinson, 1979). Trigons may be pyramidal or flat-bottomed. A reason for flat-bottomed trigons may be that they stopped developing on a surface that was resistant to etching (Robinson, 1979).

Some diamonds in this suite also exhibit hexagonal etch pits, which are typically flat-bottomed. They are believed to have formed from a combination of two etchants; oxygen producing positively oriented trigonal pits and either steam or wet carbon dioxide producing negatively oriented trigonal pits at low pressures and with temperatures between 950 and 1000 °C (Phaal, 1965). Another feature exhibited on 12 of the diamonds in the suite is large

pits that commonly have octahedral sides. These pits are interpreted to have once contained an inclusion that has subsequently been liberated from the diamond (Robinson, 1979). The octahedral sides may be the mould of an octahedral inclusion or may reflect the cleavage of diamond as a piece of it was forced away as the inclusion broke free (Prinz et al., 1975; Robinson, 1979). Resorption channels/ruts develop along cracks or planar zones of weakness in the diamond. They are caused by etchants and are often seen to radiate from inclusion pits (Robinson, 1979). Orlov (1973) suggests that sinuous ruts form from the migration of oxidising fluids along cracks within the host xenolith.

Some diamonds of this suite display fine frosting. This may occur on both TTH and octahedral surfaces, and is likely to be caused by rapid brief etching of the diamond surface (Robinson, 1979). Commonly associated with frosted diamond surfaces is the development of a fine, black, graphite coating. This may have been deposited during reasonably low temperature oxidation (Robinson, 1979).

Knob-like asperities are also observed on a few of the diamonds in this suite. They are found on octahedral and TTH diamonds. These features vary from circular on TTH surfaces to almost triangular on octahedral surfaces, otherwise they can be irregular. This feature is commonly associated with graphitisation and they are always identical in colour to the rest of the diamond. This would indicate that they are not growth features, but resorption features (Robinson, 1979).

A common feature on the TTH and partially resorbed diamonds of this suite is elongate hillocks. These are long semi-cylindrical to semi-ellipsoidal bands, which form through resorption of the diamond surface. The elongation is parallel to the growth of the octahedral layers and the hillocks therefore reflect a difference in the resistance to resorption of individual octahedral layers (Robinson, 1979).

Corrosion sculpture is defined as fairly deep, irregular depressions on the diamond surface. The bottom of the depression tends to be striated. This feature post-dates resorption; which forms hillocks, but may occur before the development of trigons (Robinson, 1979). It is believed that corrosion sculpture is formed by rapid brief etching at temperatures exceeding 950 °C, with steam as a possible etchant (Robinson, 1979).

3.4 Discussion and conclusions

The majority of diamonds of this suite are brown (93%), however this colour cannot be solely attributed to graphitisation associated with plastic deformation; as only 32% of these diamonds display lamination lines. Roughly a third of the brown diamonds must have experienced a period of deformation that either occurred before the formation of the rest of the suite, or these diamonds were not spatially associated with the other brown diamonds. The single colourless diamond that displays lamination lines was likely to have experienced deformation outside of the stability field of graphite.

About 40% of the diamonds display physical characteristics indicative of partial resorption. Haggerty (1986) suggests that resorption occurs before the diamonds become entrained in the kimberlite, during their residence in the mantle. The different degrees of resorption would indicate however, that resorption occurs in the kimberlite, as the diamonds are liberated from their host xenoliths, as suggested by Robinson et al. (1989).

It has been previously observed that trigons may post-date corrosion sculpture (Robinson, 1979). As demonstrated by Phaal (1965) trigons require a temperature of at least 950 °C to form, this gives a minimum temperature of formation for corrosion sculpture. About 20% of the diamonds in this suite display corrosion sculpture, indicating that they were released at greater depths within the kimberlite compared to the rest of the suite.

There are 57 diamonds in the suite that display xenolithic growth features such as sharp edges and flat crystal faces, serrate laminae and triangular plates. Of these 11 have trigons or hexagonal etch pits developed on their surfaces. This indicates these few diamonds must have been released from their host xenoliths at sufficient depths to allow for trigons and hexagonal etch pits to develop; however the majority of diamonds, displaying xenolithic growth features, were only released from their xenoliths at a late stage.

A comparison was made between certain physical characteristics (colour, shape and resorption features) and the mineral chemistry of the inclusions. No correlation was observed between these variables.

Plate 3.1 A colourless octahedron containing a purple Cr-pyrope and a green Cr-diopside.

Plate 3.2 A sharp edge, sharp face octahedron enclosing a large, purple Cr-pyrope inclusion.

Plate 3.3 A brown octahedron with two green diopside inclusions and some small graphite planes.

Plate 3.4 A strong brown flattened tetrahexahedroid diamond with a purple Cr-pyrope inclusion.

Plate 3.5 A light brown macle containing a purple Cr-pyrope garnet and two light green diopside inclusions.

Plate 3.6 A brown octahedral aggregate enclosing a large green diopside inclusion.

Plates 3.1 – 3.6: Each diamond is approximately 2mm in its longest dimension.

4. FOURIER TRANSFORM INFRARED SPECTROSCOPY OF THE DIAMONDS

4.1 Introduction

Most diamonds show absorption in the mid-infrared range (IR), due to substitutional impurities. Diamonds can be divided into two broad groups; Type I diamonds display IR and ultraviolet (UV) absorption and Type II do not show any absorption (Robertson et al, 1934). These groups have been further subdivided into Types IaA, IaB, Ib, IIa and IIb (Clark et al, 1992; Evans, 1992).

Type IIa diamonds are essentially free of substitutional impurities and only display intrinsic lattice absorption in the 4000-1500 cm^{-1} region due to two- and three-phonon transitions. Type IIb diamonds contain trace quantities of boron and natural diamonds of this type are extremely rare. The boron causes absorption in the two-phonon region at 2460 cm^{-1} and commonly imparts a blue colour to the diamond (Collins, 1982).

Nitrogen is incorporated into the diamond lattice as single atoms substituting for carbon during diamond growth. The nitrogen atoms cause one-phonon transitions due to an alteration in the diamond lattice symmetry. Type I diamonds carry nitrogen in different lattice arrangements. Type Ib diamonds carry nitrogen as dispersed atoms with concentrations of about 50-300 atomic ppm (Evans, 1992) and display absorption at 1130 cm^{-1}. During residence at mantle temperatures and pressures, the singly-substituted nitrogen atoms aggregate into multiples of atoms within the diamond. This occurs via a series of thermally controlled diffusion processes (Davies, 1980; Evans and Qi, 1982). Owing to long residence times of most diamonds (Richardson, 1986) there are very few natural Type Ib diamonds. Those that do exist require a young crystallization age and/or unusually cool conditions of mantle storage (Taylor et al, 1996). The first aggregates to form are A aggregates, which characterise Type IaA diamonds (Evans and Qi, 1982). A aggregates consist of two adjacent nitrogen atoms (Davies, 1976; Jones et al, 1992). Type IaA diamonds show strong absorption at 1282 cm^{-1}, with a subsidiary absorption peak at 1215 cm^{-1}. Further aggregation leads to the development of B aggregates, which are characteristic of Type IaB diamonds. These diamonds show prominent absorption at 1174 cm^{-1} and a subsidiary peak at 1282 cm^{-1}. There is another contribution to the peak at 1282 cm^{-1}, the D component, which has been ascribed to

platelets (Clark & Davey, 1984; Woods, 1986; Evans et al., 1995). The B aggregates consist of four nitrogen atoms arranged tetrahedrally about a vacancy in the diamond structure (Jones et al., 1992). Type IaAB diamonds contain A and B aggregates in differing proportions, with a large variation in nitrogen concentrations from a few hundred to several thousand ppm (Woods, 1986). Owing to the length of time required for a complete transition from Type IaA to Type IaB, at mantle temperatures, the majority of diamonds are of Type IaAB. During the aggregation of pairs of A aggregates to B aggregates there is also a subordinate pairing of A aggregates and single, dispersed nitrogen atoms to form N3 centres (Evans & Qi, 1982; Woods, 1986). These centres do not display an absorption in the one-phonon region of the IR range, but do show absorption in the visible and UV ranges (Evans & Qi, 1982; Woods, 1986).

Platelets are planar features occurring in the cubic planes of the diamond, they can be observed by electron microscope (Evans and Phaal, 1962) and in X-ray diffraction patterns (Raman, 1944). They range in size from 8nm to a few μm (Evans and Qi, 1982) and have an IR absorption peak at 1359-1378 cm^{-1} (Sobolev et al., 1968), termed B'. The position of this peak varies with the size of the platelets, with larger peaks having lower wavenumbers (Hanley et al., 1977; Clackson et al., 1990). The intensity of the integrated platelet area (I[B']) can be directly correlated to the X-ray spike intensity (Woods, 1986). The intensity is a measure of the platelet concentration.

There is a strict positive correlation between the intensity of the B' peak (I[B']) and the absorption coefficient for B aggregates at 1282 cm^{-1} (μ^B[1282]) for "regular" IaAB diamonds. This does not hold for "irregular" IaAB diamonds (Woods, 1986). These diamonds are highly aggregated with a small or deficient platelet peak. This has been attributed to catastrophic degradation of the platelets (Woods, 1986). During high-P/T experiments, it has been observed that the B' and D peaks of highly aggregated diamonds disappear at high temperatures (Evans et al., 1995). The D peak, at 1282 cm^{-1}, is therefore associated with platelets. With the degradation of platelets new defects develop, called voidites. These are believed to consist entirely of nitrogen, which grow on dislocations that bound the platelets and at the platelet/matrix interfaces (Evans et al., 1995).

There is a debate on the composition of platelets; one model suggests that nitrogen is a major constituent (e.g.: Lang, 1964), whilst the other favours carbon (e.g.: Woods, 1986).

Nitrogen is only detected at low concentrations within platelets (Berger & Pennycook, 1982), which suggests that Woods (1986) model is correct. During the formation of B aggregates, a single carbon atom is released into the diamond lattice and a vacancy is created. The platelets are suggested to form as the single carbon atoms aggregate, with minor nitrogen also able to aggregate into the structure (Woods, 1986). This would explain the degradation of platelets, as a carbon atom would relax back into the lattice at high temperatures (Mendelssohn & Milledge, 1995).

Another diamond defect is due to hydrogen. This defect is associated with peaks at 3107 cm^{-1} and 1407 cm^{-1} in the IR spectrum (Chrenko et al., 1967). These absorptions are attributed to a C-H stretch vibration (Woods & Collins, 1983). To date there is no experimental data on correlating hydrogen peak intensities to hydrogen concentrations. They are useful for comparing different diamonds and areas within individual diamonds. Carbon dioxide is another defect that causes absorption in the IR range at 650 cm^{-1} and 2376 cm^{-1} (Schrauder & Navon, 1993; Chinn, 1995). No peaks have been observed at these wavenumbers in the current study and thus they will not be considered further.

4.2 Quantitative analysis of IR absorption spectra

Using methods described in Appendix 2 the nitrogen aggregation state and nitrogen concentration of the diamonds can be obtained. This information can be used in time-temperature determinations for individual diamonds. The amount of nitrogen aggregation in a diamond is dependant upon the nitrogen concentration as well as the mantle residence time and temperature. Temperature is the more sensitive of the two parameters and can be fairly well estimated using a rough time constraint in the order of hundreds of millions to billions of years. Estimating the residence time of diamonds is less accurate as it is dependant upon temperature, which is time averaged. It is mostly utilised to separate ancient and more recent diamond populations (Mendelssohn & Milledge, 1995).

A brief explanation of the technique will be discussed here, but for a comprehensive overview of this technique, the reader is referred to Mendelssohn and Milledge (1995). The spreadsheet developed by Mendelssohn and Milledge (1995), used in this analysis, investigates the following peaks: Platelet Peak ~1365 cm^{-1} (T), Raman edge ~1328 cm^{-1} (E),

IaAmax ~1282 cm^{-1} (P), Dip ~1242 cm^{-1} (D), IaBmax ~1174 cm^{-1} (Q) and subsidiary peaks at 1100 cm^{-1} (R) and 1010 cm^{-1} (S). It is assumed that diamonds evolve in a linear combination from pure Type IaA to Type IaB; from this, simulated intermediate spectra can be used to estimate the amount of aggregation (Figure 4.1). It is essential to treat each spectrum individually as there are various changes in the spectra with differing amounts of aggregation or nitrogen concentration. An example of this is in samples with high nitrogen contents P, D and Q peaks may be off scale. Another example is in highly aggregated samples where Q shows a large variation and if there is less than 10% B aggregates it contributes to the peak at 1282 cm^{-1}, peak E becomes unreliable and peaks R and S are small in comparison with peak P. The amount of aggregation also effects the position of the Q peak and the IaA absorption at ~ 1215 cm^{-1} is swamped by the IaB absorption when IaB is ~ 7% (Davies, 1980; Mendelssohn & Milledge, 1995). From this it is possible to use the position of Q at low aggregation (B<10%) to estimate the amount of aggregation.

The nitrogen concentration of the diamonds is derived using the method of Mendelssohn & Milledge (1995) in the following way:

$$N(ppm) = :(1282\ cm^{-1}) \times [N/mm(IaA) + N/\%B \times (\%Bused)]$$

Where:

$$N/\%B = [N(B) - N(A)]/100$$

and N(A) and N(B) are experimentally derived nitrogen concentrations corresponding to absorption coefficients per millimetre diamond at 1282 cm^{-1} for A and B aggregates respectively.

There are a number of different absorption coefficients that can be used for the A and B aggregates at 1282 cm^{-1} (e.g. Evans & Qi, 1982; Woods et al, 1990). The variation in temperature calculated using these methods is only a few degrees. Therefore the absorption coefficients $:^{A}[1282]$ = 1/mm for 150 ppm and $:^{B}[1282]$ = 1/mm for 650 ppm have been used (Mendelssohn & Milledge, 1995). The measured absorption is normalised to the intrinsic absorption of the diamond, as the actual thickness is not known. The ratio of absorption at 1992 cm^{-1} is 1.23/mm, which is the known absorption value due to lattice vibrations within a 1mm diamond at that wavenumber.

The estimates of time-averaged mantle residence temperatures are calculated based upon the assumption that the formation of B aggregates from A aggregates obeys second order kinetics. The estimation is as follows:

$$T_{NA}(°C) = -E_A/R \times \{\ln(([N_{tot}/N_A] - 1)/[t_{MR} \times N_{tot} \times A])\}^{-1} - 273.15$$

Where:

N_{tot} = concentration of nitrogen (atomic ppm)

E_A/R = activation energy for A to B aggregation / gas constant (81 160 K)

E_A = 7.03 eV (Taylor et al., 1990)

$N_{(A)}$ = Nitrogen occurring as A aggregates (atomic ppm)

A = Arrhenius constant = 2.94181×10^5 $s^{-1}ppm^{-1}$

T_{MR} = Mantle residence time

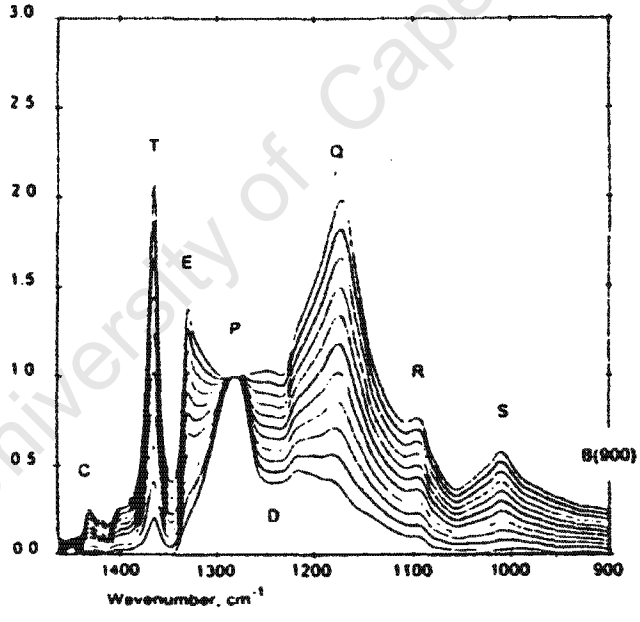

Figure 4.1 A composite spectrum showing the locations at which data are extracted for spectra in the IaA – IaB aggregation series after Mendelssohn & Milledge (1995). Variations in position and intensities are also illustrated. T: Platelet Peak ~1365 cm^{-1} E: Raman edge ~1328 cm^{-1}, P: IaAmax ~1282 cm^{-1}, D: Dip ~1242 cm^{-1}, Q: IaBmax ~1174 cm^{-1}, R: subsidiary peak at 1174 cm^{-1} and S: subsidiary peak at 1010 cm^{-1}.

The error on nitrogen concentrations and aggregation states is difficult to quantify as it is dependant on the level of fit between the measured spectrum and the modelled spectrum on a spectrum by spectrum basis. Any spectra of poor quality (bad fit) were not included in the results below. The error for nitrogen aggregation and concentration is generally accepted to be on the order of 10 – 20%, although this is dependant on spectral quality (Fanus Viljoen, Pers. comm., 2005). The errors on calculated time-averaged mantle residence temperatures also vary depending upon the quality of the spectra.

4.3 Quantitative FTIR measurement of Cullinan diamonds

4.3.1 Diamond plates

Thirteen diamonds from the peridotitic J-982 samples were polished parallel to {100} on two sides in an attempt to study the internal chemical variation within the diamonds in detail, as well as to better understand the growth of the diamonds. In order to achieve this cathodoluminescence (CL) images of both sides of each diamond were taken and these were used in conjunction with FTIR traverses across the plates. Two types of CL images were collected, one with the electron microscope (black and white images) and the other with an optical microscope (coloured images). The optical CL images show inclusions within the diamond. Bright areas on the electron microscope images correspond to blue or yellow-green areas on the optical images. Bright areas correspond to nitrogen carrying diamond or Type I diamond (Davies et al., 1999; Westerlund, 2000). The dark grey to black areas on the electron microscope images correspond to dark blue areas on the optical images. These areas are deficient in nitrogen or Type II diamond (Davies et al., 1999; Westerlund, 2000). Yellow-green luminescence has been interpreted to indicate deformation of the diamond (Daniels & Gurney, 1999). The CL images show approximate positions of the FTIR analyses, as the IR microscope does not have a sensitive position control. The procedure for FTIR and CL is given in Appendix 2. The FTIR data for the plates is presented in Table A.2.1.

Mendelssohn & Milledge (1995) show that growth layers are commonly inclined to the cut of the diamond plates therefore single IR analyses are likely to sample more than one type of growth zone. This leads to inaccurate results as demonstrated by the diagram of a

hypothetical diamond plate (Figure 4.2). This plate contains two growth layers of Type I and Type II diamond, which are inclined to the surface of the plate. The diamond core is Type I with a nitrogen concentration of 1000 ppm with the percentage of nitrogen as B aggregates (%N as B) of 50%. The outer growth layer consists of Type II diamond. Analysis (B) samples the diamond core giving a nitrogen concentration of 1000 ppm and %N as B of 50%. Analysis C samples only Type II diamond. Analysis A samples 50% of Type I and 50% of Type II diamond; this gives a nitrogen concentration of 500 ppm and the %N as B of 50%. This overestimation of the %N as B combined with a lower value for the nitrogen concentration causes an overestimation in the estimated mantle residence temperature for that analysis.

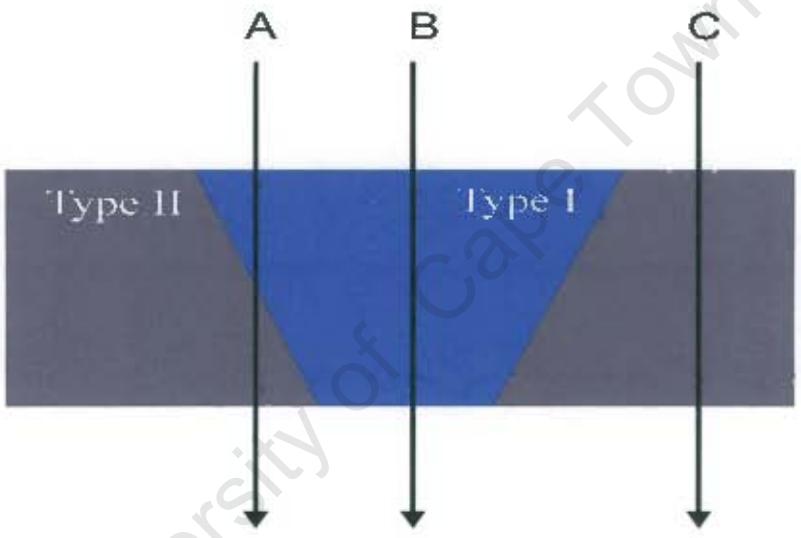

Figure 4.2 A cross-section of a hypothetical diamond plate, showing Type I and Type II diamond. The locations for paths A, B and C are shown with arrows.

Three populations of diamonds have been identified at Cullinan with respect to their age. The harzburgite paragenesis has been inferred to be 3.2 Ga; as the neodymium and strontium isotope signatures of the Cullinan harzburgitic diamonds are consistent with those diamonds from Kimberley and Finsch (Richardson et al., 1993). The lherzolite paragenesis has been dated at 1.93 ± 0.04 Ga and the eclogitic paragenesis at 1.15 ± 0.06 Ga (Richardson et al., 1993). The age of emplacement of the pipe has been dated at 1.18 ± 0.03 Ga (Allsopp & Kramers, 1977). The residence time of the different parageneses is obtained by subtracting the age of the emplacement of the pipe from the age of the paragenesis. This gives the

residence time in the mantle of 2.02 billion years for the harzburgitic paragenesis and 0.75 billion years for the lherzolitic paragenesis. It is assumed that the eclogitic inclusions formed immediately prior to the emplacement of the kimberlite pipe, as their ages are within error of one another. A residence time of 0.01 billion years has been used for the eclogitic parageneses. These residence times were initially used to calculate the time-averaged mantle temperatures for the parageneses. However, it was observed that there was very little difference between the harzburgitic and lherzolitic diamonds in terms of their nitrogen aggregation state, content and time-averaged mantle temperatures. Evidence from the mineral inclusion compositions, pressures and temperatures of formation of the diamonds (Chapters 6 & 8), show that there are continuous, linear, chemical trends between these parageneses and that they have similar temperatures and pressures of formation. For the above reasons it is believed that the harzburgitic paragenesis recrystallized during the formation of the younger lherzolitic paragenesis. Following this assumption the time-averaged mantle temperatures of the diamonds were recalculated using a mantle residence time of 0.75 billion years for both the harzburgitic and lherzolitic parageneses (unless stated otherwise).

FTIR analyses were taken at various points across the diamond plates in order to investigate the changes associated with growth of the diamonds. The following diagrams (Figures 4.3 & 4.4) show the percentage of nitrogen as B aggregates versus the nitrogen concentration in log units for the diamond plates. Lines of constant temperature (isotherms) are also shown on these plots. The information has been plotted on two diagrams for clarity. Each diamond plate is discussed in more detail in sections 4.3.1.1 – 4.3.1.13. Included with the discussion and images of each of the plates are bivariate plots of the variables obtained from the FTIR analyses. The approximate position of the FTIR analyses has been indicated by numbered boxes on the CL images. The colour of the boxes corresponds to the colour of the vertices on the bivariate plots. Those analyses not plotted on the bivariate plots are demarcated by green boxes. The coloured arrows indicate the traverse of points plotted in the bivariate plots. The tail of the arrows on the CL images correspond to the extreme left of the plots and the head of the arrows correspond to the extreme right of the bivariate plots. The numbers indicate the order of analyses, not the order of points on the bivariate plots. These numbers correspond to the analyses listed in Appendix 2 (Table A.2.1).

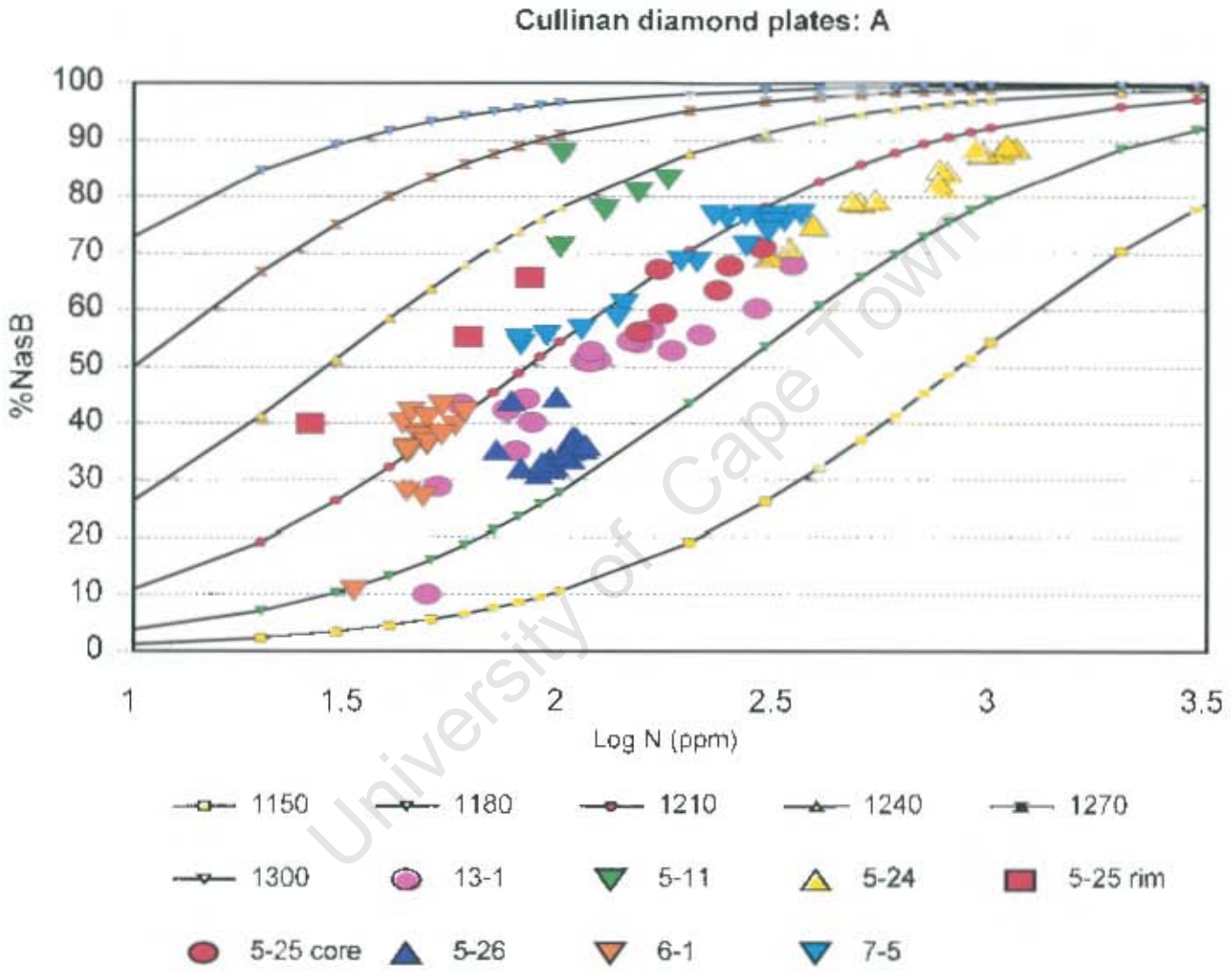

Figure 4.3 A plot of % N as B vs. nitrogen concentration in log units, for the Cullinan diamond plates using a residence time of 0.75 billion years; with the exception of Plate 5-25 core, where a residence time of 2.02 billion years was used. The values of the isotherms are in °C.

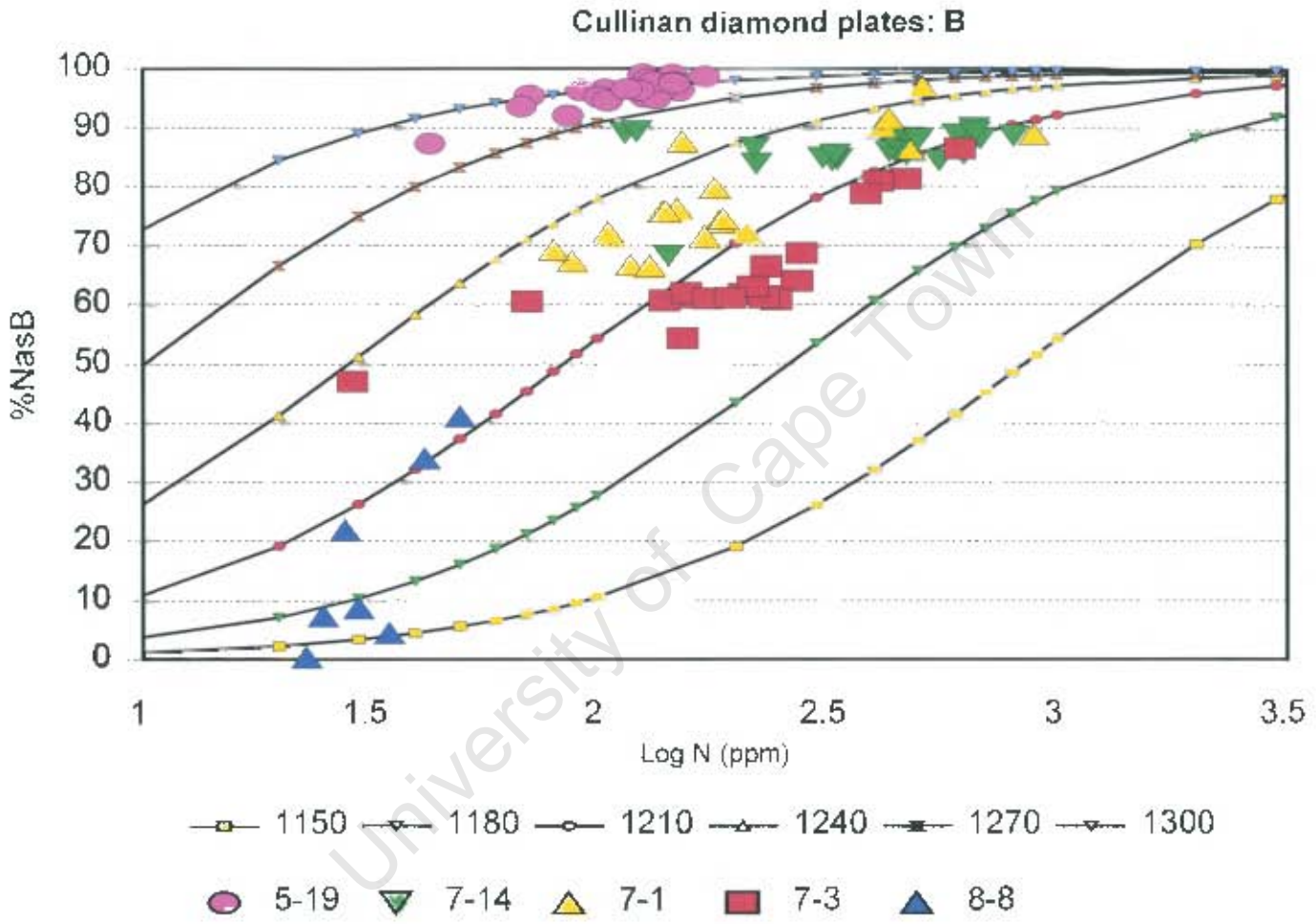

Figure 4.4 A plot of % N as B vs. nitrogen concentration in log units, for the remainder of the Cullinan diamond plates using a residence time of 0.75 billion years. The values of the isotherms are in °C.

4.3.1.1 Plate 5-25

Plate J/982 5-25 was cut from a brown, partially resorbed octahedron, which contains one purple Cr-pyrope inclusion, a few clear inclusions and a lot of small graphite planes. This plate displays a large resorbed core of high luminescence that contains all of the inclusions (Figure 4.5c). There are well developed octahedral growth zones extending from the core to the edge of the diamond plate (Figure 4.5 a & b). The octahedral zones of the plates dip inwards from the front towards the back of the plate.

The nitrogen concentration varies dramatically across the plate from below detection (20 ppm) to 294 ppm. There is very little nitrogen in the octahedral zones surrounding the core (<85 ppm); this is reflected in the sharp increase in nitrogen content in the traverses across the plate (Figures 4.5 e.i & f.i.). There is a similar trend seen in the amount of nitrogen as B aggregates in the traverse across the back of the plate, with a large range of values of 0-70% (Figure 4.5 f.ii). The trend in nitrogen as B aggregates is less pronounced in the front traverses (Figure 4.5 e.ii). The plots of platelet intensity show that it follows an almost identical trend to that of the nitrogen concentration (Figure 4.5 e.iii & f.iii). The hydrogen peak intensities generally increase across the core and drop off sharply on either side (Figure 4.5 e,iv & f.iv).

The large differences in nitrogen concentration and aggregation between the core and the rim of this diamond suggest that the core might be significantly older. It has therefore been assumed that the core formed at 3.2 Ga (during the growth of the harzburgitic diamonds) and the rim formed at 1.93 Ga (during the growth of the lherzolitic diamonds). This gives a range of temperatures of 1175 – 1187 °C for the core and 1228 – 1233 °C for the remainder of the diamond (Figure 4.3). Alternatively if the diamond is believed to have completely recrystallized at 1.93 Ga, the range of temperatures obtained is 1204 – 1233 °C.

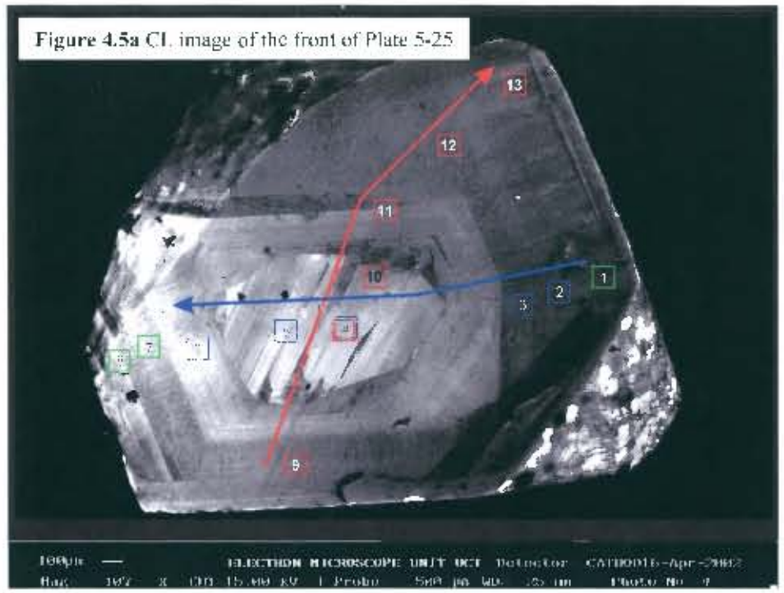

Figure 4.5a CL image of the front of Plate 5-25

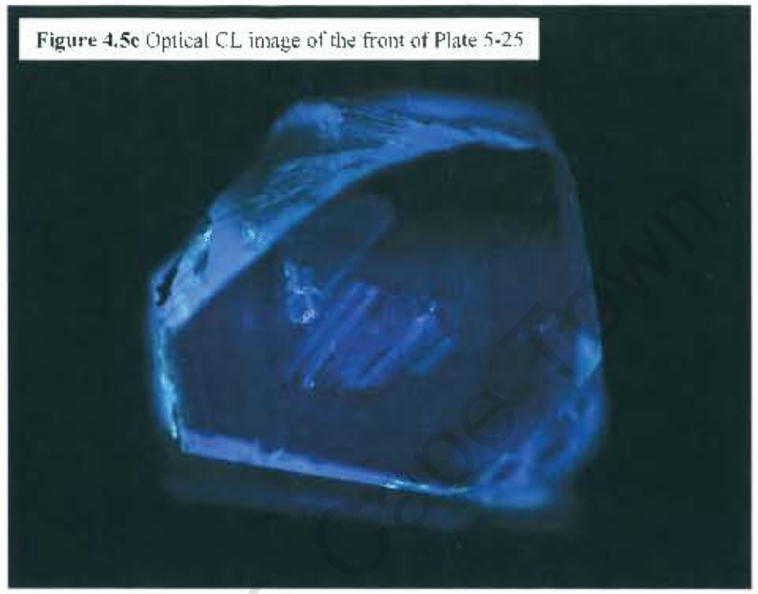

Figure 4.5c Optical CL image of the front of Plate 5-25

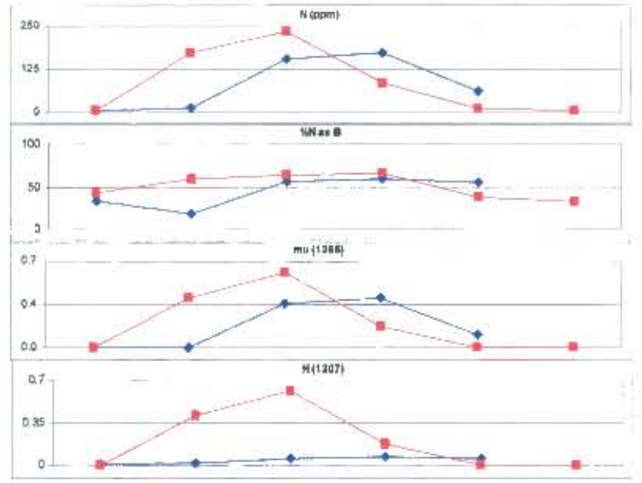

Figure 4.5e Graphs showing the variation of variables i-iv across the front of Plate 5-25: i. N (ppm), ii. %N as B; iii. mu (1365); iv. H (3107)

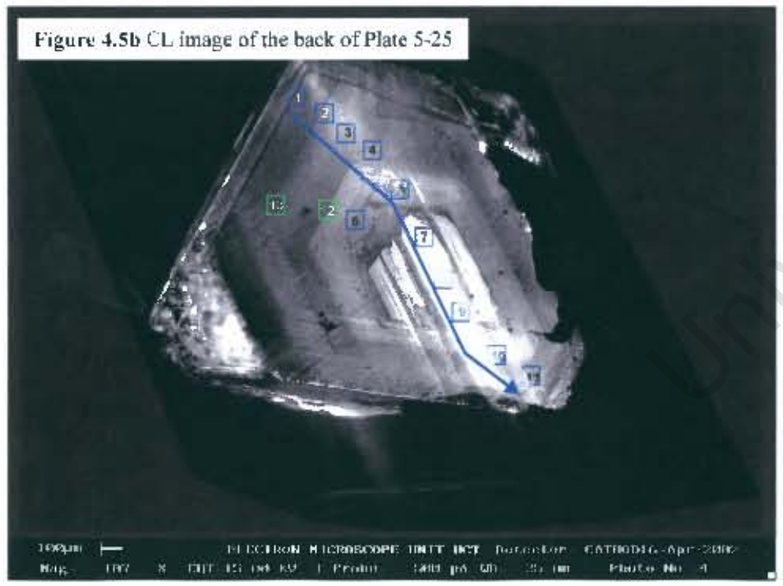

Figure 4.5b CL image of the back of Plate 5-25

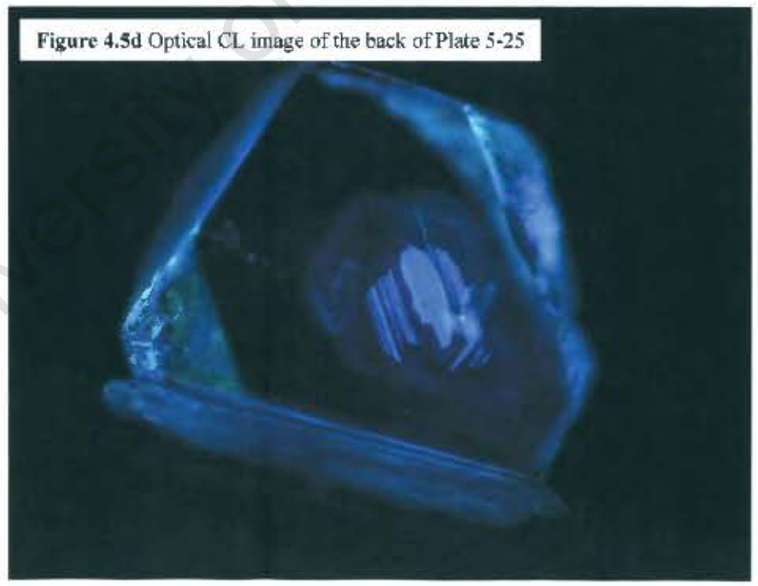

Figure 4.5d Optical CL image of the back of Plate 5-25

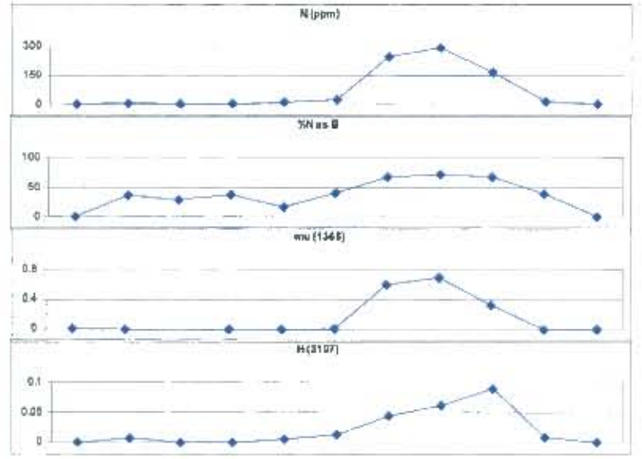

Figure 4.5f Graphs showing the variation of variables i-iv across the back of Plate 5-25: i. N (ppm), ii. %N as B; iii. mu (1365); iv. H (3107)

4.3.1.2 Plate 5-26

This plate was cut from an intense brown tetrahexahedroid containing one purple Cr-pyrope inclusion and a large inclusion pit. There is a low luminescence, Type II resorbed core visible on the optical CL image of the back of the plate (Figures 4.6b&d). Strong, Type I octahedral growth zones are visible around the core (optical CL image, 4.6d). The garnet inclusion is situated in the core of the diamond and is just visible in the optical CL image (Figure 4.6d). The front CL image does not show any growth zones, but there is an area of low luminescence seemingly on top of an area of high luminescence around the inclusion pit (Figures 4.6a&c). The area of high luminescence is likely to be associated with a crack extending from the inclusion pit.

There is a narrow range in nitrogen concentration across the plate of 71 – 114 ppm (Figure 4.6 e.i & f.i). A decrease in the nitrogen concentration is to be expected across the core owing to its low luminescence; however this trend is not evident. The back side of the plate could have been cut at the inner edge of the core, which would explain why it is not visible on the front side of the plate. If this is the case then the analyses through this region would mostly be sampling Type I material and would not reflect a decrease in nitrogen across this region. There is also very little change in the amount of nitrogen as B aggregates across the plate, with a range of 31 – 45% (4.6 e.ii & f.ii). A strong positive correlation exists between the nitrogen concentration and the platelet peak intensity (Figure 4.6 e.iii & f.iii). The hydrogen peak intensity is the only variable that shows a marked change across the core of the plate (Figure 4.6 e.iv & f.iv).

The growth from the core to the rim appears to be continuous therefore the time-averaged mantle residence temperatures have been calculated using the age of the lherzolitic diamonds (1.93 Ga). The range of temperatures is 1189 – 1209 °C (Figure 4.3). The analyses with the highest nitrogen concentrations (>100 ppm) give a narrower range of temperatures of 1189 – 1193 °C, which are most likely to be a more accurate reflection of the actual values as they are less likely to have sampled any Type II diamond. The tight cluster of points on the plot of %N as B vs. nitrogen concentration indicates that this diamond grew in a relatively constant environment with respect to nitrogen (Figure 4.3).

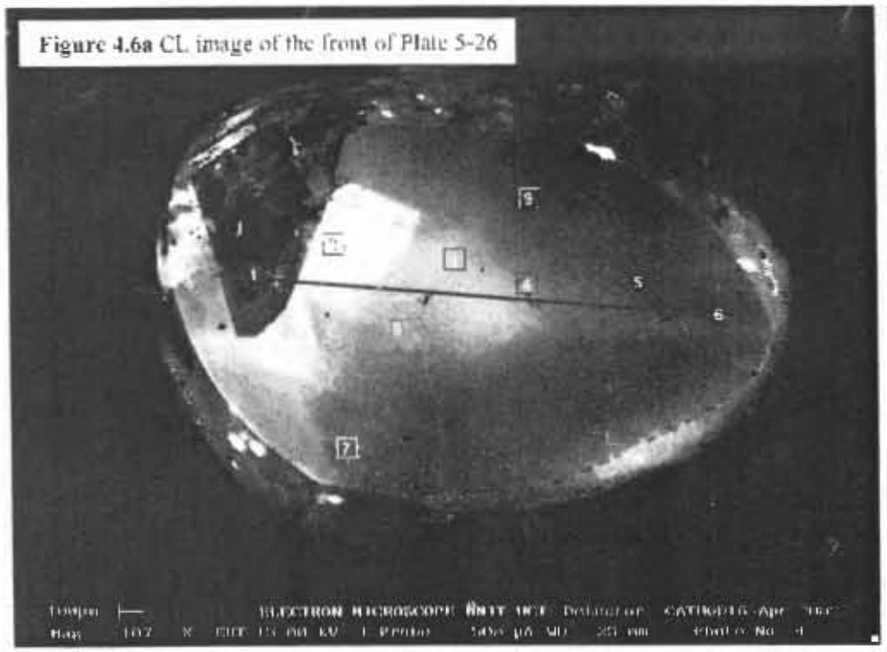

Figure 4.6a CL image of the front of Plate 5-26

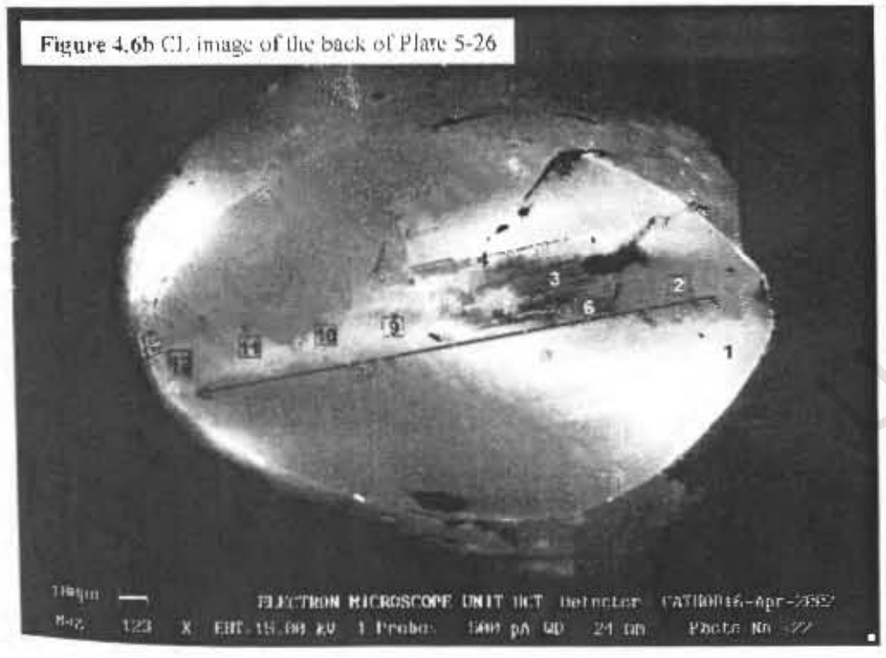

Figure 4.6b CL image of the back of Plate 5-26

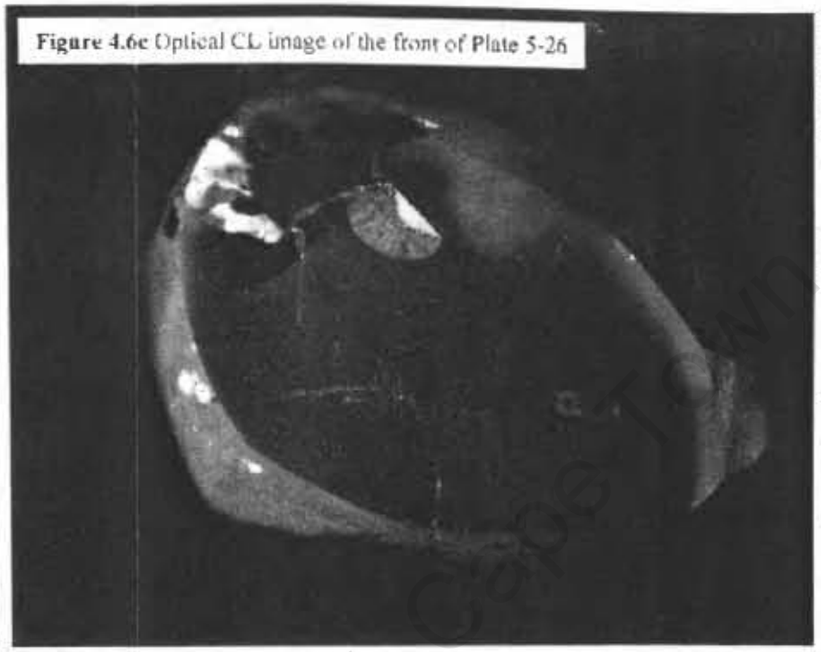

Figure 4.6c Optical CL image of the front of Plate 5-26

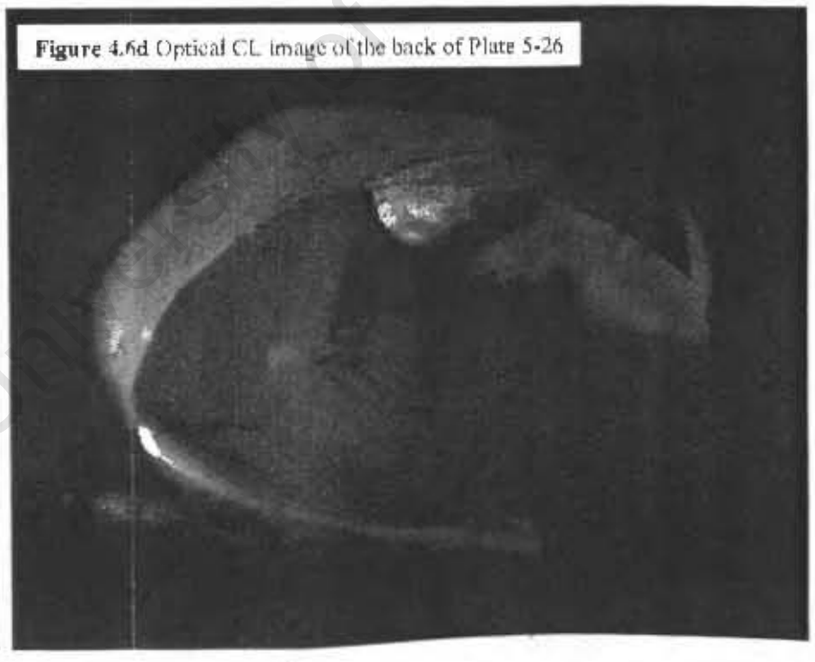

Figure 4.6d Optical CL image of the back of Plate 5-26

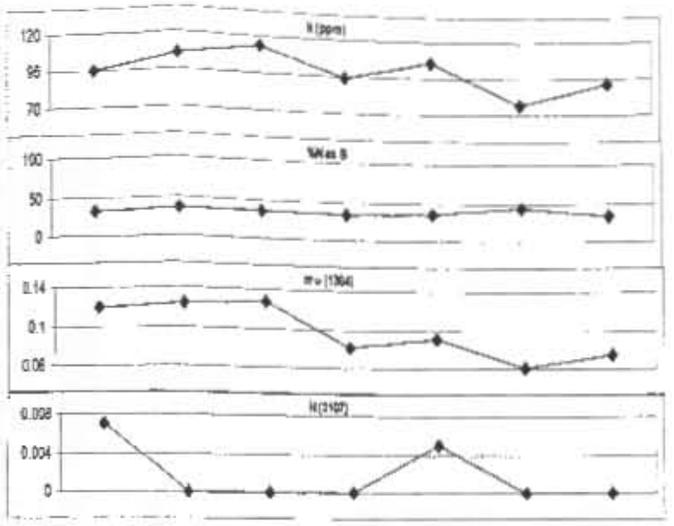

Figure 4.6e Graphs showing the variation of variables i-iv across the front of Plate 5-26: i. N (ppm), ii. %N as B; iii. mu (1365); iv. H (3107)

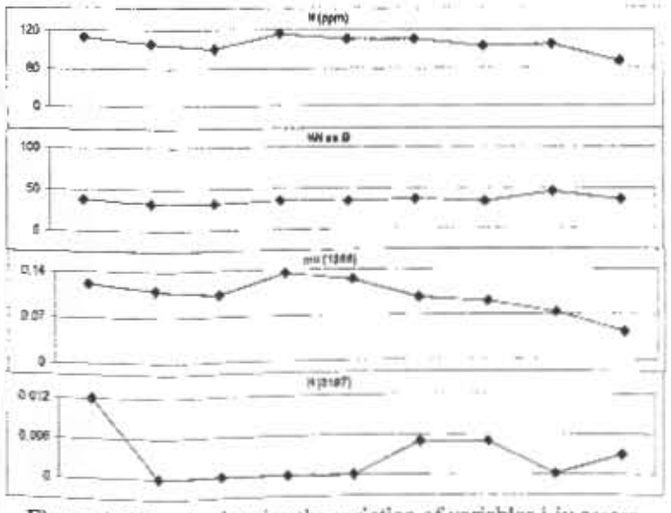

Figure 4.6f Graphs showing the variation of variables i-iv across the back of Plate 5-26: i. N (ppm), ii. %N as B; iii. mu (1365); iv. H (3107)

4.3.1.3 Plate 5-11

This plate was cut from a flattened, brown octahedron. This diamond contains one large purple Cr-pyrope inclusion and one large olivine inclusion. During polishing, an inclusion escaped leaving a roughly triangular shaped pit and a crack extending to both polished surfaces (Figure 4.7 a & c). The inclusions are located within the core of the diamond (Figure 4.7c). The diamond contains an abundance of graphite planes and consequently only a few analyses were obtained. The diamond has a large bright luminescence core, which has been resorbed (Figure 4.7 a & b). There is minor growth of Type II diamond around the core. Extending from the core is a zone made up of octahedral growth zones of variable luminescence (Figure 4.7 c & d). These growth zones also show some resorption, which is particularly evident in the lower left region of the back CL image (Figure 4.7b). A narrow more defined octahedral growth zone extends to the edge of the plate.

There is a narrow range of nitrogen concentrations of 100 – 178 ppm (Figure 4.7 e.i). There was a slight decrease in the concentration of nitrogen in the growth medium after the formation of the core. The nitrogen concentration increased again during the last octahedral growth phase of this diamond. The trend of %N as B does not follow that of nitrogen concentration, and has a range of values from 78 – 88% (Figure 4.7 e.ii). There is a positive correlation between the platelet peak intensity, hydrogen peak intensities and nitrogen concentration (Figure 4.7 e.iii & iv). There is little difference in nitrogen concentration and %N as B between the core and rim of this diamond. This indicates that the core and rim grew under similar conditions in a relatively short period of time.

The mantle residence temperatures are high, with a range of 1233 – 1262 °C (Figure 4.3). The low luminescence growth zones visible in the optical CL image (Figure 4.7 c & d) indicate that the estimated temperatures are most likely to be overestimates (Evans, 1992). If an assumption is made that each sample included a third of Type II diamond in the analysis this would account for a shift in temperature from the range obtained down to a range of 1198 - 1214 °C (similar to Plates 5-25 and 5-26).

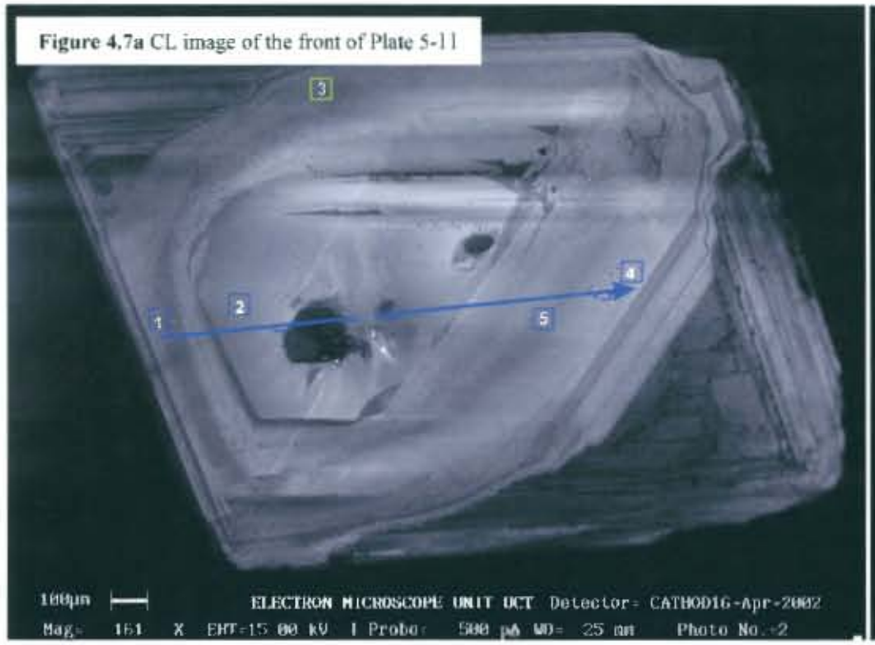

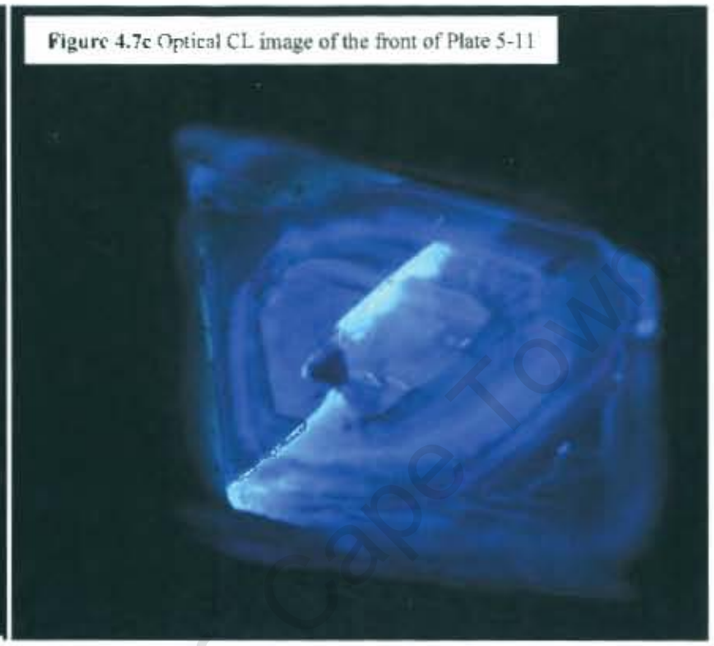

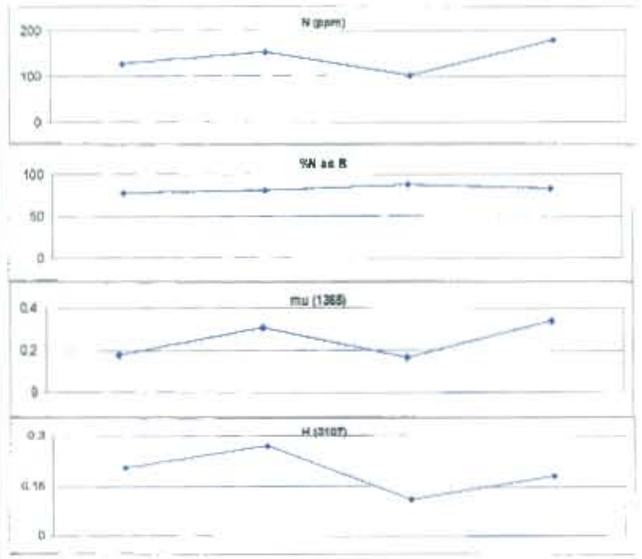

Figure 4.7e Graphs showing the variation of variables i-iv across the front of Plate 5-11: i. N (ppm), ii. %N as B; iii. mu (1365); iv. H (3107)

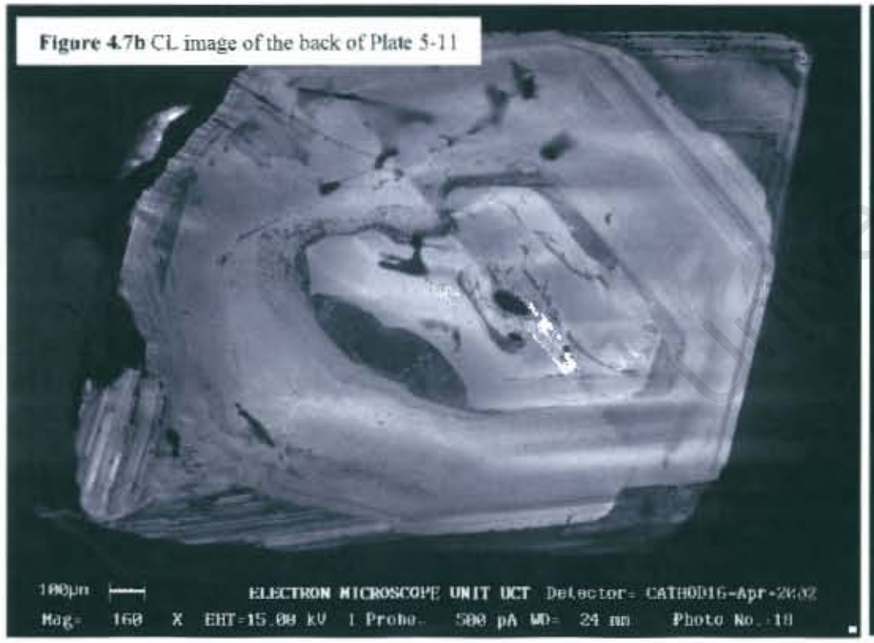

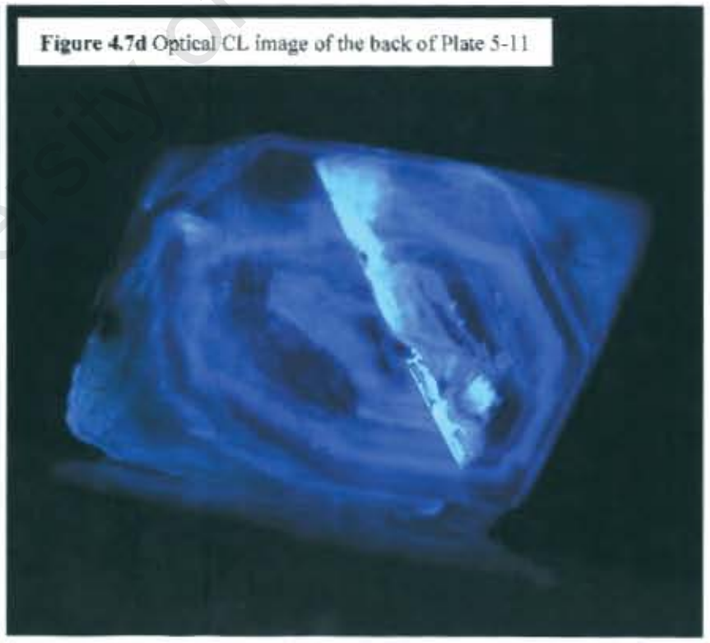

4.3.1.4 Plate 7-5

This plate was cut from a brown octahedron. This diamond contains two green clinopyroxene inclusions and one small clear inclusion (optical CL, Figure 4.8 c & d). The front CL image shows that this diamond has a small, faint, irregularly shaped, high luminescence core (Figure 4.8a). The majority of the plate appears to consist of a homogeneous, less luminescent zone: followed by octahedral growth zones with varying luminescence along the edge of the plate. The inclusions are located toward the edge of the plate (Figure 4.8c). Lamination lines are seen to cross the growth zones. The rear CL image shows all of the above features except for the luminescent core (Figure 4.8b). The blue-green luminescence of this diamond is most likely in part caused by the period of deformation it underwent, which produced the lamination lines (Figure 4.8 c & d).

The concentration of nitrogen increases from the periphery towards the centre of the plate (Figure 4.8 e.i & f.i). The range in values is 80 – 362 ppm, the highest value of 362 ppm was obtained from the analysis 4 in the core of the plate (Figure 4.8 e.i). This indicates that the source medium became depleted in nitrogen with time during the growth of this diamond. The percentage of nitrogen as B aggregates follows the same trend as the nitrogen concentration, with a range in values of 55 – 77% (Figure 4.8 e.ii & f.ii). The range in temperatures obtained is 1206 – 1220 °C. The platelet peak intensity for this traverse mirrors the nitrogen concentration and %N as B trends (Figure 4.8 e.iii & f.iii). The low absolute values of the platelet peak intensities may be due to platelet peak degradation caused by deformation. The hydrogen peak intensities, although low, increase from one side of the plate to the other. There is no apparent reason for this increase (Figure 4.8 e.iv & f.iv).

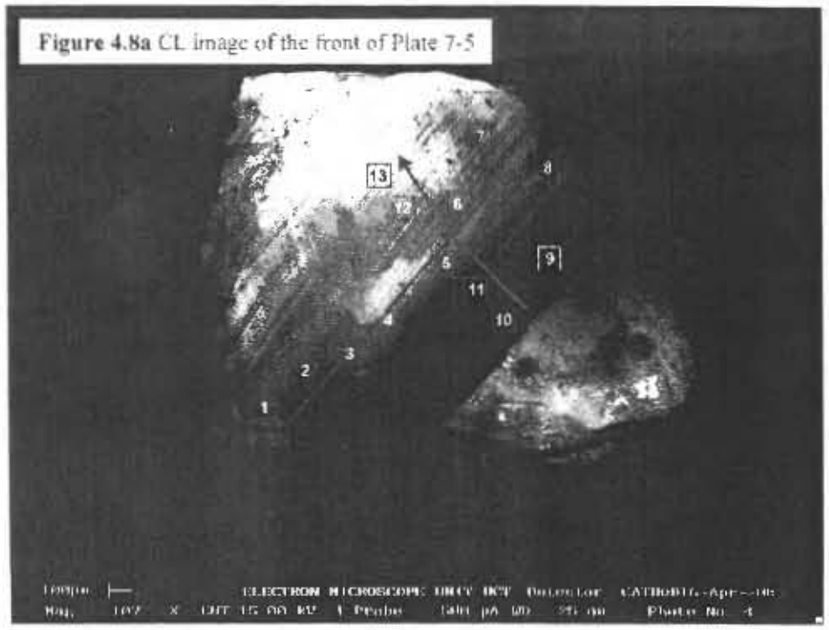

Figure 4.8a CL image of the front of Plate 7-5

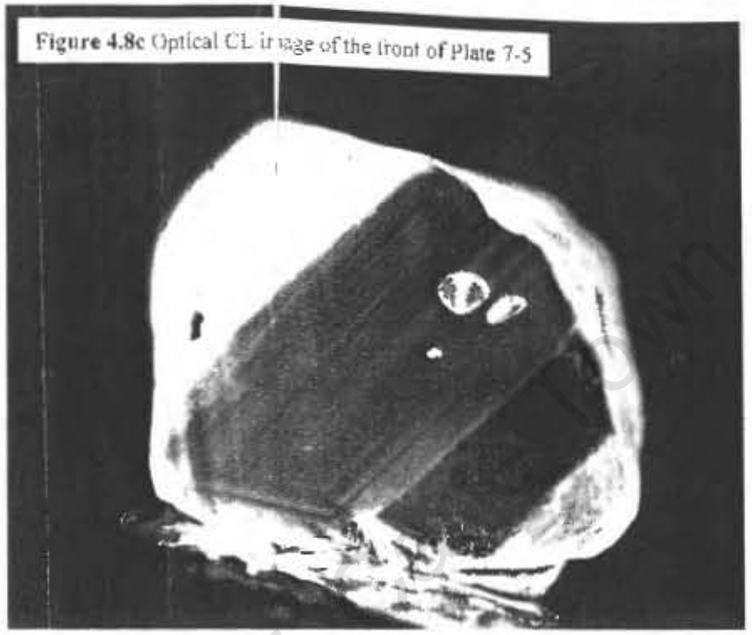

Figure 4.8c Optical CL image of the front of Plate 7-5

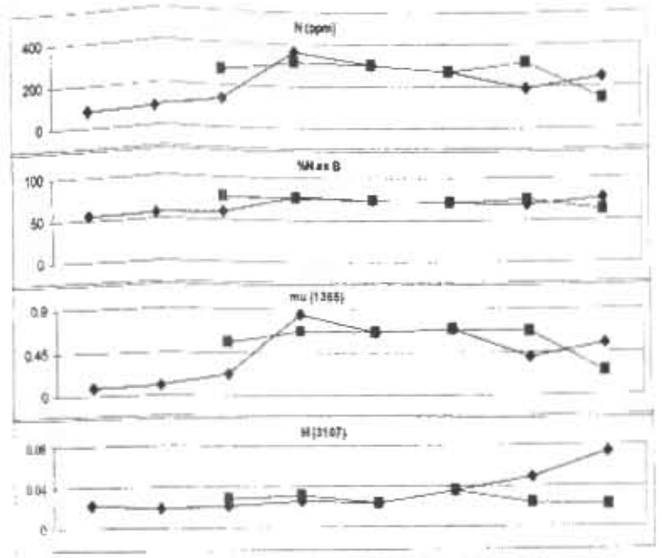

Figure 4.8e Graphs showing the variation of variables i-iv across the front of Plate 7-5: i. N (ppm), ii. %N as B; iii. mu (1365); iv. H (3107)

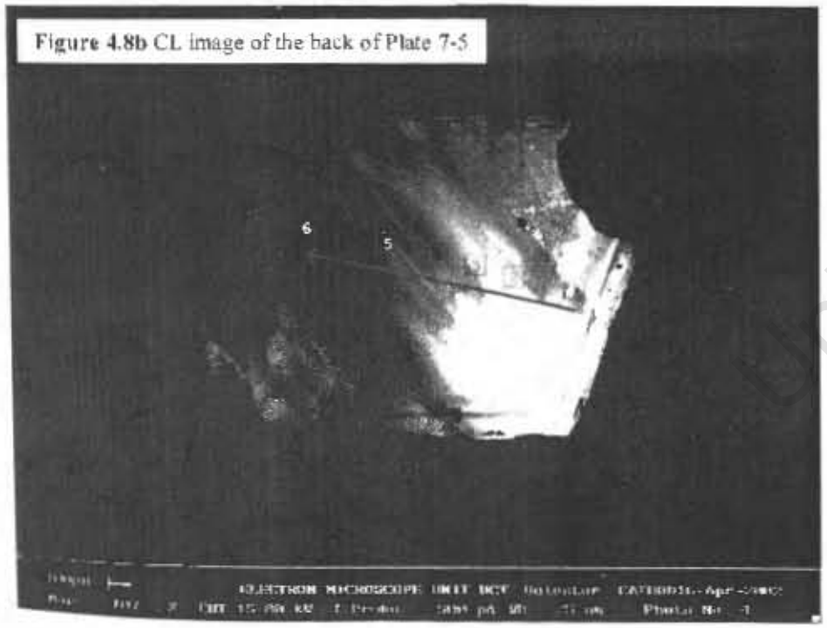

Figure 4.8b CL image of the back of Plate 7-5

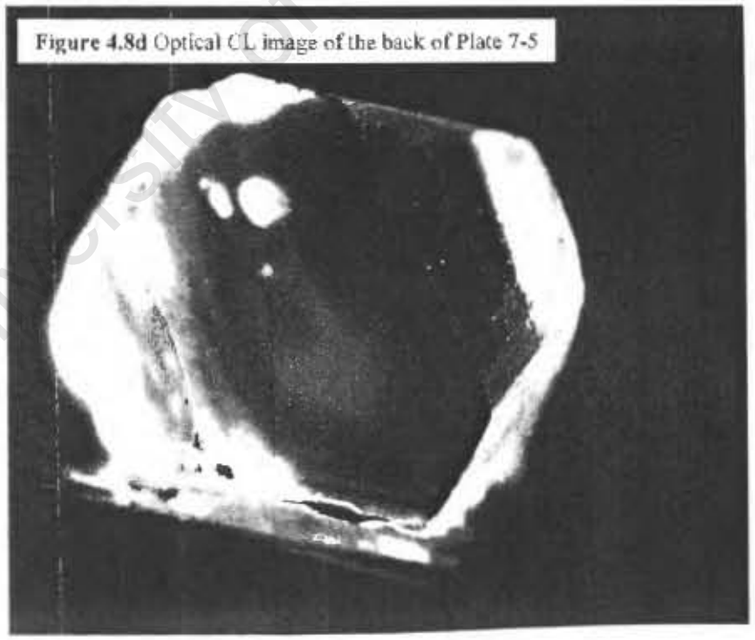

Figure 4.8d Optical CL image of the back of Plate 7-5

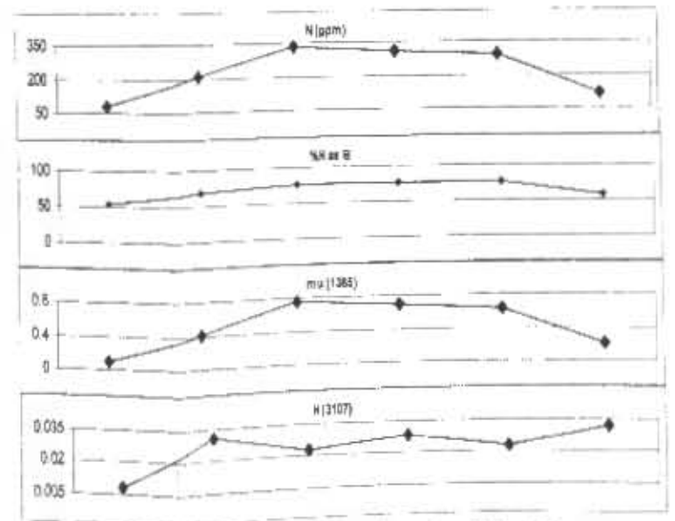

Figure 4.8f Graphs showing the variation of variables i-iv across the back of Plate 7-5: i. N (ppm), ii. %N as B; iii. mu (1365); iv. H (3107)

4.3.1.5 Plate 6-1

This plate was cut from a brown macle containing 3 purple Cr-pyrope inclusions and four clear inclusions (optical CL, Figure 4.9 c & d). The CL image of the back of the plate (Figure 4.9b) shows a crack running through a faintly discernable core that displays Type I, octahedral growth. The core was subsequently resorbed, which was followed by minor Type II growth. The larger garnet inclusion is located on the edge of the core (Figure 4.9d). The crack was not visible on the diamond surface. The core remaining to the left of this crack (viewed as shown) has been more heavily resorbed than that to the right (Figure 4.9b). Very faint octahedral growth zones are visible throughout the remainder of the plate and are truncated in some areas by Type II diamond (back CL image, Figure 4.9b). These features are not visible on the front CL image of the plate (Figure 4.9a). Scotch-plaid lamination lines are visible on both sides of the plate.

The nitrogen content of the plate is low and ranges from 43 – 60 ppm (Figure 4.9 e.i & f.i). This low nitrogen content and evidence for deformation (lamination lines) may explain the unusual blue-green luminescence seen in the optical CL (Figure 4.9d). There is a broad increase in nitrogen content from the edge to the centre of the plate, with the exception of point B1 (Figure 4.9b). This may suggest a continuous depletion in nitrogen in the medium from which the diamond grew. The overall range of values for %N as B is low for this plate, 11 - 43%, owing to the low nitrogen concentrations (Figure 4.9 e.ii & f.ii). The range of platelet peak intensities are low on both sides of the plate (Figure 4.9 e.iii & f.iii), which may indicate that plastic deformation caused catastrophic degradation of the platelet peak. The hydrogen peak intensities do not correlate well with the other variables (Figure 4.9 e.iv & f.iv).

It does not appear that the core is significantly older than the remainder of the diamond. For this reason the mantle residence time used is 0.75 Ga. The range in temperatures obtained for these analyses is 1185 – 1221 °C (Figure 4.3). The range of temperatures becomes narrower (1202 – 1221 °C) by excluding the analysis B2, which falls in an area of lower luminescence (Figure 4.9b). It is likely that the deformation experienced by this diamond has caused an elevation in the aggregation, which would in turn cause the temperatures obtained to be overestimates (Evans, 1992).

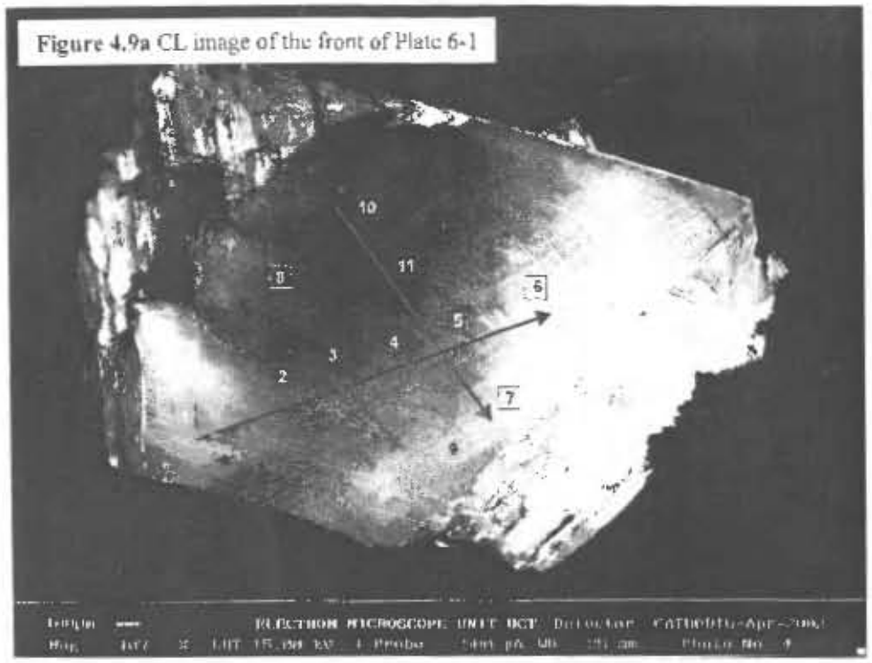

Figure 4.9a CL image of the front of Plate 6-1

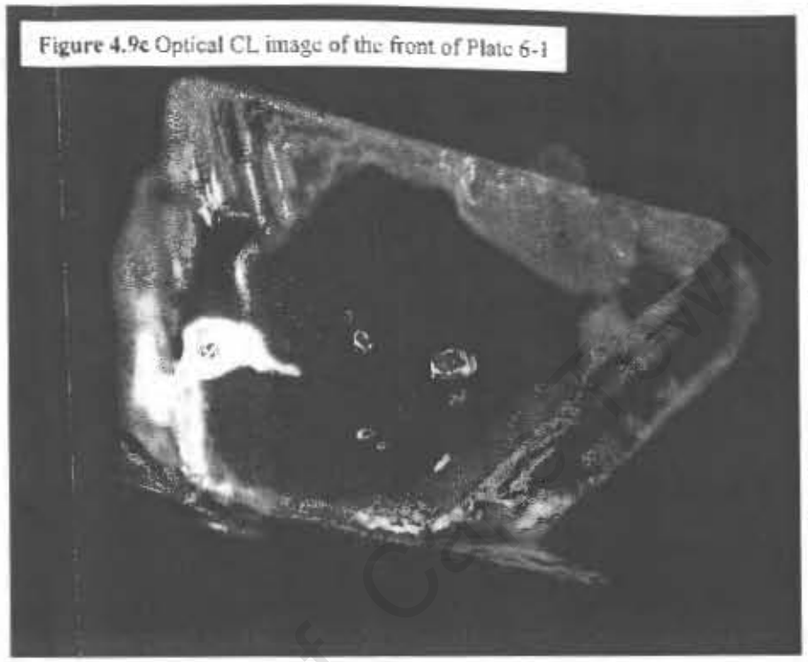

Figure 4.9c Optical CL image of the front of Plate 6-1

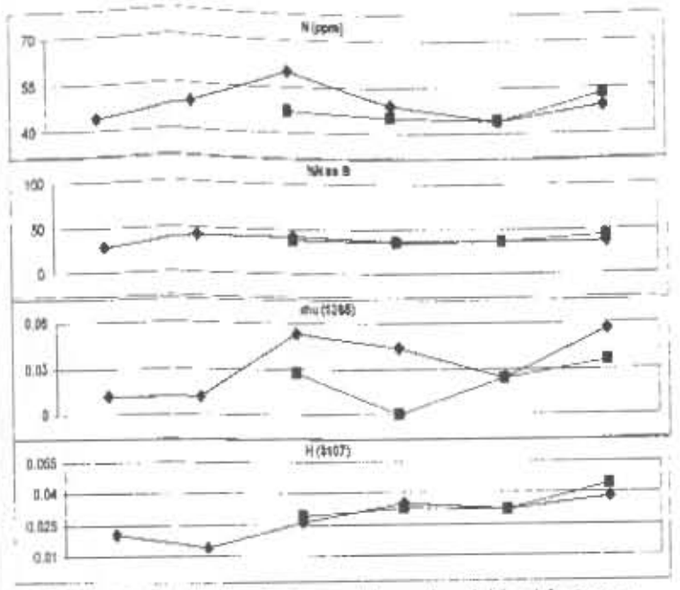

Figure 4.9e Graphs showing the variation of variables i-iv across the front of Plate 6-1: i. N (ppm), ii. %N as B; iii. mu (1365); iv. H (3107)

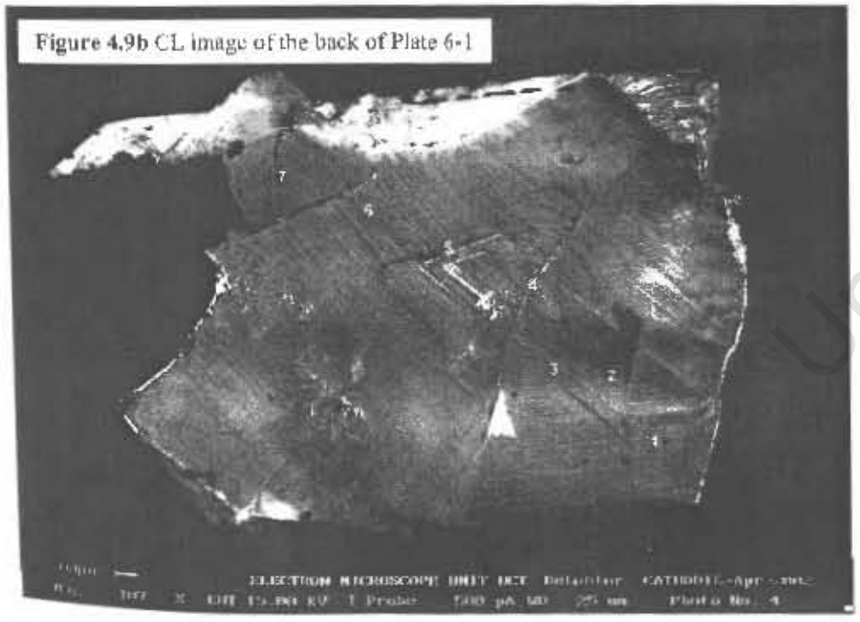

Figure 4.9b CL image of the back of Plate 6-1

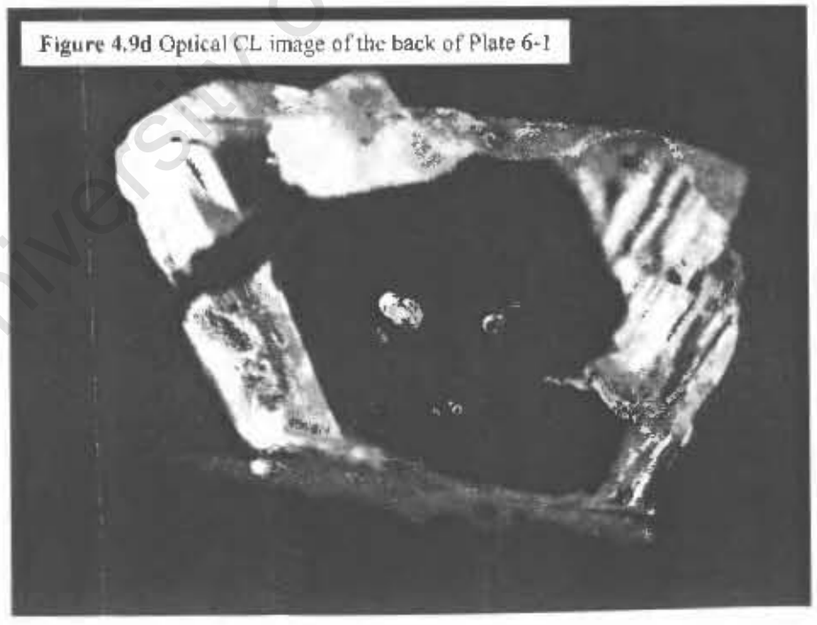

Figure 4.9d Optical CL image of the back of Plate 6-1

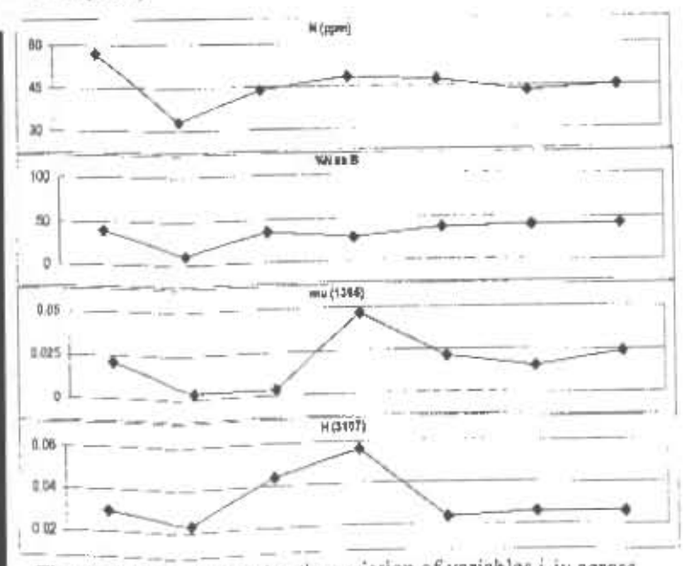

Figure 4.9f Graphs showing the variation of variables i-iv across the back of Plate 6-1: i. N (ppm), ii. %N as B; iii. mu (1365); iv. H (3107)

4.3.1.6 Plate 8-8

This plate was cut from a brown, resorbed macle, containing one green clinopyroxene inclusion and a few clear inclusions, as seen in the optical CL image (Figure 4.10 c & d). The clinopyroxene inclusion is located towards the centre of the plate, whilst the clear inclusions are situated towards the edge (Figure 4.10c). The front side of the plate gave poor FTIR spectra therefore only the FTIR results of the rear image will be discussed. This diamond appears to be made up of continuous octahedral zones of Type I diamond of identical luminescence; which are truncated by non-luminescent Type II diamond (Figure 4.10b). The growth zones are not visible on the front CL image, but lamination lines, scotch-plaid in some areas, are more clearly visible on this image (Figure 4.10a).

The nitrogen concentrations yield very low values across the plate, ranging from below the limit of detection (20 ppm) to 42 ppm (Figure 4.10 e.i). Nitrogen aggregation is also low, 0-34% of N as B aggregates (Figure 4.10 e.ii), as is to be expected from low nitrogen concentrations. The 'w'-shaped trend in nitrogen concentration may possibly be due to analyses 2 and 4 sampling mostly Type II diamond; this pattern is duplicated in the %N as B trend. The intense blue-green luminescence may be explained by low nitrogen concentrations coupled with intense deformation, which is evident from the lamination lines (optical CL, Figure 4.10 c & d). The platelet peaks are poorly developed, but do follow the general trend in nitrogen concentration (Figure 4.10 e.iii). There are also very low hydrogen peak intensities (Figure 4.10 e.iv).

The range in temperatures obtained for this plate is 1118 – 1218 °C; the uncertainty associated with low nitrogen concentrations is responsible for the large range observed (Figure 4.4). There is no systematic variation with nitrogen concentration for the analyses from this plate.

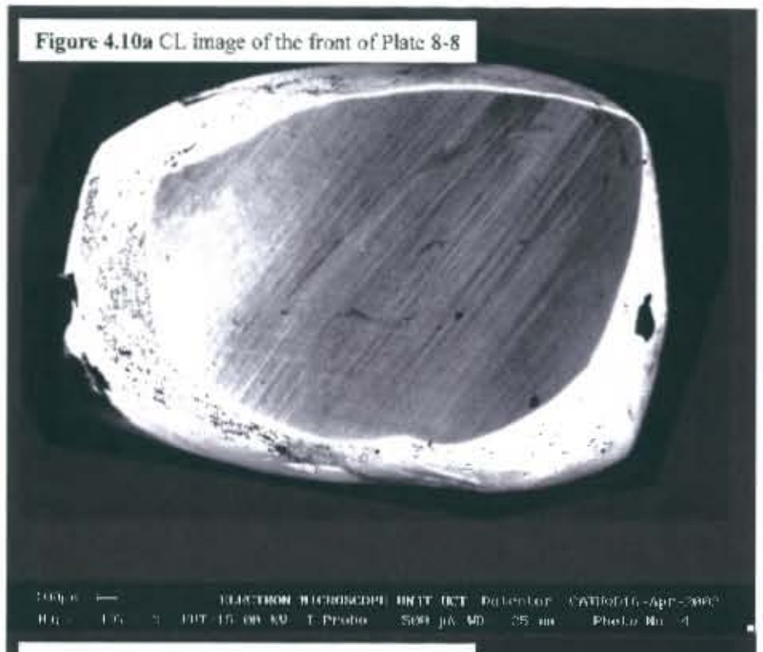

Figure 4.10a CL image of the front of Plate 8-8

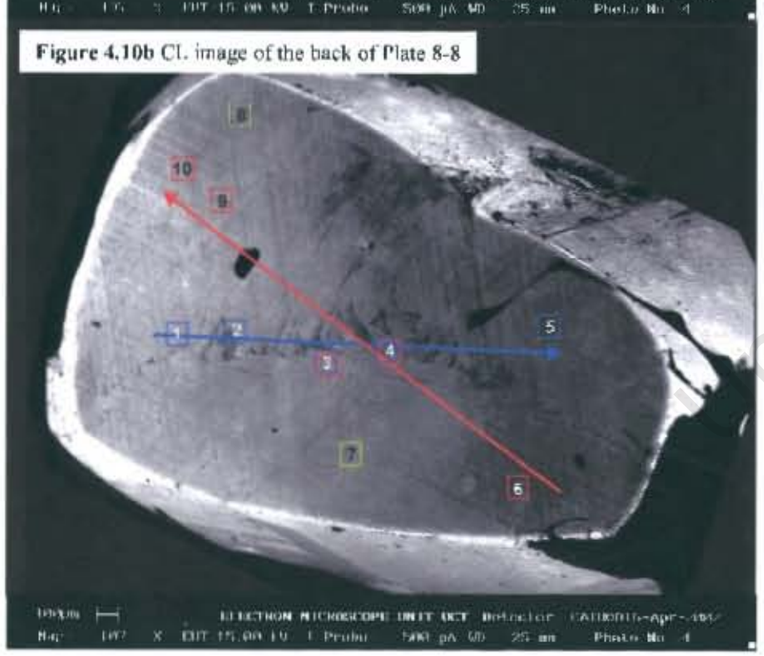

Figure 4.10b CL image of the back of Plate 8-8

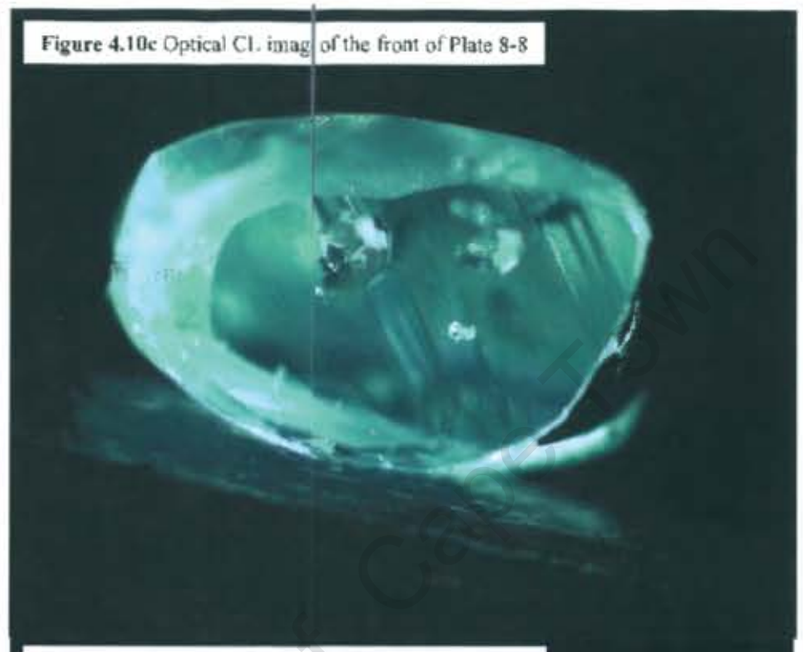

Figure 4.10c Optical CL image of the front of Plate 8-8

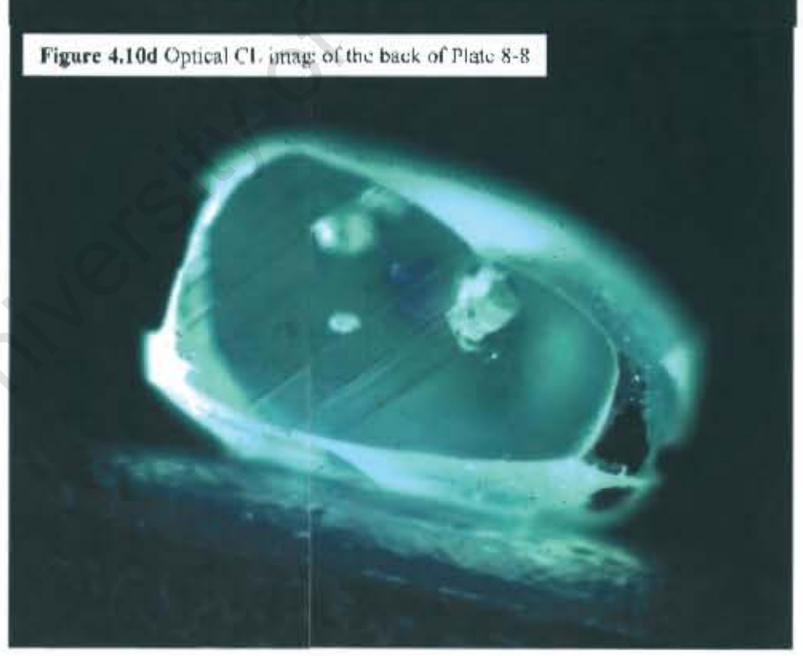

Figure 4.10d Optical CL image of the back of Plate 8-8

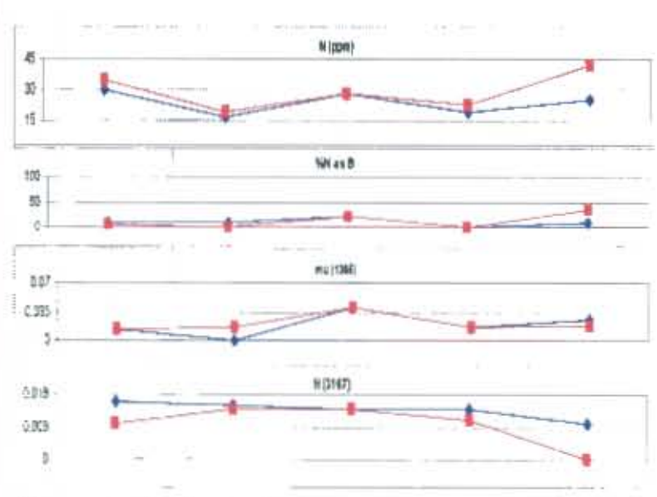

Figure 4.10e Graphs showing the variation of variables i-iv across the back of Plate 8-8:i. N (ppm), ii. %N as B; iii. mu (1365); iv. H (3107)

4.3.1.7 Plate 13-1

This plate was cut from a deep brown, elongated, highly resorbed macle. This diamond contained one large purple Cr-pyrope inclusion and four small colourless inclusions, all located in the core of the diamond (Figures 4.11c&d). The front image of the plate displays octahedral growth zones from core to rim of mostly Type I diamond, evident from the variations in luminescence (optical CL, Figure 4.11c). There is evidence for resorption and minor growth of Type II diamond along the edges of the growth zones (Figure 4.11a & b). These features are also visible on the rear image, however the truncation by Type II diamond is slightly more pronounced. These images also illustrate that the growth zones do not run perpendicularly to the surface of the plate, but instead dip outwards from the front to the rear surface (Figures 4.11 c & d).

There is an unusual increase in nitrogen concentration from core to rim seen across the front of the plate, which suggests an increase in the nitrogen concentration in the medium in which the diamond grew (Figure 4.11 e.i). The traverses across the front of the plate give a range of nitrogen values from 49 - 213 ppm. The percentage of nitrogen present as B aggregates ranges from 10 – 56% (Figure 4.11 e.ii), the %N as B roughly follows the trend of N with a general increase from core to rim. There is positive correlation between the nitrogen concentration trend and the platelet peak intensity (Figure 4.11 e.iii). The low platelet peak intensities are consistent with the low level of nitrogen aggregated as B aggregates. The hydrogen peak intensities are extremely low and do not mirror the trends as seen above (Figure 4.11 e.iv). The trends in nitrogen concentration and amount of nitrogen as B aggregates across the back of the plate are similar to those for the front of the plate, but the increase in values is not as pronounced on the right edge of the plate. The range of nitrogen concentrations is higher than that of the front plate (75 – 346 ppm), most likely due to sampling of a wider zone of relatively high luminescence and less low-nitrogen diamond (Figure 4.11 f.i). The range of %N as B is also narrower with higher values, 42 - 68%. This is positively correlated with the increase in nitrogen concentration towards the plate's periphery (Figure 4.11 f.ii). The platelet intensity, and to a lesser degree, the hydrogen peak intensity mirror the nitrogen concentration trend (Figure 4.11 f. iii & iv). The range in temperatures obtained for the analyses from the front and rear of the plate are 1168 - 1216 °C and 1191 - 1207 °C, respectively (Figure 4.3). The range obtained from the rear more likely closer to reality as these analyses do not appear to sample as much low-nitrogen diamond.

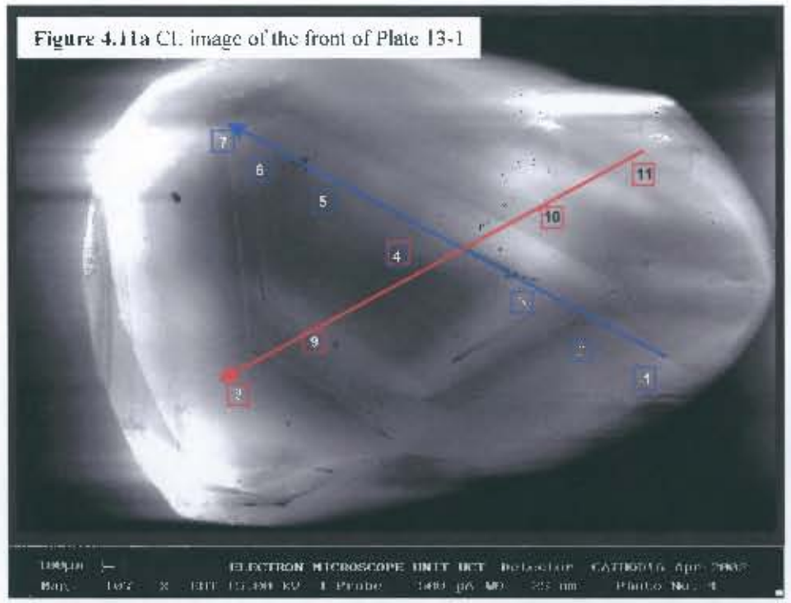

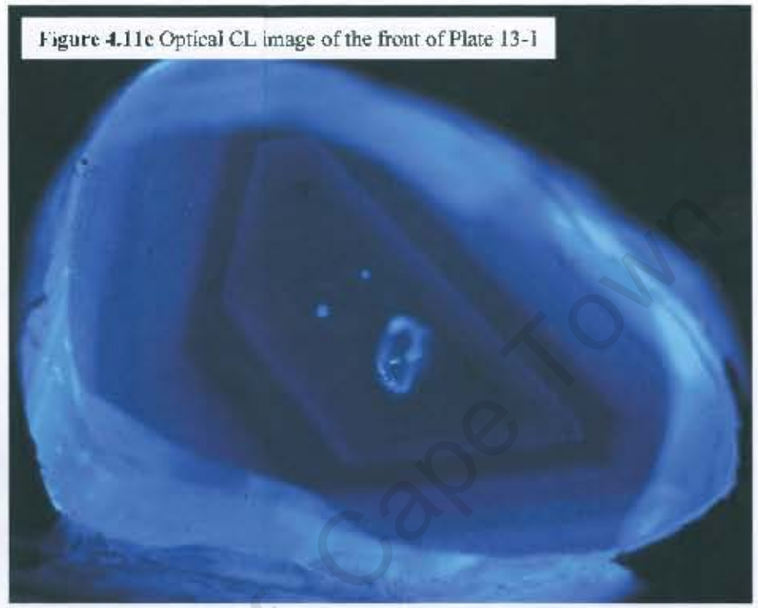

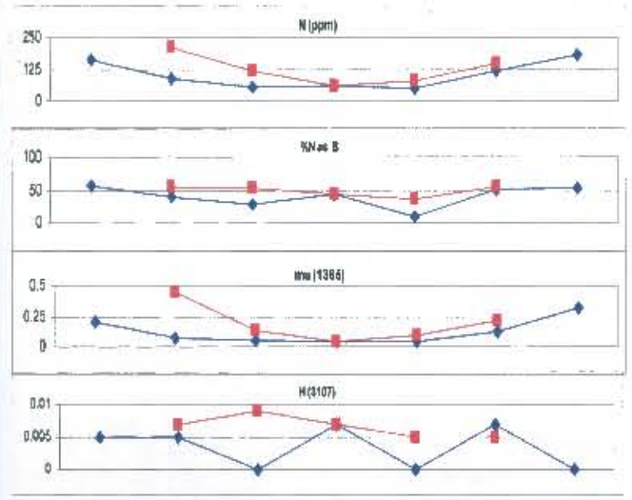

Figure 4.11e Graphs showing the variation of variables i-iv across the front of Plate 13-1: i. N (ppm), ii. %N as B; iii. mu (1365); iv. H (3107)

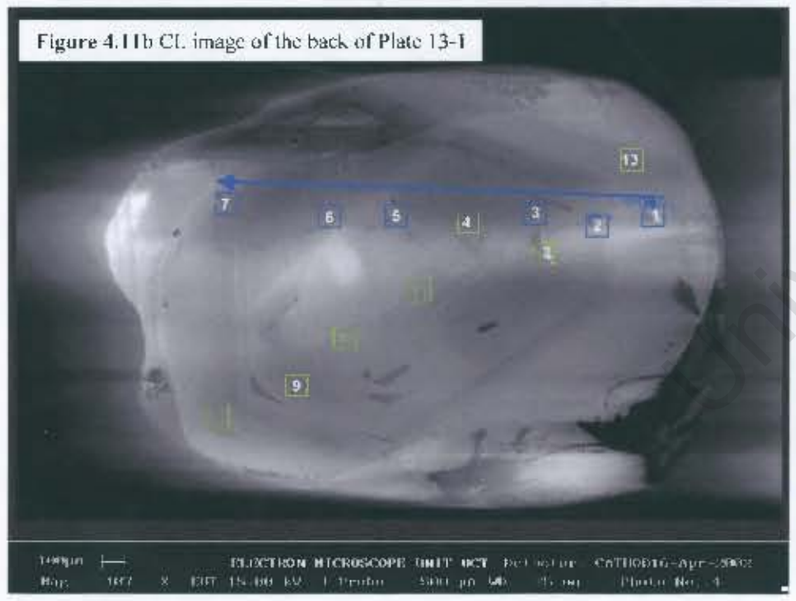

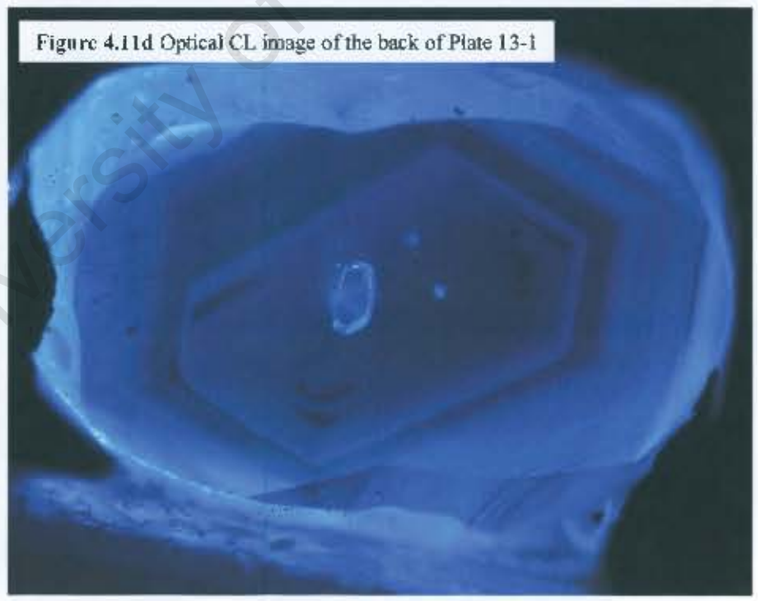

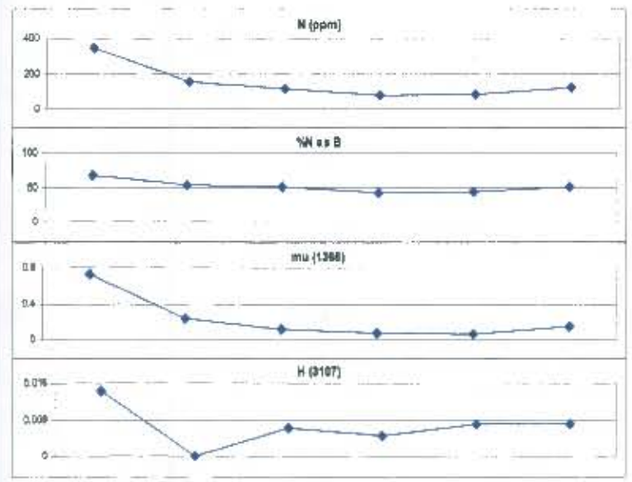

Figure 4.11f Graphs showing the variation of variables i-iv across the back of Plate 13-1: i. N (ppm), ii. %N as B; iii. mu (1365); iv. H (3107)

4.3.1.8 Plate 5-24

This plate was cut from a brown tetrahexahedroid diamond, containing one purple Cr-pyrope and four clear inclusions. The inclusions are located in the centre of the plate (Figures 4.12 c & d). There is a crack running through the centre of the diamond, which was not observed on the surface of the rough diamond (Figure 4.12 c & d). It is most likely that it developed during polishing. The blue luminescence of the diamond indicates the presence of nitrogen and no evidence for plastic deformation is observed (Figure 4.12 c & d). The CL image of the front of the plate shows evidence of continuous octahedral growth (Figure 4.12a). No growth zones are observed on the back CL image (Figure 4.12b).

The nitrogen concentrations span a wide range of values from 304 ppm to 1143 ppm and decrease sharply toward the edge of the plate (Figure 4.12 e.i & f.i). This indicates that the diamond grew in a medium that was depleted in nitrogen over time. The trend of %N as B also shows a decrease towards the edge of the plate (Figure 4.12 e.ii & f.ii). The aggregation of this plate is high, with a range of %N as B of 71 – 88% and lies on an isotherm of ~1200 °C (Figure 4.3). The trend of platelet peak intensities is identical to that of nitrogen concentration (Figure 4.12 e.iii & f.iii). The intensity of platelet peaks is high with a range of values of 0.52 – 3.14. The hydrogen peak intensities show an inverted trend when compared with the platelet peak intensities or nitrogen concentration (Figure 4.12 e.iv & f.iv); this suggests that as the growth medium became depleted in nitrogen as it was enriched in hydrogen.

The analyses for this diamond give a narrow range for the mantle residence temperature of 1196-1204 °C (Figure 4.3). High nitrogen concentrations and lack of evidence for Type II diamond within the plate indicate that the temperatures estimated are likely to be realistic and not overestimated.

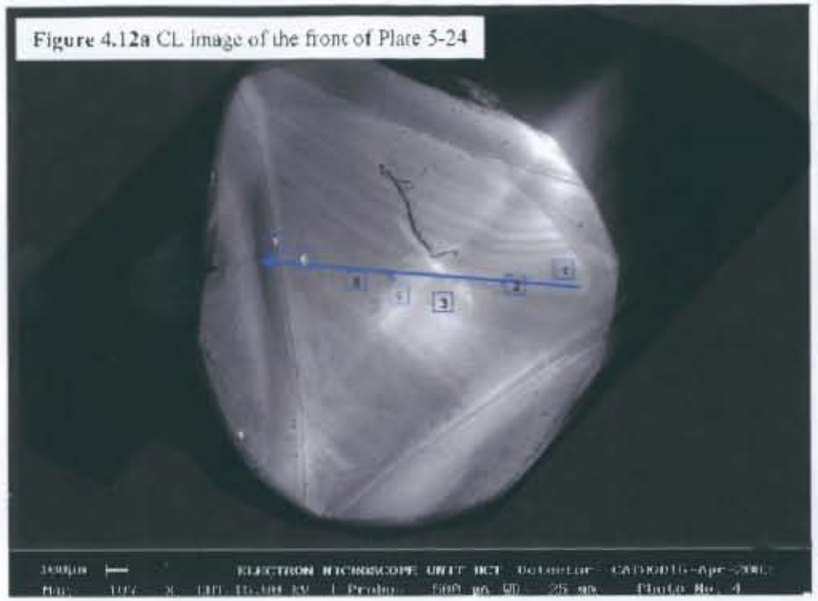

Figure 4.12a CL image of the front of Plate 5-24

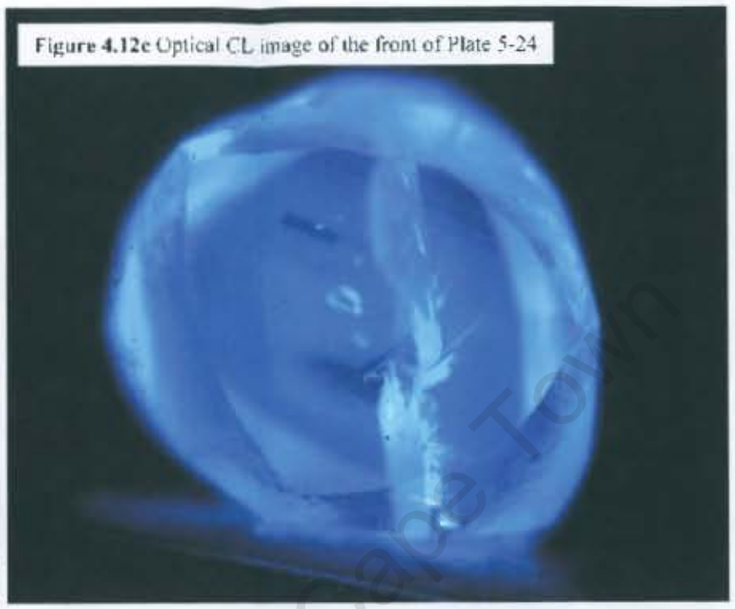

Figure 4.12c Optical CL image of the front of Plate 5-24

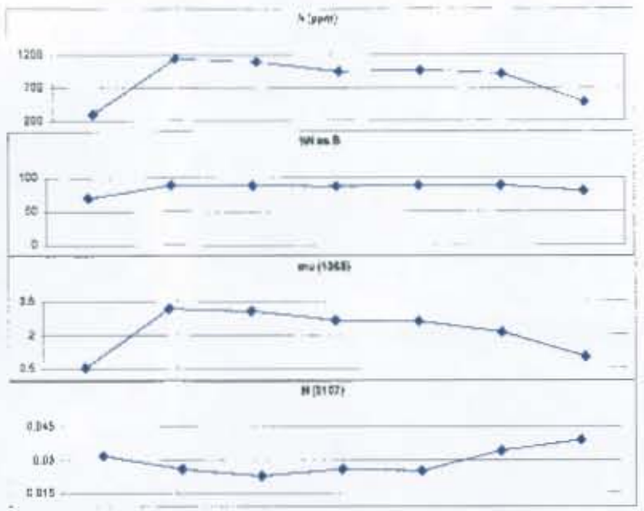

Figure 4.12e Graphs showing the variation of variables i-iv across the front of Plate 5-24: i. N (ppm), ii. %N as B; iii. mu (1365); iv. H (3107)

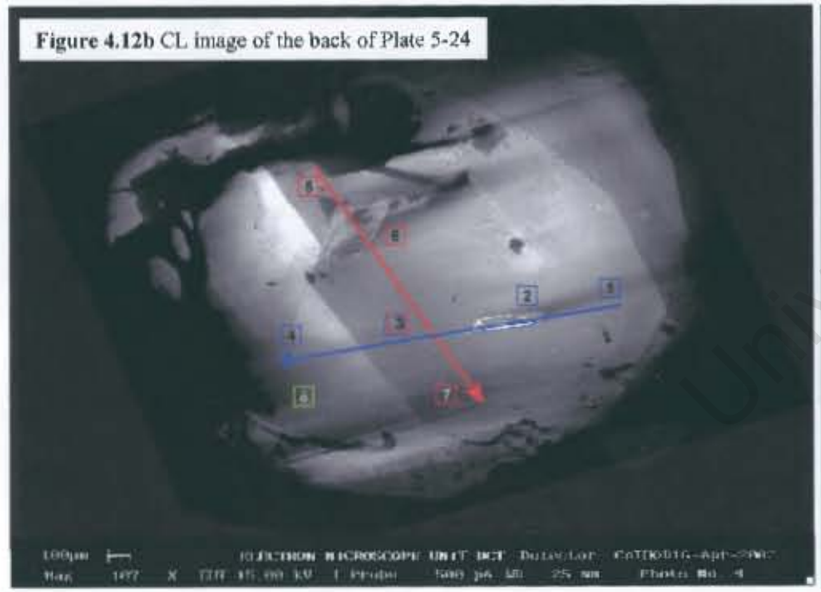

Figure 4.12b CL image of the back of Plate 5-24

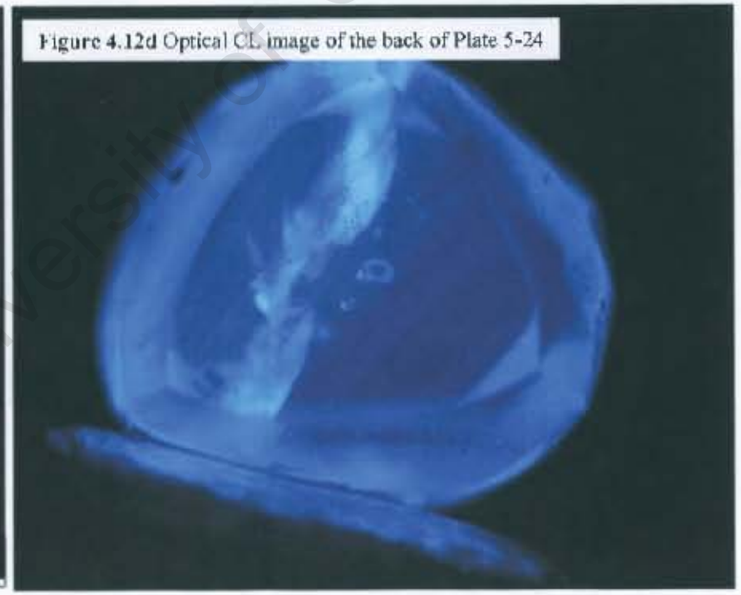

Figure 4.12d Optical CL image of the back of Plate 5-24

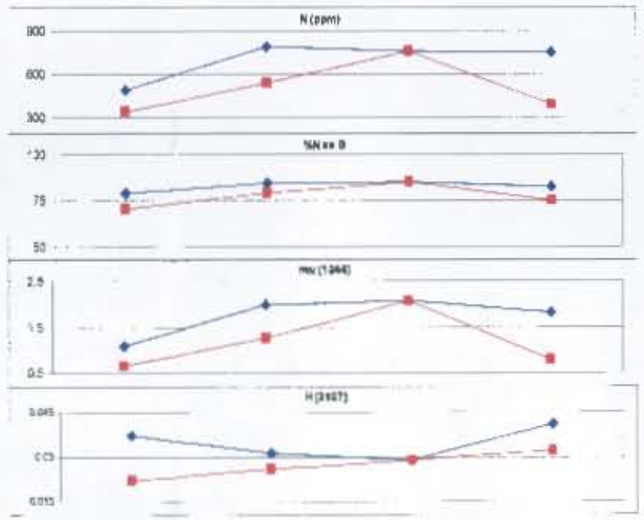

Figure 4.12f Graphs showing the variation of variables i-iv across the back of Plate 5-24: i. N (ppm), ii. %N as B; iii. mu (1365); iv. H (3107)

4.3.1.9 Plate 7-14

This plate was cut from a brown strongly resorbed octahedron, containing three green clinopyroxene inclusions and a few clear inclusions. The optical CL images show two high luminescence zones near the edges of the plate, one on the back and one on the front of the images (Figure 4.13 c & d). These zones have sharp boundaries and the remainder of the plate consists of a low luminescence zone with scotch plaid lamination lines (Figures 4.13 a & b). The clinopyroxene inclusions are located within the areas of bright luminescence (Figure 4.13c).

There is a large variation in nitrogen concentration across the plate with a range of values of 115 – 806 ppm (Figure 4.13 e.i & f.i). The nitrogen concentration increases from the area of low luminescence into the area of high luminescence and then decreases quite sharply as the far edge of the high luminescence zone is reached. An area of low luminescence may be obscured by a high luminescence 'tail' on this edge of the plate, which would explain this drop in concentration (Figure 4.13 a & b). The amount of nitrogen as B aggregates varies from 68 – 90 %, showing a flat trend as all but one analysis have %N as B below 80% (Figure 4.13 e.ii & f.ii). There is a strong positive correlation between the amount of nitrogen and the intensity of the platelet peak (Figure 4.13 e.iii & f.iii). The intensity of the platelet peaks is high with a range in values of 0.14 – 2.44. The plastic deformation of the diamond, resulting in strongly developed lamination lines, has not caused degradation of the platelet peaks. There is a broad correlation between the trend in nitrogen concentration and the hydrogen peak intensity and to a lesser degree between the platelet peak intensity and the hydrogen peak intensity (Figure 4.13 e.iv & f.iv).

There is a large range in mantle residence temperatures for this plate, with values between 1207 – 1264 °C (Figure 4.4). Those analyses of plate 7-14 that have the highest nitrogen contents (>150 ppm) give a narrower range of temperatures, 1207 – 1238 °C. The higher temperatures obtained are likely overestimates due to the sampling of the low luminescence diamond.

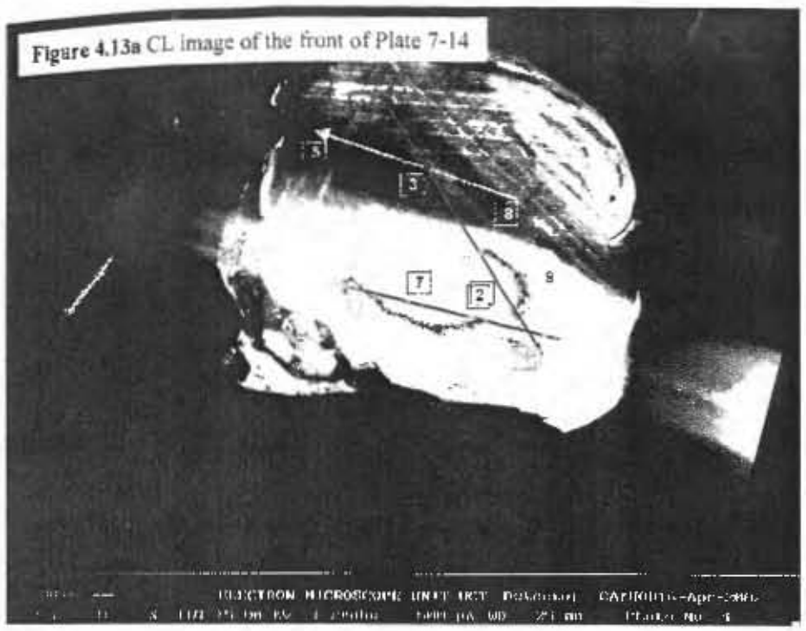

Figure 4.13a CL image of the front of Plate 7-14

Figure 4.13c Optical CL image of the front of Plate 7-14

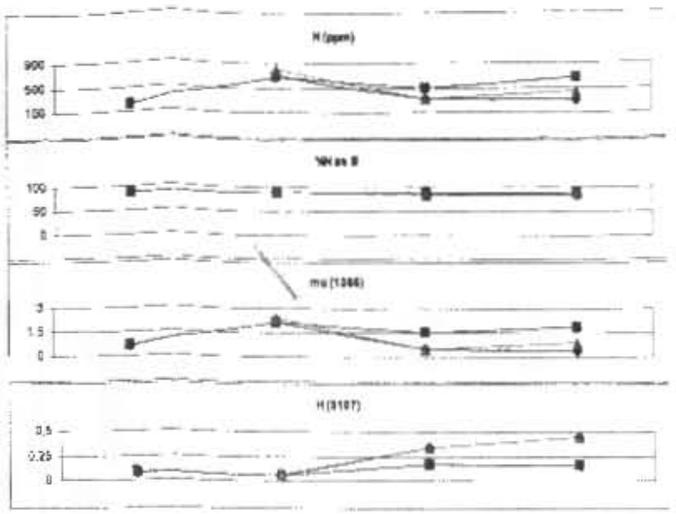

Figure 4.13e Graphs showing the variation of variables i-iv across the front of Plate 7-14: i. N (ppm), ii. %N as B; iii. mu (1365); iv. H (3107)

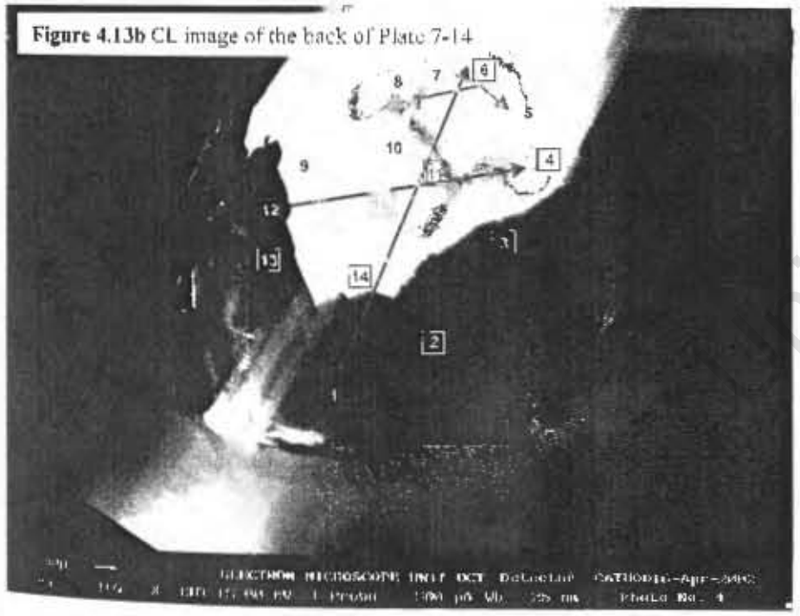

Figure 4.13b CL image of the back of Plate 7-14

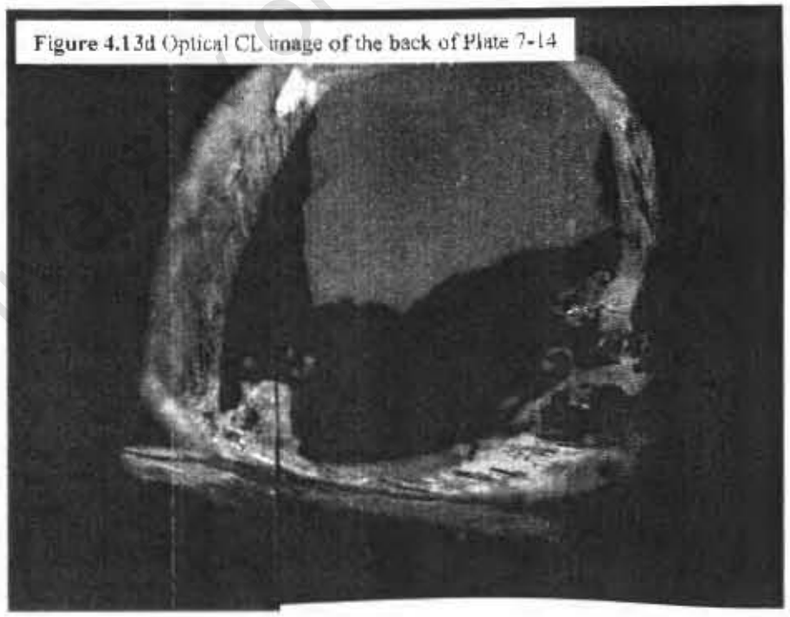

Figure 4.13d Optical CL image of the back of Plate 7-14

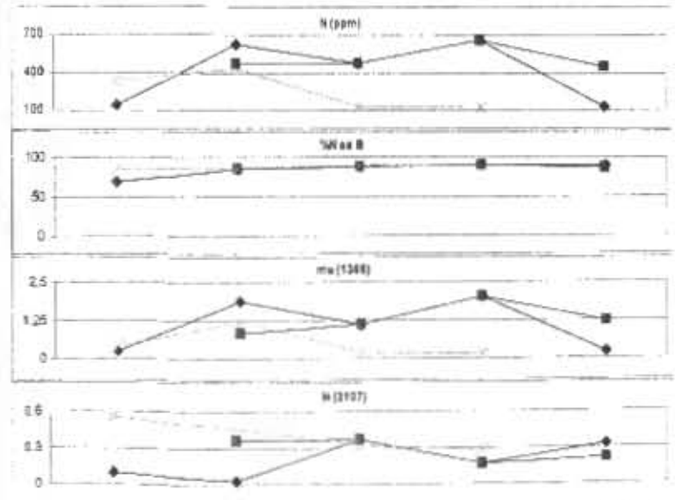

Figure 4.13f Graphs showing the variation of variables i-iv across the back of Plate 7-14: i. N (ppm), ii. %N as B; iii. mu (1365); iv. H (3107)

4.3.1.10 Plate 7-1

This plate was cut from a brown octahedron, containing 3 green clinopyroxene inclusions. The CL image, of the back of the plate, shows an area of extremely bright luminescence on the lower right. A sharp boundary separates this bright area from an area of lower luminescence (Figure 4.14b). The position of the high luminescence area on the image of the back of the plate corresponds to the large clinopyroxene inclusion (Figure 4.14d), as seen in plate 7-14. This area is not visible on the front CL image; however the front of the plate shows a separate area of high luminescence, which is associated with a surface fracture (Figure 4.14c, optical CL). There is an unusual "swirl" luminescence visible in the duller area of the back CL image (Figure 4.14b). This may be associated with fracture planes and inclusions situated close to the surface, which may cause an interference with the CL image. Scotch plaid lamination is visible in the lower luminescence area of the front CL image (Figure 4.14a), which is indicative of plastic deformation.

The nitrogen concentration drops off sharply from the area of high luminescence and remains fairly constant across the rest of the plate (Figure 4.14 e.i & f.i). The range in concentrations is 80 – 891 ppm. The trend in the percentage of nitrogen as B aggregates is similar to that of nitrogen concentration, with a range in values of 67 – 97% (Figure 4.14 e.ii & f.ii). There appears to be considerable variation in the traverse across the high luminescence area on the back of the plate, with nitrogen concentrations of 141 – 891 ppm and the range of %N as B of 76 – 97% (Figure 4.14 f.i & ii). This can be explained as some of the analyses fall outside the high luminescence area as seen on the optical CL image (Figure 4.14d). There is a strong positive correlation between the nitrogen concentration and the platelet peak intensity (Figure 4.14 e.iii & f.iii); this indicates that the plastic deformation did not cause degradation of the platelet peak. There is also a general decrease of hydrogen intensity across the plate, which is consistent with the other variables (Figure 4.14 e.iv & f.iv).

There is a large variation in mantle residence temperature across the plate, with a range of 1214 – 1260 °C (Figure 4.4). The range of concentration of nitrogen and the %N as B in the areas of high luminescence is very variable. By excluding these analyses the range of temperatures obtained is 1214 – 1237 °C.

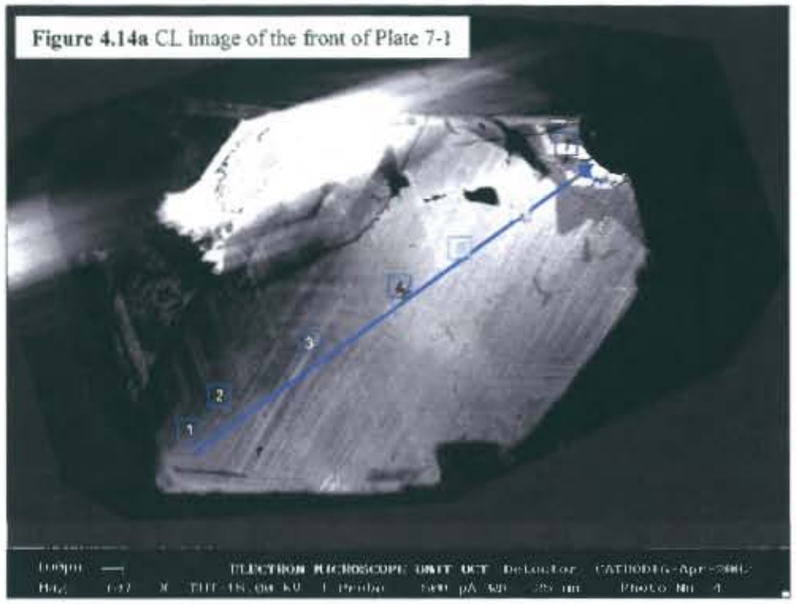

Figure 4.14a CL image of the front of Plate 7-1

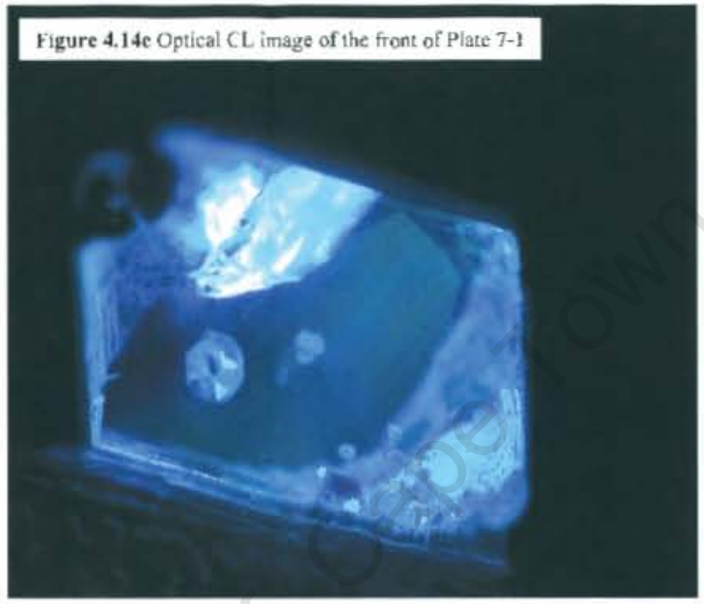

Figure 4.14e Optical CL image of the front of Plate 7-1

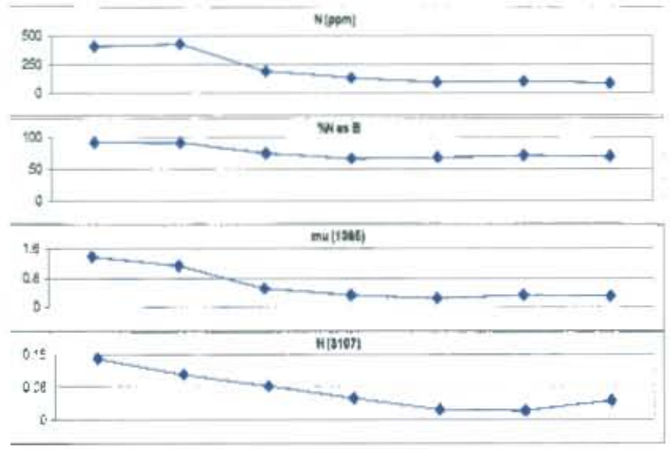

Figure 4.14e Graphs showing the variation of variables i-iv across the front of Plate 7-1: i. N (ppm), ii. %N as B; iii. mu (1365); iv. H (3107)

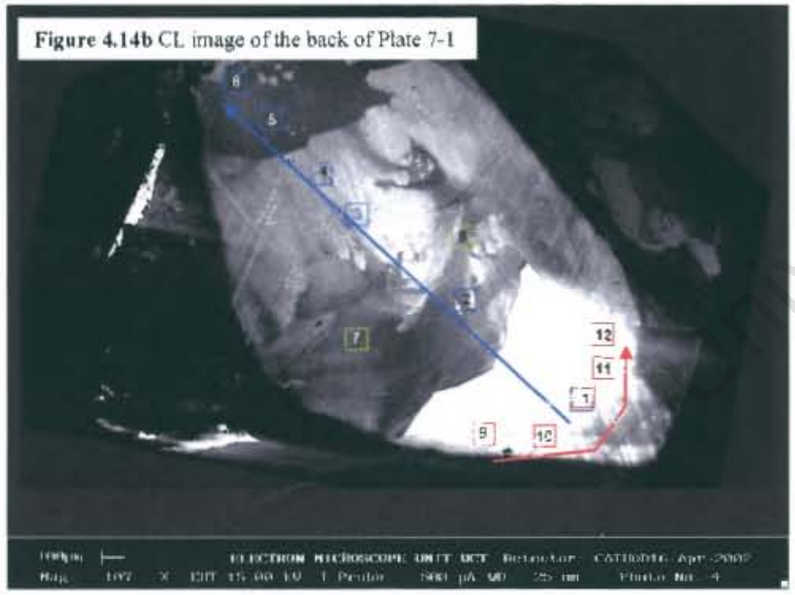

Figure 4.14b CL image of the back of Plate 7-1

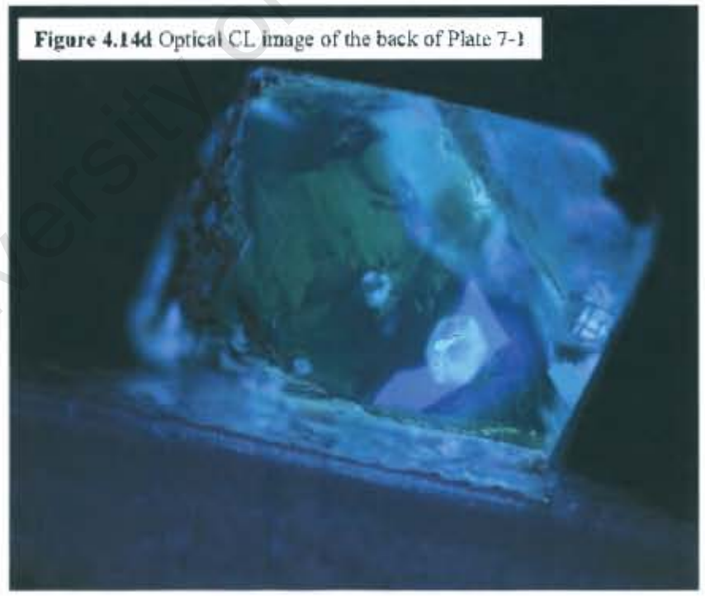

Figure 4.14d Optical CL image of the back of Plate 7-1

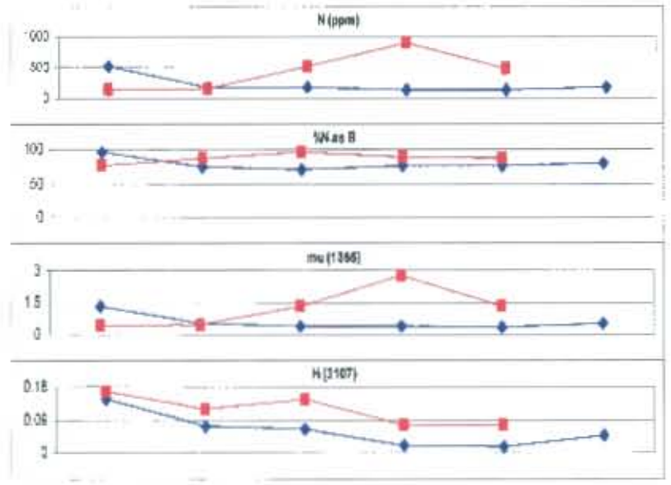

Figure 4.14f Graphs showing the variation of variables i-iv across the back of Plate 7-1: i. N (ppm), ii. %N as B; iii. mu (1365); iv. H (3107)

4.3.1.11 Plate 7-3

This plate was cut from a brown, partially resorbed octahedron. This diamond contains one green clinopyroxene inclusion and one small clear inclusion. The CL image of the front of the plate shows an area of high luminescence with a sharp boundary, associated with the clinopyroxene inclusion (Figure 4.15c). Extending from this zone is a resorbed low luminescence zone. Octahedral growth zones continue from this zone. The high luminescence zone is not seen on the CL image of the back of the plate, but the other features, as discussed above, are (Figures 4.15b).

There is a wide range in nitrogen concentrations across the plate, of 21 – 614 ppm (Figure 4.15 e.i & f.i). The nitrogen concentrations increase as the analyses move into the high luminescence area (Red & green traverse on front CL image, Figure 4.15a). There is a trend of decreasing nitrogen concentration from the irregular low luminescence zone into the octahedral growth zone (Blue traverses on front and back CL images, Figure 4.15 a & b). These trends are mirrored in the plots of %N as B (Figures 4.15 e.ii & f.ii). The range in the amount of nitrogen as B aggregates is 28 – 86%. There is a positive correlation between the intensity of platelet peaks and nitrogen concentration (Figure 4.15 e.iii & f.iii). The hydrogen peak intensity for the green traverse on the front CL image (Figure 4.15 e.iv) displays a large increase as the analyses move from the high luminescence zone into the octahedral zone. This does not correlate with the other variables, suggesting that hydrogen is more readily taken into the diamond structure during octahedral growth.

There is a large variation in temperature across this plate as with similar plates (7-1 & 7-14). The range in mantle residence temperature is 1196 – 1249 °C (Figure 4.4). This range includes a number of analyses with low-nitrogen concentrations (<100 ppm), by excluding these analyses the estimated range of mantle temperatures is 1196 – 1210 °C. From this it seems likely that the low-nitrogen analyses cause an overestimation in the temperatures. The amended temperature range is lower than that for Plates 7-1 and 7-14, an explanation for this is that the plate does not show evidence of plastic deformation which would have increased the aggregation state and therefore increased the estimated temperatures.

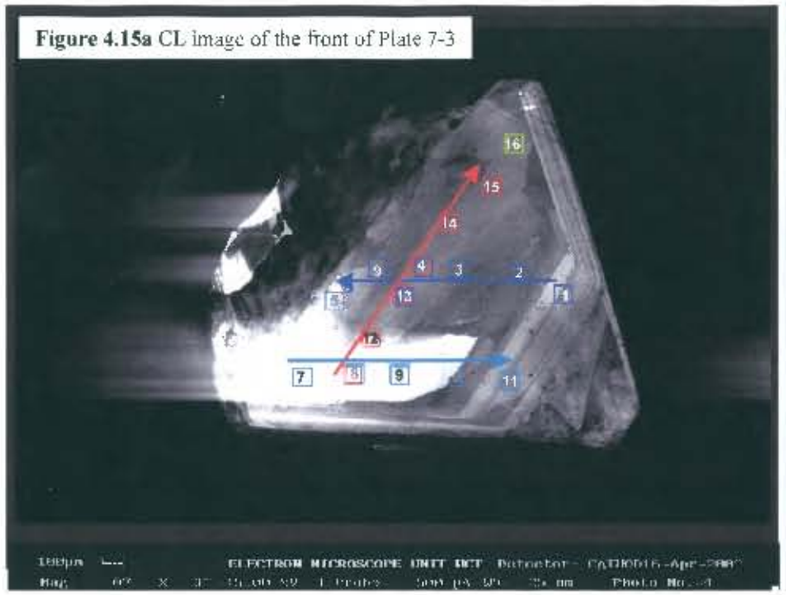

Figure 4.15a CL image of the front of Plate 7-3

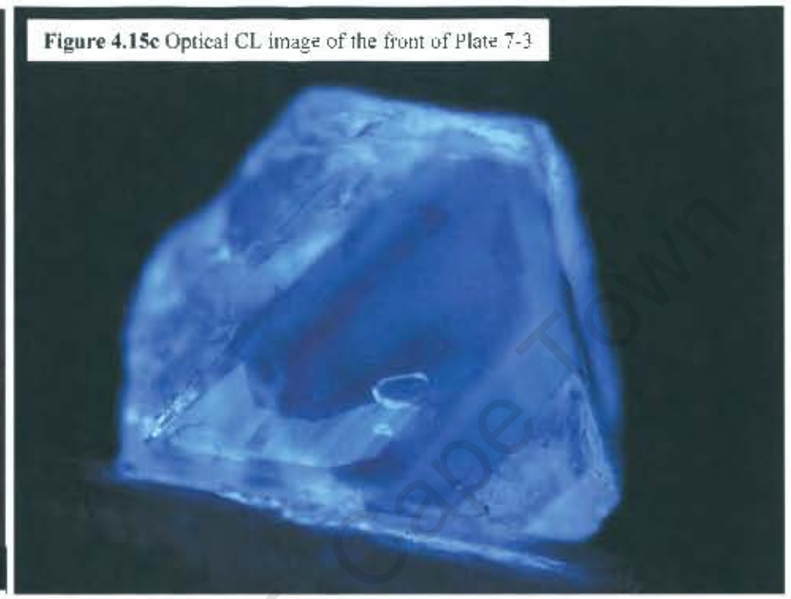

Figure 4.15c Optical CL image of the front of Plate 7-3

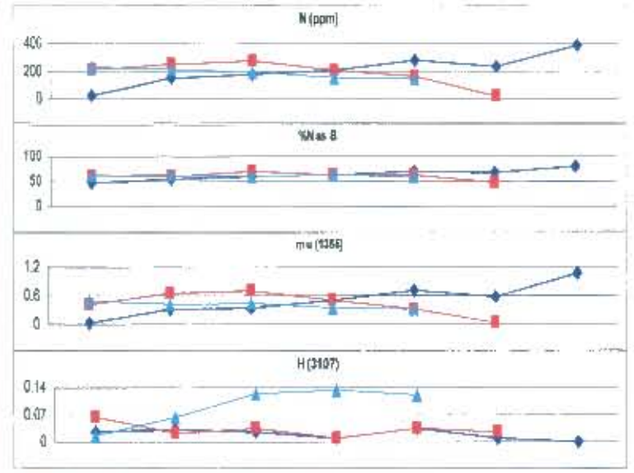

Figure 4.15e Graphs showing the variation of variables i-iv across the front of Plate 7-3: i. N (ppm), ii. %N as B; iii. mu (1365); iv. H (3107)

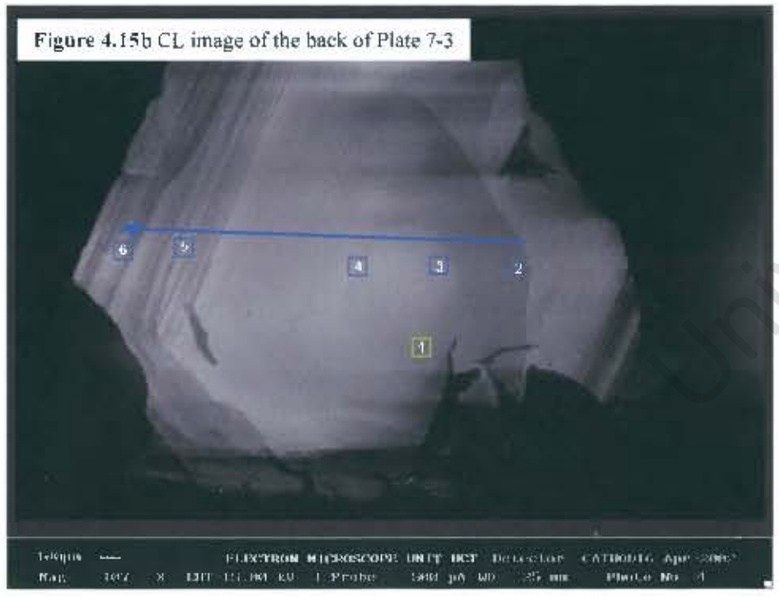

Figure 4.15b CL image of the back of Plate 7-3

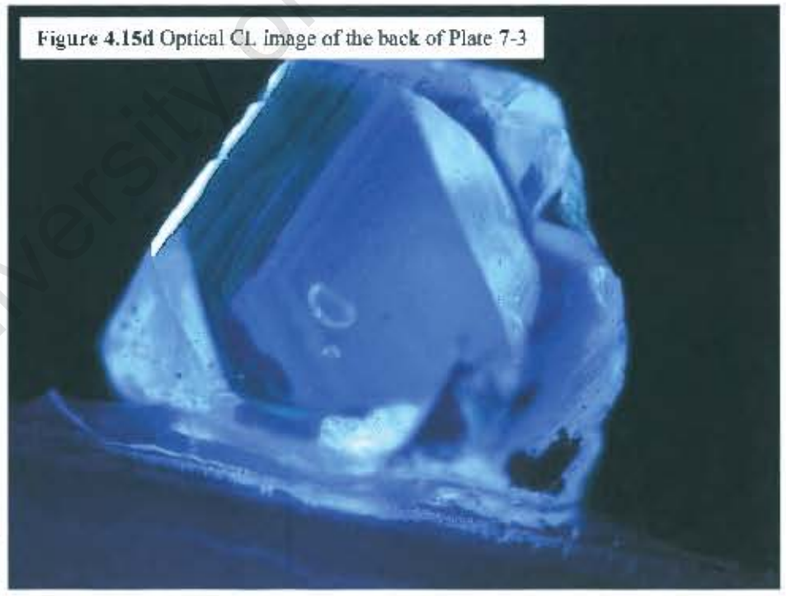

Figure 4.15d Optical CL image of the back of Plate 7-3

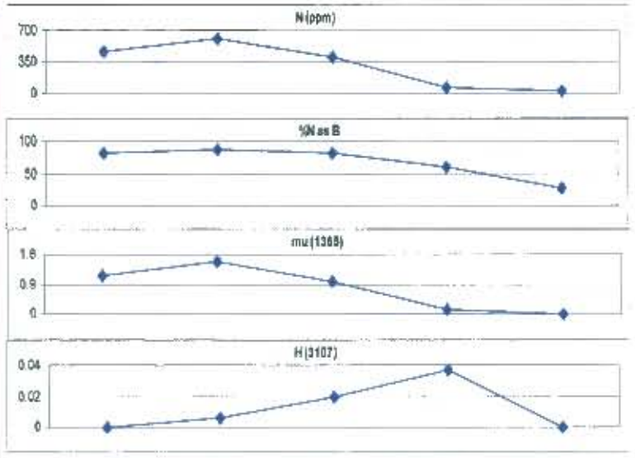

Figure 4.15f Graphs showing the variation of variables i-iv across the back of Plate 7-3: i. N (ppm), ii. %N as B; iii. mu (1365); iv. H (3107)

4.3.1.12 Plate 5-19

This plate was cut from a brown octahedron containing two purple Cr-pyrope inclusions, two clear inclusions and graphite inclusions. During polishing one of the inclusions escaped leaving an inclusion pit on the edge of the polished surface. The inclusions are located on the edges of the plate (Figure 4.16d). The CL image of the front of the plate shows multiple non-luminescent areas (Type II diamond), these areas are likely to have grown as individual nuclei with later stage of Type I growth around them. The growth zones surrounding these 'nuclei' appear to have uniform luminescence. Scotch-plaid lamination lines are evident across the front of the plate (Figure 4.16a). Good quality spectra were only obtained for the front of the plate.

The nitrogen concentrations are low and vary from 86 – 147 ppm (Figure 4.16 e.i). Where the analyses are close to the Type II 'nuclei' there is a drop in the concentration and the concentration tends to increase again away from these zones (Figure 4.16 e.i). There is a flat trend in the %N as B across the plate with a narrow range of high values of 92 – 99% (Figure 4.16 e.ii). There is poor correlation between nitrogen concentration and platelet peak intensity (Figure 4.16 e.iii). It seems likely that the plastic deformation, that caused multiple lamination lines, is responsible for catastrophic degradation of the platelet peaks. The trend in hydrogen peak intensities is similar to that of the nitrogen concentration (Figure 4.16 e.iv).

The range for estimated mantle residence temperature is very high, 1281 – 1333 °C (Figure 4.4). The deformation would cause an increase in the aggregation of the diamond and this coupled with the large amount of Type II diamond sampled would have caused an overestimation in temperature. A decrease in the aggregation state of 25% causes a decrease in the range of temperatures to 1207 - 1246 °C, which is similar to the overall range obtained for the remainder of the plates.

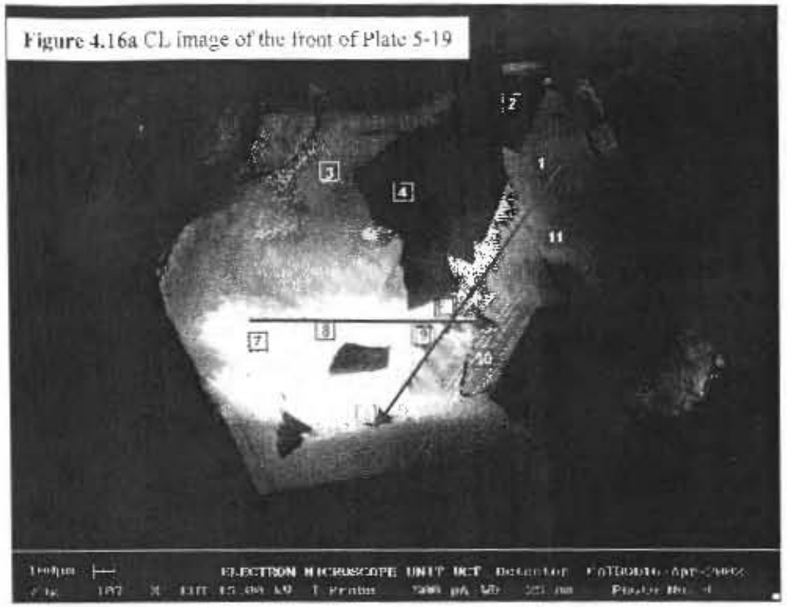

Figure 4.16a CL image of the front of Plate 5-19

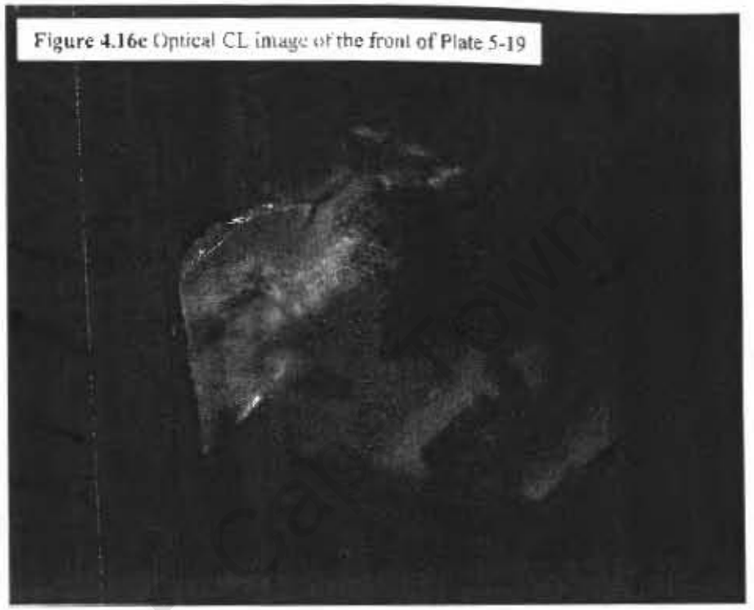

Figure 4.16c Optical CL image of the front of Plate 5-19

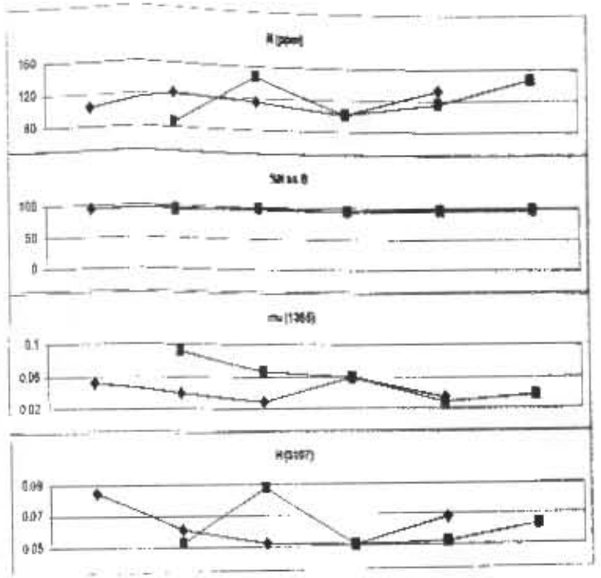

Figure 4.16e Graphs showing the variation of variables i-iv across the front of Plate 5-19: i. N (ppm), ii. %N as B; iii. mu (1365); iv. H (3107)

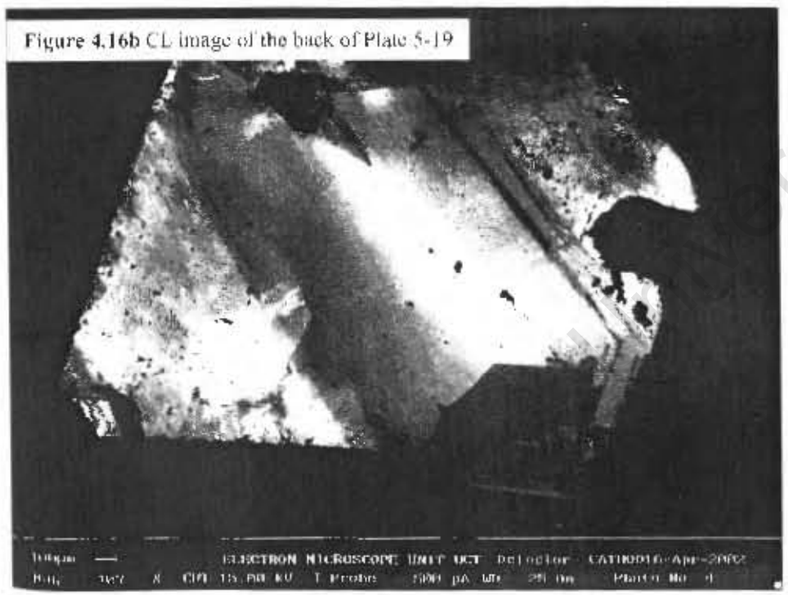

Figure 4.16b CL image of the back of Plate 5-19

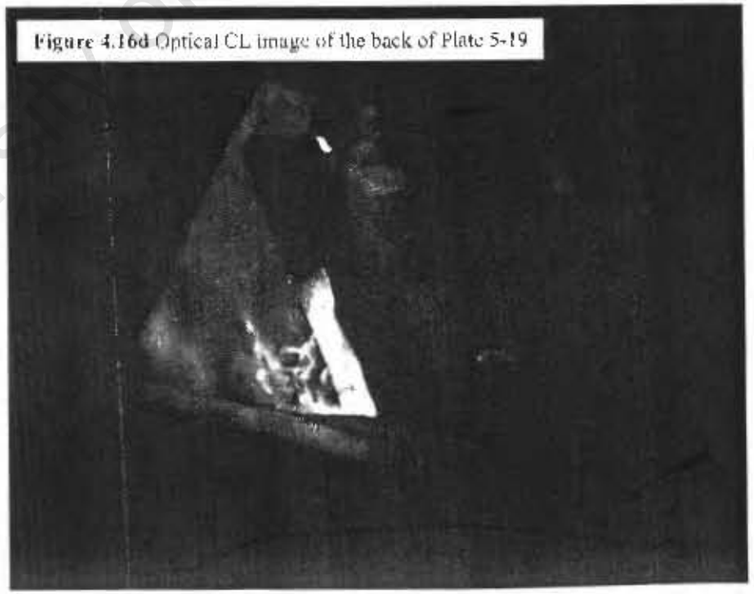

Figure 4.16d Optical CL image of the back of Plate 5-19

4.3.1.13 Plate 5-2

This plate was cut from a broken, brown tetrahexahedroid. This diamond displays a large hexagonal inclusion pit on the one surface and contains 2 purple Cr-pyrope inclusions, located in the centre of the plate, as well as numerous graphite planes (Figure 4.17c). Due to the large number of graphite planes the analyses on this diamond gave spectra that were irresolvable when run through the Opus deconvolution spreadsheet. A visual interpretation of the back CL image shows two areas of non-luminescent Type II diamond (Figure 4.17b); one of which has a cubic shape. These two zones appear to be connected by an area of banded possibly octahedral, growth. There is another zone of octahedral growth that cuts the smaller banded zone and extends to the edge of the plate. There is also some octahedral zoning developed around the inclusion pit (the centre of which has some non-luminescent glue in it). It seems likely that the two areas of Type II diamond acted as nuclei for further diamond growth, as seen in plate 5-19. After a hiatus in which some resorption occurred there was a period of octahedral growth. This was further resorbed and a final stage of octahedral growth occurred around this larger nucleus. None of these features are visible in the front CL image. There is an unusual 'swirl' luminescence visible on this side of the plate (Figure 4.17a), it may be caused by the interference from a number of graphite planes, inclusions and fracture surfaces located close to this surface (Also seen in plate 7-1).

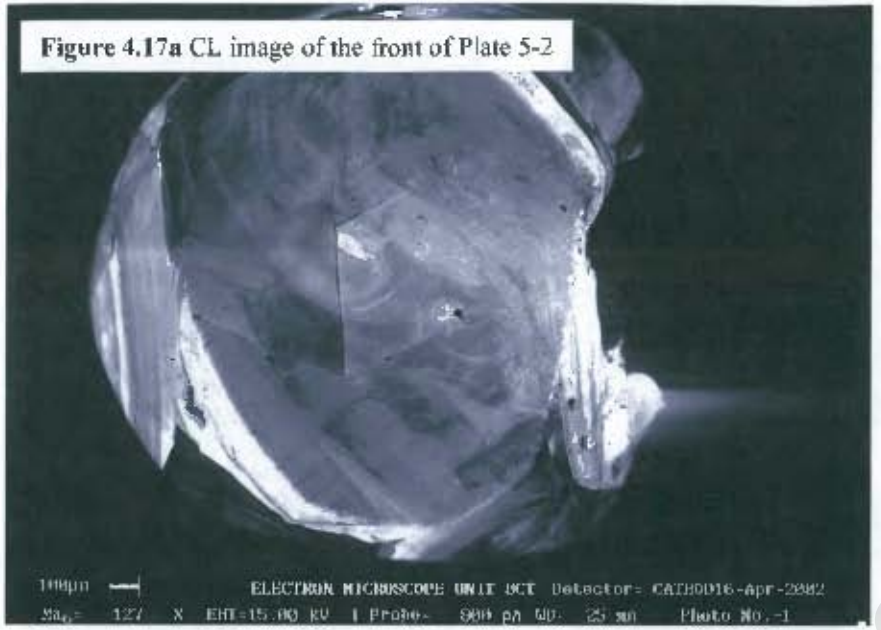

Figure 4.17a CL image of the front of Plate 5-2

Figure 4.17b CL image of the back of Plate 5-2

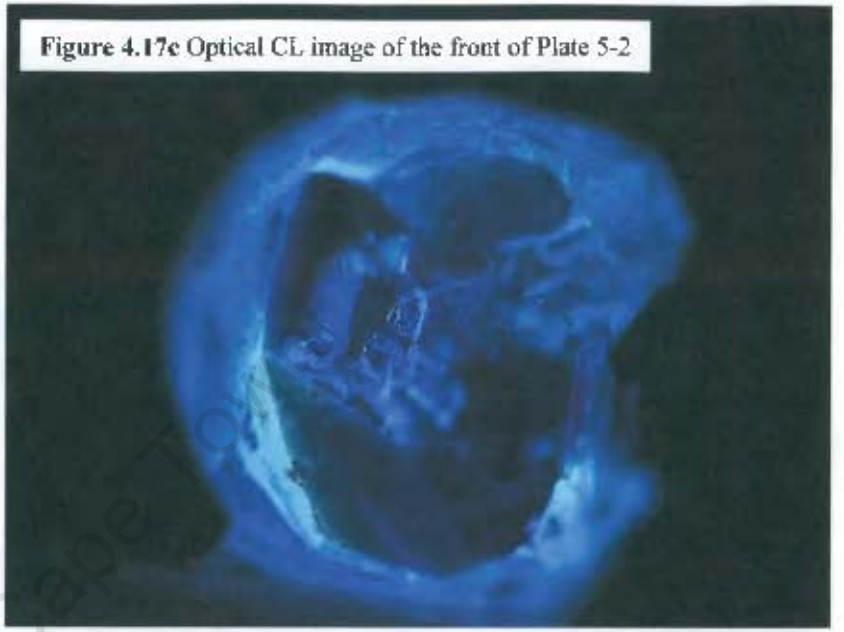

Figure 4.17c Optical CL image of the front of Plate 5-2

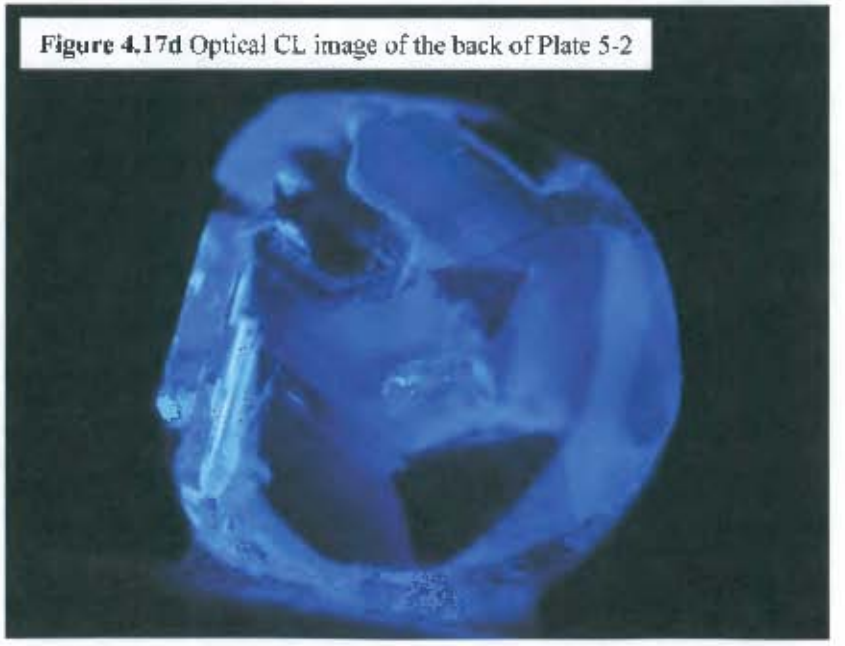

Figure 4.17d Optical CL image of the back of Plate 5-2

4.3.2 Rough diamonds

In addition to the data collected from the diamond plates the entire suite of diamonds (100 stones) were analysed using the FTIR spectrometer. This was done in order to better characterize the populations of diamonds present at Cullinan. Spectra could not be obtained for all of the diamonds and so once the inclusions were cracked out the fragments were analysed again. The fragments obtained from Steve Richardson were also analysed (P samples). The raw data for the IR analyses is given in Appendix 2, Table A.2.2 and Table A.2.3. The analyses of fragments are indicated in Tables A.2.2 and A.2.3. Visual inspection of the spectra of the whole diamonds and fragments analysed using FTIR show that 76% are Type IaAB, 15% are Type II and 9% were too distorted to distinguish Type. In order to obtain estimated values of the spectral peaks the spectra are deconvoluted through the Opus spreadsheet of Mendelssohn & Milledge (1995; Appendix 2). Analyses from about half of the suite had such low nitrogen contents that they would not run through the spreadsheet and are therefore considered to be Type II.

A study by Deines et al. (1989) on diamonds from Cullinan and Finsch showed that 25% of peridotitic (P-Type) diamonds were Type II, with only 1% of Type II diamonds for the eclogitic (E-Type) paragenesis. The P-Type diamonds make up 96% of this sample suite and of these diamonds 45% are Type I. This clearly illustrates that the present suite is not representative of the population as a whole. Of the P-Type diamonds 40% of the lherzolite diamonds are Type I, and the remainder are Type II. Of the harzburgite diamonds 51% are Type I, and the remainder are Type II. The Type I diamonds belong to the Type IaA – IaB series.

An estimated lower limit of detection for the nitrogen concentrations using FTIR is ~20 ppm (Fanus Viljoen, Pers. comm., 2002). The diamonds give a large spread in the range of nitrogen concentration from below the limit of detection to 858 ppm (Figure 4.18). The range is similar to that obtained for P-Type diamonds from Cullinan by Deines et al. (1989) of 0 - 1086 ppm. In that study, it was noted that the P-Type diamonds tend to have lower nitrogen concentrations in comparison with E-Type diamonds (Deines et al., 1989). The majority of the diamonds in this study are from the P-Type paragenesis and the nitrogen concentrations obtained from spectra of two of the E-Type diamonds are 118 and 488 ppm (Figure 4.19). The Helam and Klipspringer kimberlites have also sampled mantle in the

Bushveld region and their diamonds give a range in nitrogen concentrations of 0 – 2500 ppm (Mc Kenna, 2001; Westerlund, 2000).

The amount of nitrogen as B aggregates also spans a large range from 34 – 99% in the Cullinan suite (Figure 4.18 & 4.19). Deines et al. (1989) found a similar, wide range of 0 – 99% amount of N as B aggregates for Cullinan. It was shown that the aggregation state does not appear to be affected by the amount of nitrogen in the diamonds in those samples from Cullinan and Finsch (Deines et al., 1989). Nevertheless, there is a positive correlation between nitrogen concentration and the amount of nitrogen as B aggregates evident in the majority of samples in this study. The amount of nitrogen as B aggregates from Helam is considerably lower, from 0 – 60% (Mc Kenna, 2001). The Klipspringer diamonds show two separate groups from the Main Fissure and Sugarbird Blow pipes; one with a range in %N as B from 10 - ~50% and the other from ~ 70 – 95%. The Marsfontein pipe does not exhibit two clear groups, but instead has a range of %N as B from 0 – 95% (Westerlund, 2000). Thus, the diamonds from Cullinan show, on average, lower nitrogen concentrations and higher amounts of nitrogen as B aggregates than the diamonds from Helam and Klipspringer (Mc Kenna, 2001; Westerlund, 2000). Estimates for time-averaged mantle temperature for the harzburgitic and lherzolitic diamonds have been calculated using a residence time of 0.75 billion years, as per the diamond plates. The majority of analyses lie between the 1180 and 1240 °C isotherms, and span a total range from 1168 - 1304 °C. The three harzburgitic analyses that fall just below the 1180 °C isotherm have the highest nitrogen concentrations of the suite (788 – 858 ppm) and are therefore not likely to have sampled any Type II diamond and are most likely to reflect more accurate temperatures. The group of harzburgitic analyses with very high %N as B (>90%) and temperatures from 1264 – 1304 °C have relatively low nitrogen concentrations (83 – 141 ppm). One of these samples is 5-19, that was more intensively investigated as a plate (Section 4.3.1.). The plate showed multiple Type II areas (Figure 4.16) and catastrophic degradation of the platelet peaks. The other two diamonds may also have this unusual growth structure with extremely high %N as B aggregation giving high estimated-mantle residence temperatures. The two analyses obtained for the eclogitic diamonds give temperatures of 1263 and 1270 °C (Figure 4.19).

The temperatures for this suite are considerably hotter than that from Helam or Klipspringer of approximately 1060 – 1120 °C and 1060 – 1180 °C respectively (Mc Kenna, 2001; Westerlund, 2000). The quantity of Type II and low nitrogen growth zones in the CL

images of the plates indicates that it is also likely that there is a considerable amount of Type II or low-nitrogen diamond in the whole diamonds analysed. If this is the case the %N as B will be elevated relative to the amount of nitrogen in the analysis and the temperature will be overestimated, but by what amount is not clear. This supports the suggestion that the majority of temperatures obtained for this suite are an overestimation.

The majority of diamonds show the development of platelet peaks although the range in peak intensity is small, from 0 – 2; with the majority of diamonds giving low peak intensities of <1 (Figure 4.20). There is a strong positive correlation between nitrogen concentration and platelet intensity; there is little evidence for catastrophic degradation of the platelet peaks (as seen in some of the plates, Section 4.3.1). The platelet peak positions span a wide range of wavenumbers, from 1359 – 1383 cm^{-1}, but do not show any correlation with the estimated mantle residence temperature (Figure 4.21). There is a rough negative correlation between nitrogen concentration and estimated residence temperature for the diamonds (Figure 4.22), which supports the suggestion that a number of those diamonds with considerable quantities of Type II growth (i.e. low nitrogen concentrations) have temperatures that are over estimates.

The diamonds show a small hydrogen peak at 3107 cm^{-1}, with the majority of hydrogen intensities below 0.1. The correlation demonstrated by Westerlund (2000) between platelet peak intensities and hydrogen content does not hold for this suite.

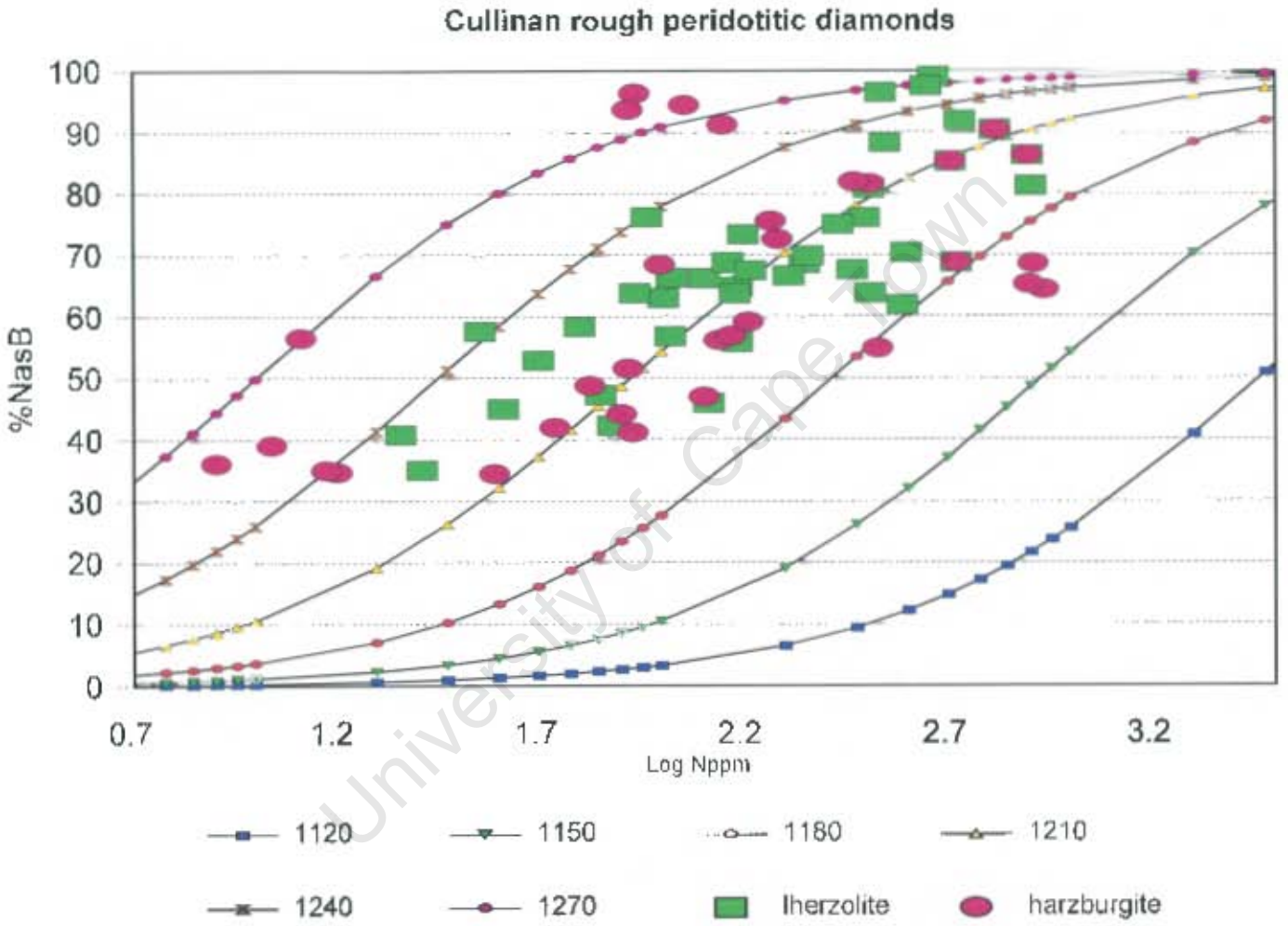

Figure 4.18 A plot of % N as B vs. nitrogen concentration in log units, for the rough peridotitic diamonds, with isotherms (°C) calculated using a residence time of 0.75 billion years. The values of the isotherms are in °C.

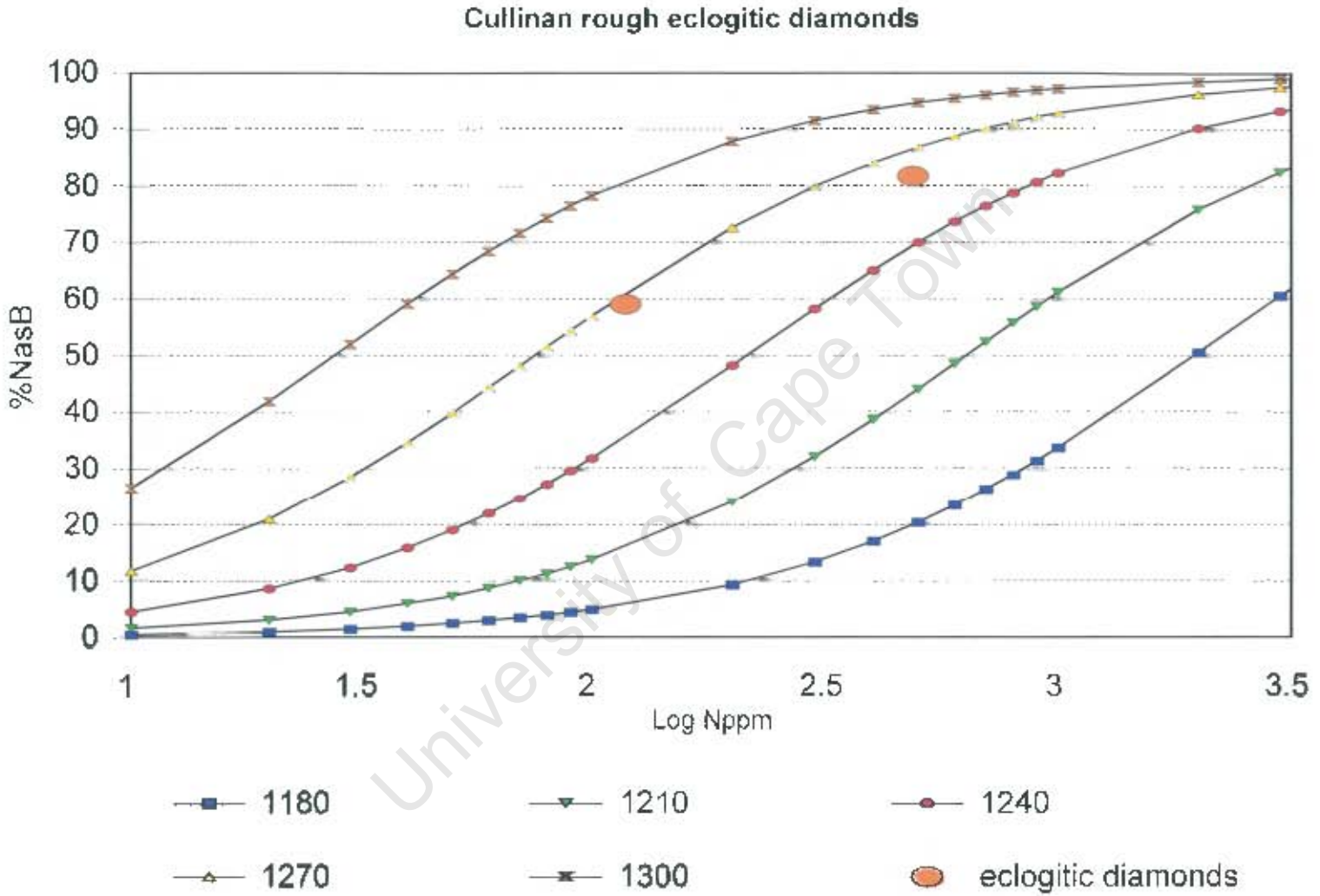

Figure 4.19 A plot of % N as B vs. nitrogen concentration in log units, for the rough eclogitic diamonds, with isotherms (°C) calculated using a residence time of 10 million years. The values of the isotherms are in °C.

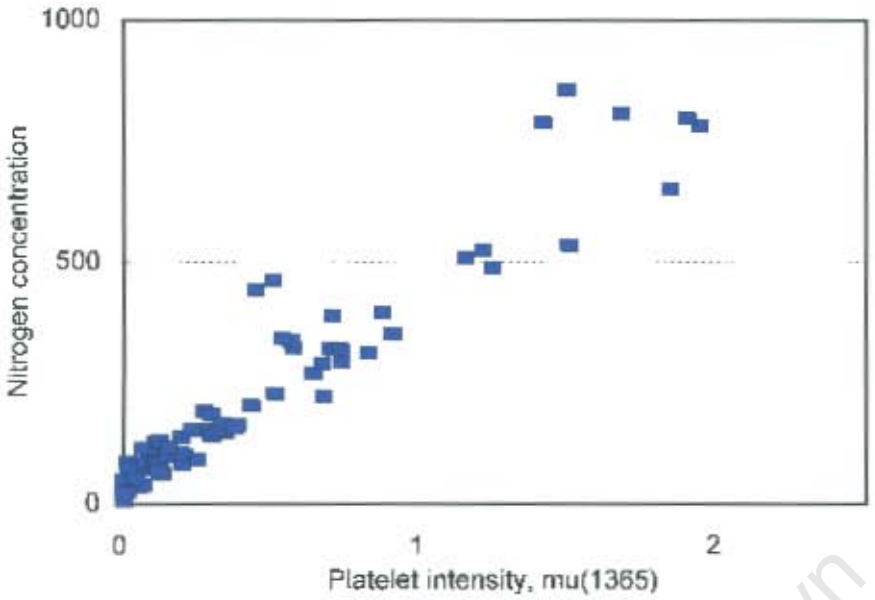

Figure 4.20 A plot of nitrogen concentration (ppm) vs. platelet intensity (mu(1365)), showing a strong positive correlation.

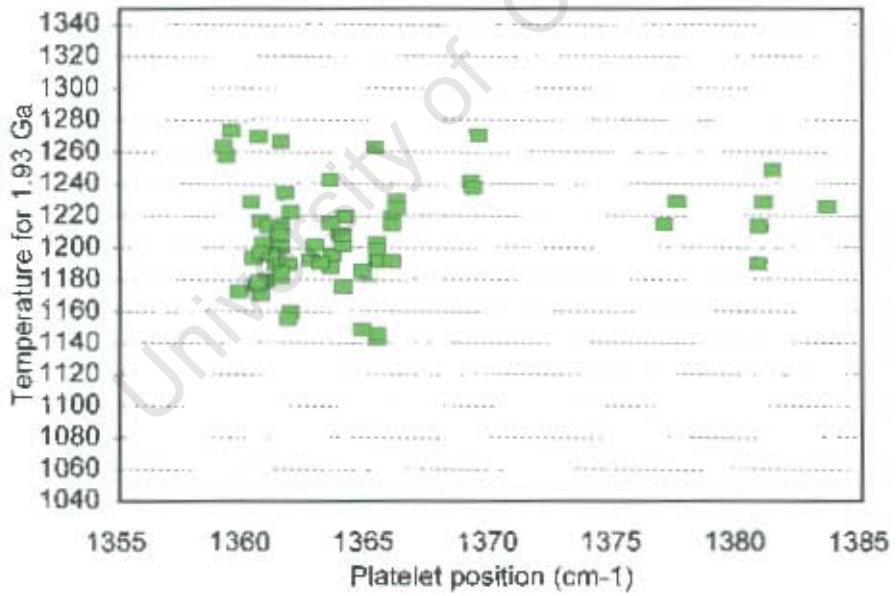

Figure 4.21 A plot of temperature (°C) vs. platelet position (cm^{-1}) for a formation age of 1.93 Ga.

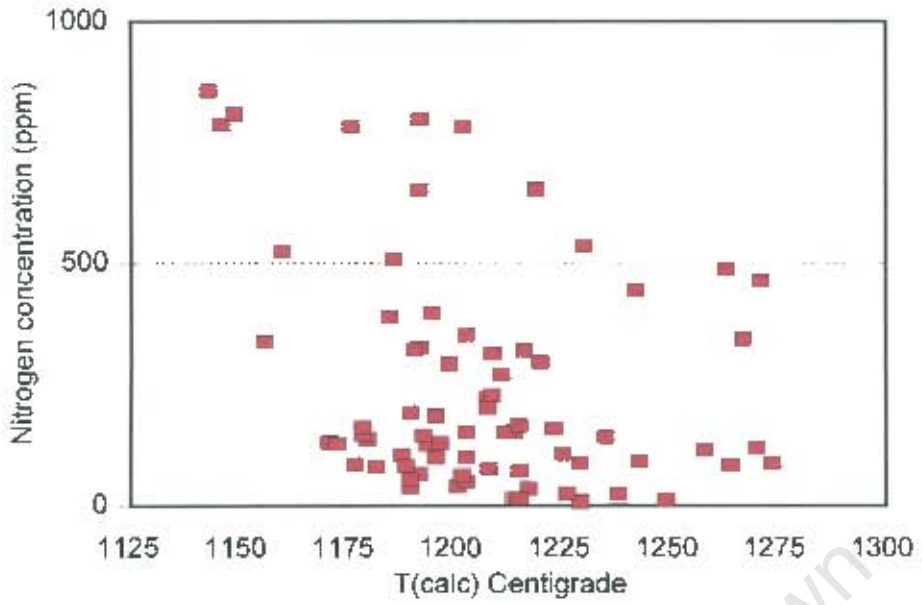

Figure 4.22 A plot of nitrogen concentration (ppm) vs. temperature (°C).

4.4 Discussion and conclusions

It is apparent that amongst the rough diamonds studied that there are two main types; those that contain nitrogen (Type I) and those that do not (Type II). Amongst those diamonds that contain nitrogen it was found that the harzburgitic and lherzolitic diamonds show remarkably similar FTIR characteristics. Continuous linear trends have also been observed between the mineral inclusion compositions of the two groups (Chapter 6). The calculations of time-averaged mantle temperatures were initially performed using the residence ages corresponding to the age of the different diamond parageneses and then recalculated after assuming that the older harzburgitic diamonds have recrystallized at the time of formation of the lherzolitic diamonds. Based on the results obtained for the time-averaged mantle temperatures for both sets of calculations as well as the reasons cited above it appears that the majority of harzburgitic diamonds have in fact recrystallized at the time of formation of the lherzolitic diamonds. The plot of %N as B vs. nitrogen concentration shows that the majority of the diamonds, both rough and plates, fall into an "isothermal envelope" between the 1180 and 1240 °C isotherms (Figures 4.3, 4.4, 4.18 & 4.19).

The diamond plates can be divided into three broad groups. The first group contain those diamonds that show regular Type I octahedral growth (Group 1). The other two groups are unusual; in one group the diamonds display areas of very high luminescence (Plates: 7-1, 7-3 and 7-14; Group 2), which may be associated with their clinopyroxene inclusions. The third group of diamond plates display multiple Type II 'nuclei' (Plates: 5-19 and 5-2; Group 3).

4.4.1 Group 1

The majority of the diamond plates show regular octahedral growth (Plates: 5-11, 5-24, 5-25, 5-26, 6-1, 7-3, 8-8 & 13-1). In this group all of the plates (except 13-1) display a decrease in nitrogen concentration and nitrogen aggregation from the centre to the edge of the plate. This trend suggests that there was a systematic decrease in the amount of nitrogen available in the growth medium over time. Some of these diamonds have cores (Plates: 5-25, 5-26, 5-11, 7-5 & 6-1), and all except Plate 5-25 do not appear to have cores that are significantly older than the rims of the diamonds. The cores have most likely acted as the catalyst for diamond growth, and in those cases where a core is not visible; it is probable that the stone was not polished through the centre (John Gurney Pers. comm., 2002). The cores show evidence of resorption, which is followed (in the majority of Plates) by Type II growth. Plates 6-1, 8-8 and 13-1 have minor Type II growth at the edges of the octahedral, Type I growth zones. This style of growth points to an episodic, cyclic growth history for all of these diamonds.

4.4.2 Group 2

Three of the five diamond plates containing clinopyroxene inclusions show an unusual very bright luminescence located at the edges of the plates (7-1, 7-3 and 7-14). This bright luminescence is associated with considerably higher nitrogen concentrations in comparison with diamond surrounding these areas. The areas of bright luminescence do not appear to be nuclei of the diamonds, but instead appear to be related to clinopyroxene inclusions situated

within or on the edge of these areas. The other two plates that contain clinopyroxene inclusions do not display zones of bright luminescence. This may be due to the chemical differences between the clinopyroxene inclusions of the diamonds. Plates 7-1, 7-3 and 7-14 have higher Ti, Al, Cr and Na and similar or lower Fe, Mn, Mg, Ca and K than plates 7-5 and 8-8 (Table 4.1).

Table 4.1 Showing the comparative chemistries of the clinopyroxene inclusions in cations per formula unit.

	Ti	Al	Cr	Fe	Mn	Mg	Ca	Na	K
7-1cpx	0.022	0.175	0.079	0.080	0.004	0.818	0.570	0.278	0.002
7-3cpx	0.008	0.122	0.070	0.075	0.002	0.850	0.656	0.179	0.002
7-14cpx	0.027	0.183	0.069	0.097	0.002	0.831	0.539	0.363	0.003
7-5cpx	0.002	0.056	0.051	0.101	0.004	1.039	0.659	0.064	0.006
8-8cpx	0.002	0.059	0.052	0.097	0.003	0.865	0.725	0.117	0.007

Plates 7-1, 7-5 and 7-14 all show a similar range of temperatures with the majority between 1200 – 1230 °C. These plates have elevated temperatures compared to plate 7-3 which has a corrected range of temperatures of 1196 – 1210 °C. Plastic deformation causes an increase in the aggregation state of the diamond and subsequently the estimated temperature. Lamination lines are seen in plates 7-1, 7-5 and 7-14, but not in plate 7-3, which would explain the lower temperatures obtained for this plate.

4.4.3 Group 3

There are two plates, 5-2 and 5-19 that have very unusual CL images with multiple Type II 'nuclei' with surrounding octahedral growth and intense deformation. Analyses were only obtained for plate 5-19 due to the number of inclusions, graphite planes and fracture surfaces in plate 5-2. There are also two other rough diamonds, 5-14 and 6-3, which have similar nitrogen concentrations and aggregation states as these two plates (Figure 4.18). Plate 5-19 shows extreme aggregation of 88 – 99%; which may imply that these diamonds are older than the remainder of the suite, as the %N as B increases with time and/or temperature. Therefore a calculation was performed where the age of formation is changed from 1.93 Ga back to 3.2

Ga and the temperatures obtained are approximately 30 °C lower than those at 1.93 Ga. It is possible that this plate is older than the remainder of the diamonds, but it seems more likely that the aggregation states of these diamonds are overestimated owing to the high amount of Type II diamond present and evidence for plastic deformation. Evans (1992) suggests that plastic deformation enhances nitrogen aggregation in diamonds by causing a higher concentration of vacancies within the diamond, but it is not stated by what degree. If the percentage aggregation state of these diamonds is reduced by 25% the range of temperatures calculated for a residence time of 0.75 billion years falls within the isothermal envelope obtained for the rest of the diamonds. It is possible that the enhancement of the nitrogen aggregation state by deformation and the overestimation of temperatures due to Type II diamond sampled could cause this plate to appear to have formed under very different conditions from the remainder of the diamonds.

4.5 General growth history for Cullinan diamonds

It is clear that the growth histories of diamonds are complex even within a single population of diamonds (i.e. lherzolitic diamonds), and certainly across multiple populations at Cullinan. This being the case a general growth history for Cullinan diamonds is proposed. The majority of diamonds in this suite appear to have grown episodically with the majority of growth being characterised as Type I octahedral growth, under variable nitrogen concentration conditions in the growth medium. There is also evidence for resorption in some cases and occasional Type II octahedral growth. This cyclic growth is suggested to have occurred over an extended period of time from around the formation of the harzburgitic paragenesis (~ 3.2 Ga), with a likely period of quiescence, starting again around the time of formation of the lherzolitic paragenesis (1.93 Ga). Evidence points to the recrystallization of the harzburgitic paragenesis around the time of lherzolitic diamond formation. The heat associated with the intrusion of the Bushveld Igneous Complex (2.05 Ga; Tankard et al., 1982) is proposed to have recrystallized, and in some cases only substantially resorbed, the harzburgitic diamonds (e.g. Core Plate 5-25). This intrusive event may also explain why the time-averaged mantle temperatures and nitrogen aggregation states obtained for the Cullinan diamonds are generally

hotter and more highly aggregated than those obtained for the Klipspringer and Helam diamonds. The Cullinan kimberlite intrudes the Bushveld Igneous Complex, whilst Klipspringer and Helam are situated north and west of the Bushveld Igneous Complex respectively (Westerlund, 2000; Mc Kenna, 2001). A similar growth cycle is predicted for the younger eclogitic diamonds although they need to be investigated further as plates to confirm this.

5. CARBON AND NITROGEN ISOTOPES

5.1 Introduction

The study of mantle-derived carbon and nitrogen is important in order to help explain the degassing history of the Earth. Only a few mantle-derived samples can give data for nitrogen as it typically occurs in low concentrations and may have been contaminated by atmospheric and organic material. It is possible to analyse both carbon and nitrogen directly from the diamond crystal, due to its resistant, unreactive nature and the relatively high concentrations of nitrogen in the lattice. These studies also provide clues to the sources of carbon and nitrogen in the mantle, which are not fully understood.

Carbon isotopes are measured relative to a known standard and reported in per mil (‰). The expression for carbon isotopes is:

$$\delta^{13}C = \frac{(^{12}C/^{13}C)_{sample} - (^{12}C/^{13}C)_{PDB}}{(^{12}C/^{13}C)_{PDB}} \times 1000\ ‰$$

The PDB standard is the isotope ratio measured from belemnite of the Cretaceous Peedee formation (Craig, 1957).

A wide range of values of carbon isotopic composition of diamonds has been found, from -35 to +3 ‰ (Sobolev et al., 1979; Galimov, 1991, Kirkley et al., 1991). There is a distinction between peridotitic (P-Type) and eclogitic (E-Type) diamonds. The former have a limited range in values, commonly between –10 to +1 ‰ with a mean of –4.6 ‰ (Sobolev et al., 1979). This range also reflects the peak of the distribution for E-Type diamonds, which is also exhibited in carbonatites, kimberlite carbonates and dissolved C and CO_2 vesicles in MORB (mid-ocean ridge basalt) and OIB (ocean island basalt) glasses (Kirkley et al., 1991). The E-Type diamonds have a far wider overall range of carbon isotopes from –35 to +3 ‰ (Sobolev et al., 1979).

Atmospheric nitrogen is isotopically homogeneous and has a $\delta^{15}N$ value of 0 ‰ (Mariotti, 1983). Air is the standard used when measuring nitrogen isotopes. The expression for nitrogen isotopes is:

$$\delta^{15}N = \frac{(^{14}N/^{15}N)_{sample} - (^{14}N/^{15}N)_{air}}{(^{14}N/^{15}N)_{air}} \times 1000\ ‰$$

The range of $\delta^{15}N$ is large for peridotitic diamonds, +10 to –24 ‰ (Cartigny et al., 1997, 1998b). The range for eclogitic diamonds is also wide, if the "low- $\delta^{13}C$" group of Boyd and Pillinger (1994) and the cores of coated stones are included, and ranges from +16.6 to –10 ‰ (Cartigny et al., 1998a,b). Nitrogen isotope results for MORB (mid-ocean ridge basalt) are mostly positive +7.5 ±1 ‰ (Exley et al., 1986). It is a possibility that fractionation occurs during degassing and eruption onto the sea floor (Javoy et al., 1986); which may explain why the negative mode obtained for diamonds differs from that of the MORB.

There is no consensus on the source of carbon and nitrogen for diamonds to explain this wide range of isotope values. The three main models will be discussed briefly here.

5.1.1 Isotopic fractionation

It has been proposed that relatively large isotope fractionation can occur during diamond formation if there is the involvement of a vapour phase (CH_4 and/or CO_2) with the fluid at high temperatures (>1000 °C) (Bottinga, 1969a,b; Deines, 1980). The fractionation factor of ~ 4-5 ‰ could account for a range of carbon isotopes from ~ -10 to +1 ‰, assuming a starting isotope value of the source region of –5 ‰ (Deines, 1980). It is difficult to account for the $\delta^{13}C$-depleted, E-Type diamonds with carbon isotope values <-10 ‰ using Rayleigh fractionation.

Another problem with this model is that it requires different fractionation mechanisms for peridotites and eclogites. These have been explained however, by different carbonation and oxidation reactions for these rock types (Cartigny et al., 1998a). It has been shown that

carbonation of olivine occurs at lower pressures than that of clinopyroxene and/or garnet. A result of this is that CO_2 is stable to higher pressures in eclogitic rocks (Luth, 1993). This implies that at the same depth and oxygen fugacity, diamond can coexist with carbonate in eclogites whereas only carbonates are stable in the peridotite. At high temperatures (~1300 °C) the carbonate or carbonatitic melts in equilibrium with eclogite release CO_2. This CO_2 degassing is suggested to cause the isotopic fractionation of carbon in the eclogitic rocks and diamonds (Cartigny et al., 1998a).

Nitrogen within the convecting mantle is suggested to be globally quite homogeneous with an isotopic value of approximately –5 ‰ (Boyd & Pillinger, 1994). These authors believe that the nitrogen isotopic range of –12 to +6 ‰ for diamonds from their "high- $\delta^{13}C$" group ($\delta^{13}C$ of –6.4 to –2.9 ‰) can be explained by fractionation of a relatively homogeneous source. Boyd et al. (1994) suggest that the growth rate of a diamond may influence its nitrogen isotopic composition and its nitrogen concentration and that the wider range of $\delta^{15}N$ values obtained compared with $\delta^{13}C$ values could be a function of kinetic reactions leading to diamond growth.

5.1.2 Primordial mantle heterogeneities

The similarity in range of carbon isotopes in iron meteorites ($\delta^{13}C$ = -30 to –3‰) with that of diamonds led researchers to suggest that the Earth may have retained its primordial isotopic inhomogeneity (Deines, 1980; Deines et al., 1987). However, the range of values for peridotitic diamonds is consistent with a homogenised mantle, with regard to carbon. It is also difficult to imagine that a primordial component has been preserved since the Earth's accretion (Kirkley et al., 1991). Iron meteorites are also assumed to be the cores of disaggregated parent bodies, which correspond to the Earth's core and not the mantle. This would mean that the range of isotopic values of iron meteorites would not necessarily reflect mantle values (Kirkley et al., 1991). Another point of interest is that iron meteorites with low $\delta^{13}C$ have oxygen isotopes that are distinct from terrestrial oxygen (Clayton et al., 1976); therefore if the Earth had not homogenised after accretion we would expect there to be oxygen isotope anomalies, which are not seen (Boyd & Pillinger, 1994).

It is possible to produce a theoretical range of isotopic compositions similar to that of all diamonds if a two-stage accretionary process of the Earth occurred, with a late stage carbonaceous chondrite-like veneer (Javoy and Pineau, 1983). The range in carbon isotope values for carbonaceous chondrite is –26 to 0 ‰ (Kerridge, 1985). However this material would have to have been kept separate from the source of peridotitic diamonds for approximately 2 billion years prior to the crystallization of eclogitic diamonds (Kirkley et al., 1991).

Cartigny et al. (1997) and Javoy (1997) suggest that the low $\delta^{15}N$ values obtained for diamonds at Fuxian, China of down to –25 ‰ may indicate a primordial reservoir of nitrogen in the mantle, which is similar to enstatite chondrites. They suggest that in comparison to carbon the flux of nitrogen in and out of the mantle is very limited, which would explain why mantle carbon is reasonably well homogenised and would allow for the retention of material depleted in ^{15}N.

5.1.3 Subduction model

This model can account for the wide range in $\delta^{13}C$ isotopes in eclogitic material. The range in carbonaceous crustal material, both recent and ancient, is wider than that seen in E-Type diamonds (Kirkley & Gurney, 1989; Kirkley et al., 1991). It is suggested that eclogitic diamonds are formed from crustal carbon that was carried into the mantle by a subducting oceanic slab (Kirkley et al., 1991). The subducted oceanic basalt slab is potential protolith for eclogite. It is essential that the slab does not completely homogenise during metamorphism, in order to preserve the range of isotope compositions. There are examples of high-grade metamorphic rocks retaining a large isotopic range, such as rocks in Naxos (Ganor et al., 1994) and graphites coexisting with carbonates in the Catalina Schists (Grove and Bebout, 1995).

A study by Boyd & Pillinger (1994) found the range of $\delta^{15}N$ values, obtained for a group of diamonds with low $\delta^{13}C$ values, is –3 to +16 ‰. This range of values is consistent with the formation of the diamond from subducted crustal material. A problem with the

subduction model with regard to nitrogen isotopes is that it is not clear whether the nitrogen in the subducting slab can be recycled into the diamond stability field (Boyd & Pillinger, 1994).

Further evidence to support the subduction model is that eclogitic sulphide inclusions in diamonds from Orapa preserve mass-independent sulphur isotope fractionations, which have been interpreted as the recycled component of Archaean sediments (Farquhar et al, 2002).

5.2 Carbon isotope results

The analyses were performed at the stable isotope laboratory at Queen's University, Kingston, Canada, using continuous flow technology. A detailed methodology and tabulated data for the carbon and isotopes is given in Appendix 3. The stable isotope data for the diamonds is presented in Table A.3.2. All of the diamonds, with the exception of those diamonds polished into diamond plates were analysed (Section 4.3.1). These analyses included the 19 diamonds (now broken and kept in separate glass phials) from Cullinan Mine, used in a previous inclusion study by Steve Richardson (Richardson et al., 1993). The mineral inclusions had already been liberated from the diamonds (See Chapter 6) and so the fragments used for each stable isotope analysis were unlikely to contain any inclusions.

The range of carbon isotope values obtained is –10.3 to –1.0 ‰ (Figure 5.1 & Figure 5.2), with an error on the analyses of ± 0.2 - 0.3‰. This range is similar to that obtained by Deines et al. (1989) of –12.34 to –1.96 ‰ for diamonds from Cullinan. Whilst there is no difference between the mean of the E- and P-Type diamonds in the study of Deines et al. (1984), they did show that a significant difference exists between the distributions of E- and P-Type diamonds from Cullinan. The authors found that 80% of E-Type diamonds fall between –4 to –6 ‰ and only 10% of P-Type diamonds lie in that range, with the remainder spread across the entire range obtained. The E-Type diamonds analysed in this study fall within the range previously defined by Deines et al. (1984) and have a range of carbon isotope values from –4.3 to –6.1 ‰ (mean = -4.92 ‰). The eclogitic samples analysed in this study fall within the range of peridotitic samples. There is no significant difference in mean

isotopic composition between diamonds of different colour and shape in this study (Table A3.1).

Figure 5.1 shows that the mean obtained for the E-Type diamonds from this study is –4.92 ‰ (± 0.84 1σ; n = 4); this value is heavier, but within error, of the mean obtained for E-Type diamonds by Deines et al. (1984) of –4.74 ‰ (± 1.38 1σ; n = 42). The same observation can be made about the P-Type diamonds (Figure 5.2). The mean obtained from this study is –4.02 ‰ (± 1.51 1σ; n = 101) and that obtained from the study of Deines et al. (1984) is –5.01 ‰ (± 2.69 1σ; n = 20). This difference in mean isotope values may be related to the difference in the number of diamonds analysed in the different studies.

There is no particular trend evident between the nitrogen concentration and the $\delta^{13}C$ values of the diamonds in this study (Figure 5.3). The samples fall largely within the range obtained by Cartigny et al. (2001) for diamonds worldwide.

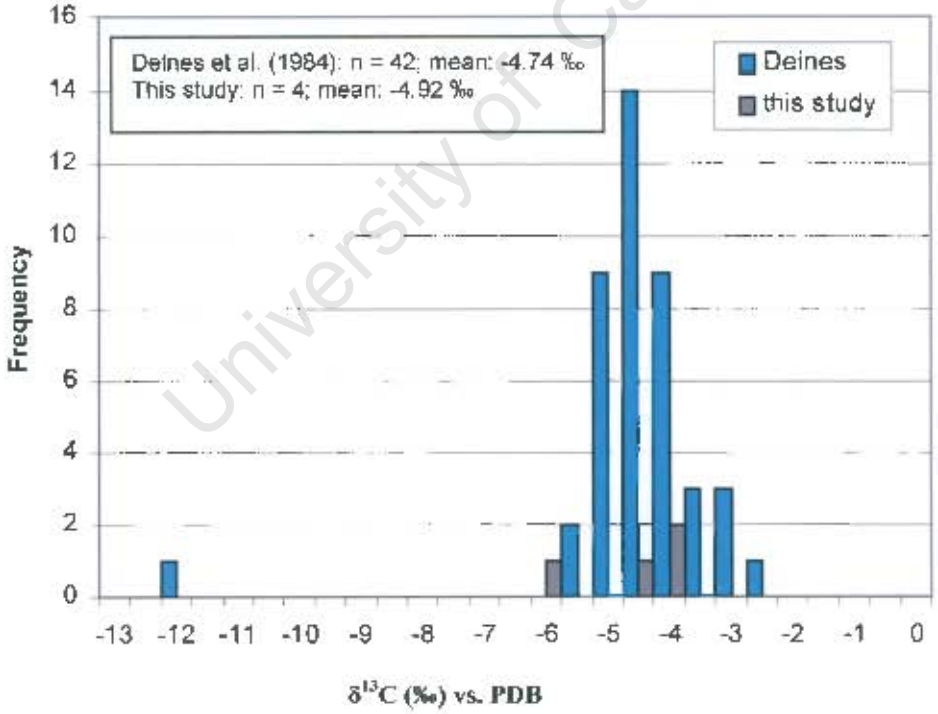

Figure 5.1 A histogram of carbon isotope results for Cullinan showing the results obtained by Deines et al. (1984) and the results from this study for E-Type diamonds.

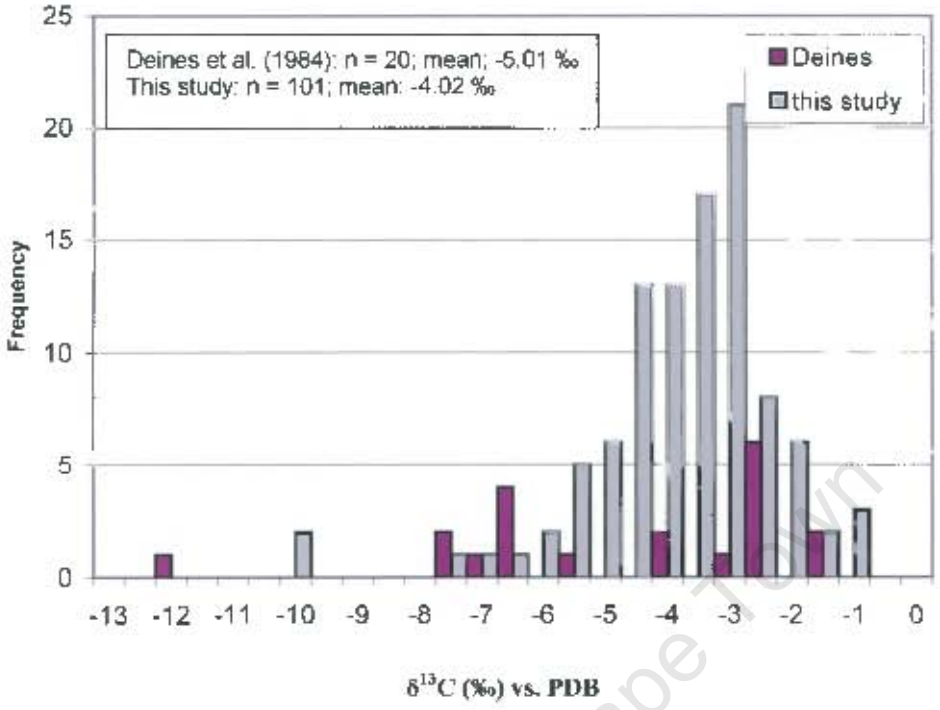

Figure 5.2 A histogram of carbon isotope results for Cullinan showing the results obtained by Deines et al. (1984) and the results from this study for P-Type diamonds.

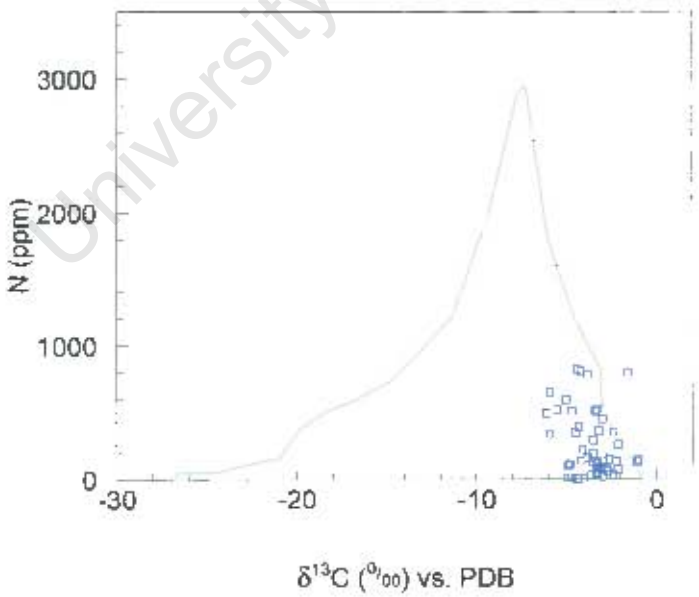

Figure 5.3 A plot of $\delta^{13}C$ vs. nitrogen concentration (ppm) after Cartigny et al. (2001). The green field indicates worldwide analyses (n = 730) and the blue squares are samples from this study (n = 48).

5.2.1. Mineral chemistry and carbon isotopes

A number of relationships were established by Deines et al. (1984) for Cullinan, between $\delta^{13}C$ and the mineral chemistry of the diamond inclusions. These relationships were investigated in this study, however no relationships were evident for the mineral inclusions.

5.2.1.1 Peridotitic Garnet

The diamonds containing lherzolitic garnets have a higher mean $\delta^{13}C$ value of -3.89 ‰ (± 1.32; n = 62) when compared with the mean of the diamonds containing harzburgitic garnets, of -4.2 ‰ (± 1.49; n = 39). Van Heerden et al. (1995) investigated the difference in paragenesis for a number of diamonds from southern Africa (including Cullinan). The authors observed that the lherzolitic diamonds were negatively skewed towards lighter $\delta^{13}C$ values, whereas the harzburgitic diamonds are more evenly spread. The authors attributed the difference in carbon isotope values for the two parageneses to a difference in the metasomatic history of their source regions. This difference is not observed in for the lherzolitic and harzburgitic parageneses of this study, as each of the parageneses is negatively skewed and within error of one another using the standard error of skewness (lherzolitic diamonds: -1.5 ± 0.3 and the harzburgitic diamonds: -1.2 ± 0.4; Figure 5.4). Deines et al. (1984) noted positive linear relationships between the major element chemistry and $\delta^{13}C$ for peridotitic garnet inclusions from Cullinan. These trends were not observed for the garnet mineral inclusions from this study (Figures 5.5 and 5.6)

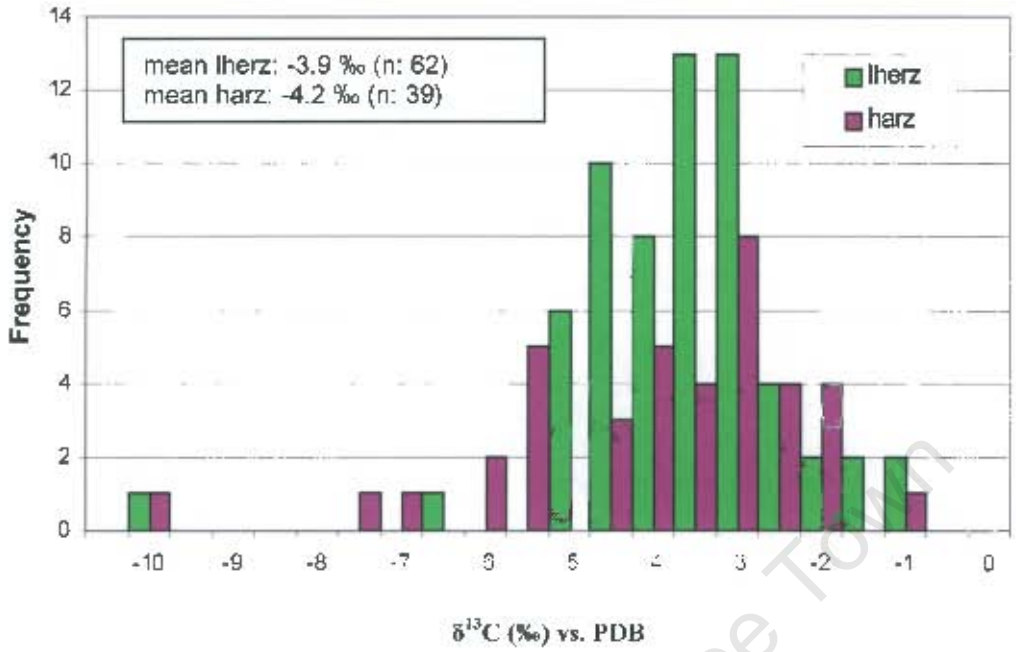

Figure 5.4 A histogram showing the carbon isotope values for the lherzolitic and harzburgitic diamonds. The error on skewness is measured in standard error of skewness

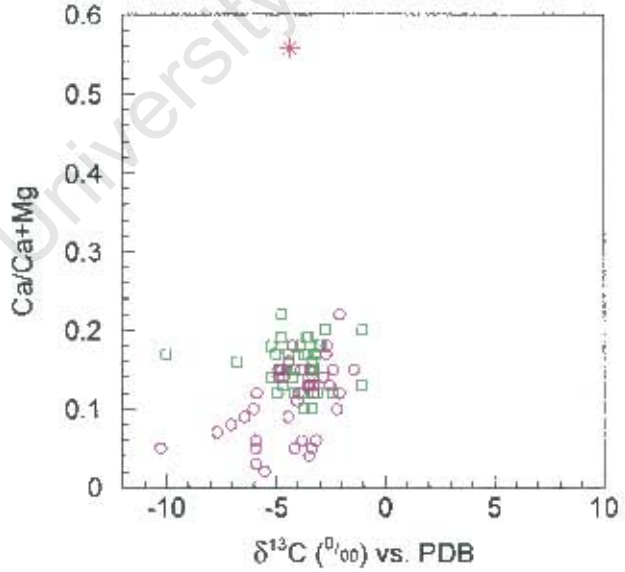

Figure 5.5 A plot of $\delta^{13}C$ vs. Ca/(Ca+Mg) for Cullinan. Squares=lherzolitic, circles–harzburgitic, asterisk–eclogitic

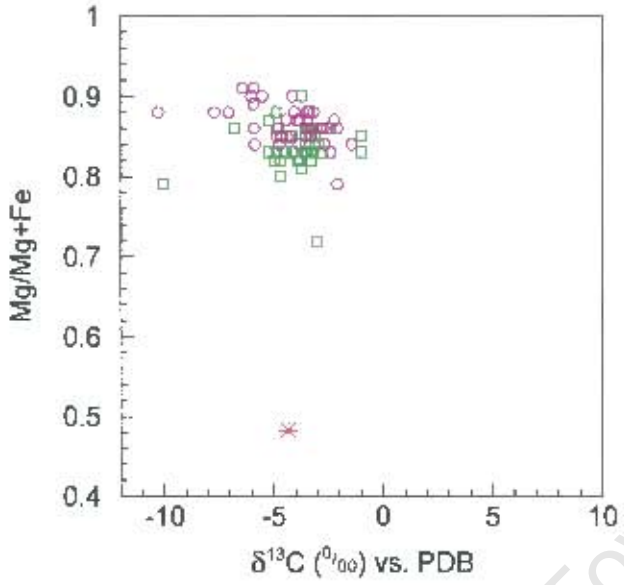

Figure 5.6 A plot of $\delta^{13}C$ vs. Mg/(Mg+Fe) for Cullinan. Squares=lherzolitic, circles=harzburgitic, asterisk=eclogitic

5.3 Nitrogen isotope results

The analyses were performed at the stable isotope laboratory at Queen's University, Kingston, Canada, using continuous flow technology. A detailed methodology and tabulated data for the carbon and isotopes is given in Appendix 3. The stable isotope data for the diamonds is presented in Table A.3.2. Only those diamonds with significant nitrogen concentrations (from FTIR estimates) were selected to be analysed for nitrogen isotopes. Unfortunately, due to the low nitrogen concentrations of the majority of this suite and poor sensitivity of the instrument used only 10 meaningful nitrogen isotopic compositions were obtained. The range in values obtained is wide, from -24.5 to +10.2 ‰, with an error on the analyses of ± 0.4 – 0.5‰.

A study of $\delta^{13}C$ and $\delta^{15}N$ of diamonds from a wide range of localities, including Cullinan, was undertaken by Boyd and Pillinger (1994). This study established two groups of diamonds on a plot of $\delta^{13}C$ vs. $\delta^{15}N$ (Figure 5.7), a "high- $\delta^{13}C$ group" (-6.4 to –2.9 ‰) and a "low- $\delta^{13}C$ group" (-19.4 to –9.5 ‰). The "high- $\delta^{13}C$ group" is characterised by nitrogen that is generally depleted in ^{15}N relative to air, whereas the "low- $\delta^{13}C$ group" generally contain nitrogen enriched in ^{15}N relative to air. The Cullinan samples fall within the "high-

$\delta^{13}C$ group"; this group defined by Boyd and Pillinger (1994) has a range of $\delta^{13}C$ values of –5.3 to –2.9 ‰ and a range in $\delta^{15}N$ values of –12.3 to –1 ‰ (Boyd & Pillinger, 1994). This range is narrower than that obtained in this study ($\delta^{13}C$: -10.3 to –1 ‰ and $\delta^{15}N$: -24.5 to +10.2‰), the plot of $\delta^{13}C$ vs. $\delta^{15}N$ shows that the samples in this study fall within and extend the "high- $\delta^{13}C$ group" to much lower $\delta^{15}N$ values (Figure 5.7). Low $\delta^{15}N$ values have also been obtained for diamonds from Fuxian in China (Cartigny et al., 1997) and Panda in Canada (Westerlund et al., 2003). The majority of the diamonds from Fuxian that were chosen for analyses were peridotitic; they yielded results for $\delta^{13}C$ of –6.05 to +0.41 ‰ and a range of $\delta^{15}N$ values of –24.2 to +7.5 ‰ (Cartigny et al., 1997). The authors have added their analyses from Fuxian to the plot of Boyd and Pillinger (1994) and the Fuxian data also falls within and beyond the "high- $\delta^{13}C$ group" in a similar range to that of the Cullinan samples in this suite (Figure 5.7). Results from a suite of peridotitic diamonds from the Panda kimberlite in Canada (Westerlund et al., 2003), also fall within and extends the "high- $\delta^{13}C$ group". The range obtained for the Panda diamonds are $\delta^{13}C$ values of ~ -10 to 0 ‰ and $\delta^{15}N$ values of -25.6 to -6.8 ‰ (Westerlund et al., 2003). The isotopic compositions of the Panda diamonds were obtained using spot analyses across polished plates using SIMS. The range in nitrogen isotope values within individual diamonds varied from 0.5 ‰ to 8 ‰ (Westerlund et al., 2003). A general negative trend between the nitrogen isotopic composition and nitrogen concentration was also observed within individual diamonds from Panda (Figure 4: Westerlund et al., 2003).

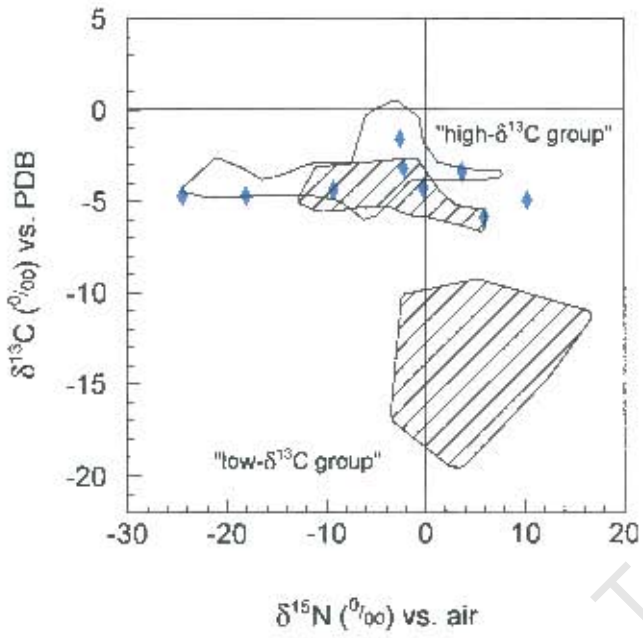

Figure 5.7 A plot of $\delta^{13}C$ vs. $\delta^{15}N$ for diamonds showing the "high-$\delta^{13}C$" group and "low-$\delta^{13}C$" group of Boyd and Pillinger (1994, hatched field) and the field obtained by Cartigny et al. (1997) for diamonds from Fuxian (blank field). Diamonds=samples from this study.

5.4 Discussion and conclusions

Boyd and Pillinger (1994) explained the isotopic compositions found in the "high-$\delta^{13}C$ group" by isotopic fractionation of both carbon and nitrogen from a globally homogeneous convecting mantle reservoir of ~ -5‰ with respect to both elements. Cartigny et al. (1998) explain the development of the majority of nitrogen isotopic compositions (-10 to +7‰) within the suite by isotopic fractionation of a globally homogeneous reservoir. They attribute the very low nitrogen isotope compositions to a portion of mantle bearing a primary $\delta^{15}N$ signature, which matches that of enstatite chondrites. Cartigny et al. (1998) suggest that the low values obtained in that study support the heterogeneous accretion model of the Earth as proposed by Javoy et al. (1984; 1986). The way in which a portion of primitive mantle is proposed to escape homogenous accretion is that a small portion of sublithospheric mantle remains isolated from the convecting mantle. Westerlund et al. (2003) attributes the wide variation in $\delta^{15}N$ observed for the Panda diamonds to differences in the source composition.

The authors also suggest that the negative correlation between nitrogen concentration and $\delta^{15}N$ within individual diamonds and the variation in $\delta^{15}N$ in individual diamonds may be related to fractionation processes. Alternatively they suggest that the trend and variations may be caused by changes in P-T-fO_2 conditions during diamond growth (Westerlund et al., 2003).

Boyd et al. (1994) suggest that the nitrogen isotopic composition of octahedral diamonds may be controlled by the growth rate of the diamond. ^{15}N bonds more strongly to the diamond surface than ^{14}N and therefore as the nitrogen content of the diamond decreases the $\delta^{15}N$ value should increase (Boyd et al., 1994). The authors suggest that differences in pressure and temperature at various diamond forming regions could have a significant effect on the surface properties and therefore the kinetics of the diamond growth reactions. They suggest that this could account for a wider spread in $\delta^{15}N$ compared with $\delta^{13}C$.

The isotopic compositions obtained for diamonds in this study indicate that they fall into the "high- $\delta^{13}C$ group" as modified by Cartigny et al. (1997). The range of $\delta^{13}C$ values (-10.3 to –1 ‰) obtained is typical of peridotitic diamonds worldwide (Sobolev et al., 1979) and similar to the range obtained in an earlier study on Cullinan diamonds (Deines et al., 1984). This range in values is most plausibly explained by fractionation of carbon from a globally homogeneous convecting mantle ($\delta^{13}C \sim -5$ ‰), with a fractionation factor of ~ 4-5 ‰ (Deines, 1980; Cartigny et al., 1998a). The wide range in nitrogen isotopic compositions is more difficult to account for. It appears that the growth rate and kinetics of the reaction only account for a variation up to ~ 8 ‰ (Westerlund et al., 2003). This would not account for the wider range in the nitrogen isotopic values in comparison with carbon isotopic values, assuming a homogenous nitrogen source. The results therefore seem to indicate a primitive source for nitrogen in the region of Cullinan. Further studies into the how nitrogen is incorporated into the diamond lattice appear necessary in order to help understand the source of nitrogen for diamonds.

6. MINERAL INCLUSIONS IN DIAMOND

6.1 Introduction

Diamonds are metastable for billions of years unless exposed to oxidising conditions (Meyer, 1987). Mineral inclusions completely enclosed within a diamond will not re-equilibrate with the surrounding environment, due to the physical strength and inert chemical nature of the diamond. This allows valuable chemical information to be obtained from the mineral inclusion, which reflects the mantle environment at the time of the diamond formation (Boyd et al., 1985). The study of mineral inclusions within diamonds (referred to from here on as 'inclusions') has increased our understanding of the chemistry of the mantle, craton development and diamond genesis.

Inclusions may be proto-, syn- or epigenetic with respect to the diamond. Syngenetic inclusions give the most valuable information about the mineralogy and chemistry of the diamond growth environment, as these inclusions are co-genetic with the diamond. It has been observed that these inclusions often show octahedral or cubo-octahedral morphologies, as the greater form energy of the diamond imposes its morphology on the inclusion (Harris & Gurney, 1979). It is common for a diamond to contain only a single inclusion; however bi- and polymineralic inclusions are more useful as they often allow for the temperature and pressure of formation of the diamond to be calculated.

6.1.1 Inclusion parageneses

The majority of inclusions found in diamonds may be assigned to either the peridotitic or eclogitic paragenesis (Table 6.1). World-wide studies have shown the most common inclusions of the peridotitic paragenesis are: olivine, enstatite, chrome-pyrope, chrome-spinel, and sulphides. Those of the eclogitic paragenesis are: omphacite, pyrope-almandine and sulphides (Meyer, 1987). Sulphide inclusions are the most abundant inclusions found within diamonds (Meyer, 1987). A study of 21 kimberlites from South Africa has indicated that peridotitic inclusions are approximately three times more abundant than eclogitic inclusions

Table 6.1 Mineral inclusions recovered from diamonds worldwide (modified from Meyer, 1987; Harris, 1992; Chinn, 1995 with additions from Harte and Harris, 1994).
After Westerlund,2000.

Syngenetic inclusions			**Lower mantle origin**	**Epigenetic inclusions**	**Uncertain origin**
Peridotitic	***Eclogitic***	***Websteritic***			
Olivine	Omphacite cpx	Cpx	Mg-wustite	Serpentine	Phlogopite
Enstatite	Pyrope-almandine	Opx	Majoritic garnet	Calcite	Muscovite
Cr-pyrope	Sulphides	Garnet	Mg-Si-perovskite	Graphite	Amphibole
Cr-spinel	Kyanite	Phlogopite	Ca-Si-perovskite	Haematite	Wollastonite
Sulphides	Sanidine			Kaolinite	Magnetite
Cr-diopside	Coesite			Acmite	Titanomagnetite
Mg-ilmenite	Corundum			Richterite	Sphene
Zircon	Ilmenite			Perovskite	Apatite
Cohenite	Rutile			Mn-ilmenite	Si-Ti-K phase
Native iron	Chromite			Spinel	Ti-K-Al silicate
Diamond	Diamond			Xenotime	Staurolite
				Sellaite	Plagioclase
				Goetite	Albite
				Cr-Sr-loparite	
				Cr-chevkinite	

and are more common on a worldwide scale (Gurney, 1989). This may reflect a sampling bias in South Africa as eclogitic inclusions are more commonly found in bigger diamonds (>2 mm), not usually studied for inclusions. A comparatively minor websteritic paragenesis also exists (orthopyroxene + clinopyroxene ± garnet), which is interpreted as intermediate between the peridotitic and eclogitic parageneses (Gurney, 1984). Unusual inclusion discoveries of ferropericlase (e.g. Scott-Smith et al., 1984; Moore et al., 1986; Wilding et al., 1989 and Davies et al., 1999), Mg-Si-perovskite and Ca-Si-perovskite (e.g. Harte & Harris, 1994; Harris et al., 1997; Hutchinson, 1997; Davies et al., 1999) and majoritic garnets (e.g. Moore & Gurney, 1985; Wilding et al., 1989) indicate a deeper origin than previously believed for some diamonds. Ferropericlase and Mg-Si-perovskite are stable below 650 km (Irifune & Ringwood, 1993). Garnet-pyroxene solid solution occurs at very high pressures, which are related to depths up to 450 km (Irifune et al., 1989).

6.1.2 Inclusion mineralogy

Peridotitic inclusions are similar in mineralogy to peridotitic xenoliths, however the depletion of magmaphile elements is more pronounced in the inclusions as they have been protected from re-equilibrating with the surrounding mantle. Olivine and orthopyroxene inclusions are Mg-rich, and display a restricted range of Mg-numbers, between 91 and 95 (Meyer, 1987). Cr_2O_3 is typically an order of magnitude greater in diamond inclusion olivine in comparison with other olivine of equivalent forsterite content (Meyer, 1987). There are two major types of clinopyroxene: Cr-diopside (peridotitic suite) and omphacite (eclogitic suite). The Cr-diopside inclusions have high Cr_2O_3 concentrations, but low Na_2O and Al_2O_3 concentrations in comparison with the omphacite inclusions (Meyer, 1987). The omphacite inclusions are chemically very similar to omphacite in xenoliths, although the K content of the inclusions extends the range of values. Ca-rich diopside was found in diamonds from south-eastern Australia by Sobolev et al. (1984) and was assigned to a separate calc-silicate paragenesis (Meyer, 1987). Two suites of garnet exist, peridotitic Cr-bearing pyrope and eclogitic pyrope-almandine. The Cr-pyrope garnets are characterised by high MgO (24 wt%) and Cr_2O_3 (up to 16 wt%) and low CaO (0-6 wt%) and FeO (5-8 wt%; Meyer, 1987). In order to

balance the Mg due to insufficient aluminium the knorringite end-member ($Mg_3Cr_2Si_3O_{12}$) is introduced (Meyer, 1987). Pyrope-almandine inclusions are chemically very similar to their xenolithic counterparts and have wide ranges in calcium and Mg-numbers. High Na in pyrope-almandine inclusions extends the range of Na found in eclogitic garnet xenoliths. Garnet and clinopyroxene of the peridotitic (or ultramafic) paragenesis have more restricted compositional ranges in comparison to those of the eclogitic paragenesis, as seen on Ca-Mg-Fe diagrams illustrating worldwide compositions as reported by Meyer (1987; Figures 6.1 and 6.2).

6.2 Inclusions in diamonds from Cullinan mine

Gurney et al. (1985) undertook a study on mineral inclusions in diamonds from Cullinan diamond mine. In that study of the 1 593 diamonds that contained inclusions, sulphides were the most common (~33% of the population, these were not assigned to the harzburgitic, lherzolitic or eclogitic parageneses). The split between the eclogitic paragenesis and peridotitic paragenesis was found to be 60/40. Inclusions assigned to the eclogitic paragenesis are garnet (20% abundance), clinopyroxene (40% abundance), one kyanite and one coesite inclusion. The inclusions recovered from the peridotitic paragenesis, in order of abundance, were olivine (26%), orthopyroxene (12%), Cr-pyrope (1.5%), one Cr-diopside and one chromite inclusion.

The major element compositions of the inclusions in the present study were determined using the Cameca Camebax electron microprobe at the University of Cape Town. Detailed methodology is provided in Appendix 4. The diamonds selected for this study were specifically chosen for their rare Cr-diopside inclusions and are in no way representative of the entire population of Cullinan mine diamonds. They do allow for a unique opportunity to study the rarer lherzolite diamond paragenesis. This suite consists of 94 peridotitic diamonds and 6 eclogitic diamonds. All the inclusions appeared to be syngenetic upon visual assessment. The majority had a cubo-octahedral morphology and no cracks or protogenetic inclusions were observed.

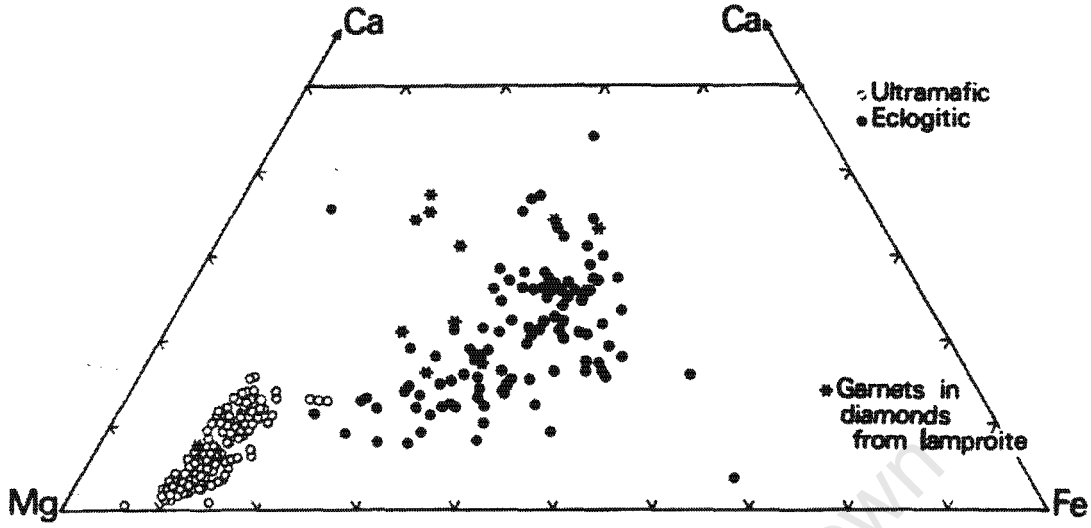

Figure 6.1: Worldwide compositions of diamond garnet inclusions. After Meyer 1987.

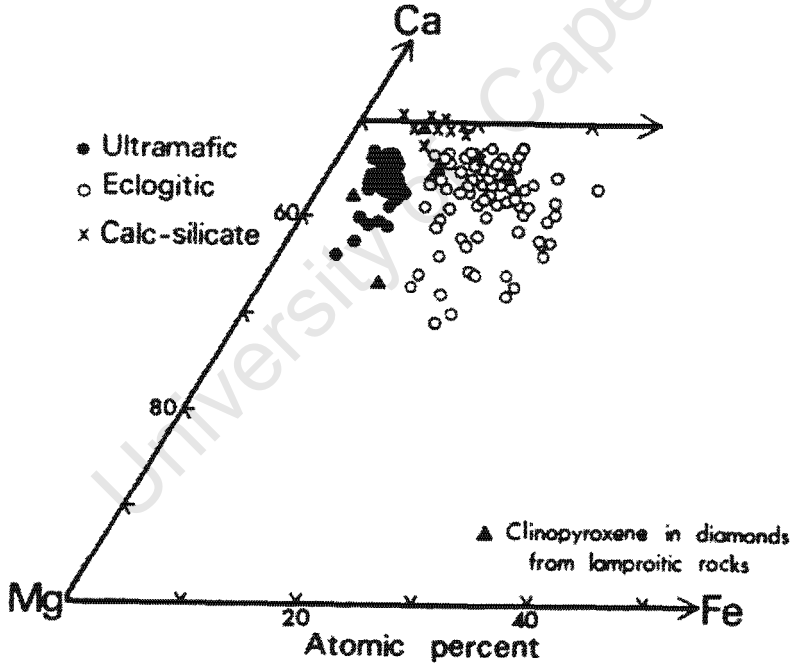

Figure 6.2: Worldwide compositions of diamond clinopyroxene inclusions. After Meyer 1987.

The peridotitic inclusions that were recovered are presented in Table 6.2. It was initially assumed that all those diamonds that contained garnet *without* a co-existing clinopyroxene inclusion were harzburgitic and those garnet inclusions that co-existed *with* clinopyroxene were lherzolitic. This assumption was corrected after studying the mineral chemistry of the garnets as some of the "harzburgitic" garnets plotted in the lherzolitic field and were therefore reclassified.

Table 6.2: Number of inclusions recovered in the peridotitic assemblage

Mono-mineralic assemblages	**no.**
Pyrope (gt)	36
Cr-diopside (cpx)	38
Enstatite (opx)	0
Olivine (ol)	0

Bi-mineralic assemblages	**no.**
gt-cpx	19
gt-ol	6
gt-opx	2
cpx-ol	4

Tri-mineralic assemblages		**no.**
gt-cpx-ol		1
gt-cpx-opx	(gt-cpx touching)	1

Five of the eclogitic diamonds each contained a non-touching garnet and clinopyroxene inclusion and the other eclogitic diamond contained a single clinopyroxene inclusion (initially visually identified as Cr-diopside). Due to the crumbly nature of the eclogitic inclusions only four clinopyroxene inclusions and one garnet inclusion were recovered. This may suggest that the inclusions had experienced some late stage alteration, possibly through cracks in the diamond.

6.3 Garnet inclusions

6.3.1 Peridotitic garnets

The chemical compositions for the peridotitic garnet inclusions can be found in Appendix 4, Table A.4.3. The chemical composition of 19 Cr-pyropes that were analysed in a previous study on Cullinan mine diamonds (Richardson et al., 1993) have been included with these results. These 19 inclusions were recovered from diamonds whose fragments were used to supplement the samples from the current investigation for stable isotope analysis (Section 3.2). The Cr-pyrope inclusions have been plotted on a ternary Ca-Fe-Mg plot together with the fields for garnet inclusions previously analysed for diamonds from Cullinan diamond mine (KRG database; Figure 6.3). The peridotitic inclusions lie almost entirely within the previously defined field, with a few lherzolitic inclusions extending the field towards higher Ca contents. The range of values is 16.5 - 25 wt% for MgO, 4 - 12 wt% for FeO_{total}, and 0.6 - 6.7 wt% for CaO.

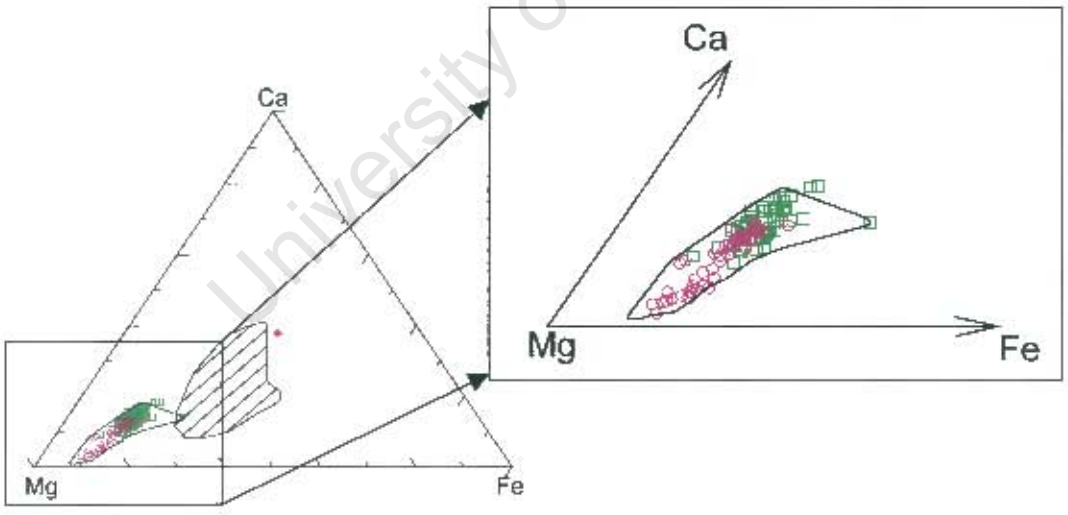

Figure 6.3 Ca-Mg-Fe diagram for Cullinan garnet inclusions (pink circles: harzburgitic inclusions, green squares: lherzolitic inclusions, solid diamond: eclogitic inclusion). Inserted fields represent garnet compositions obtained previously for Cullinan mine (hatched: eclogitic, open: peridotitic; KRG database). A portion of the plot has been enlarged to show the variation between harzburgitic and lherzolitic garnet inclusions.

A plot of CaO vs. Cr_2O_3 using the division of Gurney (1984) between the high and low calcium field (G9 and G10 Cr-pyropes); shows that the Cr-pyrope inclusions range from subcalcic to calcium saturated compositions (Figure 6.4). This division between G9 and G10 is commonly used to separate the harzburgitic and lherzolitic parageneses (Sobolev et al., 1973; Harris, 1992). A number of the Cr-pyrope inclusions analysed coexisted with Cr-diopside and are therefore classified as lherzolitic. The majority of these inclusions lie on the G9 (lherzolitic) side of the line as is expected, although a few lie in the subcalcic G10 (harzburgitic) field. These inclusions have been differentiated with diamond markers and are termed "subcalcic lherzolitic". The majority of Cr-pyrope inclusions that did not coexist with Cr-diopside lie in the subcalcic, G10 field, and are considered to be harzburgitic. There are a few of these Cr-pyrope inclusions however that plot to the calcium saturated side of the G9-G10 line have therefore been interpreted to be lherzolitic.

The subcalcic group is interesting in that there are three sub-parallel linear trends from a region of high Cr_2O_3 and low CaO towards increasing CaO and lower Cr_2O_3 (Figure 6.4). The direction of these trends from the harzburgitic inclusions (found in the older diamonds) to the lherzolitic inclusions (found in the younger diamonds) is explained further in Section 6.7. A number of Cr-pyrope inclusions that fall on or close to the G9-G10 division have been marked with asterisks to differentiate them from the other harzburgitic inclusions in later plots. There is also a group of unusual, tightly clustered low Cr_2O_3 and CaO inclusions evident on the plot (marked with triangles). This group also appears to define a trend towards the calcium saturated Cr-pyrope inclusions. The range of Cr_2O_3 for the lherzolitic and harzburgitic inclusions is 2.4 – 10 wt% and 2.6 – 20 wt% respectively. The range of CaO for the lherzolitic and harzburgitic inclusions is 3 – 6.8 wt% and 0.6 – 5.5 wt% respectively. This is almost identical to the range obtained previously for Cr-pyrope inclusions from Cullinan (Cr_2O_3: 2 – 20 wt% and CaO: 0.5 – 6.7 wt%; KRG database).

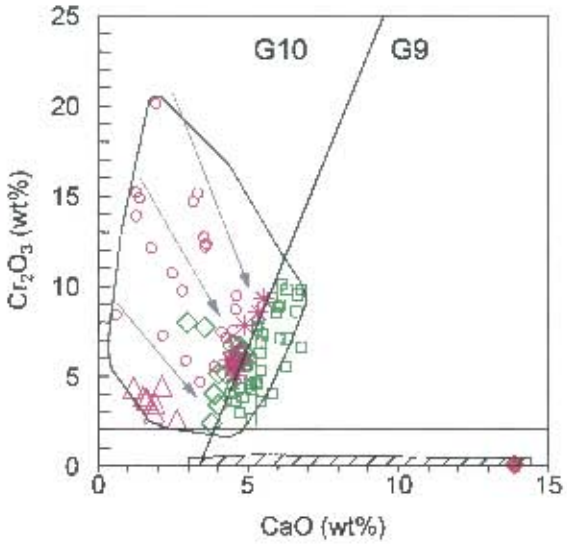

Figure 6.4 Plot of Cr_2O_3 vs. CaO for the Cr-pyrope inclusions (green markers: lherzolitic, pink markers: harzburgitic and red marker: eclogitic. □: lherzolitic Cr-pyrope, ○: harzburgitic Cr-pyrope, ◊: 'subcalcic lherzolitic' Cr-pyrope, Δ: 'low-Cr low-Ca' harzburgitic Cr-pyrope and ∗: 'borderline lherzolitic' Cr-pyrope.). Inserted fields represent garnet inclusion compositions obtained previously for Cullinan mine (hatched: eclogitic, open: peridotitic; KRG database). Arrows indicate linear trends. G10/G9 division after Gurney (1984).

In a number of the following graphs the mineral inclusion compositions are plotted as cations rather than oxides; this is to highlight the petrogenetic processes responsible for the compositional differences between different inclusions. As expected a plot of Mg-number vs. Fe for Cr-pyrope shows a negative correlation between the two variables, with the harzburgitic inclusions displaying higher Mg-numbers and lower Fe contents than the lherzolitic inclusions (Figure 6.5a). Figure 6.5b shows a rough negative correlation between Mg-number and Ca. The harzburgitic inclusions are on the low Ca, high Mg-number end and there is a continuous trend towards the lherzolitic inclusions with higher Ca contents and lower Mg-numbers. A plot of Ca vs. Fe gives a positive correlation with the harzburgitic inclusions at lower Ca and Fe contents and trending towards the lherzolitic inclusions with higher Ca and Fe contents (Figure 6.5c). Figure 6.5d shows a plot of Mg vs. Ca; which has a broad negative correlation. The harzburgitic inclusions have high Mg and low Ca and trend towards the lherzolitic inclusions with lower Mg and high Ca. As is to be expected the harzburgitic inclusions are more

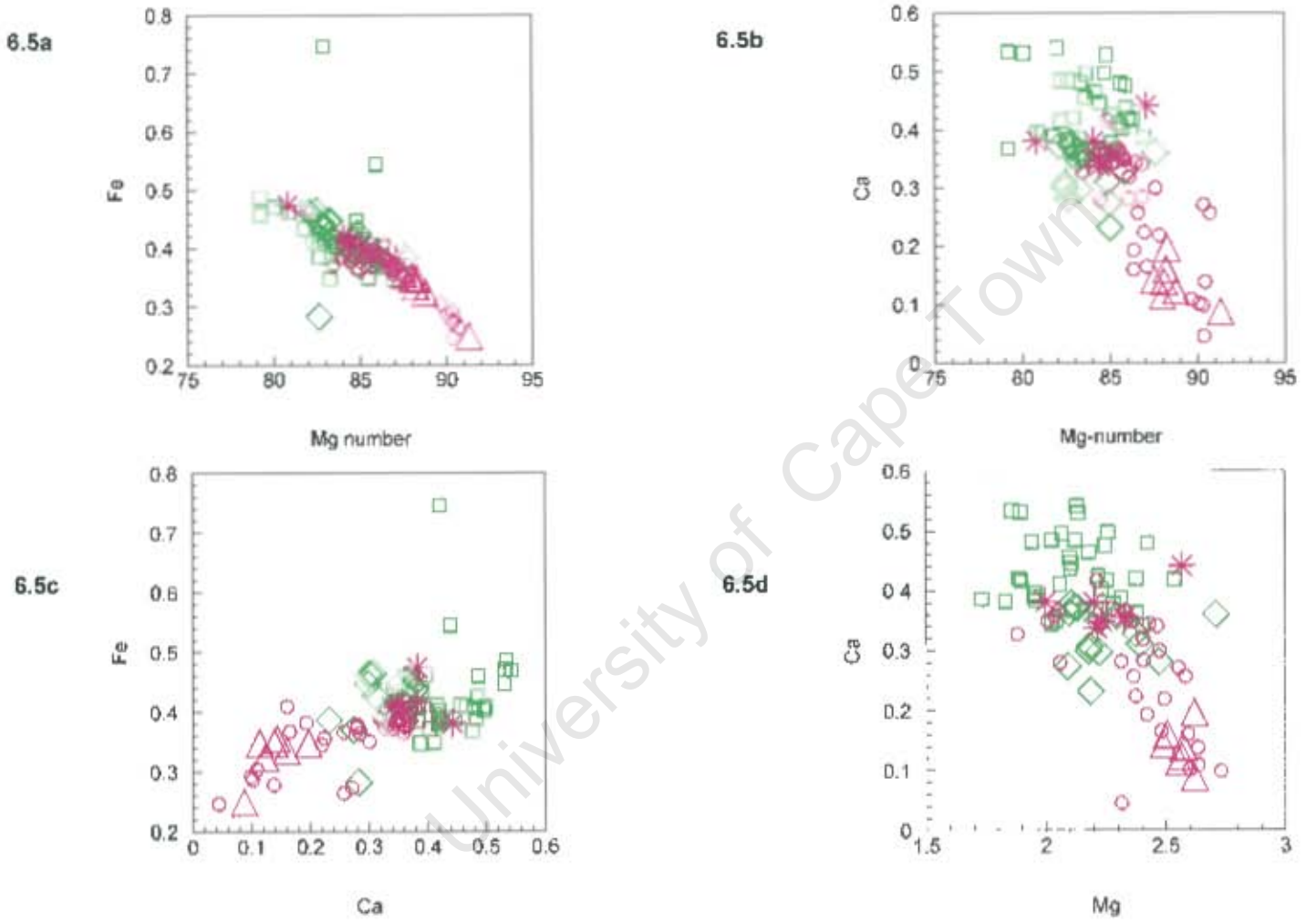

Figure 6.5: Mineral chemistry plots (in cations per formula unit) for the Cr-pyrope inlusions. (green markers: lherzolitic and pink markers: harzburgitic. □: lherzolitic Cr-pyrope, ○: Harzburgitic Cr-pyrope, ◊: 'subcalcic lherzolitic' Cr-pyrope, Δ: 'low-Cr low-Ca' harzburgitic Cr-pyrope and •: 'borderline lherzolitic' Cr-pyrope.)

refractory than the lherzolitic inclusions, in each plot the inclusions define a linear trend from the most subcalcic inclusions to the most calcium saturated inclusions. The harzburgitic inclusions that fall on the G9-G10 divide ("borderline lherzolitic"; marked with asterisks) tend to overlap with the range of values obtained for the lherzolitic inclusions. The "subcalcic lherzolitic" (marked with diamonds) Cr-pyropes also tend to be intermediate between the subcalcic harzburgitic Cr-pyropes and the lherzolitic Cr-pyropes and cluster together on the plots.

The pyrope content (100Mg / Mg + Fe_{total} + Ca + Mn) vs. Ti was plotted for the Cr-pyrope inclusions (Figure 6.6). From this plot it is evident that only the lherzolitic and 'borderline lherzolitic' Cr-pyropes (marked with asterisks) have a significant Ti content (> 0.01 cations per formula unit). The "true" lherzolitic inclusions (i.e. those on the G9 side of the field) have lower pyrope contents overall than the 'subcalcic lherzolitic' inclusions that lie in the G10 field (marked with diamond symbols). The 'borderline lherzolitic' inclusions (marked with asterisks) have lower pyrope contents than the more subcalcic harzburgitic inclusions. The range of TiO_2 is from the lower limit of detection (LLD) to 0.9 wt% for the lherzolitic inclusions and LLD - 0.5 wt% for the harzburgitic inclusions.

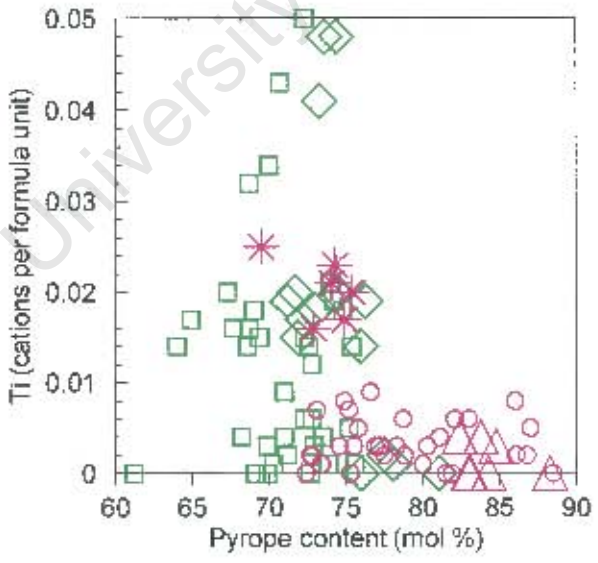

Figure 6.6 Plot of Ti vs. pyrope content for the Cr-pyrope inclusions (green markers: lherzolitic and pink markers: harzburgitic. □: lherzolitic Cr-pyrope, ○: harzburgitic Cr-pyrope, ◊: 'subcalcic lherzolitic' Cr-pyrope, Δ: 'low-Cr low-Ca' harzburgitic Cr-pyrope and *: 'borderline lherzolitic' Cr-pyrope.).

Na_2O is typically low in peridotitic garnets, but it is marginally higher in the lherzolitic suite LLD 0.25 wt% compared with LLD – 0.13 wt% in the harzburgitic suite. A plot of Mn vs. Ca gives a rough positive correlation, with the harzburgitic Cr-pyropes displaying the lowest Ca and Mn values and trending towards the lherzolitic inclusions with higher Mn and Ca (Figure 6.7). The MnO values are 0.2 - 0.5 wt% and 0.1 – 0.4 wt% for the lherzolitic and harzburgitic parageneses respectively, which is similar to the range previously obtained from Cullinan (KRG database).

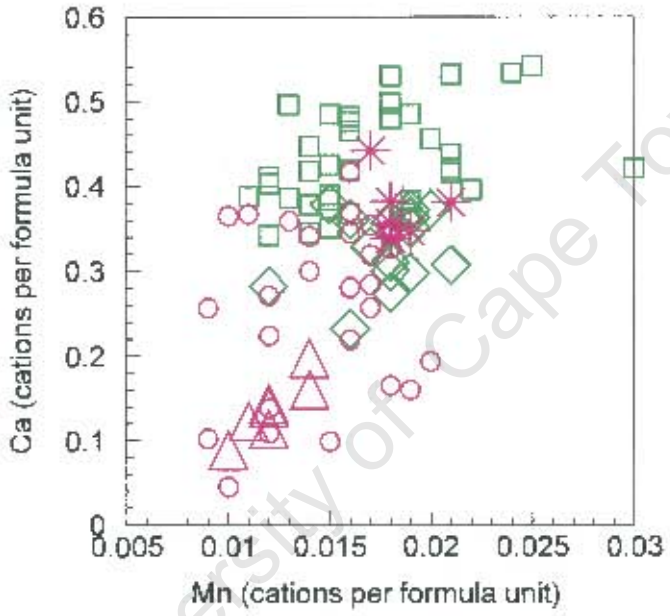

Figure 6.7 Plot of Ca vs. Mn for the Cr-pyrope inclusions (green markers: lherzolitic and pink markers: harzburgitic. □: lherzolitic Cr-pyrope, ○: harzburgitic Cr-pyrope, ◇: 'subcalcic lherzolitic' Cr-pyrope, △: 'low-Cr low-Ca' harzburgitic Cr-pyrope and ✳: 'borderline lherzolitic' Cr-pyrope.).

The Al/Cr ratio of the Cr-pyrope inclusions is used as a measure of their fertility. The Al/Cr ratios of the lherzolitic inclusions range from 2 to 13.5 (highly fertile) and the harzburgitic inclusions range from (extremely depleted) 0.6 to 10. The range of Al_2O_3 values for the lherzolitic and harzburgitic parageneses are 15 – 23 wt% and 8 – 21 wt% respectively. These values are on the high end of the range for previously analysed Cr-pyropes from Cullinan of 3.5 – 23 wt% (KRG database).

6.3.2 Eclogitic garnets

The chemical composition for the eclogitic garnet can be found in Appendix 4, Table A.4.4. Only one of the five eclogitic garnets was suitable for analysis, as the others crumbled upon liberation from the diamonds. This garnet falls within the area defined for eclogitic garnets worldwide (Meyer, 1987); however it lies just outside the range defined previously for Cullinan (Figure 6.3; KRG database). It has a Mg-number of 48.3 mol%. It has major element compositions of TiO_2: 0.82 wt%, Al_2O_3: 22.13 wt%, Cr_2O_3: 0.08 wt%, MnO 0.28 wt%, CaO 13.87 wt% and NaO 0.09 wt%.

6.4 Clinopyroxene inclusions

A total of 72 peridotitic and eclogitic clinopyroxene inclusions were recovered from the diamonds. Sixty-eight of these are peridotitic; of these 27 are associated with non-touching Cr-pyrope inclusions, 3 are associated with non-touching Cr-pyrope and olivine inclusions, 1 Cr-diopside is touching a Cr-pyrope garnet and coexists with 2 non-touching enstatite inclusions. Two Cr-diopside inclusions are associated with olivine inclusions, 1 Cr-diopside touches an olivine inclusion and 34 inclusions were the sole inclusions in the diamond. Four eclogitic clinopyroxene inclusions were recovered, 3 of these coexisted with eclogitic garnet. One of the clinopyroxene inclusions recovered was believed to be a Cr-diopside upon visual assessment, although it has a chemical signature of an omphacite inclusion and has been added to the diamonds of the eclogitic paragenesis (J982/7-13).

6.4.1 Peridotitic clinopyroxene

The chemical compositions for the Cr-diopside inclusions can be found in Appendix 4, Table A.4.5. The Mg-numbers of the inclusions range between 89.2 – 94.0 mol%. This range is similar to that obtained from the limited database for peridotitic Cr-diopside inclusions from Cullinan of 89.9 – 93.2 mol% (KRG database). A ternary plot of Mg, Fe and Ca shows the end-member compositions of the clinopyroxene inclusions (Figure 6.8). The Cr-diopside

inclusions that coexist with Cr-pyropes in the G10 field ('subcalcic lherzolites', Figure 6.4) have been marked with diamond symbols to differentiate them in the following plots.

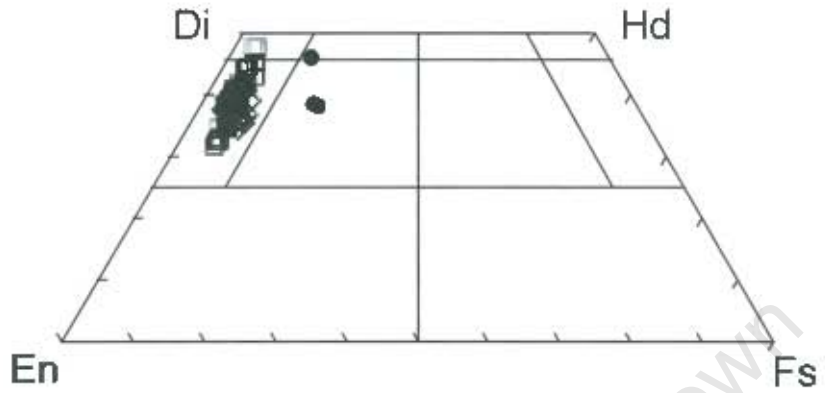

Figure 6.8 Plot showing the end-member compositions of Cullinan clinopyroxene inclusions (□: Cr-diopside, ◊: 'subcalcic lherzolitic' Cr-diopsides, •: omphacite). En = Enstatite, Fs = Ferrosilite, Hd = Hedenbergite, Di = Diopside.

The range in TiO_2 for these inclusions is LLD – 1.10 wt%, which is far wider than that obtained previously for Cullinan (0.04 - 0.27 wt%, KRG database). A plot of Na vs. Al shows a strong positive trend (Figure 6.9a). The range in values for Al_2O_3 is 0.8 - 4.2 wt% and Na_2O is 0.7 – 5 wt%, these values extend the range previously obtained for Cullinan (Al_2O_3: 0.9 - 3.2 wt% and Na_2O: 0.5 - 3.1 wt%; KRG database). A plot of Na vs. Fe shows that the range in Fe content of the inclusions is 1.7 – 3.6 wt% (Figure 6.9b), which is wider than the range obtained previously for Cullinan (2.4 – 3.5 wt%; KRG database). Figure 6.9c shows a positive correlation between Mg-number and Ca. A plot of Na vs. Cr shows a rough positive trend (Figure 6.9d). The range in values obtained for, Cr_2O_3 is 0.9 - 3 wt% and MnO is LLD – 0.15 wt%. These are similar to values previously obtained for Cullinan Cr-diopside inclusions, but tend to extend the ranges to higher values (KRG database). The Cr-diopside inclusions define continuous trends and no groups are apparent. The Cr-diopside inclusions that coexisted with a 'subcalcic lherzolitic' Cr-pyrope inclusion (diamond symbols, Figure 6.4) are separated into two groups according to Mg-number, but otherwise tend to cluster mid-range on the plots.

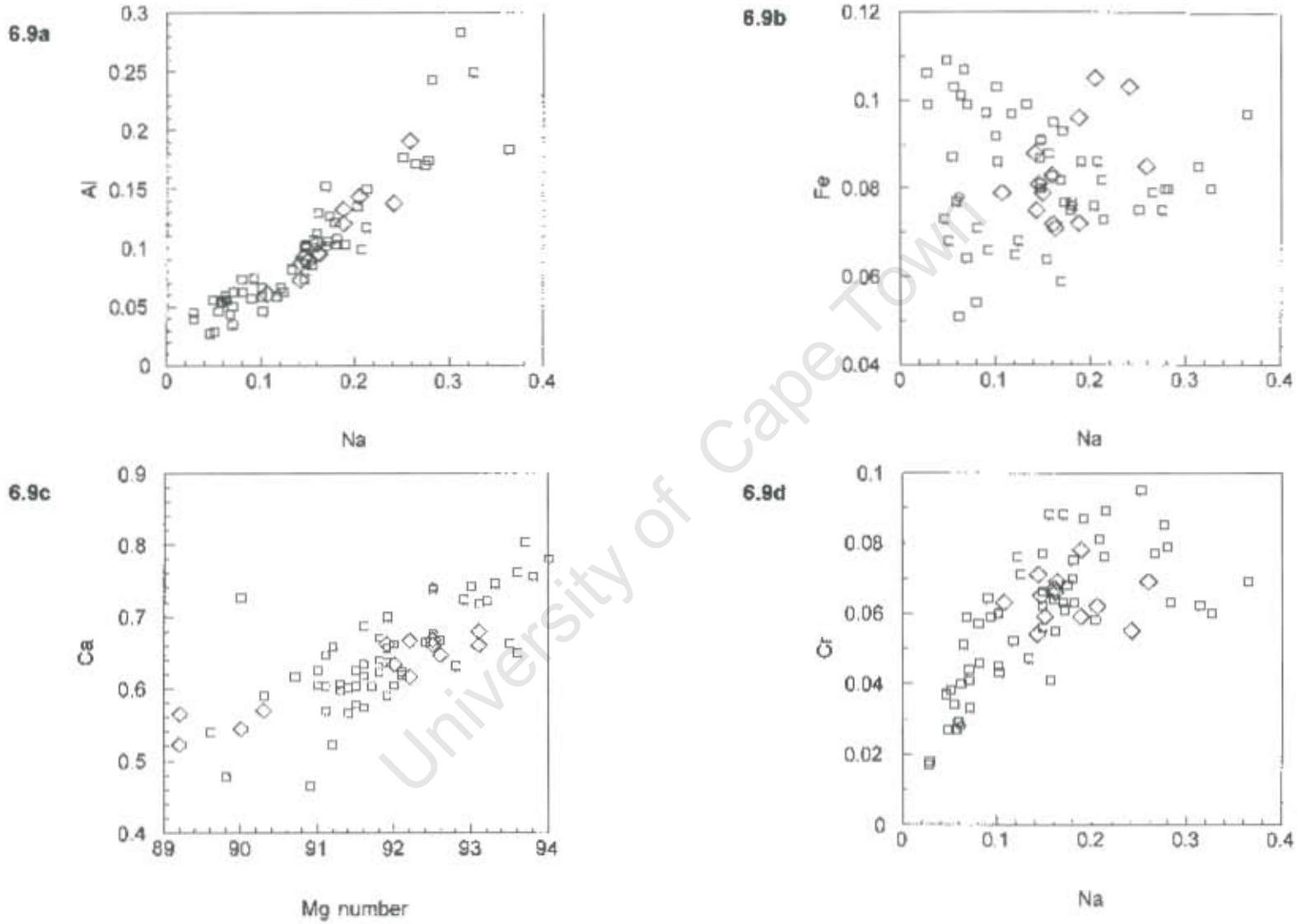

Figure 6.9: Mineral chemistry plots (in cations per formula unit) for the Cr-diopside inclusions. □ : Cr-diopside, ◊: 'subcalcic lherzolitic'

6.4.2 Eclogitic clinopyroxene

The chemical compositions for the eclogitic clinopyroxenes can be found in Appendix 4, Table A.4.6. Only four of six inclusions were recovered from the eclogitic clinopyroxene inclusions. Five of these inclusions coexisted with orange eclogitic garnet inclusions and one was a lone inclusion in the diamond. A ternary plot shows the end-member compositions of the clinopyroxene (Figure 6.8). The range in Mg-numbers for these inclusions is 72.6 - 93 mol%, which is similar to the range obtained for the numerous samples from the KRG database of 68-91 mol%. The high Mg-numbers obtained are due to relatively low FeO contents of 2-8 wt%. The majority of element oxide ranges lie towards the low end of the range obtained previously for Cullinan omphacitic inclusions (KRG database). The range of values obtained for: TiO_2 is 0.1-0.7 wt%, Al_2O_3 is 2.4-7.9 wt%, MnO is 0.07-0.09 wt%, Na_2O is 1.9-4.3 wt% and K_2O is below detection to 0.03wt%. The range of values obtained for Cr_2O_3 is LLD - 1.8 wt% and CaO is 14 - 20 wt%, which lies toward the high end of those samples previously obtained for Cullinan (KRG database).

6.5 Olivine inclusions

The olivine inclusions were predominantly colourless to pale green in colour, with the exception of the inclusion in diamond J-982 11-2, which displayed a strong green colour, and was initially believed to be a Cr-diopside upon visual assessment. Fourteen olivine grains were recovered; of those grains 4 are associated with Cr-diopside, 3 with Cr-pyrope, 6 with both Cr-diopside and Cr-pyrope and one touching a Cr-diopside inclusion. The chemical compositions of the olivine inclusions can be found in Appendix 4, Table A.4.7. A plot of CaO vs. Cr_2O_3 for the Cr-pyropes coexisting with olivine (Figure 6.10) shows that only one olivine inclusion is associated with a truly subcalcic, harzburgitic Cr-pyrope and that the remainder are associated with calcium saturated Cr-pyropes.

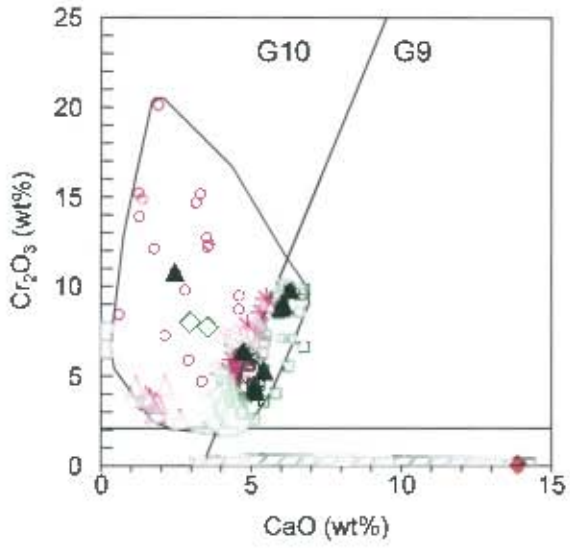

Figure 6.10 Plot of Cr_2O_3 vs. CaO for the Cr-pyrope inclusions highlighting the six Cr-pyropes coexisting with olivine (black diamonds: Cr-pyropes coexisting with olivine, green markers: lherzolitic Cr-pyrope, pink markers: harzburgitic Cr-pyrope, red marker: eclogitic garnet, □: lherzolitic Cr-pyrope, ○: harzburgitic Cr-pyrope, ◊: 'subcalcic lherzolitic' Cr-pyrope, Δ: 'low-Cr low-Ca' harzburgitic Cr-pyrope and *: 'borderline lherzolitic' Cr-pyrope.). Inserted fields represent garnet inclusion compositions obtained previously for Cullinan mine (hatched: eclogitic, open: peridotitic; KRG database). G10/G9 division after Gurney (1984).

The forsterite content ranges from 90.9 to 93.3 mol%, which is within the range for olivine inclusions world-wide (87-97 mol%, after Stachel and Harris, 1997a) and within the range previously obtained for peridotitic inclusions from Cullinan (89-95 mol%, KRG database). A bimodal distribution was obtained in a previous study of peridotitic olivine inclusions from Cullinan (Gurney et al., 1985). The more refractory olivines (94.5-95 mol% forsterite) were assigned to the harzburgitic paragenesis, whilst a less refractory, intermediate harzburgitic paragenesis was also assigned (91-93 mol% forsterite) and the least refractory olivines were assigned to the lherzolitic paragenesis (90-92 mol% forsterite). The olivine inclusions from this study do not exhibit a bimodal distribution, which may be due to the low number of inclusions recovered; alternatively it could suggest a continuum. The olivine coexisting with the subcalcic Cr-pyrope has the most refractory forsterite value of the group, of 93.3%. The remainder of olivine inclusions show a range of forsterite values of 90.9-92.9 mol%, which is similar, but wider than the range obtained for the lherzolitic assemblage of Gurney et al. (1985).

The range in NiO for the olivine inclusions is 0.4-0.5 wt%, with the exception of the inclusion that touches a Cr-diopside (J/982 8-8); it has a NiO content considerably higher than the remainder of the group (0.61 wt%). The error on the NiO values calculated from counting statistics on the electron microprobe is 0.03 wt%. The bulk of the values obtained are on the high end of the world-wide range (0.20-0.46 wt%, after Stachel and Harris, 1997a) and the range obtained previously for Cullinan of LLD - 0.48 wt% (KRG database). The olivine inclusion that touches a Cr-diopside extends these ranges. The harzburgitic olivine falls toward the lower end of this range (0.43 wt%). There is no paragenesis distinction in the Cr_2O_3 values for these inclusions (LLD - 0.12 wt%). The range is similar to that obtained previously for olivine inclusions from Cullinan (LLD - 0.15 wt%, KRG database). The range in MnO values of 0.08-0.14 wt% falls within the world-wide range and from previous work from Cullinan (Stachel & Harris, 1997a; KRG database), there is no clear distinction between the lherzolitic and harzburgitic olivines with respect to MnO. The olivine inclusion touching a Cr-diopside gives the highest MnO concentration for the group, of 0.14 wt%. The range of values for CaO (0.01-0.12 wt%), fall within the world-wide range and within the range previously obtained for Cullinan olivine inclusions from below detection to 0.23 wt% (Stachel & Harris, 1997a; KRG database). The olivine inclusion touching a Cr-diopside shows the highest CaO value (0.12 wt%) and the group displays a rough increase in CaO with a decrease in Mg-number.

6.6 Orthopyroxene inclusions

Four colourless enstatite inclusions were found in three of the diamonds; two of these diamonds also contained Cr-pyrope inclusions and the other diamond contained a touching Cr-pyrope and Cr-diopside inclusion. The chemical compositions of the orthopyroxene inclusions can be found in Appendix 4, Table A.4.8. The range of Mg-numbers is narrow, from 92.6 - 93.4 mol%, and lies towards the lower end of the world-wide range (92.5 – 96 mol%; Stachel & Harris, 1997a) and the range for enstatite inclusions previously analysed from Cullinan (92.6 - 96 mol%, KRG database). The two enstatite inclusions coexisting with Cr-pyrope have lower Mg-numbers (92.6 - 93 mol%) than the two enstatite inclusions

coexisting with touching Cr-diopside and Cr-pyrope inclusions (93.1 - 93.4 mol%). MnO falls within the range defined by the worldwide trend (Stachel and Harris, 1997a), with a range of 0.09 - 0.12 wt%. This range is similar to that previously obtained for Cullinan (MnO: LLD - 0.12 wt%, KRG database). CaO ranges from 1.05 - 1.20 wt%. These high values are indicative of enstatite crystallising in equilibrium with Cr-diopside, although three of the enstatites are found in diamonds with Cr-pyrope and no Cr-diopside, suggesting a harzburgitic paragenesis. A plot of Cr_2O_3 vs. CaO for the Cr-pyrope inclusions coexisting with enstatite shows that the one Cr-pyrope is lherzolitic and the other Cr-pyropes are calcium saturated and lie close to the lherzolitic boundary (Figure 6.11). The values obtained for CaO are on the high end of the range obtained previously for Cullinan enstatite inclusions, of 0.09-1.45 wt% (KRG database). The range of Na_2O is below detection to 0.15 wt% and K_2O is not detected. Al_2O_3 has a wide range of values from 0.32 - 1.02 wt% and Cr_2O_3 ranges from 0.13 - 0.43 wt%. These are within the range for enstatites worldwide (Stachel and Harris, 1997a). The Al_2O_3 values obtained are within the range previously found for Cullinan (0.30 - 1.22 wt%, KRG database), but the Cr_2O_3 values obtained are lower than those previously obtained for Cullinan (0.21 - 0.82 wt%, KRG database).

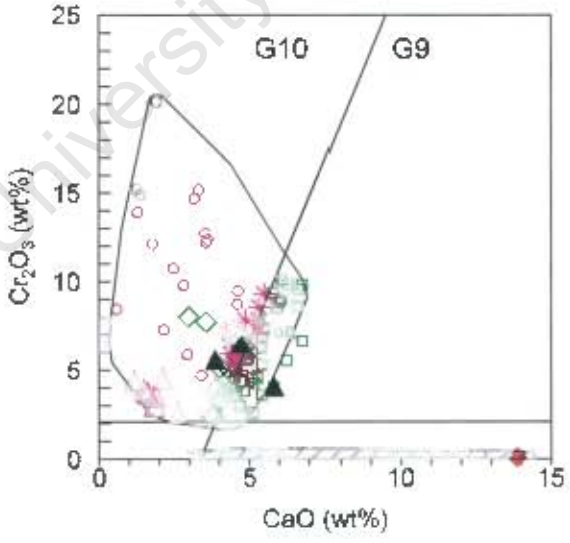

Figure 6.11 Plot of CaO vs. Cr_2O_3 for the Cr-pyrope inclusions highlighting the three Cr-pyropes coexisting with enstatite (black triangles: Cr-pyropes coexisting with enstatite, green markers: lherzolitic, pink markers: harzburgitic, red marker: eclogitic). Inserted fields represent garnet inclusion compositions obtained previously for Cullinan mine (hatched: eclogitic, open: peridotitic; KRG database). G10/G9 division after Gurney (1984).

6.7 Discussion and conclusions

This study has highlighted a number of different parageneses of diamonds at Cullinan. The eclogitic paragenesis has been shown previously to be the predominant paragenesis (~60%) at Cullinan (Gurney et al., 1985). It is only a minor component of the suite chosen for this study however. This study has highlighted three distinct peridotitic parageneses: a low-Cr, low-Ca bearing harzburgitic paragenesis (open triangle markers), a sub-calcic, Cr-pyrope bearing harzburgitic paragenesis (gt + ol + opx – pink markers) and a more calcic, Cr-diopside bearing lherzolitic paragenesis (cpx, gt + ol + opx – green markers). The Cr-diopside bearing paragenesis is extremely rare at most localities. Three major parageneses have been identified at Cullinan through dating studies (Richardson et al., 1993). The harzburgitic paragenesis yields an Archean age (>3000 Ma) of formation and the lherzolitic inclusions yield a Sm-Nd isochron age of 1930 Ma, which is ~100 Ma less than the emplacement of the Bushveld Complex into which the kimberlite intrudes (Richardson et al., 1993). The eclogitic paragenesis has been dated at ~1150 ± 60 Ma (Richardson, 1986), which when taking the errors into account just predates the emplacement of the kimberlite pipe dated at 1180 ± 30 Ma (Allsopp & Kramers, 1977).

Although the harzburgitic and lherzolitic inclusions at Cullinan are separated by a large difference in formation ages the majority of Cr-pyrope plots show a linear evolution from the depleted, subcalcic Cr-pyrope inclusions towards more fertile, calcium saturated Cr-pyrope inclusions. The olivine and orthopyroxene inclusions also tend to be more refractory if associated with subcalcic Cr-pyropes and more fertile if associated with lherzolitic Cr-pyrope or with Cr-diopside. These continuous elemental trends indicate that the harzburgitic and lherzolitic parageneses may be petrogenetically linked by fractionation processes.

Burgess and Harte (1999) studied the mineral chemistry across individual Cr-pyropes from peridotitic xenoliths from Jagersfontein. Two major trends were observed on a plot of CaO vs. Cr_2O_3 for the Cr-pyropes, these trends were parallel to the G10-G9 divide and perpendicular to this divide from the sub-calcic region towards the calcic region (Burgess and Harte, 1999; Figure 8). The authors suggest that a metasomatic fluid, as opposed to solid state diffusion, is likely to have generated the compositional changes observed in the Cr-pyropes. A mestasomatic melt is preferred as it provides a source for minor elements (such as Ti and

Na) that were typically enriched in the rims of the garnets. A melt would also add elements at a rate that allows chemical gradients to build up between the cores and rims on the Cr-pyropes (Burgess and Harte, 1999). The trend parallel to the G10-G9 divide has been explained by Burgess and Harte (1999) as an infiltration of melt into existing depleted harzburgite. The author's propose that the melt interacted along the grain boundaries of the harzburgite and it evolved towards lherzolitic equilibria, in terms of its major elements. The minor elements evolved through crystal fractionation. The lherzolitic paragenesis at Jagersfontein is interpreted to have crystallized from this melt. As this melt percolated to shallower depths it is suggested to have modified the existing sub-calcic Cr-pyropes toward lherzolitic compositions. This gives a trend of Cr-pyrope evolution directly towards the G9-G10 divide. This infiltration also allows for the growth of Cr-diopside if the original bulk composition is sufficiently altered. Trends perpendicular to the G10/G9 divide are evident in a plot of the Cr-pyrope inclusions in this study (Figure 6.4).

It is possible that similar processes could account for the petrogenetic link between the harzburgitic and lherzolitic parageneses at Cullinan, a possible sequence of enrichment is proposed below. Minerals of a depleted harzburgitic source were encapsulated in diamonds at ~3200 Ma. This depleted harzburgite source rock was then later refertilized due to the infiltration of fluid most likely associated with the intrusion of the Bushveld Complex at ~2020 Ma. This would have led to the crystallization of the lherzolite, by modal metasomatism; as well as causing the existing depleted harzburgitic paragenesis to evolve towards more fertile compositions by cryptic metasomatism. The formation of the next diamond paragenesis at 1930 Ma would have encapsulated minerals of the new lherzolitic material and enriched harzburgitic material.

7. TRACE ELEMENT DATA FOR GARNET INCLUSIONS IN DIAMOND

7.1 Introduction

The trace elements of garnet peridotites from kimberlites and associated rocks have been widely studied (e.g. Frey and Green, 1974; Shimizu, 1975; Nixon et al., 1981). These studies identified that there are two groups of garnet peridotites with respect to REE (rare earth element) patterns. The first have near chondritic REE patterns and are typically associated with sheared, fertile peridotites. The other group has strongly fractionated LREE/HREE (light rare earth element / heavy rare earth element), and enriched LREE patterns and are associated with coarse granular, depleted peridotites (McDonough and Frey, 1989). These two patterns have been interpreted as representing a two-stage evolutionary history for garnet peridotites (Frey and Green, 1974; Nixon et al. 1981). During the first stage partial melting removes a basaltic component from the peridotites, creating a depleted lithosphere. The second stage involves the upward migration of melt and/or fluids, which enriches the peridotites in incompatible trace elements (e.g. Smith and Boyd, 1987; Griffin et al., 1989a).

Shimizu and Richardson (1987) were the first authors to study sub-calcic garnet inclusions in diamond from Kimberley and Finsch pipes in South Africa. They found that all of the peridotite suite garnets display a general enrichment of LREE, relative to HREE and Ti and Zr concentrations that are considerably lower than fertile lherzolite xenoliths. The REE patterns of the inclusions and concentrate garnets indicated a close genetic link (supported by the major element chemistry as shown by Gurney and Switzer, 1973). Shimizu and Richardson (1987) indicate that these data are inconsistent with the inclusions forming in equilibrium with silicate or carbonate liquids. Instead the authors suggest that the sub-solidus metasomatism of a residual harzburgite would account for the depleted signature of the magmaphile elements and the subsequent enrichment in the LREE and Cr contents of the garnet inclusions.

More recent studies have confirmed that harzburgitic and lherzolitic garnet inclusions in diamond can be characterized by two main REE patterns. The harzburgitic inclusions tend to display sinusoidal REE patterns (Stachel et al., 2004). The lherzolitic inclusions can also exhibit sinusoidal patterns, but more commonly exhibit "normal" patterns (Stachel et al.,

2004). "Normal" patterns have a positive slope in the LREE and flat and enriched MREE to HREE (Stachel et al., 2004). These patterns are similar to what is seen in garnets from peridotites.

7.2 Trace element results

7.2.1 Rare earth element results

Owing to the small size of the garnet inclusions in comparison with the spot size of the laser, only those grains larger than 50 µm were selected for trace element analysis. Only peridotitic grains were large enough for analysis. The analyses were performed at the University of Cape Town using a Perkin Elmer Elan 6000 ICP-MS (inductively coupled plasma – mass spectrometer) instrument is coupled to a Cetac LSX-200 laser ablation module that uses a 266nm frequency quadrupled Nd-YAG laser. Detailed methodology is provided in Appendix 5, the trace element data results can be found in Table A.5.2. The spot size of the laser was set to 50 µm in order to compromise between the size of the ablation hole and count times required to obtain sufficient ablated material for the analyses. In a few cases the inclusions were big enough to allow for re-analysis of the grain with a spot size of 100 µm. In a number of instances the laser blasted through the grain before the analysis was complete, as a result only 25 analyses from 20 grains have been utilised. The following elements were analysed during the runs: Ni, La, Ce, Nd, Sm, Eu, Gd, Dy, Er and Yb. The error bars indicated in the following REE plots are one standard deviation normalised errors. The following in-house standards were used: JJG1424, MON34 and ROM33. Figures 7.1 to 7.3 show graphs of the REE for the standards after normalising to C1-chondrite (C1-chondrite values are from Sun and McDonough, 1989). The shape of the patterns will be discussed further, as the actual concentrations of REE are dependant on factors such as the amount of modal garnet present as well as the presence of clinopyroxene associated with the lherzolitic garnets (Stachel et al., 2004).

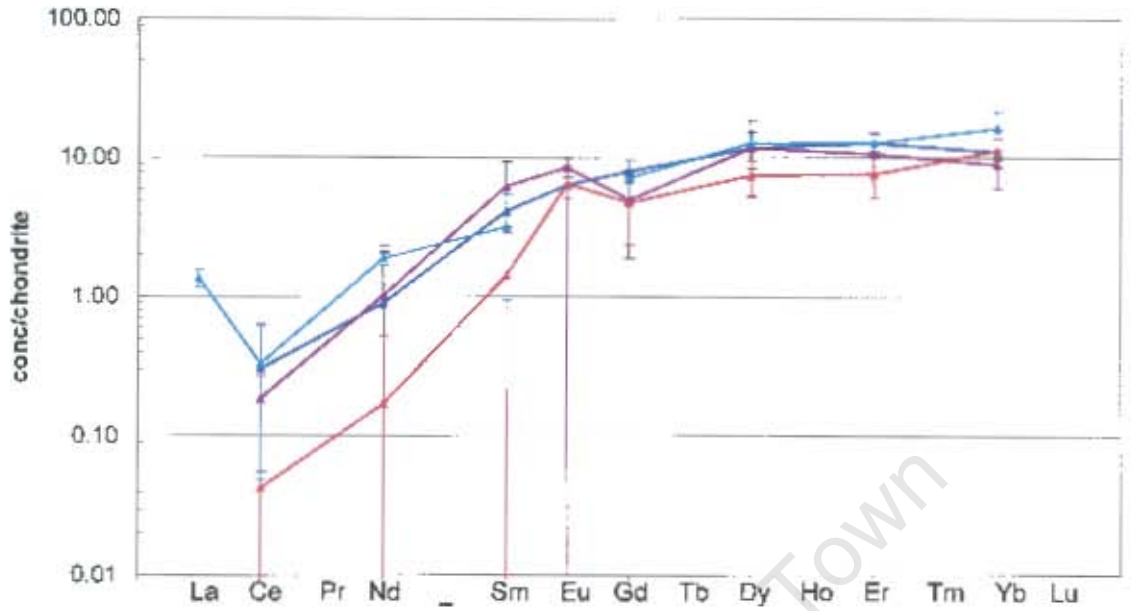

Figure 7.1 AREE plot of the analyses obtained from the JJG1424 standard (normalised to chondrite). The error bars represent 1 standard deviation after normalisation.

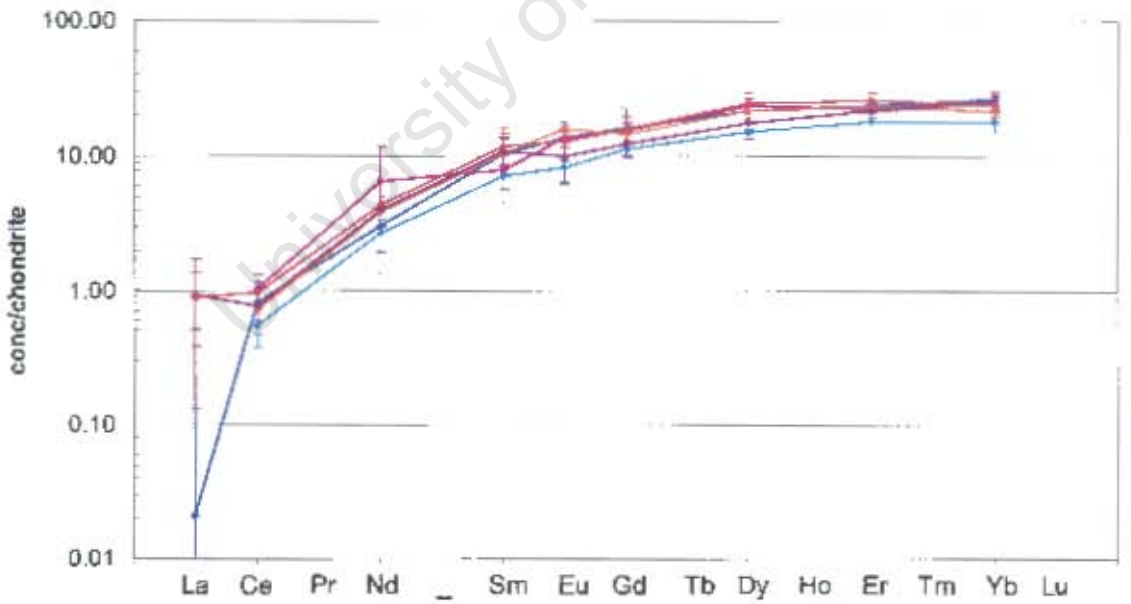

Figure 7.2 AREE plot of the analyses obtained from the MON34 standard (normalised to chondrite). The error bars represent 1 standard deviation after normalisation.

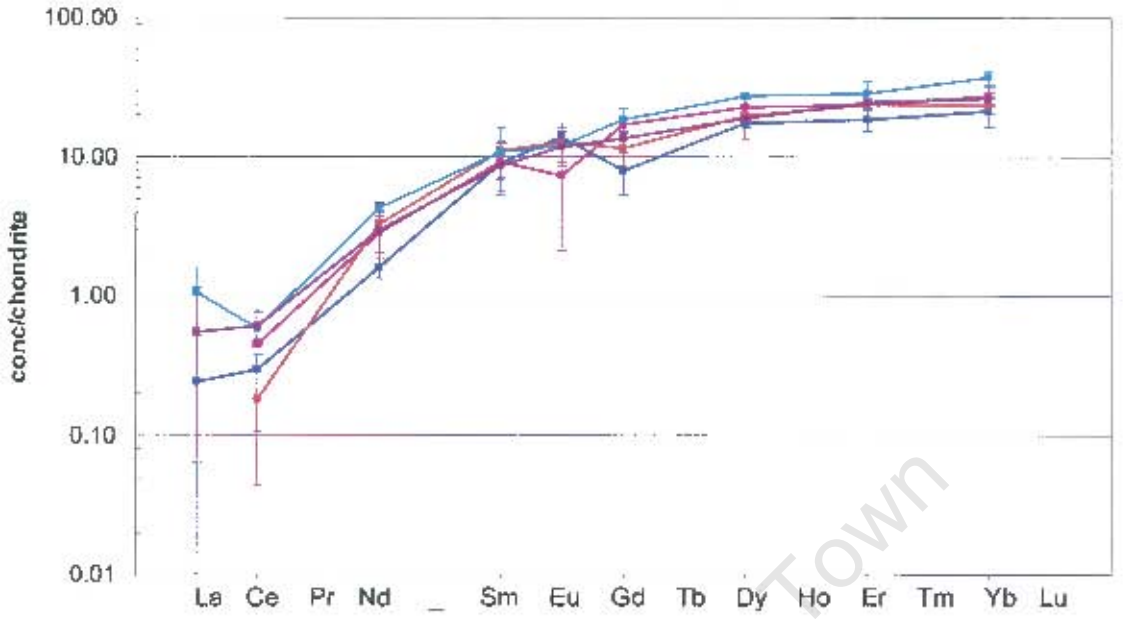

Figure 7.3 AREE plot of the analyses obtained from the ROM33 standard (normalised to chondrite). The errors bars represent 1 standard deviation after normalisation.

Three main groups of REE patterns have been identified from this study (Groups 1 to 3); in all cases the REE concentrations have been normalized to C1-chondrite (C1-chondrite values are from Sun and McDonough, 1989). It must be noted that there are no definite anomalies present in the patterns around Eu-Gd, outside of the analytical errors applicable to the data. The garnets of Group 1 display sinusoidal REE patterns (Figure 7.4). This group corresponds to that of depleted harzburgitic garnet inclusions (Stachel et al., 2004). Two of the garnets in Group 1 in this study lie on the G10/G9 line that has been used as a division between harzburgitic and lherzolitic garnets; the remainder are harzburgitic (Figure 7.7). The garnets of Group 2 have positive LREE slopes and flat MREE-HREE slopes (Figure 7.5), and are described as having "normal" lherzolitic trends (Stachel et al., 2004). The garnets of Group 3 have almost flat REE patterns, similar to chondrite compositions. There is a slight negative slope from LREE to HREE (Figure 7.6). The majority of the inclusions for Groups 2 and 3 are lherzolitic, although harzburgitic inclusions are also included in these groups (Figure 7.7). All except one of the harzburgitic inclusions cluster around the G10/G9 divide (Figure 7.7).

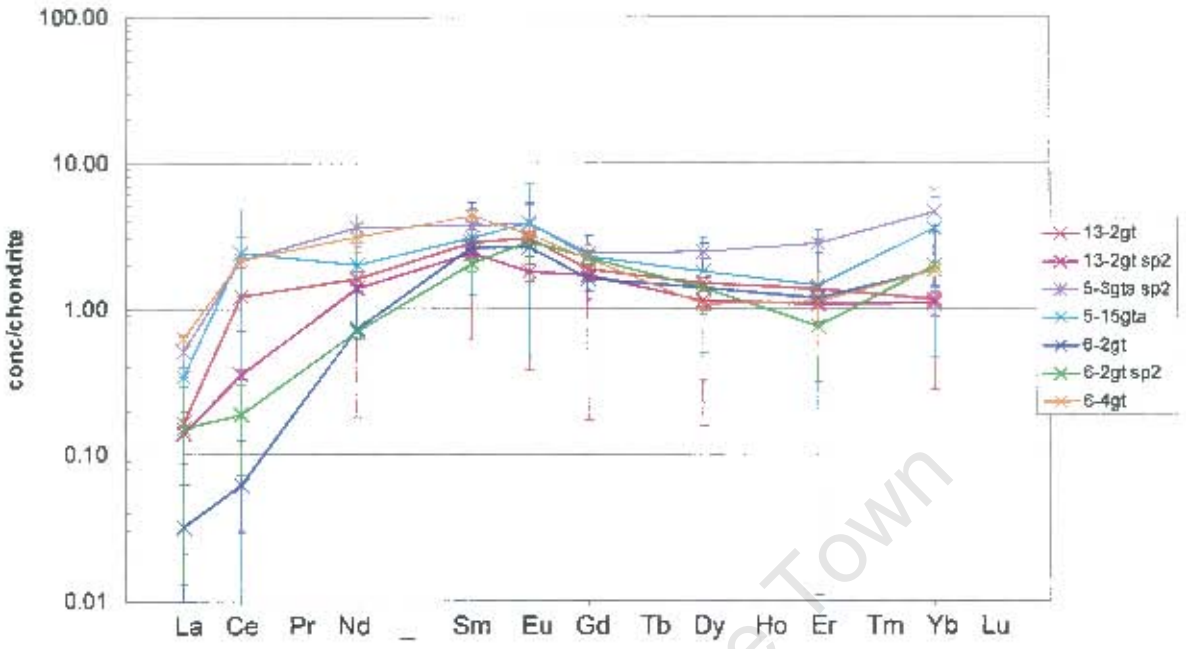

Figure 7.4 A REE plot for the garnet analyses (normalized to chondrite) illustrating sinusoidal patterns (Group 1).

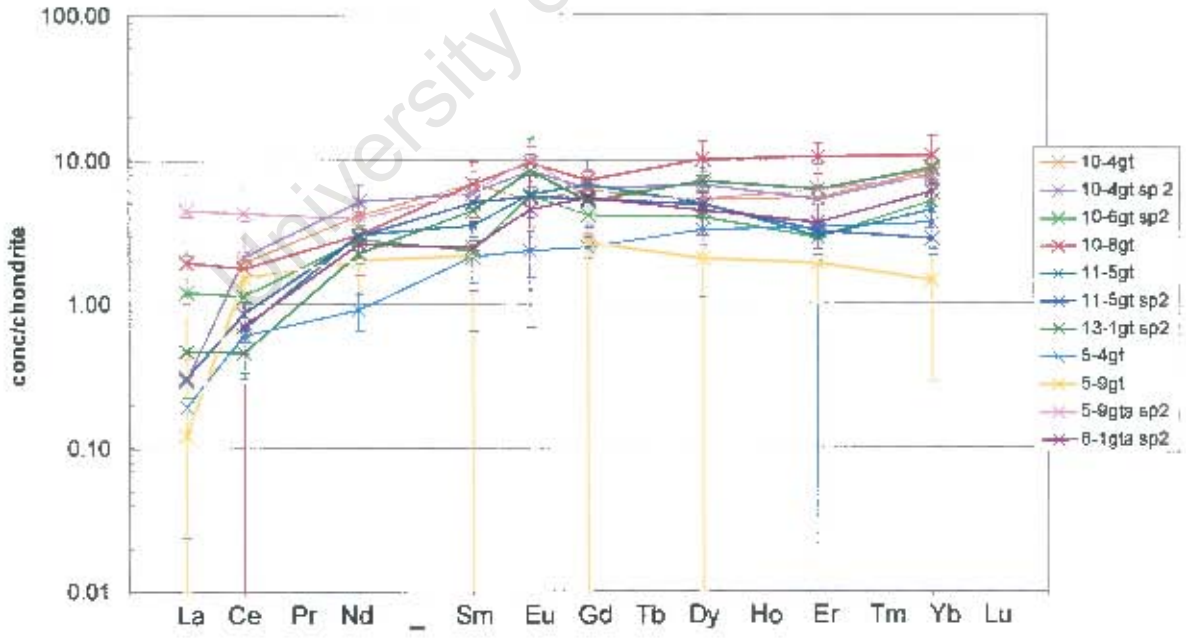

Figure 7.5 A REE plot for the garnet analyses (normalized to chondrite) illustrating flat MREE-HREE patterns with positive LREE slopes or "normal" lherzolitic patterns (Group 2).

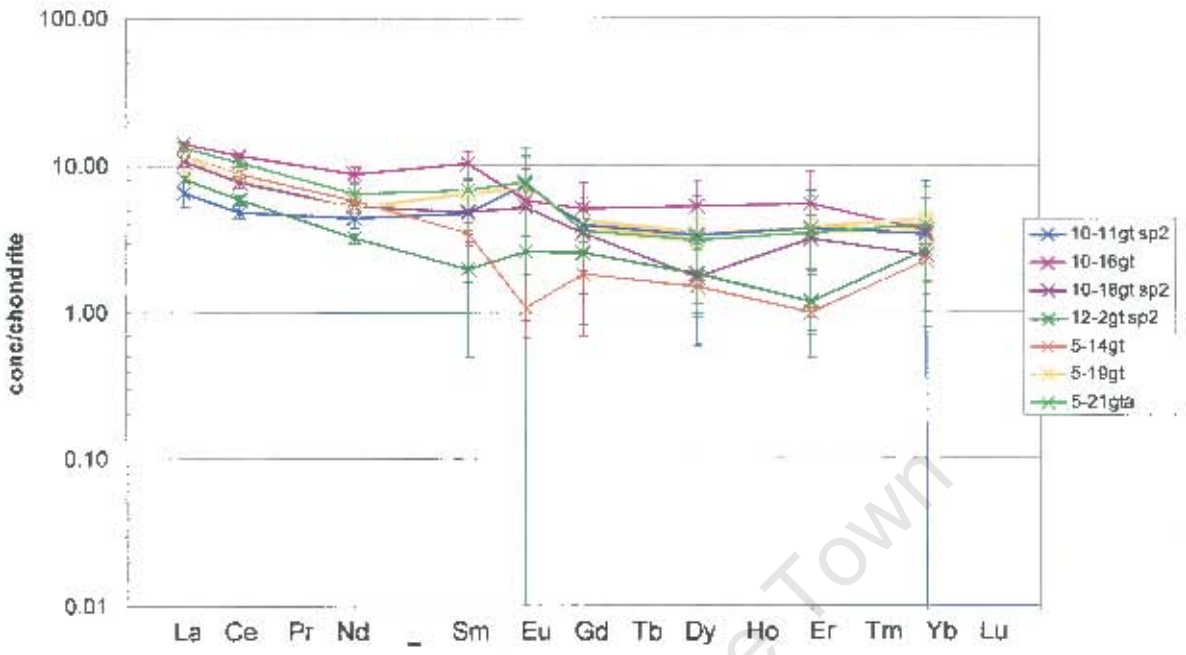

Figure 7.6 A REE plot for the garnet analyses (normalized to chondrite) illustrating the reasonably flat patterns (Group 3).

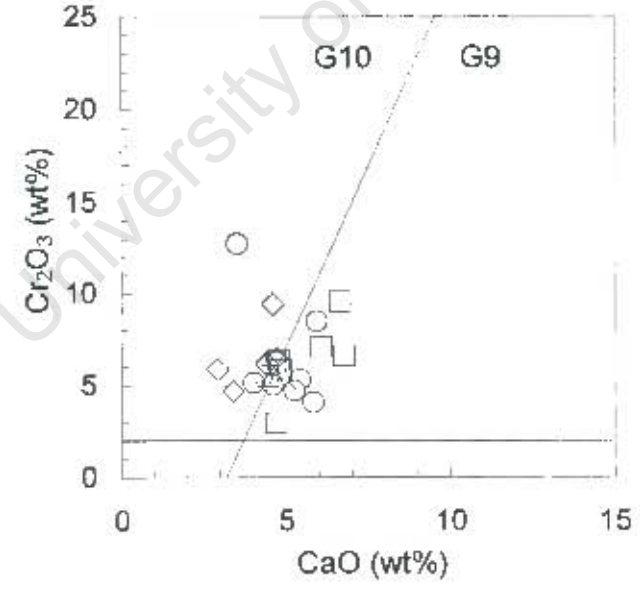

Figure 7.7 A plot of CaO vs. Cr_2O_3 for the garnets with REE analyses. ◊: Group 1 (sinusoidal patterns), □: Group 2 ("normal" lherzolitic patterns) and ○: Group 3 (flat patterns).

The Cr-number of garnets (100Cr / (Cr + Al)) can be used as a proxy for the degree of depletion of the major elements in the garnet (Stachel et al., 2004). Stachel et al. (2004) used the Cr-number of the garnet inclusions to investigate possible correlations between major and trace elements for a global dataset. The authors found that garnets with sinusoidal patterns are restricted to highly depleted lithologies (Cr-numbers up to ~50), whilst flat or positive LREE-MREE slopes are restricted to less depleted rocks (Cr-numbers typically less than 30). This observation does not hold for the analyses in this study. The Cr-numbers for the garnet grains analysed are all below 30 with the exception of inclusion J-982 5-21gta, which has a Cr-number of 38.5 (Figure 7.8). All of the harzburgites analysed, with the exception of J-982 5-21gta, have relatively fertile chemistries (Figure 7.7).

A further investigation between Cr-number and trace elements was carried out by Stachel et al. (2004), using La to represent the LREE and Yb to represent HREE. The authors did not observe strict linear correlations between Cr-number and the REE for both the harzburgitic and lherzolitic garnets. Stachel et al (2004) did however observe that the highest La contents occur at Cr-numbers greater than 25 and those garnets with the highest concentrations in MREE-HREE are restricted to Cr-numbers below 30. No correlation is observed between Cr-number and La (representing LREE) or Yb (representing HREE) for the analyses in this study.

Stachel et al. (2004) suggest that the absence of linear correlations between the garnet REE and bulk rock major element chemistry (using Cr-number as a proxy) indicates that primary processes may be excluded as the determining factor for the variations in trace element composition.

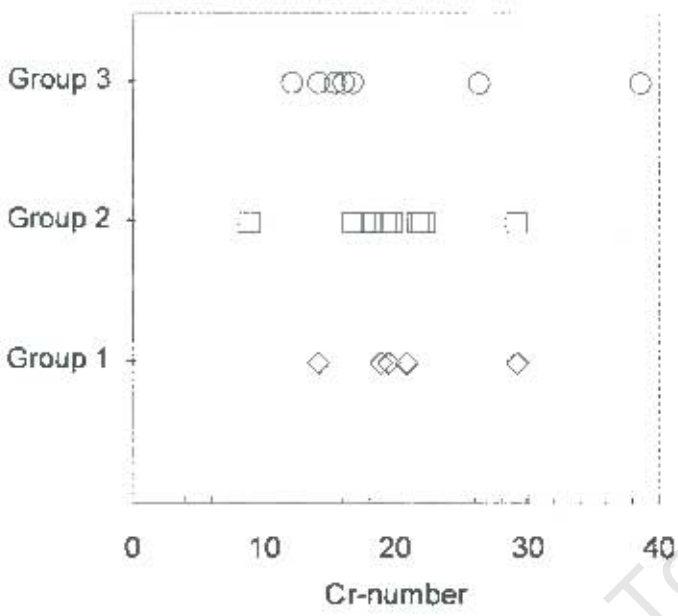

Figure 7.8 A plot showing the Cr-numbers of the garnets for the three REE groups. Group 1: sinusoidal patterns, Group 2: flat patterns, Group 3: near chondritic patterns.

7.2.2 Nickel thermometry results

Nickel was analysed in the garnets in order to obtain estimates of temperatures of formation using Ni-thermometry. These results will be discussed further in Chapter 8 and compared with the other geothermometers utilised. There is no significant difference between the lherzolitic and harzburgitic parageneses with regard to Ni-thermometry temperatures. The temperatures range from 959 – 1392 °C utilizing the Ni-thermometer of Canil (1999), with the majority of temperatures greater than 1190 °C (Figure 7.9). The reasons for the choice of the Canil (1999) thermometer are given in Chapter 8.

No trend is evident between Cr-number and temperature for the lherzolitic garnets (Figure 7.9). A strong positive correlation exists between Cr-number and temperature for the harzburgitic garnets however (Figure 7.9). This suggests that there is an increased solution of Cr-spinel into the harzburgitic garnets with increasing pressure and temperature (Grütter and Sweeney, 2000). Stachel et al. (2004) found that the lherzolitic and harzburgitic garnets

displayed a rough negative correlation, which indicates a decrease in the degree in chemical depletion with an increase in temperature.

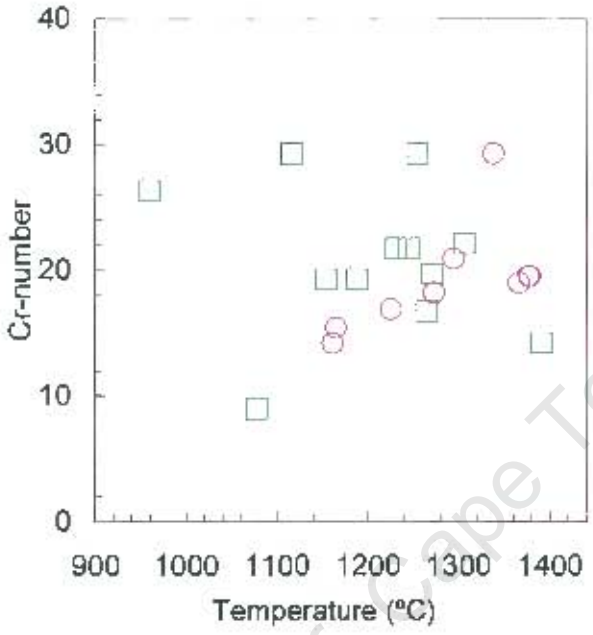

Figure 7.9 A plot of temperature (using Ni thermometry) vs. Cr-number for the garnets. Pink circles: harzburgitic inclusions; green squares: lherzolitic inclusions.

7.3 Discussion and conclusions

Stachel et al. (2004) have proposed a model to explain the differences observed between the two main REE patterns observed (i.e. sinusoidal and flat "normal" patterns) for garnet inclusions in diamonds world-wide. The authors did not consider disequilibrium models after work by Van Orman et al. (2002) has shown that there is no difference in the diffusion rates between LREE and HREE. Instead, Stachel et al. (2004) suggest metasomatism by CHO-fluids with highly fractionated trace element compositions (high ratio of LREE to MREE, HREE and other HFSE) to account for the sinusoidal patterns of the harzburgitic garnets. The authors suggest that the metasomatism affecting the lherzolitic garnets is supersolidus percolation of melts that re-fertilize the diamond sources in both major and trace elements.

These melts are characterised by a moderate enrichment of LREE over MREE, HREE and HFSE. This style of metasomatism is also suggested to affect the harzburgitic garnets at temperatures above 1190 °C, introducing HREE and possibly re-fertilizing the bulk rock major elements. Stachel et al. (2004) have indicated that these two models should be viewed as end-members of a continuum rather than separate processes.

The garnets with sinusoidal patterns (Group 1) are mostly harzburgitic (with two grains plotting on the boundary separating the G10 and G9 fields; Figure 7.7). These grains have high Ni-thermometry temperatures (1161 – 1378 °C). At these temperatures it is likely that the source garnet would be affected by melt metasomatism, which is likely to have re-enriched the garnet in both major and trace element chemistry. The major element chemistry indicates that these inclusions are relatively fertile. It is therefore likely that the depleted harzburgite source region underwent a degree of major element enrichment before these inclusions were encapsulated by the diamonds (Figure 7.7 & 7.8). The Group 1 patterns do not exhibit strong LREE enrichment like the majority of sinusoidal patterns, which may also indicate a transition between CHO-fluid metasomatism and supersolidus metasomatism.

The garnets with "normal" lherzolitic REE patterns (Group 2) have Ni-thermometry temperatures of 1077 – 1306 °C, and all except three inclusions have temperatures greater than 1190 °C. Four of the garnets in this group straddle the G10/G9 divide, whilst the other four plot in the lherzolitic field (Figure 7.7). The garnets have fertile major element compositions, flat REE patterns and high temperatures of formation, which suggests that the source peridotite would have been affected by melt metasomatism.

The Group 3 patterns are enriched in LREE and have similar HREE in comparison with Group 2. These garnets have the widest range of Cr-numbers (12.1 – 38.5), although all but two garnets have Cr-numbers less than 17. A similar REE pattern has been shown by Stachel and Harris (1997b) for one high-Cr lherzolitic garnet, although the authors do not explain its origin. This author is not aware of any other work illustrating similar patterns for garnet inclusions in diamonds or peridotites. It seems likely that these patterns represent further enrichment of the source peridotite by supersolidus melt leading to garnet that is slightly enriched in the LREE with comparison to the MREE and HREE.

The continuous major element trends between the harzburgitic and lherzolitic inclusions lead to the suggestion that a melt has caused the initial depleted harzburgitic source

to evolve towards lherzolitic compositions. A number of the harzburgitic inclusions that display typically sinusoidal "depleted" patterns have in fact got relatively fertile major element compositions (compared with the harzburgitic suite as a whole, Chapter 6) and high temperatures suggesting the influence of melt metasomatism (Figure 7.7 & 7.8). A significant proportion of the garnet grains analysed exhibit flat REE patterns in conjunction with high temperatures and these patterns are also suggested to be caused by melt metasomatism (Stachel et al., 2004). The REE patterns support the suggestion that a melt, most likely related to the intrusion of the Bushveld Igneous Complex, has refertilized the peridotitic mantle in this region. It is suggested that the diamonds with depleted harzburgitic inclusions formed at ~3.2 billion years. A metasomatic event most likely at ~2.05 billion years metasomatised the depleted source rock by varying degrees. Shortly after this another suite of diamonds formed encapsulating more fertile harzburgitic inclusions as well as lherzolitic inclusions.

8. MINERAL INCLUSION GEOTHERMOBAROMETRY

8.1 Introduction

Mineral inclusions in diamond not only provide a unique opportunity to understand the chemistry of the earth's upper mantle, but they also allow information to be obtained on the temperatures and pressures of formation of diamonds. Non-touching inclusions cannot re-equilibrate once enclosed in a diamond and are thus useful for giving estimates of the temperatures and pressures of formation of diamonds. It must be noted that a true temperature of formation will only be obtained if the minerals are in chemical equilibrium to begin with. This is not always the case as inclusions may be incorporated at different times, under different chemical conditions or at different temperature conditions. Touching mineral inclusions are able to equilibrate and therefore give temperature and pressure estimates after the formation of the diamond. The number of inclusions liberated from the diamonds in this study allows for a number of different geothermometers and geobarometers to be utilized. These will be discussed briefly in the sections below.

8.1.1 Gt-cpx exchange geothermometers

There have been a number of calibrations of the gt-cpx exchange thermometer (Raheim and Green, 1974; Mori and Green, 1978; Ellis and Green, 1979; Saxena, 1979; Krogh, 1988; Ai, 1994; Berman, 1995; Krogh, 2000). These thermometers are based upon the temperature dependence of the Fe^{2+}-Mg cation exchange between garnet and clinopyroxene. This reaction is more sensitive to temperature than pressure as the reaction involves little changes in volume compared with entropy. The thermometers of Ellis and Green (1979), Ai (1994) and Krogh (2000) have been applied to the mineral chemistry data.

The experimental geothermometer developed by Ellis and Green (1979) used basaltic compositions and compositions within the CaO-MgO-FeO-Al_2O_3-SiO_2 system. The range of temperatures and pressures used were 750 - 1300 °C and 24 - 30 kbars. The experiments showed that K_d is strongly dependant upon the Ca concentration in garnet and clinopyroxene.

This was attributed to non-ideal Ca-Mg substitution. They treated the dependence of $\ln K_d$ on X_{Ca} as rectilinear. Ellis and Green (1979) state that $\ln K_d$ is not solely dependent on the Ca content of garnet. Instead the X_{Ca} term of their geothermometer represents the net effect of the influence of different solid solutions on lnKd.

Krogh (1988) used the experimental data of Raheim and Green (1974), Mori and Green (1978) and Ellis and Green (1979) to derive a geothermometer. Krogh (1988) suggests that the substitution of Ca into the octahedrally co-ordinated site in garnet would lead to an expansion of the site, as the Ca^{2+} ion is considerably larger than the Fe^{2+} and Mg^{2+} ions. This may lead to a distortion of the structure owing to the varying sizes of the octahedrally co-ordinated sites. The smaller Fe^{2+} and Mg^{2+} ions may subsequently occupy sub-sites within the expanded octahedral sites. This would occur to a larger extent with the Mg^{2+} ions owing to their smaller size in comparison with the Fe^{2+} ions. This would occur up to a maximum Ca content where Mg and Fe would occupy the sub-sites randomly. This theory supports a curvilinear relationship between $\ln K_d$ and X_{Ca}, in contrast to the rectilinear relationship suggested by Ellis and Green (1979). Krogh (1988) applied the geothermometer to eclogites from the Tromso Nappe Complex in Scandinavian Caledonides; and concluded that $\ln K_d$ is not dependent on the Mg-number of the garnet or the Na content of the clinopyroxene (within the experimental range: Mg-number (gt) 0.17 - 0.55 and Na < 0.44 atoms per formula unit).

Ai (1994) investigated previously published experimental data over a range of 10 - 60 kbar and 600 - 1500 °C. Ai (1994) also found no relationship between calculated temperatures and the Na content of clinopyroxene. However in contrast to Krogh (1988), Ai (1994) demonstrated a negative relationship between $\ln K_d$ and the Mg-number of garnet. Ai (1994) applied a curvilinear relationship between $\ln K_d$ and X_{Ca} and assumed a linear dependence of $\ln K_d$ on X_{Ca}. A strong negative, linear correlation is evident between $\ln K_d$ and X_{Ca} at a number of temperatures when the Mg-number of garnet is > 75 - 80 (Figure 1; Ai, 1994). The correlation does not appear to hold for Mg-number's of garnet < 75 - 80.

Krogh (2000) presents the results of multiple regressions of an extended database covering a range of temperatures from 600 to 1740 °C and pressures from 10 to 60 GPa. This thermometer includes a curvilinear relationship between $\ln K_d$ and X_{Ca}; it also takes into account the negative relationship between $\ln K_d$ and Mg-number of garnet. A further consideration in this derivation is the effect of the Mn content of garnet on the K_d value. As

with other authors the Na content of clinopyroxene is shown not to affect the Fe^{2+}-Mg equilibrium in the range of Na: 0 – 0.51 atoms per formula unit.

The geothermometer of Krogh (1988) are subparallel when plotted against Krogh (2000). Ai (1994) generally has lower temperatures than this determination. The Ellis and Green (1979) geothermometer tends to overestimate the temperatures in the intermediate range in comparison with the Krogh (2000) geothermometer, for a wide range of compositions.

8.1.2 Pyroxene solvus geothermometry

Pyroxene thermometry is a powerful method for the estimation of temperatures of equilibration of natural lherzolites as it is less sensitive to uncertainties of Fe^{2+}/Fe^{3+}. A number of researchers have done experimental studies on the orthopyroxene and clinopyroxene solid solution series in order to develop geothermometers based upon the diopside-enstatite miscibility gap. Two pyroxene thermometry is usually based on the exchange of the enstatite component between clinopyroxene and orthopyroxene, which is described by the equation:

$$Mg_2Si_2O_6 \leftrightarrow Mg_2Si_2O_6$$
$$Opx \leftrightarrow Cpx$$

Various geothermometer formulations have been produced based on experimental studies (e.g. Wood and Banno, 1973; Saxena and Nehru, 1975; Lindsley and Dixon, 1976). A problem with these formulations is that little was known about the effect of Fe^{2+} and Al^{3+} on the above reaction. Davidson and Lindsley (1985) found that Ca is strongly decreased in clinopyroxenes and is increased in the coexisting orthopyroxene in the presence of Fe^{2+}. The Al^{3+} effect is still not well understood and in a more recent study (Brey and Köhler, 1990) it was ignored because of a lack of accurate thermodynamic data. The geothermometers developed by Brey and Köhler (1990) are utilised in this study. They are based on reversed experiments of Brey et al. (1990) from natural lherzolitic compositions in the pressure and

temperature range from 10 - 60kbar and 900 - 1400 °C. The one geothermometer is a pyroxene solvus thermometer (TBKN) that uses $(\ln K_d)^2$ instead of $\ln K_d$, as the relationship is linear between $(\ln K_d)^2$ and 1/Temperature (T) for the CMAS and CMASCr systems. The authors then fitted the midpoints of the experimental brackets for the CMS, CMAS, and CMASCr systems to the following equation:

$$T = (a + b\,P) / (c + (\ln K_d)^2$$

Where $K_d = a^{cpx}_{en} / a^{opx}_{en} = (1- Ca^{M2})^{cpx} / (1- Ca^{M2})^{opx}$, this is based upon the assumption that Ca is restricted to the M2 site of pyroxenes and that $Mg^{M1}_{cpx} / Mg^{M1}_{opx}$ is approximately unity (Bertrand and Mercier, 1985). A correction for Na was introduced for the natural system, which greatly improved the calculated T versus the experimental T. The other thermometer developed by Brey and Köhler (1990) is based upon the Ca content of orthopyroxene ($T_{Ca\text{-}in\text{-}opx}$). The authors advised that the Ca-in-opx thermometer be used with caution, as they had not devised a correction for the influence of Na on the Ca content of orthopyroxene in natural compositions.

Nimis and Taylor (2000) have synthesised clinopyroxene at a pressure and temperature range of 0 - 60 kbar and 850 - 1500 °C in the CMS, CMAS-Cr and in more complex lherzolitic systems. They have developed a Cr-clinopyroxene barometer (discussed further in 8.1.6) and an enstatite-in-clinopyroxene thermometer for Cr-diopsides derived from garnet peridotites. The authors have stated that in natural peridotitic rocks a^{opx}_{en} is close to unity and not very sensitive to temperature and compositional variations. This simplifies the K_d term in the expression of Brey and Köhler (1990) and gives:

$$T = (a+bP) / (c+(\ln a^{cpx}_{en})^2, \text{ where } a^{cpx}_{en} = (1 - Ca - Na)*(1- \tfrac{1}{2}(Al + Cr + Na)$$

A number of minor components were taken into account (Na, Fe, Ti, Al, K and Cr) and the thermometer reproduced the experimental temperatures to ± 30 °C.

8.1.3 Garnet-olivine Fe^{2+}-Mg geothermometry

The distribution of Fe^{2+} and Mg between garnet and olivine is based upon the exchange reaction:

$$3Fe_2SiO_4 + 2Mg_3Al_2Si_3O_{12} \leftrightarrow 3Mg_2SiO_4 + 2Fe_3Al_2Si_3O_{12}$$
$$\text{Fayalite} + \text{Pyrope} \leftrightarrow \text{Fosterite} + \text{Almandine}$$

A thermometer based upon this exchange reaction was devised by O'Neill and Wood (1979). It is a widely used geothermometer as it can be used for lherzolitic and harzburgitic assemblages. O'Neill and Wood (1979) conducted reversed experiments in the FMAS system, at 30 kbar and temperatures ranging from 900 – 1400 °C. The authors found that $\ln K_d$ of the above equation was dependent upon temperature, the Mg content of olivine and the Ca content of garnet. A simple, non-ideal, solution model best described the experimental data. This produced a geothermometer that works best for temperatures below 1300 °C, where K_d is substantially greater than 1. The pressure dependence of the equation raises the temperature by 3 - 6 °C per kilobar.

8.1.4 Ni geothermometry

Griffin et al. (1989b) and Ryan et al. (1996) developed an empirical calibration single garnet geothermometer based upon the Ni-Mg exchange between garnet and olivine, which may be expressed by the following reaction:

$$2Mg_3Al_2Si_3O_{12} + 3Ni_2SiO_4 \leftrightarrow 2Ni_3Al_2Si_3O_{12} + 3Mg_2SiO_4$$
$$\text{garnet} + \text{olivine} \leftrightarrow \text{garnet} + \text{olivine}$$

Griffin et al. (1989b) showed that the partitioning of Ni between Cr-pyrope and olivine is strongly temperature dependent (using conventional geothermometers). The microprobe analyses of the grains also showed that the range of Ni contents in peridotite

olivine (3000 ±300 ppm) is narrow compared to that in peridotite garnet (<10 – 120 ppm). The authors found that garnet accepts more Ni into its structure as the temperature increases and that the relationship between log K_d (where K_d = ppm Ni_{gt} / ppm Ni_{ol}) and 1/T is linear over a temperature range of ~700 °C. The thermometer is reported to have produced estimated temperatures with an average error of ± 50 °C. Ryan et al. (1996) used a wider range of garnet compositions to refine the geothermometer of Griffin et al. (1989b). The authors also reported an error on the calculation of ± 50 °C, but showed that the temperatures estimated by Griffin et al. (1989b) are lowered by ~35 °C at low temperatures and by ~90 °C at high temperatures.

Sources for error for the empirical Ni-in-garnet geothermometers are that existing major element geothermometers are used to derive the formulations. The conventional geothermometers are known to contain sources of error, which may be compounded in the use of the empirical Ni-in-geothermometer. Also the results obtained will be strongly dependent on the geothermobarometer used (Finnerty and Boyd, 1987).

Canil (1994) studied the partitioning of Ni between olivine and garnet in two multi-component synthetic compositions as a function of temperature and pressure. In the experiments Canil (1994) doped the starting compositions with NiO above natural levels to allow for analysis of the products on the electron microprobe. The author suggested that the elevated Ni contents did not change the partitioning model that occurs at trace levels, as Ni substitution in Mg-Fe-Ni olivine obeys Henry's law to concentrations up to 60 wt% (according to Beattie, 1993). Henry's law states that at high dilution the activity coefficient k^j_i for trace component *i* in phase j is constant, such that the activity a^j_i of *i* in *j* is directly proportional to its concentration X^j_i in *j*. This is defined by: $a^j_i = k_i X^j_i$. Two Ni partitioning experiments were carried out on natural fertile peridotite at 1600 and 1700 °C, in order to ensure a high enough concentration of NiO was partitioned into garnet for electron microprobe analysis (Canil, 1994). These results were criticised by Ryan et al. (1996) because the Ni content of 1700 ppm used in Canil's (1994) experimental runs is far greater than natural compositions (<10 to 120 ppm). They also observed that the application of the experimental calibration to a typical natural lherzolite with an equilibration temperature of ~1400 °C would predict a Ni content of ~250ppm. Canil (1996) responded to the criticism stating that Brey and Köhler (1990) had shown Fe^{2+}-Mg exchange garnet olivine

geothermometry to have errors up to ±113 °C. If this error is taken into account then the empirical and experimental Ni geothermometers are within error of each other at 1400 °C. The experimentally derived Ni geothermometer reportedly reproduced 90% of the experimental data to within ±90 °C. It agrees with the Ni geothermometer of Griffin et al. (1989b) to within ±50 °C (between 900 and 1200 °C). Outside of this range the experimental calibration gives lower temperature estimates at high temperatures and higher estimates at low temperatures in comparison to the empirical calibration. Canil (1999) then repeated the experimental calibration of the Ni thermometer at natural abundances. Once again the thermometer showed different results to the thermometer of Ryan et al. (1996) and very similar results to that of Canil (1994).

8.1.5 Garnet-orthopyroxene geobarometry

This is typically based upon the pressure sensitive solubility of garnet in orthopyroxene coexisting with garnet defined by the following exchange reaction:

$$Mg_2Si_2O_6 + MgAl_2SiO_6 \leftrightarrow Mg_3Al_2Si_3O_{12}$$
$$\text{Enstatite} + \text{MgTs} \leftrightarrow \text{garnet}$$

Nickel and Green (1985) produced a geobarometer based upon the solubility of garnet in enstatite. The authors take into account the presence of minor amounts of Ti, Cr, Na and Mn in both orthopyroxene and garnet. The experiments were conducted in the CMAS, FMAS, CFMAS, CMASCr systems in the pressure range of 10 to 35 kbar. They report the experimental data is reproduced to within ±3 kbar.

Brey and Köhler (1990) tested a number of geobarometers using the experimental data of Brey et al. (1990). They identified a need for a new barometer, which is capable of reproducing experimental conditions for all available systems, and over the whole pressure range applicable to natural peridotites. They calibrated a garnet-orthopyroxene geobarometer applicable to these conditions, using experimental data from MAS, CMAS, FMAS and

CMASCr. They report that the experimental data of Brey et al. (1990) is reproduced to 2.2 kbar (1σ).

8.1.6 Cr-in-clinopyroxene barometer

Brey et al. (1990) showed that the Cr content of clinopyroxene in equilibrium with garnet is also pressure sensitive and that in complex system lherzolitic compositions Cr is more soluble in clinopyroxene than in orthopyroxene (Nimis and Taylor, 2000). Peridotitic garnets have relatively low Na contents and therefore the exchanged Cr component must be Tschermakitic (e.g. $CaCrAlSiO_6$) in which Al substituting for Si in the tetrahedral site balances the excess charge of Cr. Data from Brey et al.'s (1990) experiments show that there is a lower effect of temperature on Cr exchange than the other tschermakitic components. The Cr exchange between clinopyroxene and garnet can be described by:

$$CaMgSi_2O_6 + CaCrAlSiO_6 \leftrightarrow \tfrac{1}{2}(Ca_2Mg)Cr_2Si_3O_{12} + \tfrac{1}{2}(Ca_2Mg)Al_2Si_3O_{12}$$
$$Di + CaCrTs \leftrightarrow uv_2kn_1 + gr_2py_1$$

The relationship between the activity of CaCrTs and pressure was compared for a set of experimental clinopyroxenes, covering as wide a range of natural peridotitic compositions as possible; with pressures and temperatures ranging from 20 – 60kbar and 900 – 1400 °C (Nimis and Taylor, 2000). It was found that the experimental data were satisfactorily reproduced by an expression that takes the activity of CaCrTs, Na, Cr-number and temperature of the clinopyroxenes into account and is independent of the composition of garnet. The temperature dependence of the barometer is reported as 1.2 - 2.4 kbar/50 °C. No systematic error was observed between the calculated and experimental pressures (Nimis and Taylor, 2000).

8.2 Geothermobarometry estimations

Several of the geothermobarometers described above were used to obtain estimates of temperatures and pressures of equilibration for the diamond inclusions. Temperatures have been calculated using the thermometers of Ellis and Green (1979), Ai (1994), Krogh (2000), Nimis and Taylor (2000), O'Neill and Wood (1979), Brey and Köhler (1990; T-BKN and $T_{Ca\text{-}in\text{-}opx}$), Ryan et al. (1996) and Canil (1999). The pressures have been calculated using Nimis and Taylor (2000) and Brey and Köhler (1990). A number of assumptions have been made in order to calculate the temperatures and pressures of these inclusions. The first is that the inclusions were in equilibrium at the time of formation of the diamond, although it is possible that the inclusions were incorporated into the diamond at different times or under different temperatures or mantle conditions. A further assumption is that all the iron present is Fe^{2+}, as the microprobe cannot discriminate between Fe^{2+} and Fe^{3+}. It is believed that diamonds originate from a reduced lithosphere (Haggerty, 1986) and so all the iron will be present as Fe^{2+}.

8.2.1 Geothermometry results

8.2.1.1 Peridotitic diamonds

The results of the geothermometer estimations can be located in Appendix 6, Table A.6.1. The temperatures were calculated at assumed pressures of 40, 50 and 55 kbar. It was found that a pressure of 55 kbar gave temperatures that fall mostly within the diamond stability field and so the following discussion and Table A.6.1 deals with the temperatures obtained using 55 kbar.

The range of temperatures obtained for the garnet and clinopyroxene mineral inclusion pairs using Krogh (2000; referred to from here as T-KR00) is wide from 1064 – 1573 °C. A similar range was obtained for the formulation of Ai (1994; referred to from here as T-Ai94) of 1052 – 1585 °C. A ternary plot of the 25 garnet-clinopyroxene pairs shows that four pairs have tielines that cross the remainder of the group (Figure 8.1). This implies that these

minerals were not in equilibrium at the time of formation and would therefore give spurious results. As was expected the temperatures obtained using these pairs are unrealistically high and have been excluded from the Fe^{2+}-Mg exchange thermometer results. There are two mineral pairs (J/982 10-3 gt-cpx and J/982 10-16 gt-cpx) that also give anomalously high temperatures; and although they appear to be in equilibrium it has been decided to exclude them from the main group. After removing the anomalous inclusions the range of temperatures is narrower, 1052 – 1342 °C for T-Ai94 and 1064 – 1343 °C for T-KR00. The temperatures obtained with T-Ai94 are mostly lower than those from T-KR00, with a maximum difference between the two estimations of 24 °C. The range obtained from the thermometer of Ellis and Green (1979; referred to from here as T-EG79) after excluding the anomalous inclusions, is 1077 – 1280 °C. The results from T-EG79 tend to overestimate temperatures at lower temperatures and underestimate temperatures at higher temperature in comparison with T-Ai94 and T-KR00. This is due to the different treatment of the mathematical relationship between $\ln K_d$ and X_{Ca} by Ellis and Green (1979) compared with Ai (1994) and Krogh (2000). The maximum difference in temperatures between T-EG79 and T-Ai94 and T-KR00 for a single inclusion pair is 47 and 39 °C respectively. The thermometers of Ai (94) and Krogh (2000) are believed to be more accurate than Ellis and Green (1979).

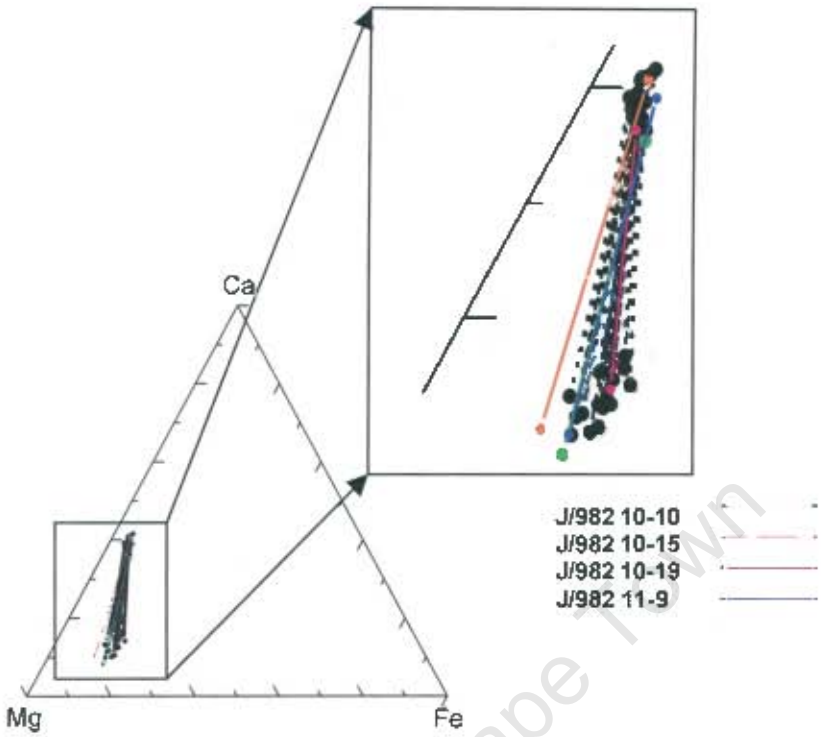

Figure 8.1 A ternary plot of the tielines connecting the Cr-diopside and Cr-pyrope mineral pairs. The coloured lines highlight the inclusions that are in disequilibrium with the remainder of the group. A portion of the plot has been enlarged.

The range of values obtained from clinopyroxene inclusions using the thermometer of Nimis and Taylor (2000; referred to from here as T-NT00) is comparable, but wider than the ranges obtained with other Fe^{2+}-Mg exchange thermometers. T-NT00 gives a range of temperatures from 902 – 1427 °C. A group of clinopyroxene inclusions with temperatures on the high end of this range show a linear dependence between their temperatures and enstatite content (Figure 8.2). These inclusions are the most refractory of the group; amongst these are inclusions J/982 10-3 and J/982 10-16. In fact inclusion J/982 10-16 shows the highest temperature of the group, of 1427 °C. These two inclusions made up part of the anomalously high group in the garnet-clinopyroxene Fe^{2+}-Mg exchange geothermometer, but did not show disequilibrium in the ternary plot.

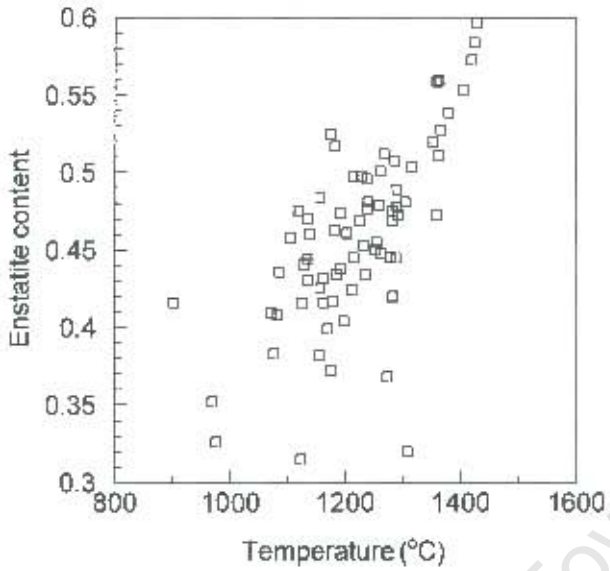

Figure 8.2 A plot illustrating the linear dependence of the temperature on the enstatite content for the Cr-diopside inclusions. Temperatures calculated using T-NT00.

The range of temperatures obtained using the thermometer T-NT00 that correspond to the inclusions used in the Fe^{2+}-Mg exchange thermometers (T-EG79, T-Ai94 and T-KR00); is 1132 – 1316 °C. This range is slightly narrower than the ranges obtained for T-Ai94 and T-KR00. The range of temperatures obtained for the Cr-diopside inclusions that made up part of the disequilibrium pairs (Figure 8.1), in the Fe^{2+}-Mg exchange thermometers, are 1132 – 1277 °C; which falls on the low end of the range obtained for the whole group using T-NT00. This further supports the suggestion that these garnet and clinopyroxene pairs were not included under equilibrium conditions.

The range obtained using the calibration of O'Neill and Wood (1979, referred to from here as T-OW79) is 891 – 1391 °C. This is very similar to the full range obtained from T-NT00. The highest temperature in this range is again from the anomalous J/982 10-3 inclusion (1391 °C). There are three harzburgitic inclusion pairs included in this calibration they give temperatures of 943, 1106 and 1366 °C. This suggests that the harzburgitic paragenesis has a similar range of temperatures in comparison to the lherzolitic group, although it is not possible to qualify without more analyses.

Two thermometers of Brey and Köhler (1990) were also used. The Ca content of orthopyroxene is referred to as $T_{Ca\text{-}in\text{-}opx}$ and the two-pyroxene thermometer is referred to as

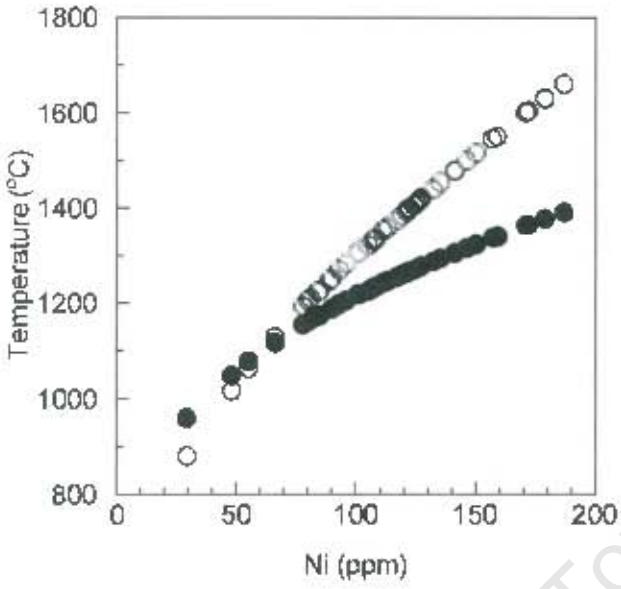

Figure 8.3 A plot of Ni (ppm) in garnets vs. temperature (°C) showing a comparison between the Ni-thermometers of Ryan et al. (1996; open circles) and Canil (1999; filled circles).

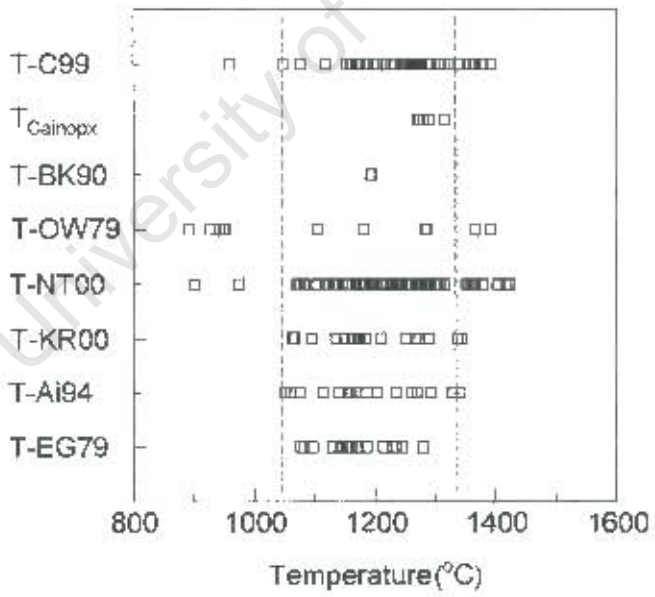

Figure 8.4 A plot showing the range of temperatures for the various geothermometers used, pressures set at 55kbar, with the exception of T-C99 which does not require a pressure estimate.

T-BK90. Only one mineral pair was available for the T-BK90 thermometer and the temperature obtained for the lherzolitic pair is 1194 °C. The three mineral pairs used in $T_{Ca\text{-}in\text{-}opx}$ gave a range of temperatures from 1271 – 1315 °C. Two of the mineral pairs are harzburgitic and these give temperatures of 1291 and 1315 °C respectively. These estimates are within the ranges obtained using the other thermometers.

The range obtained using the Ni thermometry calibration of Ryan et al. (1996; referred to from here on as T-R96) is 881 – 1661 °C and that of Canil (1999; referred to from here as T-C99) is 959 – 1392 °C. A plot of Ni content vs. temperature for the two thermometers shows that T-R96 gives considerably higher temperatures at high Ni concentration in comparison with T-C99 as explained in Section 8.1.4 (Figure 8.3). The range of temperatures obtained with T-C99 correlates very well with the range of temperatures obtained using the other geothermometers, whilst T-RG96 tends to grossly overestimate the temperatures in comparison with the other thermometers. For this reason T-C99 appears to be more realistic than the range obtained with T-RG96. It must be noted that a pressure estimate is not required to calculate Ni-thermometry temperatures. There is a good correlation between temperatures obtained using T-C99 and the other thermometers; this indicates that the assumed pressure is most likely realistic. A number of the inclusions that were analysed for Ni contents are harzburgitic (10 grains), these inclusions give a range of temperatures from 1161 – 1378 °C. These grains span a similar range of temperatures in comparison with the range obtained from the lherzolitic inclusions (11 garnet grains) of 959 – 1306 °C using Ni-thermometry.

Figure 8.4 shows a comparison between the ranges of temperatures obtained using the thermometers mentioned in the text. The dashed lines indicate that the majority of temperatures of formation fall between 1050 and 1330 °C.

8.2.1.2 Eclogitic diamonds

The diamond labelled M3 was the only eclogitic diamond in which both the garnet and clinopyroxene inclusions were recovered whole. The temperatures obtained for this diamond using T-KR00, T-Ai94 and T-EG79 are 1252, 1301 and 1213 °C respectively, using an assumed pressure of 55 kbar. T-NT00 cannot be used for eclogitic inclusions as it was only set up for use on peridotitic inclusions.

8.2.2 Geobarometry results

8.2.2.1 Peridotitic inclusions

The pressures calculated from the various geobarometers can be found in Appendix 6, Table A.6.2. The temperature used to obtain estimates of pressures of formation is 1200 °C. The barometer of Nimis and Taylor (2000, referred to from here as P-NT00) gives a range of pressures from 37 – 74 kbar. A plot of temperature (T-NT00) vs. pressure (P-NT00) shows that there are 5 inclusions with a pressure above 58 kbar (Figure 8.5). There appears to be a rough positive correlation between Cr-number of the clinopyroxene inclusions and their pressures of formation (Figure 8.6). Those inclusions with the lowest Cr-numbers have the lowest pressures. There does not appear to be a strict correlation between the inclusions that give very high pressures and Cr-number.

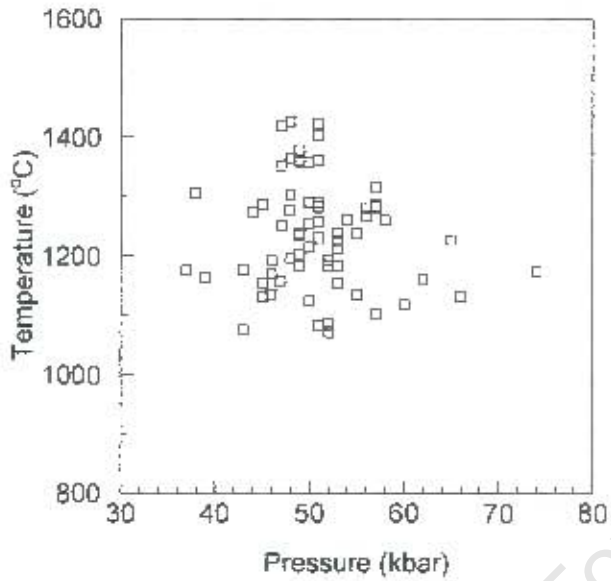

Figure 8.5 A plot of pressure vs. temperature for the Cr-diopside inclusions, calculated using Nimis and Taylor (2000).

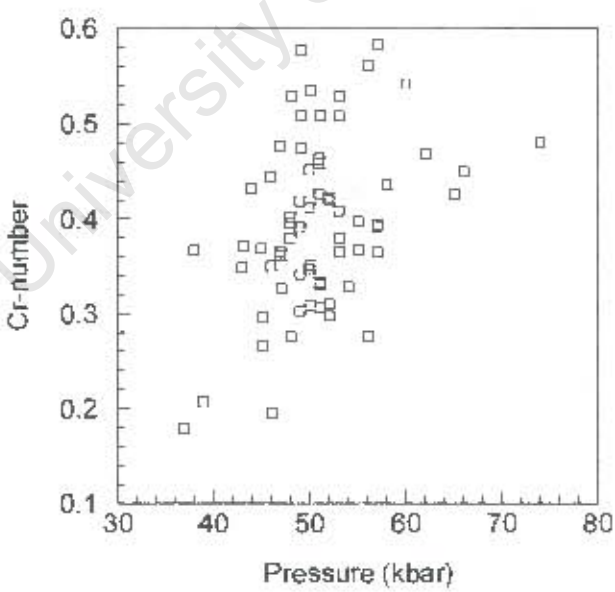

Figure 8.6 A plot of pressure vs. Cr-number for the Cr-diopside inclusions displaying a positive correlation, calculated using Nimis and Taylor (2000).

The Ca in pyroxene barometer of Brey and Köhler (1990; referred to from here as P-BK90) gives a range of pressures from 8 – 77 kbar. The three lowest pressures of 8, 13 and 19 kbar correspond to inclusions J/982 8-8, J/982 10-2 and J/982 10-3. Inclusions J/982 10-2 and J/982 10-3 gave high temperatures in the calibration of T-NT00. It seems likely that they are in disequilibrium and have given spurious results for temperature and pressure. The inclusion J/982 8-8 has a touching olivine and garnet inclusion and may have re-equilibrated at shallower depths after transport in the kimberlite. This may have occurred due to the influence of fluids through cracks in the diamond, although no cracks were visible on inspection of the diamond. If these three inclusions are excluded, the range of pressures is 39 – 77 kbar, which is very similar to P-NT00.

8.2.2.2 Eclogitic inclusions

The pressures of diamonds M3, M4, M5 and J/982 7-13 cannot be calculated using the geobarometer of Nimis and Taylor (2000) as the barometer was only developed for peridotitic clinopyroxene compositions and is not suitable for eclogitic inclusions.

8.2.3 Relation to the continental geotherm

Temperatures estimated with the Fe^{2+}-Mg exchange geothermometers at a pressure of 55 kbar and the temperature and pressure estimates using Nimis and Taylor (2000) were plotted on a pressure-temperature plot together with a lithospheric model geotherm of 40 mW/m^2 and the diamond/graphite phase transition (Figure 8.7; after Kennedy and Kennedy, 1976). These temperatures obtained using the Fe^{2+}-Mg exchange thermometers lie in the diamond stability field, as is to be expected (Only T-KR00 is shown). The temperature and pressure estimates obtained using T&P-NT00 (Figure 8.7) show however, that the estimates lie on both sides of the diamond-graphite boundary. Those that lie in the diamond stability field tend to fall around the 40 mWm^{-2} continental geotherm. A number of these points lie close to the diamond-graphite boundary and it could be the error associated with the calculation ±2.3 kbar

(1σ) (Nimis and Taylor, 2000) that has caused them to plot in the graphite stability field. A plot of the points obtained using P-BK90 and T-NT00 shows that they tend to scatter across the plot, although the majority fall in the diamond stability field.

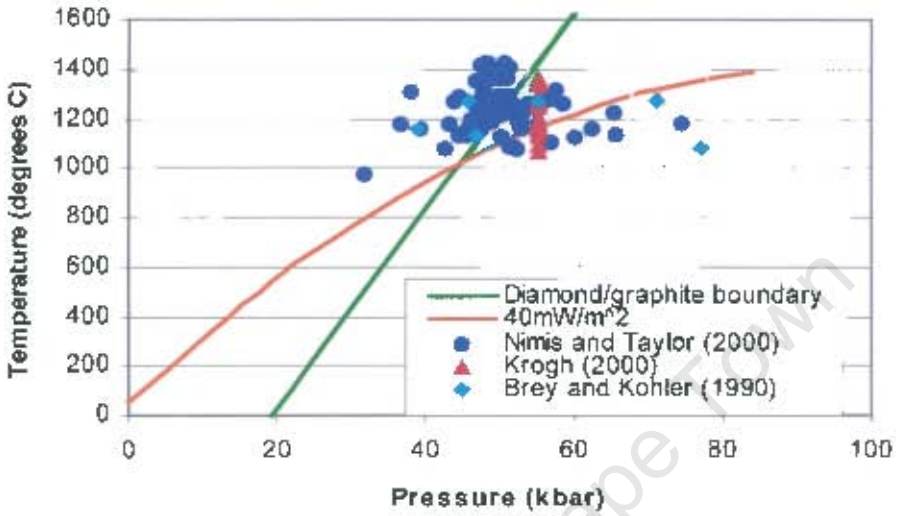

Figure 8.7 A plot of pressure (kbar) vs. temperature (°C) for the estimations using T-KR00 at 55 kbar, T-NT00 and P-NT00. The diamond graphite boundary is after Kennedy & Kennedy (1976). The conductive geotherm is calculated after Pollack and Chapman (1977).

8.3 Discussion and conclusions

Few studies have been carried out on the geothermobarometry of inclusions from Cullinan mine, which has not allowed for an extensive comparison. The range of temperatures obtained for the inclusions in this study is similar to those obtained by Griffin et al. (1992) for peridotitic garnet inclusions from Cullinan using nickel thermometry. The temperatures were calculated using the thermometer of Griffin et al. (1989b). The range obtained by Griffin et al. (1992) is 1150 – 1600 °C, although the high temperatures are likely to be overestimates (as discussed in Section 8.1.4). Gurney et al. (1985) obtained an average temperature for four peridotitic diamonds from Cullinan of 1205 °C and an average temperature for twenty-two eclogitic diamonds of 1285 °C. These temperatures were calculated at 50 kbar using Ellis and Green (1979).

Trapping temperatures less than 1100 °C are interpreted to indicate the formation of diamond under sub-solidus conditions and those diamonds with trapping temperatures between 1100 and 1300 °C are interpreted to have formed in the presence of a small amount of melt (Griffin et al., 1992). It is likely that these diamonds (between 1100 and 1300 °C) have formed at different depths (150 – 200km) along a cratonic geotherm (Griffin et al., 1992). Those diamonds with trapping temperatures above 1300 °C are likely to have formed in the presence of a silicate melt in a system devoid of fluids (Griffin et al., 1992). These higher temperature diamonds must either be derived from depths in excess of 250 km or are formed during thermal perturbations at shallower depths (Griffin et al., 1992). Thermal perturbations may be explained as short-term phenomena relating to the infiltration of melts prior to kimberlite eruption (Smith and Boyd, 1987; Griffin et al., 1989a).

The range of pressures obtained for this suite is wide and suggests that a number of inclusions have undergone late stage alteration at shallower depths, possibly by interaction with fluids through cracks in the diamonds. No cracks were visible during the description of the diamonds physical characteristics. Although the cracks might not have been visible under low magnification or alternatively they may have annealed after alteration. The pressures on the high end of the range suggest a relatively deep origin for a few of the diamonds. Overall however the pressures are lower than expected for the range of temperatures obtained, as a number of the diamonds inclusions fall within the graphite stability field (Figure 8.7).

The intrusion of the Bushveld Igneous Complex immediately prior to the formation of the lherzolitic suite of diamonds in the Cullinan region would have caused a substantial thermal perturbation. This thermal perturbation is likely to account for the high temperatures of formation for a portion of the lherzolitic suite (>1300 °C) and may explain why the pressures associated with these inclusions are lower than expected. The harzburgitic diamonds formed substantially prior to the intrusion of the Bushveld Complex, although some diamonds have temperatures > 1300 °C. This may indicate that these diamonds formed at depths in excess of 250 km or in the presence of melt in an earlier thermal perturbation at ~3.2 Ga during the harzburgitic diamond formation. Pressure estimates could not be calculated for the "high" temperature harzburgitic diamonds and therefore it is not clear as to which of the above explanations is more plausible.

The remainder of the lherzolitic diamonds and the majority of the harzburgitic diamonds would have most likely formed due to the presence of a small amount of melt in the range of 150 – 200 km depth; the REE patterns support the suggestion of melt interaction. The fact that the temperatures are similar for these two paragenoses, despite the low number of analyses for the harzburgite inclusions, indicates that these diamonds are intermixed vertically in the source region. The eclogitic inclusions give temperature estimates, using Fe^{2+}-Mg exchange thermometers that are similar to what has previously been obtained for Cullinan (Gurney et al., 1985). It is not possible to obtain estimates of pressure for the eclogitic inclusions and therefore it is not clear whether the eclogitic diamonds occur at greater depths in the source region in comparison to the peridotitic diamonds.

9. DISCUSSION AND CONCLUSIONS

9.1 Mantle stratigraphy and thermal state

It has been demonstrated that the mantle beneath the Bushveld Igneous Complex is associated with considerably lower seismic velocities in comparison with the majority of the remainder of the Kaapvaal Craton (James et al., 2001). This area of low velocity may either indicate a thermal anomaly existing in this region or alternatively chemical modification of the mantle in this region. Chemical modification of the mantle is preferred and has been attributed to the emplacement of the Bushveld Igneous Complex (~2.05 Ga). It has been suggested that re-fertilization of the mantle due to iron-enrichment would account for the lower seismic velocities (James et al., 2001). Carlson (2001) analysed the Re-Os ages of peridotites from Cullinan and found that they give young ages of ~2.2 Ga. This is consistent with incorporation of new mantle into the lithosphere or extensive reworking of the lithosphere during the emplacement of the Bushveld Igneous Complex. Hoal (2003) also studied peridotite xenoliths from Cullinan and found that they are iron-rich, which has also been interpreted to reflect re-fertilization of the mantle.

It is also possible that significant volumes of eclogitic material would cause a reduction in velocity and decrease in density of the depleted mantle (Shirey et al., 2001). The inclusions in diamonds from Cullinan, Helam and Klipspringer kimberlites have all sampled mantle in the Bushveld region and all appear to be predominantly eclogitic (Gurney et al., 1985; Mc Kenna, 2001; Westerlund, 2000). It is likely that the volume of eclogitic material in this region coupled with chemical modification of the mantle gives rise to the area of lower velocity observed.

This study comprises a number of different parageneses: harzburgitic, lherzolitic and eclogitic. Richardson et al. (1993) dated the harzburgitic, lherzolitic and eclogitic parageneses at 3.2 Ga (inferred), 1.93 Ga and 1.15 Ga respectively. The formation of the lherzolitic suite postdates the intrusion of the Bushveld Igneous Complex (2.05 Ga) and the formation of eclogitic suite occurs immediately prior to the emplacement of the kimberlite pipe.

Evidence for the thermal state of the mantle in the vicinity of Cullinan has been obtained by two methods in this study. The FTIR analyses were used to obtain time-averaged mantle temperature estimates through the relationship between the nitrogen aggregation state of the diamonds and their age. Another method used to obtain the temperatures of formation of the diamonds is through the use of various geothermometers. The range of time-averaged mantle temperatures obtained is 1168 - 1304 °C for the whole stones from both the harzburgitic and lherzolitic suites. These are similar to the range obtained using geothermometers. The majority of temperatures of formation were obtained for the lherzolitic paragenesis, although the values obtained for the harzburgitic and eclogitic inclusions fall within the range of the lherzolitic inclusions. The temperatures span a wide range, from ~1050 – 1330 °C. These values are higher than those obtained for diamonds in other kimberlites in the vicinity of the Bushveld Igneous Complex (Mc Kenna, 2001; Westerlund, 2000). The estimated pressures of formation for the diamonds span a wide range from ~40 to 77 kbar, suggesting that some diamonds may have formed at considerable depths.

9.2 Formation of the Cullinan diamonds

9.2.1 Episodic diamond growth

The different ages obtained for the three main diamond parageneses show that the diamonds have crystallized episodically (Richardson et al., 1993). The FTIR analyses and cathodoluminescence images of 13 diamond plates supports the idea of episodic growth on a shorter time frame. The cathodoluminescence images show that individual diamonds grow in stages; with the majority of the plates analysed showing alternating octahedral growth zones of Type I and Type II diamond. Commonly the growth zones in the diamonds show regions of resorption, followed by further growth. Another line of evidence supporting episodic growth of the diamonds is that a number of the non-touching diamond inclusion pairs were not in equilibrium. This indicates that they were incorporated at different stages during the growth of the diamond.

9.2.2 The environment and timing of crystallization

9.2.2.1 Peridotitic inclusions

There was a period of ~1.27 billion years between the formation of the harzburgitic and lherzolitic populations. The harzburgitic inclusions are characterised by low nitrogen contents (below detection to 858 ppm), high nitrogen aggregation (up to 99%), typical peridotitic carbon isotopic compositions (~ -10 to –1 ‰), subcalcic to calcic mineral compositions and temperatures of formation between 943 and 1378 °C. The lherzolitic inclusions are characterised by low nitrogen contents (below detection to 799 ppm), high nitrogen aggregation (up to 99%), typical peridotitic carbon isotopic compositions (~ -10 to –1 ‰), "borderline" subcalcic to calcic mineral compositions and temperatures of formation between ~1050 and 1330 °C. The nitrogen concentration of the peridotitic diamonds typically decreases from the core to the rim, indicating that the crystallization environment became progressively depleted in nitrogen with time. The mineral chemistry plots show continuous, linear trends between the two peridotitic parageneses, which suggest that the parageneses are related by fractionation processes. These two populations are difficult to separate on the basis of the above variables. This gives rise to two possible explanations for the formation of these two suites:

The harzburgitic population formed episodically at ~3.2 Ga in an environment of relatively low nitrogen concentrations, under typical carbon isotopic compositions. These diamonds then remained stable in the mantle until ~2 Ga. A metasomatic event, possibly related to the infiltration of the Bushveld Igneous Complex, changed the compositions of the source harzburgite towards more fertile lherzolitic compositions. A second suite of diamonds then grew episodically in an environment of relatively low nitrogen saturation and typical carbon isotopic compositions. This implies that the source of carbon and nitrogen in the diamonds remained essentially unchanged for around 1.3 billion years.

Another option is that the harzburgitic diamonds formed at 3.2 Ga, under conditions described above, trapping mineral inclusions of a depleted nature. At ~2 Ga years a metasomatic event, possibly related to the infiltration of the Bushveld Igneous Complex, then altered the compositions of the source harzburgite towards more fertile compositions. The

existing harzburgitic diamonds were resorbed, possibly due to the influx of heat during this event, leaving diamond cores around the inclusions. After a period of time new diamond crystallized episodically around the harzburgitic diamond cores. The lherzolitic diamond suite also crystallized episodically at this time. This would have occurred in an environment of relatively low nitrogen saturation and under typical carbon isotopic compositions, explaining why the nitrogen concentrations and carbon isotopic compositions of the two suites are so similar.

9.2.2.2 Evidence for the recrystallization of the harzburgitic paragenesis

The FTIR estimates of time-averaged mantle temperature have been re-calculated assuming that the diamonds formed at the same time (1.93 Ga). This gives an average temperature for the two groups that are within error of one another. The majority of the harzburgitic plates exhibit well developed cores that contain the garnet inclusions. Obvious cores are not seen in the cathodoluminescence images of the lherzolitic plates, suggesting that they grew in one period, albeit episodically. The harzburgitic cores tend to have higher nitrogen concentrations and aggregation states when compared with the rims of the plates. The change in values from core to rim is narrow however, and does not show conclusively that the cores formed considerably earlier than the rims (with the exception of Plate 5-25). These differences may have been "smoothed out" by the rapid nitrogen migration under high temperatures. The internal growth structure and resorption boundaries of the cores, implies that they formed at different times.

The carbon isotopes span a range from -10.3 to -1 ‰, and the two parageneses are intermixed over this range. The carbon isotope measurements were obtained using fragments of the diamonds and so it is not possible to determine whether the cores of the harzburgitic diamonds have significantly different carbon isotopic compositions in comparison to the rims. The mean carbon isotopic compositions obtained for the two groups are slightly different from one another, however. It is not clear if this is to do with the difference in the number of samples analysed or a real effect from the addition of the older cores.

The nitrogen isotopes are unusual, ranging from -24.5 to +10.2 ‰. The values were obtained for both harzburgitic and lherzolitic diamonds and the values are intermixed across the range. In order for both parageneses to record these substantial changes in nitrogen isotopic conditions of the mantle they most likely crystallized at the same time. The two parageneses cannot be separated in terms of their physical characteristics; the diamonds mostly show evidence of plastic deformation and late stage oxidation processes.

From the collective evidence it seems likely that the harzburgitic paragenesis recrystallized around the time of the lherzolitic diamond formation. This is suggested to occur without altering the mineral inclusions, most likely due to shielding of the inclusions by diamond "coats" or cores. The harzburgitic paragenesis is initially believed to have formed from a depleted harzburgitic source. This source is suggested to be the residual material remaining after extraction of komatiites during the Archean. This source rock is believed to have been re-fertilized through modal and cryptic metasomatism, by fluids possibly associated with the emplacement of the Bushveld Igneous Complex. This would have given rise to a peridotite source rock with compositions varying from enriched harzburgitic to lherzolitic depending on the spatial relation of the peridotite to the metasomatic fluids. The minerals making up this peridotite were incorporated as inclusions in the newly forming lherzolitic paragenesis. This explains how the peridotitic mineral inclusions range in composition from depleted to enriched at Cullinan mine. The inclusions inside the diamonds reflect the changes in the source rock over time and do not indicate that the inclusions themselves were metasomatised after being incorporated into the diamond. The range of temperatures obtained for the formation of the diamonds suggests that they have formed in the presence of varying amounts of melt (depending on their temperature) and not under sub-solidus conditions. This is supported by the majority of REE patterns obtained for the garnet inclusions.

9.2.2.3 Eclogitic inclusions

The eclogitic inclusions are the predominant diamond type at the Cullinan pipe. Only a few stones were available for this study, however. They have been dated 1 - 10 million years prior

to the emplacement of the kimberlite pipe (Richardson et al., 1993). The carbon isotopic compositions fall towards the low end of the range obtained overall (~ - 6 to -4 ‰), but are similar to those obtained for the peridotitic diamonds. Only a few mineral chemistry analyses were obtained for this paragenesis and the compositions are similar to previous studies of eclogitic inclusions from Cullinan. The temperatures of formation obtained are also within the range of what has previously been obtained for eclogitic inclusions from Cullinan. The radiogenic isotopes (Richardson, 1986) combined with the stable carbon isotopes suggest a MORB-type mantle carbon source for the eclogitic inclusions.

9.3 The history of the diamonds subsequent to their formation

The analysis of the physical characteristics of the diamonds in this suite indicates that they have been released from their host rocks at various stages on route to the surface. The majority of the diamonds have brown coloration (93%), which suggests that they have undergone graphitisation associated with plastic deformation. There are a significant number of diamonds that have a completely resorbed TTH (tetrahexahedroid) form. These diamonds would have been liberated from their host rocks the earliest in the suite. The majority of the suite, show primary crystal forms (octahedra, macles and aggregates); however 40% of these have been partially resorbed. This indicates that they were partially shielded by their host rocks. There are also a significant number of diamonds that show surface features that are associated with oxidation and etching. These features develop at around 950 °C and are likely to develop in the kimberlite magma. Some diamonds in the suite have pristine crystal forms and/or growth features on their surfaces. These diamonds are likely to be shielded from the kimberlite magma by their host rocks. A few diamonds show features associated with oxidation and etching, on top of growth features. This indicates that the diamonds were liberated en route to the surface with enough time for etching and oxidation to occur.

9.4 Further study

Further study should be considered in order to confirm the hypothesis that the harzburgitic diamonds have recrystallized. One way of achieving this would be to analyse carbon isotopic compositions in traverses across the diamond plates. It may also be beneficial to do more trace element work on peridotitic inclusions from Cullinan diamonds, to help explain the unusual near chondrite patterns obtained. Ion microprobe or proton microprobe studies would be better suited to such small grains.

10. REFERENCES

Ai, Y. 1994. A revision of the garnet-clinopyroxene Fe^{2+}-Mg exchange geothermometer. *Contrib. Mineral. Petrol.*, **115**: 467-473.

Allsopp, H.L. and Kramers, J.D. 1977. Rb-Sr and U-Pb age determinations on southern African kimberlite pipes. *2nd Int. Kimberlite Conf., Sante Fe, New Mexico, (extended abstracts).*

Anhaeusser, C.R. and Burger, A.J., 1982. An interpretation of U-Pb zircon ages for Archaean tonalitic gneisses from the Johannesburg-Pretoria granite dome. *Trans. Geol. Soc. S. Afr.*, **85:** 111-116.

Bartlett, P.J. 1998. Premier Mine. *7th Int. Kimberlite Conf., Cape Town, Large mines field excursion guide.* 39–49.

Beattie, P. 1993. On the occurrence of apparent non-Henry's law behaviour in experimental partitioning studies. *Geochim. Cosmochim. Acta,* **57**: 47-55.

Berger, S.D. and Pennycock, S.J. 1982. Detection of nitrogen at {100} platelets in diamond. *Nature,* **298**: 635-637.

Berman, R.G., Aranovich, L.Ya. and Pattison, D.R.M. 1995. Reassessment of the garnet-clinopyroxene Fe-Mg exchange thermometer: II. Thermodynamicv analysis. *Contrib. Mineral. Petrol.*, **119**: 30-42.

Bertrand, P. and Mercier, J-C.C. 1985. The mutual solubility of coexisiting ortho- and clinopyroxene: toward an absolute geothermometer for the natural system? *EAPL*, **76**: 109-122.

Bottinga, Y. 1969a. Calculated fractionation factors for carbon and hydrogen isotope exchange in the system calcite-carbon dioxide-graphite-methane-hydrogen-water vapor. *Geochim. Cosmochim. Acta,* **33**: 49-64.

Bottinga, Y. 1969b. Carbon isotope fractionation between graphite, diamond and carbon dioxide. *EAPL*, **5**: 301-307.

Bovenkerk, H.P., 1961. Some observations on the morphology and physical characteristics of synthetic diamond. *The American Mineralogist,* **46**: 952-963.

Boyd, F.R. and Finnerty, A.A. 1980. Conditions of origin of natural diamonds of peridotitic affinity. *J.Geophys. Res.*, **85**: No.B12, 6911-6918.

Boyd, F.R., Gurney, J.J. and Richardson, S.H. 1985. Evidence for a 150-200 km thick Archean lithosphere from diamond inclusion thermobarometry. *Nature*, **315**: 387-389.

Boyd, F.R. and Gurney, J.J. 1986. Diamonds and the African Lithosphere. *Science*, **232**: 472-477.

Boyd, S.R., Pineau, F. and Javoy, M. 1994. Modelling the growth of natural diamonds. *Chem. Geol.*, **116**: 29-42.

Boyd, F.R. and Pillinger, C.T. 1994. A preliminary study of $^{15}N/^{14}N$ in octahedral growth form diamonds. *Chem. Geol.*, **116**: 43-59.

Brey, G.P., Köhler, T. and Nickel, K.G. 1990. Geothermobarometry in four-phase lherzolites I. Experimental results from 10 to 60 kb. *J. Petrol.*, **31**: 1313 – 1352.

Brey, G.P. and Köhler, T. 1990. Geothermobarometry in four-phase lherzolites II. New thermometers and practical assessment of existing thermobarometers. *J. Petrol.*, **31**: 1353 – 1378.

Bundy, F.P. 1980. The P, T phase and reaction diagram for elemental carbon. *Journal of Geophysical Research,* **85** (B12): 6930-6936.

Burgess, S.R. and Harte, B. 1999. Tracing lithosphere evolution through the analysis of heterogeneous G9/G10 garnets in peridotitic xenoliths, I: Major element chemistry. *Proc. 7th Int. Kimberlite Conf.*, **1**: 66-80. University of Cape Town.

Canil, D. 1994. An experimental calibration of the 'Nickel in garnet' geothermometer with applications. *Contrib. Mineral. Petrol.*, **117**: 410-420.

Canil, D. 1996. An experimental calibration of the nickel in garnet geothermometer with applications: reply. *Contrib. Mineral. Petrol.*, **124**: 219-223.

Canil, D., 1999: The Ni in garnet geothermometer: calibration at natural abundances. *Contrib. Mineral. Petrol.*, **136**: 240-246.

Carlson, R.W. 2001. Chemical and age structure of the southern African mantle. *Proc. Slave-Kaapvaal Workshop.* Merrickville, Ontario. Unpaged.

Carlson, R.W., Pearson, D.G., Boyd, F.R., Shirey, S.B., Irvine, G., Menzies, A.H. and Gurney, J.J. 1999. Re-Os systematics of lithospheric peridotites: Implications for lithosphere formation and preservation. *Proc. 7th Int. Kimberlite Conf.*, **1**: 99-108. University of Cape Town.

Carlson, R.W., Boyd, F.R., Shirey, S.B., Janney, P.E., Grove, T.L., Bowring, S.A., Schmitz, M.D., Dann, J.C., Bell, D.R., Gurney, J.J., Richardson, S.H., Tredoux, M., Cartigny, P., Boyd, S.R., Harris, J.W. and Javoy, M. 1997. Nitrogen isotopes in peridotitic diamonds from Fuxian, China: the mantle signature. *Terra Nova*, **9**: 175-179.

Cartigny, P., Harris, J.W. and Javoy, M. 1998a. Eclogitic diamond formation at Jwaneng: No room for a recycled component. *Science*, **280**: 1421-1424.

Cartigny, P., Harris, J.W., Phillips, D., Girad, M and Javoy, M. 1998b. Subduction-related diamonds? – The evidence for a mantle-derived origin from coupled $\delta^{13}C$-$\delta^{15}N$ determinations. *Chem. Geol.*, **147**: 147-159.

Cartigny, P., Harris, J.W., Javoy, M. 2001. Diamond genesis, mantle fractionations and mantle nitrogen content: a study of $\delta^{13}C$-N concentrations in diamonds. *EAPL*, **185**: 85-98.

Chinn, I.L. 1995. A study of unusual diamonds from the George Creek K1 kimberlite dyke, Colorado. Unpubl. PhD. Thesis, University of Cape Town, South Africa.

Chrenko, R.N., McDonald, R.S., and Darrow, K.A. 1967. Infrared spectra of diamond coat. *Nature*, **213**: 474-476.

Clackson, S.G., Moore, M., Walmsley, J.C. and Woods, G.S. 1990. The relationship between platelet size and the frequency of the B' infrared absorption peak in type Ia diamond. *Phil. Mag.*, **B62**: 115-128.

Clark, C.D. and Davey, S.T. 1984. One-phonon infrared absorption in diamond. *J. Phys. C:Solid St. Phys.*, **17**: 1127-1140.

Clark, C.D., Collins, A.T. and Woods, G.S. 1992. Optical spectroscopy of diamond. In: J. Field (ed). *The properties of natural and synthetic diamond.* Academic Press.: 35-69.

Clayton, R.N., Onuma, N. and Mayeda, T.K. 1976. A classification of meteorites based on oxygen isotopes, *Earth. Planet. Sci. Lett.*, **30**: 10-18.

Collins, A.T. 1982. Vacancy enhanced aggregation of nitrogen in diamond. *J. Phys. C. Solid St. Phys.*, **13**: 2641 – 2650.

Craig, H. 1957. Isotopic standards for carbon and oxygen and correction factors for mass spectrometric analysis of carbon dioxide. *Geochim.Cosmochim. Acta,* **12**: 133-149.

Daniels, L.R.M. and Gurney, J.J. 1999. Diamond inclusions from the Dokolwayo Kimberlite, Swaziland. In: J.J. Gurney, J.L. Gurney, M.D. Pascoe, S.H. Richardson (eds), *Proc. 7th Int. Kimberlite Conf.*, **1**: 134-142. University of Cape Town.

Davidson, P.M. and Lindsley, D.H. 1985. Thermodynamic analysis of quadrilateral pyroxenes, Part II. *Contrib. Mineral. Petrol.*, **91**: 390-404.

Davies, G. 1976. The A nitrogen aggregate in diamond – its symmetry and possible structure. *J. Phys C:Solid St. Phys.*, **9**: L537-542.

Davies, G. 1980. Determining the amount of nitrogen in natural diamond. *Industrial Diamond Review:* 466-469.

Davies, R.M., Griffin, W.L., Pearson, N.J., Andrew, A., Doyle, B.J., and O'Reiley, S.Y. 1999. Diamonds from the deep: Pipe DO-27, Slave Craton. In: J.J. Gurney, J.L. Gurney, M.D. Pascoe, S.H. Richardson (eds), *Proc. 7th Int. Kimberlite Conf.*, **1**: 148-155. University of Cape Town.

De Vries, R.C. 1975. Plastic deformation and 'work hardening' of diamond. *Mat. Res.Bull.*, **10**: 1193-1200.

de Wit, M.J. Roering, C., Hart, R.J., Armstrong, R.A., de Rhonde, C.E.J., Green, R.W.E., Tredoux, M., Peberdy, E., and Hart, R.A. 1992. Formation of an Archean continent. *Nature*, **357**: 553-562.

Deines, P. 1980. The carbon isotopic composition of diamonds: relationship to diamond shape, color, occurrence and vapor composition. *Geochim. Cosmochim. Acta*, **44**: 943-961.

Deines, P., Gurney, J.J. and Harris, J.W. 1984. Associated chemical and carbon isotopic composition variations in diamonds from Finsch and Premier kimberlite, South Africa. *Geochim. Cosmochim. Acta*, **48**: 325-342.

Farquhar, J., Wing, B.A., McKeegan, K.D., Harris, J.W., Cartigny, P. and Thiemens, M.H. 2002. Mass-independent sulfur of inclusions in diamond and sulfur recycling on early earth. *Science*, **298**: 2369– 2372.

Frey, F.A. and Green, D.H. 1974. The mineralogy, geochemistry and origin of lherzolite inclusions in Victorian basanites. *Geochim. Cosmochim. Acta,* **38**: 1023-1059.

Finnerty, A.A. and Boyd, F.R. 1984. Evaluation of thermobarometers for garnet peridotites. *Geochim. Cosmochim. Acta,* **48**: 15-27.

Galimov, E.M. 1991. Isotope fractionation related to kimberlite magmatism and diamond formation. *Geochim. Cosmochim. Acta*, **55**: 1697-1708.

Ganor J., Matthews A., Schliestedt M. 1994. Post metamorphic low $\delta^{13}C$ calcite veins in the Cycladic complex (Greece) and their implications for modeling fluid infiltration processes using carbon isotope compositions. *Eur. J. Mineral.*, **6**: 365-379.

Green, T.H. 1982. Anatexis of mafic crust and high pressure studies of andesites. In: R.S. Thorpe (Ed), Andesites. Wiley, New York, N.Y., pp. 465 – 487.

Griffin, W.L., Jaques, A.L.S.S.H., Ryan, C.G., Cousens, D.R., and Suter, G.F. 1988. Conditions of diamond growth: A proton microprobe study of inclusions in West Australian diamonds. *Contrib. Mineral. Petrol.*, **99**: 143-158.

Griffin, W.L., Smith, D., Boyd, F.R., Cousens, D.R., Ryan, C.G., Sie, S.H. 1989a. Trace element zoning in garnets from sheared mantle xenolith. *Geochim. Cosmochim. Acta,* **53**: 561-567.

Griffin, W.L., Cousens, D.R., Ryan, C.G., Sie, S.H. and Suter, G.F. 1989b. Ni in chrome pyrope garnets: a new geothermometer. *Contrib. Mineral. Petrol.* **103**: 199-202.

Griffin, W.L., Gurney, J.J. and Ryan, C.G. 1992. Variations in trapping temperatures in peridotite-suite inclusions from South African diamonds: Evidence for two inclusion suites, and implications for lithosphere stratigraphy. *Contrib. Mineral. Petrol.*, **110**: 1-15.

Griffin, W.L., Pokhilenko, N.P., Ryan, C.G., Sobolev, N.V., Win, T.T. and Yefimova, E.S. 1993. Trace elements in garnets and chromites: Diamond formation in the Siberian lithosphere. *Lithos.*, **29:** 235-256.

Griffin, W.L., O'Reilly, S.Y., Natapov, L.M. and Ryan, C.G. 2003. The evolution of lithospheric mantle beneath the Kalahari Craton and its margins. *Lithos*, **71**: 215-241.
Grove, M., and Bebout, G.E. 1995. Cretaceous tectonic evolution of coastal southern California: Insights from the Catalina Schist. *Tectonics*, **14**: 1290-1308.

Grütter, H.S. and Sweeney, R.J. 2000. Tests and constraints on single-grain Cr-pyrope barometer models: some initial results. GAC-MAC GeoCanada 2000 Conference, Calgary, (CD).

Gurney, J.J. 1984. A correlation between garnets and diamonds in kimberlites. In: J.E. Glover & Harris, P.G. (eds). *Kimberlite Occurrence and Origin; A basis for conceptual models in exploration.* Geology Department and University Extension, University of western Australia, Publication No. **8**: 143-166.

Gurney, J.J. 1989. Diamonds. In: J Ross (ed), *Kimberlites and Related rocks, Vol. 2. Their Mantle/Crust Setting, Diamonds and Diamond Exploration.* Geol Soc. Aust., Spec. Publ. No. **14**, Blackwell: 935-965.

Gurney, J.J. and Switzer, G.S. 1973. The discovery of garnets closely related to diamonds in the Finsch pipe, South Africa. *Contrib. Mineral. Petrol.*, **39**: 103-116.

Gurney, J.J., Harris, J.W., Rickard, R.S. and Moore, R.O. 1985. Inclusions in Premier diamonds. *Trans. Geol. Soc. S. Afr.*, **88**: 301-310.

Haggerty, S.E. 1986. Diamond Genesis in a multiply-constrained model. *Nature*, **320**: 34-38.

Hanley, P.L., Kiflawi, I., and Lang, A.R. 1977. On topographically identifiable sources of cathodoluminescence in natural diamonds. *Phil. Trans. Roy. Soc.*, **A284**: 329-368.

Harris, J.W. 1987. Recent physical, chemical, and isotopic research of diamond. In: P.H. Nixon (ed), *Mantle Xenoliths*. John Wiley & Sons Ltd.: 477-500.

Harris, J.W. 1992. Diamond Geology. In: J.E. Field (ed). *The Properties of Natural and Synthetic Diamond,* Academic Press, London: 345-393.

Harris, J.W., Hawthorne, J.B., Oosterveld, M.M. and Wehmeyer, E. 1975. A classification scheme for diamond and a comparative study of South African diamond characterisitics. *Phys. Chem. Earth,* **9**: 765 – 783.

Harris, J.W. and Gurney, J.J. 1979. Inclusions in Diamond. In: J.E. Field (ed). *The Properties of Diamond*, Academic Press, London: 555-591.

Harris, J.W., Hutchinson, M.T., Hursthouse, M., Light, M. and Harte, B. 1997. A new tetragonal silicate mineral occurring as inclusions in lower-mantle diamonds. *Nature*, **387**: 486-488.

Harte, B.J., Gurney, J.J. and Harris, J.W. 1980. The formation of peridotitic suite inclusions in diamonds. *Contrib. Mineral. Petrol.,* **72:**181-190.

Harte, B. and Harris, J.W. 1994. Lower mantle mineral associations preserved in diamonds. *Mineral. Mag.,* **58A**: 384-385.

Helmstaedt, H and Gurney, J.J. 1984. Kimberlites of southern Africa – Are they related to subduction processes? In: J. Kornprobst (Ed). *Kimberlites and related rocks, Vol. 1, Proc. 3rd Int. Kimberlite Conf., Elsevier, Amsterdam,* 425-434.

Hoal, K.O. 2003. Samples of Proterozoic iron-enriched mantle from the Premier kimberlite. *Lithos*, **71**: 259-272.

Hutchinson, M.T. 1997. Constitution of the sub-lithospheric mantle as shown by diamonds and their inclusions. Unpubl. PhD Thesis, University of Edinburgh.

Irifune, T., Sekine, T., and Ringwood, A.E. 1986. The eclogite-garnetite transformation at high pressure and some geophysical implications. *Earth and Planetary Science Letters*, **77:** 245–256.

Irifune, T., Hibberson, W.O. and Ringwood, A.E. 1989. Eclogite-garnetite transformation at high pressure and its bearing on the occurrence of garnet inclusions in diamond. In: J. Ross et al. (Eds), Kimberlites and related rocks. GSA Spec. Publ. 14. Blackwell, Carlton, pp. 877-882.

Irifune, T. and Ringwood, A.E. 1993. Phase transformations in subducted oceanic crust and buoyancy relationships at depths of 600-800 km in the mantle. *Earth Planet. Sci. Lett.*, **117**: 101-110.

Jagoutz, E., Dawson, J.B., Hoernes, S., Spettel, B. and Wänke, H. 1984. Anorthositic oceanic crust in the Archean earth. *Abstract: 15th Lunar Planetary Science Conference*, Housten (Unpaginated).

James, D.E., Fouch, M.J. VanDecar, J.C., van der Lee, S. and Kaapvaal Seismic Group. 2001. Tectospheric structure beneath southern Africa. *Geophys. Res. Lett.* **28** (13): 2485-2488.

Javoy, M. 1997. The major volatile elements of the Earth: their origin behaviour and fate. *GRL*, **24**: 177-180.

Javoy, M. and Pineau, F. 1983. Stable isotope constraints on a model earth from a study of mantle nitrogen. *Meteoritics*, **18**: 320-321.

Javoy, M., Pineau, F. and Demaiffe, D. 1984. Nitrogen and carbon isotopic composition in the diamonds of Mbuji Mayi (Zaïre). *EAPL*, **68**: 399-412.

Javoy, M., Pineau, F. and Delorme, H. 1986. Carbon and nitrogen isotopes in the mantle. *Chem. Geol.*, **57**: 41-62.

Jones, M.Q.W. (1988). Heat flow in the Witwatersrand basin and environs and its significance for the South African shield geotherm and lithosphere thickness. *J. Geophys. Res.*, **93**: (B4) 3243-3260.

Jones, R., Briddon., P. and Oberg, S. 1992. First principals theory of nitrogen aggregates in diamond. *Phil. Mag. Lett.* **66**: 67-74.

Kennedy, C.S. and Kennedy, G.C. 1976. The equilibrium boundary between graphite and diamond. *J. Geophys. Res.*, **81**: 2467-2470.

Kerridge, J.F. 1985. Carbon, hydrogen and nitrogen in carbonaceous chondrites: Abundance and isotopic compositions in bulk samples. *Geochim. Cosmochim. Acta,* **49**: 1707-1714.

Kesson, S.E. and Ringwood, A.E. 1989. Slab-mantle interactions (2): The formation of diamonds. *Chem. Geol.*, **78**: 97-118.

Kirkley, M. B. and Gurney, J.J. 1989. Carbon isotope modelling of biogenic origins for carbon in eclogitic diamonds. *Extended Abstract 28th International Geological Congress Workshop on diamonds*, pp. 40-43.

Kirkley, M.B., Gurney, J.J., Otter, M.L., Hill, S.J. and Daniels, L.R. 1991. The application of C isotope measurements to the identification of the sources of C in diamonds: a review. *Applied Geochemistry*, **6**: 477-494.

Krogh, E.J. 1988. The garnet-clinopyroxene Fe-Mg geothermometer – a reinterpretation of existing experimental data. *Contrib. Mineral. Petrol.*, **99**: 44-48.

Krogh Ravana, E.J. 2000. The garnet-clinopyroxene Fe^{2+}-Mg geothermometer: an updated calibration. *J. Metamorphic Geol.*, **18**: 211-219.

Lang, A.R. 1964. A proposed structure for nitrogen impurity platelets found in diamond. *Proc. Phys. Soc. London.*, **84**: 871-876.

Lindsley, D.H. and Dixon, S.A. 1976. Diopside-enstatite equilibria at 850°C to 1,400°C, 5 to 35 kbar. *Am. J. Sci.*, **276**:1282-1301.

Luth, R.W. 1993. Diamonds, eclogites, and the oxidation state of the Earth's mantle. *Science*, **261 (5117)**: 66-68.

MacGregor, I.D. and Manton, W.I. 1986. Roberts-Victor eclogites – Ancient oceanic crust. *Journal of Geophysical Research –Solid Earth and Planets.* **91 (B14)**: 14063 – 14079.

Mariotti, A. 1983. Atmospheric nitrogen is a reliable standard for ^{15}N abundance measurements. *Nature*, **303**: 685-687.

McDonough, W.F. and Frey, F.A. 1989. Rare earth elements in upper mantle rocks. In: B.R. Lipin & G.A. McKay (Eds), Geochemistry and mineralogy of rare earth elements, Reviews in Mineralogy, Mineral. Soc. Amer., **21**, 99-145.

Mc Kenna, N. 2001. A study of the diamonds, diamond inclusion minerals and other mantle minerals from the Swartruggens kimberlite, South Africa. Unpubl. MSc Thesis, University of Cape Town, South Africa.

Mendelssohn, M.J. and Milledge, H.J. 1995. Geologically significant information from routine analysis of the mid-infrared spectra of diamonds. *International Geology Review*, **37**: 95-110.

Menzies, A.H., Carlson, R.W., Shirey, S.B. and Gurney, J.J. 1999. Re-Os systematics of Newlands peridotite xenoliths: Implications for diamond and lithosphere formation. *Proc. 7th Int. Kimberlite Conf.*, **2**: 566 - 573. University of Cape Town.

Meyer, H.O.A. 1987. Inclusions in diamond. In: P.H. Nixon (ed). *Mantle Xenoliths*. John Wiley & Sons: 501-523.

Moore, R.O. and Gurney, J.J. 1985. Pyroxene solid-solution in garnets included in diamond. *Nature*, **318**: 553-555.

Moore, R.O., Otter, M.L., Richardson, R.S., Harris, J.W., and Gurney, J.J. 1986. The occurrence of moissanite and ferro-periclase as inclusions in diamond. In: *Ext. Abstr. 4th Int. Kimberlite Conf. Geol. Soc. Austr.*, **16**: 409-411.

Mori, T. and Green, D.H. 1978. Laboratory duplication of phase equilibria observed in natural garnet lherzolites. *J. Geol.*, **86**: 83-97.

Nickel, K.G. and Green, D.H. 1985. Empirical geothermobarometry for garnet peridotites and implications for the nature of the lithosphere, kimberlites and diamonds. *EAPL*, **73**: 158-170.

Nimis, P and Taylor, W.R. 2000. Single clinopyroxene thermobarometry for garnet peridotites. Part I. Calibration and testing of a Cr-in-cpx barometer and an enstatite-in-cpx thermometer. *Contrib. Mineral. Petrol.*, **139**: 541-554.

Nixon, P. H., Rogers, N.W., Gibson, I.L. and Grey, A. 1981. Depleted and fertile mantle xenoliths from southern African kimberlites. *Annu. Rev. Earth Planet. Sci.*, **9**: 285–309.

O'Neill, H.StC. and Wood, B.J. 1979. An experimental study of Fe-Mg partitioning between garnet and olivine and its calibration as a geothermometer. *Contrib. Mineral. Petrol.*, **70**: 59 – 70.

Orlov, Yu. 1973. *Mineralogy of the diamond.* Izdatel' stvo Nauka S.S.S.R. Translated in 1977 from the Russian, John Wiley and Sons, New York: 235pp.

Otter, M.L. 1990. Diamonds and their mineral inclusions from the Sloan diatremes of the Colorado-Wyoming State Line Kimberlite District, North America. Unpubl. PhD. Thesis, University of Cape Town, Cape Town.

Phaal, C. 1965. Surface studies of diamond. *Ind. Diamond. Rev.*, **25**: 486-489.

Pollack, H.N. and Chapman, D.S. 1977. On the regional variation of heat flow geotherm and lithospheric thickness. *Tectonophysics*, **38**: 279 – 296.

Prinz, M., Manson, D.V., Hlava, P.F. and Keil, K. 1975. Inclusions in diamond: garnet lherzolite and eclogitic assemblages. In: L.H. Arens, J.B. Dawson, A.R. Duncan and A.J. Erlank (eds). *Phys. Chem. Earth*, **9**: 797-815.

Raheim, A. and Green, D.H. 1974. Experimental determination of the temperature and pressure dependence of the Fe-Mg partition coefficient for coexisting garnet and clinopyroxene. *Contrib. Mineral. Petrol.*, **48**: 179-203.

Raman, C.V. 1944. Crystal symmetry and structure in diamond. *Proc. Ind. Acad. Sci.*, **19**: 188-199.

Richardson, S.H. 1986. Latter-day origin of diamonds of eclogitic paragenesis. *Nature*, **322**: 623-626.

Richardson, S.H., Gurney, J.J., Erlank, A.J. and Harris, J.W. 1984. Origin of diamonds in old enriched mantle. *Nature*, **310**: 198-202.

Richardson, S.H., Harris, J.W. and Gurney, J.J. 1993. Three generations of diamonds from old continental mantle. *Nature*, **336**: 256-258.

Robertson, R., Fox, J.J. and Martin, A.E. 1934. Two types of diamond. *Phil. Trans. Roy. Soc.*, **A323**: 463.

Robinson, D.N. 1979. Surface textures and other features of diamonds. Unpubl. PhD. Thesis, University of Cape Town, Cape Town.

Robinson, D.N., Scott, J.A., Van Niekerk, A. and Anderson, V.G. 1989. The sequence of events reflected in the diamonds of some southern African kimberlites. In: Kimberlites and Related rocks, Vol. 2. *Their Mantle/Crust Setting, Diamonds and Diamond Exploration.* Geol. Soc. Aust., Spec. Publ. No. 14, Blackwell: 990-1000.

Rudnick, R.L. 1995. Nature and composition of the continental crust: A lower crustal perspective. *Rev. Geophysics,* **33**: 267-309.

Ryan, C.G., Griffin, W.L. and Pearson, N.J., 1996. Garnet Geotherms: a technique for derivation of P-T data from Cr-pyrope garnets. *J. Geophys. Res.*, **101:** 5611-5625.

Saxena, S.K. 1979. Garnet-clinopyroxene geothermometry. *Contrib. Mineral. Petrol.*, **70**: 229-235.

Saxena, S.K. and Nehru, C.E. 1975. Enstatite-diopside solvus and pyroxene geothermometry. *Contr. Mineral. Petrol.* **49:** 259-267.

Schrauder, M. and Navon, O. 1993. Solid carbon dioxide in natural diamond. *Nature*, **365**: 42-44.

Schulze, D.J. 1986. Calcium anomalies in the mantle and a subducted metaserpentinite origin for diamonds. *Nature*, **319**: 483-485.

Scott-Smith, B.H., Danchin, R.V., Harris, J.W. and Strake, K.J. 1984. Kimberlites near Orroroo, South Australia. In: J. Kornprobst (ed). *Proc. 3rd Int. Kimberlite Conf.* Kimberlites I: Kimberlites and their related rocks. Elsevier, Amsterdam.: 121-142.

Shimizu, N. 1975. Rare earth elements in garnets and clinopyroxenes from garnet lherzolite nodules in kimberlites. *EPSL,* **25**: 26-32.

Shimizu, N. and Richardson, S.H. 1987. Trace element abundance patterns of garnet inclusions in peridotite-suite diamonds. *Geochim. Cosmochim. Acta*, **51**: 755-758.

Shirey, S.B., Harris, J.W., James, D., Deines, P., Richardson, S.H., Cartigny, P. and Viljoen, F. 2001. Geochemical and geophysical perspectives on diamond formation beneath southern Africa. *Proc. Slave-Kaapvaal Workshop.* Merrickville, Ontario. Unpaged.

Shirey, S.B., Harris, J.W., Richardson, S.H., Fouch, M., James, D.E., Cartigny, P., Deines P. and Viljoen, F. 2003. Regional patterns in the paragenesis and age of inclusions in diamond, diamond composition, and the lithospheric seismic structure of Southern Africa. *Lithos,* **71**: 243-258.

Smith, D. and Boyd, F.R. 1987. Compositional heterogeneities in a high-temperature lherzolite nodule and implications for mantle processes. In: P.H. Nixon (ed). *Mantle Xenoliths.* J. Wiley & Sons, England. 551-561.

Sobolev, E.V., Lisoivan, V.I., and Lenskaya, S.V. 1968. X-ray diffraction peaks as related to optical properties of natural diamonds. *Doklady Akademii Nauk SSSR,* **175**: 665–668.

Sobolev, N.V., Lavrent'ev, Y.G., Pokhilenko, N.P., Usova, L.V., 1973. Chrome-rich garnets from the kimberlites of Yakutia and their paragenesis. *Contrib. Mineral. Petrol.* **40**: 39-52.

Sobolev, N.V., Galimov, E.M., Ivanovskaya, I.N. and Yefimova, E.S. 1979. Isotopic composition of carbon of diamonds containing crystalline inclusions. *Sov. Phys. Dokl.*, **249**: 1217-1220.

Sobolev, N.V., Yefimova, E.S., Laverent'yev, Yu. G. and Sobolev, V.S. 1984. Dominant calcsilicate association of crystalline inclusions in placer diamonds from southeastern Australia. *Dokl. Akad. Nauk. S.S.S.R.*, **274**: 148-153.

Sobolev, N.V., Kaminsky, F.V., Griffin, W.L., Yefimova, E.S., Win, T.T., Ryan, C.G. and Botkunov, A.I. 1997. Mineral inclusions in diamonds from the Sputnik kimberlite pipe, Yakutia. *Lithos.*, **39**: 135-157.

Stachel, T. and Harris, J.W. 1997a. Syngenetic inclusions in diamond from the Birim field (Ghana) – a deep peridotitic profile with a history of depletion and re-enrichment. *Contrib. Mineral. Petrol.*, **127**: 336-352.

Stachel, T. and Harris, J.W. 1997b. Diamond precipitation and mantle metasomatism – evidence from the trace element chemistry of silicate inclusions in diamonds from Akwatia, Ghana. *Contrib. Mineral. Petrol.*, **129(2-3)**: 143-154.

Stachel, T., Aulbach, S., Brey, G.P., Harris, J.W., Leost, I., Tappert, R and Viljoen, K.S., 2004. The trace element composition of silicate inclusions in diamonds: a review. *Lithos.***77**: 1-19.

Sun, S.-s and McDonough, W.F. 1989. Chemical and isotopic systematics of oceanic basalts: implications for mantle composition and processes. In: Saunders, A.D. & Norry, M.J. (Eds) *Magmatism in the ocean basins. Geological Society London, Special Publications*, **42**, 313-345.

Sutton, J.R. 1928. Kimberley diamonds: especially cleavage diamonds. *Trans. Roy. Soc. S. Afr.*, **7**: 65-96.

Tankard, A. J., Jackson, M. P. A., Eriksson, K. A., Hobday, D. K., Hunter, D. R., and Minter, W. E. L., 1982. Crustal evolution of southern Africa: 3.8 billion years of Earth history: New York, Springer-Verlag, 523 p.

Taylor, W.R., Bulanova, G.P. and Milledge, H.J. 1995. Quantitative nitrogen aggregation study of some Yakutian diamonds: constraints on the growth, thermal, and deformation history of peridotitic and eclogitic diamonds. *6th Int. Kimberlite Conf., Novosibirsk, Russia (extended abstracts),*608-610.

Taylor, W.R., Canil, D. and Milledge, H.J. 1996. Kinetics of Ib to IaA nitrogen aggregation in diamond. *Geochim. Cosmochim. Acta*, **60**: 4725-4733.

Urusovskaya, A.A. and Orlov, Yu. L. 1964. Nature of plastic deformation of diamond crystals. *Dokl. Akad. Nauk. S.S.S.R.*, **154**: 112-115.

van Heerden, L.A., Gurney, J.J. and Deines, P. 1995. The carbon isotopic composition of harzburgitic, lherzolitic, websteritic and eclogitic paragenesis diamonds from southern Africa: a comparison of genetic models. *S. Afr. J. Geol.***98 (2)**: 119 – 125.

Van Orman, J.A., Grove, T.L., Shimizu, N. and Layne, G.D. 2002. Rare earth element diffusion in a natural pyrope single crystal at 2.8 Gpa. *Contrib. Mineral.Petrol.,***142**: 416-424.

Wentorf, R.H. 1965. Diamond synthesis. *Advances in Chemical Physics*, 365-404.

Westerlund, K.J. 2000. A geochemical study of diamonds, diamond inclusion minerals and other mantle minerals from the Klipspringer Kimberlites, South Africa. Unpubl. MSc Thesis. University of Cape Town, Cape Town.

Westurlund, K.J., Hauri, E.H. and Gurney, J.J. 2003. FTIR absorption and stable nitrogen and carbon isotope microanalysis of mid-archaean diamonds from the Panda kimberlite, Slave craton. *8th Int. Kimb. Conf. Long Abst.* p. 5.

Wilding, M.C., Harte, B. and Harris, J.W. 1989. Evidence of an asthenospheric source for diamonds from Brazil. *28th International Geological Congress, Abstracts,* **3**, Washington, D.C.: 359-360.

Wood, B.J. and Banno, S. 1973. Garnet-orthopyroxene and orthopyroxene-clinopyroxene relationships in simple and complex systems. *Contrib. Mineral.Petrol.*, **42**: 109-124.

Woods, G.S. 1986. Platelets and the infrared absorption of Type Ia diamonds. *Proc. R. Soc.*, **A407**: 219-238.

Woods, G.S. and Collins, A.T. 1983. Infrared absorption spectra of hydrogen complexes in Type I diamonds. *J. Phys. C: Solid St. Phys.*, **51**: 1191-1197.

Woods, G.S., Purser, G.C., Mtimkulu, A.S.S. and Collins, A.T. 1990. The nitrogen content of Type Ia natural diamonds. *J. Phys. Chem. Solids*, **51**: 1191-1197.

APPENDIX 1

PHYSICAL CHARACTERISITICS OF DIAMONDS FROM CULLINAN

Key to the abbreviations used:

SHAPE

A	$x = y = z$
B	$x = y \neq z$
C	$x >> z$

COLOUR

B	brown
W	colourless
E	grey

INTENSITY

0	no colour
1	discernable colour
2	light colour
3	medium colour
4	strong colour

CLARITY

1	no inclusions
2	small inclusion
3	a few small or a large inclusion
4	up to 40% of the diamond is occupied by inclusions
5	visibility through the stone is obscured from inclusions

TYPE

octa	octahedron
agg	aggregate
tth	tetrahexahedroid
macle	macle
p.r.	partially resorbed
irreg	irregular

INCLUSION TYPES

P	purple inclusion
G	green inclusion
C	colourless inclusion
B	black inclusion
O	orange inclusion
g	graphite

SURFACE TEXTURES

T.P.	trigonal plates
S.L.	serrate laminae
H.B.	herringbone
S.F.	sharp faces
S.E.	sharp edges
T.E.P.	trigonal etch pits
H.E.P.	hexagonal etch pits
I.P.	inclusion pits
F	frosting on surface
G	graphite on surface
K-L A	knob-like asperities
C.S.	corrosion sculpture
R.C.	resorption channel
E.H.	elongate hillocks
L.L.	lamination lines

The J-982 samples are peridotitic, with the exception of J982 7-13 and the M samples are eclogitic (Section 3.2).

Table A.1: Physical characterisitics of each diamond in this study

Sample No.	Weight (g)	Carats	Shape	Colour	Intensity	Clarity	Type	Inclusions
J-982 10-1	0.01601	0.08005	B	B	2	3	octa (p.r.)	P, G, g
J-982 10-2	0.01258	0.06290	B	B	2	2	octa	P, G, C, g
J-982 10-3	0.01276	0.06380	B	B	3	3	octa (p.r.)	2P, 3G, 4C, g
J-982 10-4	0.00958	0.04790	B	W	0	3	agg (octa)	P, G, g
J-982 10-5	0.01598	0.07990	B	B	2	3	agg (octa)	2P, G, B
J-982 10-6	0.00911	0.04555	A	B	1	3	octa	4P, 3G
J-982 10-7	0.01058	0.05290	B	B	3	3	tth	P, G, g
J-982 10-8	0.01279	0.06395	B	B	3	4	octa (p.r.)	P, G, g, C
J-982 10-9	0.00939	0.04695	B	B	1	4	octa (broken)	P, G, C, g
J-982 10-10	0.01016	0.05080	B	B	1	4	octa	P, lots G, g
J-982 10-11	0.01548	0.07740	B	B	3	3	octa (p.r.)	P,G, g
J-982 10-12	0.01367	0.06835	C	B	3	4	tth (flattened)	P, G, g
J-982 10-13	0.01105	0.05525	B	B	3	3	agg (octa - p.r.)	P,G, g
J-982 10-14	0.01113	0.05565	B	B	2	3	agg (octa)	Can't see
J-982 10-15	0.01544	0.07720	B	B	3	4	octa (p.r.)	P, G, g
J-982 10-16	0.01840	0.09200	B	B	3	3	agg (octa)	P, G, g
J-982 10-17	0.01453	0.07265	B	B	2	3	tth	P, 2G, g
J-982 10-18	0.00961	0.04805	B	W	0	4	agg (octa)	P, G, C, g
J-982 10-19	0.01007	0.05035	B	B	2	4	octa	P, lots G, g
J-982 10-20	0.02022	0.10110	C	B	3	3	tth (flattened)	P, G, C, g
J-982 11-1	0.00747	0.03735	B	B	2	2	macle	P, G, g
J-982 11-2	0.01147	0.05735	B	B	2	2	macle (p.r.)	P, G, g
J-982 11-3	0.00905	0.04525	B	B	3	4	macle (p.r.)	P, G, C, g
J-982 11-4	0.02407	0.12035	B	B	3	4	macle (p.r.)	P, G, C, g
J-982 11-5	0.01681	0.08405	B	B	3	2	macle (p.r.)	P, G, g
J-982 11-6	0.01382	0.06910	B	B	2	3	macle (p.r.)	P, G, g
J-982 11-7	0.00769	0.03845	B	B	3	2	macle (p.r.)	P,G, C, g
J-982 11-8	0.01249	0.06245	B	B	3	2	macle (p.r.)	P, G, C, g
J-982 11-9	0.00926	0.04630	B	W	0	3	macle	P?, G
J-982 11-10	0.01264	0.06320	B	B	3	3	macle (p.r.)	dark incl - irr surface
M1	0.00416	0.02080	B	B	2	2	tth	O, G
M2	0.00475	0.02375	C	B	1	2	tth (flattened)	O, G
M3	0.00208	0.01040	B	B	2	3	tth (rounded)	O, G?, g
M4	0.00367	0.01835	C	B	2	3	tth (flattened)	O, G, W
M5	0.00312	0.01560	B	B	2	3	macle	O, G
J-982 5-1	0.02000	0.10000	B	W	0	1	tth	2P
J-982 5-2	0.01039	0.05195	B	B	2	3	tth (broken)	2P, G, g
J-982 5-3	0.01194	0.05970	A	B	2	2	octa	P, g, G?
J-982 5-4	0.01053	0.05265	B	B	2	2	octa	P
J-982 5-5	0.00982	0.04910	A	B	2	2	octa	3P, C
J-982 5-6	0.01035	0.05175	B	B	2	2	octa	P, C
J-982 5-7	0.00965	0.04825	A	B	2	2	octa	P
J-982 5-8	0.00800	0.04000	B	B	3	2	octa	2P, 2C/G?
J-982 5-9	0.00788	0.03940	B	W	0	2	octa	P, C/G?
J-982 5-10	0.00956	0.04780	B	B	2	2	octa (broken)	P
J-982 5-11	0.01178	0.05890	B	B	4	3	octa	P, C, g
J-982 5-12	0.01318	0.06590	A	B	3	3	octa	P, C, g
J-982 5-13	0.00959	0.04795	B	B	2	3	octa	P, C/G?, g
J-982 5-14	0.00785	0.03925	B	B	3	3	octa	P, G, C
J-982 5-15	0.00928	0.04640	B	B	3	2	octa	P, C
J-982 5-16	0.01002	0.05010	B	B	2	3	octa	P, C
J-982 5-17	0.00849	0.04245	B	B	3	2	octa	P, C
J-982 5-18	0.00929	0.04645	B	B	1	3	octa	P, C, M, G?
J-982 5-19	0.01113	0.05565	B	B	3	2	octa (p.r.)	P, C, g
J-982 5-20	0.01024	0.05120	B	W	0	3	agg (octa)	P, B, g
J-982 5-21	0.01286	0.06430	A	B	1	2	octa	P
J-982 5-22	0.00954	0.04770	B	B	2	3	octa (p.r.)	P, g, C
J-982 5-23	0.01093	0.05465	B	B	4	3	tth	P
J-982 5-24	0.01029	0.05145	B	B	3	3	tth	P, C
J-982 5-25	0.01078	0.05390	B	B	1	3	octa (p.r.)	P, g, C
J-982 5-26	0.01405	0.07025	B	B	4	2	tth	P

Table A.1: continued

Sample No.	Weight (g)	Carats	Shape	Colour	Intensity	Clarity	Type	Inclusions
J-982 6-1	0.01170	0.05850	B	B	3	2	macle	3P, g, G?
J-982 6-2	0.01032	0.05160	B	B	3	3	macle	P, g
J-982 6-3	0.00992	0.04960	B	B	3	3	macle (p.r.)	P, 2C
J-982 6-4	0.00690	0.03450	B	B	3	2	macle	3P, 5C,
J-982 7-1	0.01177	0.05885	B	E	2	3	octa	W, G
J-982 7-2	0.01161	0.05805	B	B	3	3	octa (p.r.)	3G, C
J-982 7-3	0.01030	0.05150	B	B	3	2	octa (p.r.)	G
J-982 7-4	0.00909	0.04545	A	B	2	3	octa	G, C
J-982 7-5	0.01181	0.05905	B	B	3	2	octa (p.r.)	2G
J-982 7-6	0.01133	0.05665	B	B	3	1	octa	G
J-982 7-7	0.01125	0.05625	B	B	3	4	octa	6+G, g
J-982 7-8	0.00949	0.04745	B	B	2	4	octa (p.r.)	10+G, g
J-982 7-9	0.01542	0.07710	B	B	3	2	octa (p.r.)	G
J-982 7-10	0.01202	0.06010	B	B	2	4	agg (octa)	G, g
J-982 7-11	0.01141	0.05705	A	B	2	4	octa	G, g, C
J-982 7-12	0.01132	0.05660	B	B	1	2	octa (broken)	2G
J-982 7-13	0.01122	0.05610	B	B	4	2	tth (broken & resorbed)	G, B
J-982 7-14	0.01477	0.07385	B	B	1	2	tth	3G, g
J-982 7-15	0.00975	0.04875	B	B	1	2	octa (p.r.)	G, g
J-982 7-16	0.01373	0.06865	B	B	1	2	octa (p.r.)	2G, g
J-982 7-17	0.00901	0.04505	B	B	2	3	agg (octa - p.r.)	G, C, g
J-982 7-18	0.00806	0.04030	B	B	3	4	octa (broken)	2G, C, g
J-982 7-19	0.00801	0.04005	B	B	3	2	octa	G, C
J-982 7-20	0.01044	0.05220	B	B	2	4	agg (octa)	G, g
J-982 8-1	0.00742	0.03710	B	B	3	3	macle (p.r.)	G within g
J-982 8-2	0.01217	0.06085	B	B	2	3	macle (p.r.)	G, g
J-982 8-3	0.00880	0.04400	B	B	3	3	macle (p.r.)	G, g
J-982 8-4	0.00945	0.04725	B	B	3	4	macle (p.r.)	2G, g
J-982 8-5	0.00708	0.03540	B	B	3	3	macle (p.r.)	7G, g
J-982 8-6	0.0086	0.04300	B	B	3	3	macle (p.r.)	G, g
J-982 8-7	0.00668	0.03340	B	B	1	2	macle	G, g, C
J-982 8-8	0.01207	0.06035	B	B	2	2	macle (p.r.)	G, g, C
J-982 8-9	0.01393	0.06965	B	B	1	3	macle (p.r.)	G, g
J-982 8-10	0.00828	0.04140	B	B	3	4	macle (p.r.)	G, g
J-982 12-1	0.00949	0.04745	B	B	2	2	macle (p.r.)	P, g
J-982 12-2	0.01834	0.09170	B	B	4	3	irreg (broken & resorbed)	2P, g
J-982 13-1	0.02505	0.12525	B	B	4	1	macle (p.r.)	P
J-982 13-2	0.01857	0.09285	B	B	3	3	macle (p.r.)	P, g
J-982 13-3	0.01919	0.09595	B	B	3	2	macle (p.r.)	2P

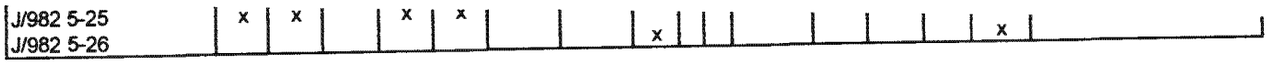

APPENDIX 2

FOURIER TRANSFORM INFRA-RED (FTIR) AND CATHODOLUMINESCENCE (CL) ANALYSIS OF WHOLE DIAMONDS, DIAMOND FRAGMENTS AND DIAMOND PLATES FROM CULLINAN

FTIR ANALYSIS

The whole diamonds and diamond fragments were cleaned in water and ethanol to remove surface dirt. The diamonds were then mounted, in a row, on double-sided tape along the length of a glass side. The flattest faces were chosen to lie parallel to the slide. The spectra were measured at the University of Cape Town using a Nicolet Magna-IR 560 Spectrometer. A KBr beam splitter and MCT/A detector are attached to the spectrometer. The detector is kept cool with liquid nitrogen. The samples were purged with nitrogen gas to prevent the build up of CO_2 around the sample. A resolution of 8 cm^{-1} was used and the spectra were recorded over a range of 4000 – 650 cm^{-1}. In order to remove non-sample, atmospheric contributions to the spectra a background spectrum was run after each sample; set at the same range and resolution. This correction was made on-line using the Nicolet OMNIC 5.0 software.

The Bruker OPUS/3D software was used to deconvolute and extract the peaks from the raw spectra. This information was imported into the Quattro-Pro spreadsheet developed by Mendelssohn and Milledge (1995) to obtain a quantitative estimation of the diamond defect contents. The amount of aggregation was qualitatively estimated for each diamond by comparison with "thumb-nail" spectra (Mendelssohn & Milledge, 1995). These "thumb-nail" spectra were developed using synthetic mixtures of different proportions of A and B aggregates, with variable peak intensity (Fig A2.1). The study of thousands of natural spectra illustrated than natural diamonds display a wide variability in platelet peak height (B') relative to the height of the A-defect peak at 1282 cm^{-1}. The spectral types of K, L, M and N represent the ratios of the B' peak height and the 1282
cm^{-1} peak height of approximately 0, 1, 2 and 2.4 respectively. There is a decrease in platelet peak degradation from types K to N. Type K would represent a completely "irregular" diamond and type N would represent a completely "regular" diamond. The estimations of aggregation for each diamond were used to assess which

absorption peak ratios calculated in the Quattro-Pro spreadsheet should be used to estimate nitrogen aggregation (see Section 4.2).

CATHODOLUMINESCENCE ANALYSIS

The diamond plates were cleaned in water and ethanol to remove surface dirt and mounted on double sided tape on aluminium plates. The plates were carbon coated and the diamond conductivity was further enhanced with a drop of water-soluble carbon dag. CL imaging of the plates was carried out at the Electron Microscope Unit at the University of Cape Town, using a Cambridge S200 scanning electron microscope at 15 kV and an electron beam current of between 1.5 – 2.0 nA. The images were obtained for both sides of the diamond plates. Colour CL images were also acquired for both sides of the diamond plates using an optical microscope attached to a Technosyn luminescence generator with an accelerating voltage of 12 – 15 kV and an electron beam current of 0.8 mA. The diamonds were mounted along a glass slide and fixed with double-sided tape as for the FTIR analysis. Detailed FTIR analysis was conducted on the front and back of the diamond plates, in transects, using the same method as above. This was performed in order to record subtle chemical changes across growth zones of the diamonds. The positions of the analyses can be seen on the cathodoluminescence images in Section 4.3.1.

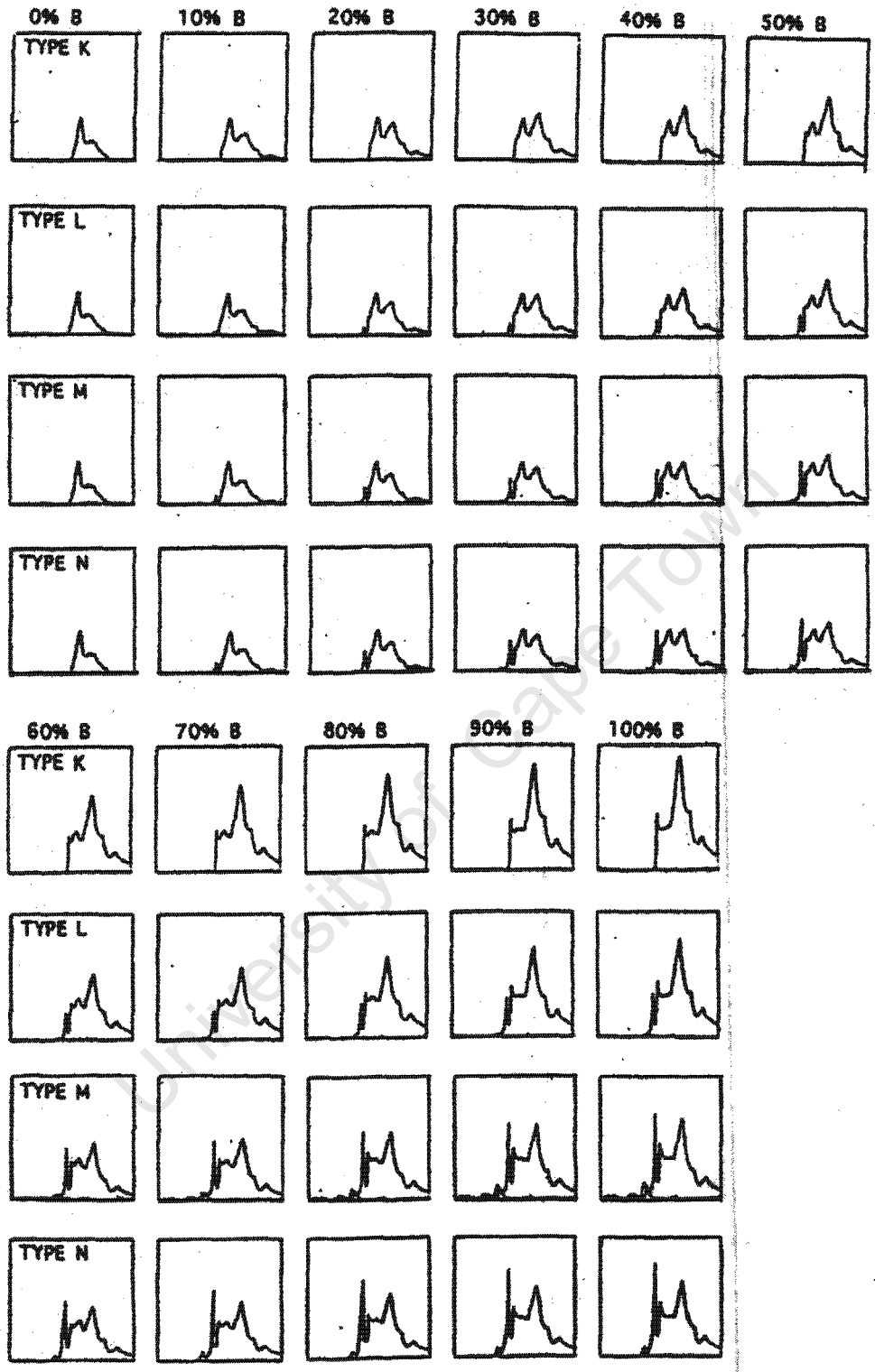

Figure A2.1 Reference "thumb-nail" spectra for aggregation sequences K to N displaying different rates of platelet peak development. Vertical axis represents arbitrary absorption units and horizontal axis ranges from 1750 cm^{-1} to 900 cm^{-1} (from Chinn, 1995).

Table A.2.1 IR properties for the diamond plates

Label	T(cm-1)	H(3107)	H(3237)	mu(1430)	mu(1365)	Nppm	Appm	Bppm	%NasB	T(°) calc	Residence age (Ga)
13-1B1	1361.5	0.016	0.000	0.000	0.726	346	110.7	235.3	67.9	1195	0.75
13-1B2	1361.2	0.000	0.000	0.000	0.231	152	69.7	82.3	54.1	1202	0.75
13-1B3	1360.2	0.007	0.000	0.000	0.114	114	56.1	57.9	51	1206	0.75
13-1B5	1360.3	0.005	0.003	-0.002	0.070	75	43.6	31.4	42.3	1207	0.75
13-1B6	1360.1	0.008	0.000	-0.002	0.067	83	46.3	36.7	44.3	1207	0.75
13-1B7	1361.3	0.008	0.000	0.000	0.150	122	60.2	61.8	51.1	1204	0.75
13-1B8	1361.5	0.030	0.000	0.001	0.636	287	114.5	172.5	60.2	1191	0.75
13-1F1	1360.9	0.005	0.000	-0.002	0.207	162	70.7	91.3	56.4	1202	0.75
13-1F2	1359.8	0.005	0.000	-0.002	0.073	86	51.8	34.2	40.1	1201	0.75
13-1F3	1359.7	0.000	0.000	0.001	0.049	52	37.3	14.7	28.8	1201	0.75
13-1F4	1359.5	0.007	0.000	-0.014	0.037	59	33	26	43.3	1216	0.75
13-1F5	1359.7	0.000	0.000	-0.005	0.038	49	44.4	4.6	10.1	1168	0.75
13-1F6	1360.7	0.007	0.000	-0.002	0.126	117	57.4	59.6	50.8	1205	0.75
13-1F7	1361.3	0.000	0.000	0.001	0.312	182	86.3	95.7	52.8	1195	0.75
13-1F8	1361.5	0.007	0.000	0.000	0.446	213	94.3	118.7	55.6	1194	0.75
13-1F9	1360.7	0.009	0.000	-0.001	0.133	118	56.1	61.9	52.6	1207	0.75
13-1F10	1360.2	0.005	0.000	0.005	0.091	79	51.4	27.6	35.1	1198	0.75
13-1F11	1361.4	0.005	0.003	0.001	0.214	146	66.6	79.4	54.5	1203	0.75
5-11F1	1360.9	0.205	0.000	-0.001	0.176	127	28	99	78	1236	0.75
5-11F2	1361.4	0.271	0.003	0.011	0.310	152	29	123	81	1237	0.75
5-11F3	1360.7	0.118	0.000	0.003	0.118	100	29	71	71	1233	0.75
5-11F4	1361.5	0.180	0.003	0.021	0.340	178	30	148	83	1237	0.75
5-11F5	1361.5	0.110	0.000	0.012	0.167	101	13	88	88	1262	0.75
5-19B2	1359.4	0.086	0.000	0.004	0.031	129	2	127	98	1317	0.75
5-19B3	1359.4	0.084	0.003	-0.002	0.036	151	5	146	96	1291	0.75
5-19B4	1359.5	0.063	0.003	-0.005	0.051	138	5	133	96	1296	0.75
5-19B5	1359.4	0.059	0.003	-0.002	0.036	127	6	121	95	1289	0.75
5-19B6	1359.6	0.059	0.000	0.003	0.036	104	4	100	97	1300	0.75
5-19B7	1359.7	0.039	0.000	-0.008	0.085	68	5	64	94	1295	0.75
5-19B8	1359.5	0.091	0.000	-0.027	0.091	134	7	127	95	1284	0.75
5-19B9	1359.4	0.102	0.003	-0.002	0.073	171	2	169	99	1322	0.75
5-19B10	1359.7	0.070	0.003	-0.008	0.056	126	2	124	99	1329	0.75
5-19B11	1359.2	0.081	0.003	-0.016	0.053	146	1	145	99	1333	0.75

Table A.2.1 continued

Label	T(cm-1)	H(3107)	H(3237)	mu(1430)	mu(1365)	Nppm	Appm	Bppm	%NasB	T(°) calc	Residence age (Ga)
5-19B12	1359.6	0.055	0.000	0.010	0.055	71	3	68	96	1305	0.75
5-19B13	1359.4	0.018	0.003	0.001	0.016	43	6	38	87	1287	0.75
5-19F1	1359.1	0.053	0.000	-0.006	0.091	86	7	79	92	1281	0.75
5-19F2	1358.6	0.065	0.003	0.003	0.052	92	3	89	96	1308	0.75
5-19F5	1358.7	0.063	0.003	-0.005	0.037	147	4	143	98	1300	0.75
5-19F6	1359.5	0.051	0.000	0.001	0.060	101	5	96	95	1295	0.75
5-19F7	1359.4	0.085	0.000	0.007	0.052	105	5	100	95	1291	0.75
5-19F8	1359.8	0.062	0.003	-0.002	0.040	123	5	118	96	1295	0.75
5-19F9	1358.9	0.052	0.000	0.004	0.028	116	4	112	97	1301	0.75
5-19F10	1359.0	0.068	0.003	0.001	0.034	133	3	130	98	1312	0.75
5-19F11	1359.3	0.088	0.000	-0.006	0.067	147	3	144	98	1311	0.75
5-24B1	1361.5	0.037	0.003	0.024	1.085	493	103	390	79	1201	0.75
5-24B2	1364.8	0.031	0.000	0.105	1.989	789	123	666	84	1198	0.75
5-24B3	1365.4	0.029	0.000	0.128	2.068	760	114	646	85	1200	0.75
5-24B4	1363.5	0.041	0.003	0.099	1.812	753	131	622	83	1196	0.75
5-24B5	1361.5	0.022	0.000	0.006	0.655	340	99	241	71	1200	0.75
5-24B6	1362.0	0.026	0.000	0.055	1.253	538	111	428	80	1200	0.75
5-24B7	1361.6	0.032	0.000	0.019	0.776	386	96	290	75	1202	0.75
5-24B8	1365.2	0.032	0.003	0.189	2.746	1051	128	923	88	1198	0.75
5-24F1	1361.5	0.032	0.006	0.003	0.525	304	93	211	69	1200	0.75
5-24F2	1365.4	0.026	0.003	0.209	3.136	1143	130	1013	89	1198	0.75
5-24F3	1365.4	0.023	0.003	0.234	3.090	1091	117	974	89	1201	0.75
5-24F4	1365.4	0.026	0.003	0.184	2.653	947	117	830	88	1201	0.75
5-24F5	1365.4	0.025	0.000	0.170	2.610	961	115	846	88	1201	0.75
5-24F6	1364.8	0.034	0.003	0.120	2.134	922	104	818	89	1204	0.75
5-24F7	1361.5	0.039	0.000	0.016	1.006	474	98	376	79	1203	0.75
5-25B6	1360.7	0.013	0.000	0.009	0.014	26	16	10	40	1233	0.75
5-25B7	1362.1	0.044	0.000	0.004	0.603	248	80	168	68	1178	2.02
5-25B8	1362.6	0.062	0.000	0.013	0.695	294	85	209	71	1177	2.02
5-25B9	1361.5	0.089	0.000	-0.003	0.330	170	56	115	67	1187	2.02
5-25F4	1361.5	0.052	0.000	0.001	0.354	153	67	86	56	1178	2.02
5-25F5	1361.5	0.064	0.000	0.001	0.403	173	71	102	59	1177	2.02
5-25F6	1361.5	0.052	0.000	0.001	0.105	61	27	34	55	1228	0.75

Table A.2.1 continued

Label	T(cm-1)	H(3107)	H(3237)	mu(1430)	mu(1365)	Nppm	Appm	Bppm	%NasB	T(°) calc	Residence age (Ga)
5-25F10	1362.2	0.046	0.003	0.012	0.607	233	85	148	63	1175	2.02
5-25F11	1361.5	0.050	0.000	0.004	0.171	85	29	56	66	1231	0.75
5-26B1	1360.0	0.007	0.000	-0.002	0.127	107	67	40	38	1193	0.75
5-26B2	1359.7	0.012	0.000	-0.007	0.122	109	68	41	38	1192	0.75
5-26B3	1359.7	0.000	0.000	-0.002	0.102	89	61	28	31	1190	0.75
5-26B4	1359.6	0.002	0.000	-0.002	0.100	95	62	33	34	1193	0.75
5-26B5	1360.1	0.000	0.000	0.000	0.124	106	70	36	34	1189	0.75
5-26B6	1359.7	0.000	0.000	-0.004	0.111	97	65	32	32	1190	0.75
5-26B7	1359.8	0.000	0.000	0.000	0.136	113	73	40	36	1189	0.75
5-26B8	1359.9	0.000	0.003	-0.002	0.146	114	73	41	36	1189	0.75
5-26B9	1359.5	0.005	0.000	0.000	0.096	105	66	39	37	1193	0.75
5-26B10	1359.4	0.005	0.000	-0.002	0.090	94	62	32	34	1192	0.75
5-26B11	1359.7	0.000	0.000	0.001	0.073	98	54	44	45	1203	0.75
5-26B12	1359.3	0.003	0.000	-0.002	0.043	71	46	25	35	1201	0.75
5-26F1	1360.2	0.007	0.000	-0.002	0.120	95	65	30	32	1190	0.75
5-26F2	1359.9	0.000	0.000	-0.004	0.124	106	69	37	35	1190	0.75
5-26F3	1359.7	0.000	0.000	-0.002	0.082	94	63	31	33	1191	0.75
5-26F4	1359.5	0.005	0.000	-0.007	0.091	106	68	38	36	1192	0.75
5-26F5	1359.5	0.000	0.000	-0.003	0.062	77	43	34	44	1209	0.75
5-26F6	1359.4	0.000	0.000	-0.004	0.075	91	61	30	33	1192	0.75
5-26F7	1360.3	0.003	0.000	0.003	0.143	115	74	41	36	1189	0.75
5-26F8	1360.0	0.000	0.000	-0.002	0.128	114	72	42	36	1190	0.75
5-26F9	1359.6	0.000	0.000	-0.005	0.077	102	67	35	34	1190	0.75
5-26F10	1359.1	0.000	0.003	0.003	0.063	81	55	26	32	1194	0.75
6-1B1	1361.5	0.030	0.003	0.000	0.021	57	35	23	40	1212	0.75
6-1B2	1360.5	0.023	0.000	0.001	0.003	33	29	4	11	1185	0.75
6-1B3	1361.5	0.044	0.003	-0.002	0.003	44	29	15	35	1213	0.75
6-1B4	1361.5	0.056	0.000	-0.002	0.047	48	35	13	27	1202	0.75
6-1B5	1361.5	0.023	0.000	-0.002	0.021	47	29	19	38	1217	0.75
6-1B6	1361.5	0.026	0.000	0.003	0.015	43	26	17	40	1219	0.75
6-1B7	1361.5	0.026	0.000	0.001	0.024	45	26	19	42	1221	0.75
6-1F1	1361.4	0.020	0.000	-0.002	0.012	44	32	12	28	1205	0.75
6-1F2	1361.5	0.014	0.000	-0.002	0.012	49	29	20	41	1219	0.75

Table A.2.1 continued

Label	T(cm-1)	H(3107)	H(3237)	mu(1430)	mu(1365)	Nppm	Appm	Bppm	%NasB	T(°) calc	Residence age (Ga)
6-1F3	1361.5	0.026	0.003	-0.002	0.053	60	35	25	42	1213	0.75
6-1F4	1361.5	0.035	0.003	0.001	0.044	49	32	18	36	1212	0.75
6-1F5	1361.5	0.032	0.000	0.001	0.024	44	28	16	36	1214	0.75
6-1F6	1361.5	0.038	0.000	0.001	0.056	49	31	18	37	1212	0.75
6-1F7	1361.5	0.044	0.003	0.001	0.035	53	31	22	43	1217	0.75
6-1F8	1361.5	0.032	0.000	-0.002	0.041	53	33	20	38	1212	0.75
6-1F9	1361.5	0.055	0.003	-0.006	0.017	44	28	16	35	1214	0.75
6-1F10	1361.5	0.029	0.000	0.001	0.027	47	30	17	38	1214	0.75
6-1F11	1361.9	0.033	0.000	-0.002	0.000	45	30	16	35	1213	0.75
7-14B1	1364.6	0.096	0.000	0.011	0.253	143	45	98	68	1220	0.75
7-14B2	1365.2	0.034	0.000	0.090	1.639	555	85	470	85	1208	0.75
7-14B3	1365.4	0.060	0.003	0.118	1.909	608	67	541	89	1216	0.75
7-14B4	1366.0	0.210	0.008	0.092	1.216	445	61	384	86	1218	0.75
7-14B5	1366.7	0.281	0.008	0.051	0.136	115	12	103	89	1264	0.75
7-14B6	1366.0	0.325	0.011	0.046	0.195	122	13	109	90	1263	0.75
7-14B7	1365.6	0.455	0.020	0.125	1.207	432	60	372	86	1218	0.75
7-14B8	1372.8	0.555	0.014	0.124	0.405	333	51	282	85	1222	0.75
7-14B9	1373.1	0.297	0.009	0.077	0.286	222	36	186	84	1232	0.75
7-14B10	1365.5	0.401	0.011	0.145	1.095	443	60	383	87	1218	0.75
7-14B11	1365.4	0.162	0.009	0.151	2.005	660	66	594	90	1217	0.75
7-14B12	1366.4	0.358	0.012	0.137	0.846	472	68	404	86	1215	0.75
7-14B13	1365.4	0.077	0.003	0.108	1.872	632	80	552	87	1211	0.75
7-14B14	1365.3	0.022	0.000	0.089	1.859	627	90	537	86	1207	0.75
7-14B15	1365.5	0.367	0.011	0.127	1.095	476	56	420	88	1221	0.75
7-14F1	1364.8	0.088	0.005	0.027	0.649	220	30	190	87	1238	0.75
7-14F2	1365.4	0.051	0.003	0.138	2.160	682	80	602	88	1211	0.75
7-14F3	1371.4	0.341	0.008	0.093	0.427	325	50	275	85	1223	0.75
7-14F4	1374.0	0.444	0.011	0.102	0.367	310	47	264	85	1225	0.75
7-14F5	1366.2	0.450	0.017	0.124	0.912	436	51	385	88	1224	0.75
7-14F6	1365.4	0.173	0.008	0.103	1.494	499	59	440	88	1220	0.75
7-14F7	1365.4	0.163	0.006	0.156	1.922	663	71	592	89	1215	0.75
7-14F8	1365.4	0.060	0.003	0.160	2.438	806	92	714	89	1207	0.75

Table A.2.1 continued

Label	T(cm-1)	H(3107)	H(3237)	mu(1430)	mu(1365)	Nppm	Appm	Bppm	%NasB	T(°) calc	Residence age (Ga)
7-14F9	1364.8	0.026	0.000	0.034	0.724	329	47	282	86	1225	0.75
7-1B1	1365.4	0.147	0.010	0.098	1.306	511	15	496	97	1260	0.75
7-1B2	1364.1	0.071	0.000	0.015	0.492	184	48	136	74	1220	0.75
7-1B3	1363.4	0.064	0.000	0.010	0.406	171	49	122	72	1219	0.75
7-1B4	1363.5	0.021	0.000	0.007	0.382	149	35	114	76	1229	0.75
7-1B5	1363.7	0.018	0.002	0.010	0.358	139	34	105	76	1231	0.75
7-1B6	1363.9	0.049	0.002	0.016	0.496	180	36	144	80	1230	0.75
7-1B7	1363.0	0.070	0.000	0.008	0.245	118	39	79	67	1223	0.75
7-1B8	1363.4	0.041	0.000	0.017	0.534	212	58	154	72	1214	0.75
7-1B9	1362.7	0.166	0.005	0.013	0.382	141	34	107	76	1231	0.75
7-1B10	1364.4	0.118	0.008	0.031	0.443	153	19	134	88	1251	0.75
7-1B11	1365.4	0.076	0.005	0.224	2.767	891	97	794	89	1206	0.75
7-1B12	1364.3	0.075	0.003	0.076	1.323	479	65	414	86	1216	0.75
7-1F1	1365.5	0.149	0.010	0.103	1.382	415	41	374	90	1230	0.75
7-1F2	1364.2	0.109	0.008	0.066	1.114	430	36	394	92	1234	0.75
7-1F3	1364.2	0.082	0.002	0.013	0.490	188	48	140	75	1221	0.75
7-1F4	1363.5	0.053	0.000	0.008	0.302	130	44	86	67	1220	0.75
7-1F5	1363.7	0.026	0.000	0.005	0.231	88	29	59	68	1232	0.75
7-1F6	1363.8	0.021	0.000	0.010	0.304	105	29	76	72	1233	0.75
7-1F7	1363.8	0.047	0.005	0.007	0.267	80	25	55	69	1237	0.75
7-3B1	1361.5	0.017	0.000	0.006	0.651	272	98	174	64	1197	0.75
7-3B2	1362.3	0.000	0.003	0.049	1.165	468	87	381	81	1207	0.75
7-3B3	1364.3	0.006	0.000	0.045	1.580	614	83	531	87	1210	0.75
7-3B4	1361.5	0.020	0.000	0.017	0.995	408	77	331	81	1210	0.75
7-3B5	1361.0	0.037	0.000	0.008	0.145	70	27	43	61	1230	0.75
7-3B6	1358.9	0.000	0.000	0.006	0.007	21	16	5	28	1222	0.75
7-3F1	1360.2	0.026	0.000	0.007	0.036	29	15	14	47	1240	0.75
7-3F2	1361.2	0.031	0.003	0.007	0.318	153	70	83	54	1202	0.75
7-3F3	1361.2	0.024	0.003	0.004	0.336	174	68	106	61	1205	0.75
7-3F4	1361.5	0.009	0.000	0.001	0.502	207	79	128	62	1202	0.75
7-3F5	1362.9	0.000	0.000	0.020	1.069	384	82	303	79	1207	0.75
7-3F6	1361.5	0.011	0.000	0.004	0.579	233	78	155	67	1204	0.75
7-3F7	1361.2	0.016	0.000	0.021	0.497	230	89	141	61	1198	0.75

Table A.2.1 continued

Label	T(cm-1)	H(3107)	H(3237)	mu(1430)	mu(1365)	Nppm	Appm	Bppm	%NasB	T(°) calc	Residence age (Ga)
7-3F8	1361.4	0.064	0.006	-0.005	0.420	217	80	137	63	1202	0.75
7-3F9	1361.5	0.124	0.003	0.003	0.434	194	75	119	61	1203	0.75
7-3F10	1361.5	0.135	0.003	0.001	0.351	154	59	95	61	1209	0.75
7-3F11	1361.5	0.121	0.000	0.001	0.316	140	55	85	61	1211	0.75
7-3F12	1361.5	0.023	0.006	0.003	0.649	245	95	150	61	1196	0.75
7-3F13	1361.5	0.035	0.000	0.001	0.696	278	87	191	69	1202	0.75
7-3F14	1361.3	0.036	0.003	-0.002	0.326	156	59	97	62	1210	0.75
7-3F15	1359.9	0.025	0.000	-0.003	0.029	21	11	10	48	1249	0.75
7-5B1	1359.7	0.008	0.000	0.001	0.089	81	38	43	54	1218	0.75
7-5B2	1361.2	0.031	0.000	0.000	0.412	208	65	143	68	1210	0.75
7-5B3	1361.5	0.023	0.000	0.003	0.750	332	82	250	76	1206	0.75
7-5B4	1361.5	0.028	0.000	0.003	0.687	309	76	233	75	1208	0.75
7-5B5	1361.5	0.023	0.000	0.006	0.623	289	68	221	77	1212	0.75
7-5B6	1360.6	0.032	0.000	-0.002	0.199	112	49	63	57	1213	0.75
7-5F1	1360.0	0.022	0.000	0.003	0.080	80	36	44	55	1220	0.75
7-5F2	1359.6	0.019	0.000	-0.002	0.100	93	42	51	56	1216	0.75
7-5F3	1360.6	0.021	0.000	0.001	0.222	136	57	80	59	1209	0.75
7-5F4	1361.5	0.026	0.000	0.008	0.840	362	84	278	77	1206	0.75
7-5F5	1361.5	0.023	0.000	0.003	0.656	304	79	225	74	1206	0.75
7-5F6	1361.5	0.036	0.000	0.006	0.694	271	78	193	71	1206	0.75
7-5F7	1361.4	0.049	0.000	-0.002	0.396	191	59	132	69	1212	0.75
7-5F8	1361.5	0.073	0.003	0.003	0.543	244	58	186	76	1216	0.75
7-5F9	1361.5	0.026	0.000	0.003	0.445	228	53	175	77	1219	0.75
7-5F10	1361.5	0.028	0.003	0.003	0.545	270	63	207	77	1214	0.75
7-5F11	1361.5	0.031	0.003	0.003	0.672	313	73	240	77	1210	0.75
7-5F12	1361.5	0.023	0.000	0.006	0.664	311	77	235	75	1208	0.75
7-5F13	1360.4	0.021	0.000	-0.002	0.244	141	55	86	61	1211	0.75
8-8B1	1361.5	0.016	0.003	-0.006	0.013	30	27	3	9	1179	0.75
8-8B3	1360.5	0.014	0.002	0.030	0.040	28	22	6	22	1208	0.75
8-8B5	1361.5	0.010	0.000	0.031	0.026	25	23	2	8	1183	0.75
8-8B6	1358.1	0.010	0.002	-0.001	0.014	35	34	1	5	1151	0.75
8-8B7	1358.4	0.018	0.004	0.001	0.007	50	29	21	41	1218	0.75
8-8B10	1360.1	0.000	0.003	0.000	0.018	42	28	14	34	1213	0.75

Table A.2.2 IR properties for the rough peridotitic diamonds, calculated using a residence age of 0.75 billion years.

Label	T(cm-1)	H(3107)	H(3237)	mu(1430)	mu(1365)	Nppm	Appm	Bppm	%NasB	T(°)calc
J-982 5-1	1361.9	0.019	0.010	0.011	1.210	525	163	362	69	1149
J-982 5-3a	1377.5	0.005	0.002	-0.004	-0.004	11	7	4	39	1216
J-982 5-3b	1380.8	0.008	0.000	0.022	-0.002	16	11	6	35	1201
J-982 5-6a	1365.4	0.016	0.005	0.045	1.492	858	305	553	64	1131
J-982 5-6b	1365.4	0.017	0.000	0.046	1.412	788	273	515	65	1134
J-982 5-9a	1361.5	0.119	0.000	-0.001	0.110	80	45	35	44	1170
J-982 5-9b	1361.3	0.089	0.006	0.002	0.121	67	34	33	49	1180
J-982 5-10a	1363.1	0.027	0.000	0.020	0.699	322	59	263	82	1178
J-982 5-10b	1361.3	0.038	0.002	0.002	0.272	192	53	139	73	1178
J-982 5-11a	1360.8	0.163	0.002	-0.003	0.146	99	32	68	69	1190
J-982 5-11b	1361.1	0.174	0.004	0.041	0.297	185	45	140	76	1183
J-982 5-14	1359.5	0.071	0.002	0.001	0.015	86	4	83	96	1260
J-982 5-16	1377.0	0.030	0.002	-0.001	-0.001	15	10	5	35	1203
J-982 5-17a	1360.7	0.128	0.000	-0.002	0.344	148	64	84	57	1167
J-982 5-17b	1360.6	0.075	0.000	-0.001	0.385	163	67	96	59	1167
J-982 5-18	1364.8	0.060	0.000	0.049	1.676	810	254	556	69	1137
J-982 5-19a	1359.3	0.069	0.002	-0.004	0.066	114	6	108	95	1245
J-982 5-19b	1359.2	0.053	0.000	-0.003	0.045	83	5	78	94	1250
J-982 5-21	1361.8	0.065	0.002	0.008	0.565	337	152	185	55	1144
J-982 5-23	1380.8	0.013	0.005	0.075	0.067	39	26	14	35	1178
J-982 5-24	1364.0	0.073	0.007	0.106	1.939	784	108	677	86	1165
J-982 5-25	1361.5	0.065	0.002	-0.003	0.198	83	40	43	52	1177
J-982 5-26	1359.8	0.010	0.010	0.001	0.116	127	67	60	47	1161
J-982 6-1	1361.8	0.044	0.005	-0.006	0.038	55	32	24	42	1178
J-982 6-2	1381.4	0.005	0.003	-0.004	-0.001	13	5	8	57	1236
J-982 6-3	1361.7	0.068	0.005	0.000	0.298	141	13	128	91	1223
J-982 6-4	1381.0	0.000	0.000	0.000	0.002	8	6	3	36	1216
J-982 7-1a	1364.1	0.069	0.000	0.041	0.735	295	54	241	82	1220
J-982 7-1b	1363.9	0.075	0.010	0.053	0.826	313	74	239	76	1209
J-982 7-1c	1363.5	0.048	0.002	0.017	0.732	320	61	259	81	1216
J-982 7-3	1361.5	0.022	0.000	0.007	0.641	270	68	202	75	1211
J-982 7-4	1361.5	0.150	0.005	0.018	0.536	343	12	331	97	1267
J-982 7-5a	1361.0	0.024	0.000	-0.021	0.231	153	54	100	65	1214

Table A.2.2 continued

Label	T(cm-1)	H(3107)	H(3237)	mu(1430)	mu(1365)	Nppm	Appm	Bppm	%NasB	T(°)calc
J-982 7-5b	1361.4	0.024	0.000	0.002	0.429	204	68	137	67	1208
J-982 7-6 (frag)	1360.7	0.016	0.000	-0.004	0.122	130	70	60	46	1197
J-982 7-7	1364.0	0.036	0.002	-0.004	0.018	76	44	32	42	1208
J-982 7-8	1365.4	0.045	0.009	0.006	0.668	292	95	197	68	1199
J-982 7-11a	1361.5	0.043	0.000	0.000	0.317	151	55	96	64	1212
J-982 7-11b	1361.5	0.023	0.000	0.007	0.509	228	69	159	70	1209
J-982 7-12	1365.5	0.079	0.006	0.125	1.898	799	149	650	81	1192
J-982 7-17a	1383.6	0.031	0.000	-0.044	0.014	26	17	9	35	1226
J-982 7-17b	1369.3	0.051	0.000	-0.007	0.000	23	14	9	41	1238
J-982 7-19	1361.5	0.042	0.000	0.005	0.702	388	148	240	62	1185
J-982 7-20a	1366.2	0.063	0.003	0.000	0.192	106	36	70	66	1225
J-982 7-20b	1366.0	0.079	0.005	0.020	0.331	165	53	112	68	1215
J-982 8-1	1361.9	0.029	0.002	0.010	0.377	158	43	116	73	1223
J-982 10-1 (frag)	1361.9	0.019	0.010	0.011	1.210	525	163	362	69	1161
J-982 10-3a	1360.4	0.027	0.000	0.016	0.108	127	43	84	66	1195
J-982 10-3b	1360.7	0.016	0.000	-0.004	0.122	130	70	60	46	1172
J-982 10-4	1364.8	0.061	0.005	0.062	1.150	508	75	433	85	1187
J-982 10-5	1361.5	0.024	0.001	0.005	0.041	41	22	19	45	1202
J-982 10-6a	1363.6	0.041	0.000	0.007	0.206	101	38	63	63	1197
J-982 10-6b	1362.7	0.041	0.000	0.007	0.294	145	45	100	69	1195
J-982 10-9	1365.4	0.049	0.000	0.052	0.907	352	41	311	88	1204
J-982 10-10	1365.4	0.074	0.004	0.005	0.001	50	24	26	53	1204
J-982 10-11a	1369.5	0.089	0.010	0.093	0.503	463	4	459	99	1272
J-982 10-11b	1369.2	0.066	0.009	0.068	0.443	444	11	433	98	1243
J-982 10-13	1360.7	0.039	0.002	0.009	0.050	36	16	21	58	1218
J-982 10-14	1362.9	0.155	0.007	0.010	0.132	63	27	36	58	1204
J-982 10-15	1363.5	0.116	0.002	0.029	0.087	105	45	60	57	1190
J-982 10-17	1360.3	0.023	0.007	0.032	0.123	86	31	55	64	1203
J-982 10-18	1363.5	0.082	0.000	0.006	0.247	92	22	70	76	1216
J-982 10-19a	1365.4	0.162	0.004	0.008	0.572	324	117	207	64	1168
J-982 10-19b	1365.4	0.206	0.004	0.038	0.872	396	117	279	70	1170
J-982 10-20 (frag)	1364.0	0.073	0.007	0.106	1.939	784	108	677	86	1178
J-982 11-1a	1366.0	0.260	0.013	0.167	1.843	652	62	590	91	1193

Table A.2.2 continued

Label	T(cm-1)	H(3107)	H(3237)	mu(1430)	mu(1365)	Nppm	Appm	Bppm	%NasB	T(°)calc
J-982 11-1b	1366.2	0.233	0.012	0.140	1.500	536	42	494	92	1204
J-982 11-7	1361.5	0.045	0.000	0.015	0.674	223	70	153	69	1183
J-982 11-8	1361.5	0.027	0.007	-0.005	0.269	153	67	86	56	1179
J-982 11-9	1361.5	0.141	0.007	0.021	0.084	71	37	34	47	1189
J-982 13-1	1360.5	0.008	0.000	0.008	0.103	85	50	35	41	1165
J-982 13-2	1360.9	0.020	0.003	-0.002	0.195	138	60	78	56	1168
P137 (frag)	1364.8	0.061	0.005	0.062	1.150	508	75	433	85	1186
P146 (frag)	1366.0	0.260	0.013	0.167	1.843	652	62	590	91	1192

Table A.2.3 IR properties for rough eclogitic diamonds, calculated using a residence age of 10 million years.

Label	T(cm-1)	H(3107)	H(3237)	mu(1430)	mu(1365)	Nppm	Appm	Bppm	%NasB	T(°)calc
M2 (frag)	1360.6	0.057	0.000	-0.004	0.152	118	49	69	59	1270
M4 (frag)	1365.3	0.076	0.007	0.043	1.243	488	89	399	82	1263

APPENDIX 3

CARBON AND NITROGEN ISOTOPES OF CULLINAN MINE DIAMONDS

ISOTOPE ANALYSIS

The carbon and nitrogen isotopes of the Cullinan diamonds were measured in the stable isotope laboratory at Queens University, Kingston, Canada. The isotopes were measured on a Carlo Erba Instruments NCS2500 Elemental Analyser coupled with a Finnigan Mat 252 mass spectrometer using continuous flow technology. The analysis of carbon and nitrogen isotopes is performed using separate samples of the same diamond as the mass spectrometer can only recognize one element at a time. The continuous flow method involves combusting the diamond in oxygen, converting it into CO_2 and N_2 gas. The CO_2 and N_2 gas, carried in a He carrier gas is then separated and purified with a Gas Chromatographic column (GC). The CO_2 and N_2 gas are ionized by the mass spectrometer and the isotopic composition is measured. The values of $\delta\ ^{13}C$ and $\delta\ ^{15}N$ are calculated relative to known standards

The fragments of diamonds were weighed and loaded separately into 6 x 4 mm ultra-clean tin cups. The weight of the fragments used in each carbon isotope measurement was between 0.009 and 0.04 mg, although the majority weighed between 0.02 and 0.03mg. Larger samples are required for the nitrogen isotope analyses due to the low abundance of nitrogen in the diamond's crystal lattice. The range in weight of the fragments used in each nitrogen isotope analysis varied between 1.4 and 1.8 mg. A blank was run after every three samples in order to remove any excess carbon. A standard was run after every six samples (on average) to ensure that the machine was operating within acceptable error limits.

Key to Table A.3.1:

Parageneses

E: Eclogitic
P: Peridotitic
Lherzolitic: Sub-division of the Peridotite paragenesis
Harzburgitic: Sub-division of the Peridotite paragenesis

Shape

octa: Octahedron
agg: Aggregate
tth: Tetrahexahedroid
macle: Macle
irreg: Irregular

Table A.3.1 A summary table of the mean and standard deviation of carbon isotopes (‰) for various groups of the Cullinan diamonds

Colour and shape

white	brown	octa	tth	agg	macle	irreg	
-4.33	-3.84	-3.47	-4.39	-3.51	-3.94	-4.39	**mean**
1.58	1.27	1.12	1.12	0.75	0.91	1.22	**sd**
13	81	44	13	10	32	2	**n**

Paragenesis

E-Type	P-Type	lherzolitic	harzburgitic	
-4.92	-4.02	-3.89	-4.23	**mean**
0.84	1.51	1.32	1.49	**sd**
4	101	62	39	**n**

Table A.3.2 A table of the carbon isotope and nitrogen isotope values (‰) and paragenesis for individual diamonds from Cullinan.
J-982 samples are peridotitic, the P samples are the supplementary peridotitic diamonds and the M samples are eclogitic (Section 3.2)

Sample number	$\delta^{13}C$ (‰)	$\delta^{15}N$(‰)	paragenesis
J-982 10-1	-3.27		lherz
J-982 10-2	-5.00		lherz
J-982 10-3	-3.55		lherz
J-982 10-4	-4.74	-18.13	lherz
J-982 10-4 (duplicate)	n.d.	-24.51	lherz
J-982 10-5	-3.27		lherz
J-982 10-6	-3.32		lherz
J-982 10-7	-5.18		lherz
J-982 10-8	-4.71		lherz
J-982 10-9	-2.42		lherz
J-982 10-10	-3.34		lherz
J-982 10-11	-2.98		lherz
J-982 10-12	-3.37		lherz
J-982 10-13	-3.59		lherz
J-982 10-14	-2.69		lherz
J-982 10-15	-4.90		lherz
J-982 10-16	-4.75		lherz
J-982 10-17	-3.30		lherz
J-982 10-18	-3.12		lherz
J-982 10-19	-3.22	-2.16	lherz
J-982 10-20	-3.83		lherz
J-982 11-1	-4.99	10.20	lherz
J-982 11-2	-5.25		lherz
J-982 11-3	-3.91		lherz
J-982 11-4	-4.42		lherz
J-982 11-5	-4.52		lherz
J-982 11-6	-3.75		lherz
J-982 11-7	-4.14		lherz
J-982 11-8	-1.01		lherz
J-982 11-9	-3.32		lherz
J-982 11-10	-4.14		lherz
J-982 5-1	-5.52		harz
J-982 5-3	-4.87		harz
J-982 5-4	-2.72		harz
J-982 5-5	-3.07		harz
J-982 5-6	-4.41	-9.31	harz
J-982 5-7	-3.38		harz
J-982 5-8	-4.04		harz
J-982 5-9	-2.10		harz
J-982 5-10	-2.10		harz
J-982 5-12	-3.84		harz
J-982 5-13	-3.46		harz
J-982 5-14	-2.84		harz
J-982 5-15	-4.63		harz
J-982 5-16	-4.73		harz
J-982 5-17	-2.55		harz
J-982 5-18	-4.15	4.87	harz
J-982 5-20	-3.46		harz
J-982 5-21	-5.88	5.85	harz
J-982 5-22	-1.44		harz
J-982 5-23	-2.40		harz
J-982 6-2	-3.95		harz

Table A.3.2 continued

Sample number	$\delta^{13}C$ (‰)	$\delta^{15}N$(‰)	paragenesis
J-982 6-3	-4.24		harz
J-982 6-4	-4.44		harz
J-982 7-2	-1.98		lherz
J-982 7-4	-4.54		lherz
J-982 7-6	-1.10		lherz
J-982 7-7	-2.14		lherz
J-982 7-8	-3.51		lherz
J-982 7-9	-3.41		lherz
J-982 7-10	-5.28		lherz
J-982 7-11	-3.53		lherz
J-982 7-12	-1.63	-2.60	lherz
J-982 7-13	-4.14		lherz
J-982 7-15	-3.76		lherz
J-982 7-16	-5.14		lherz
J-982 7-17	-3.02		lherz
J-982 7-18	-3.49		lherz
J-982 7-19	-4.25	-0.20	lherz
J-982 7-20	-2.99		lherz
J-982 8-1	-3.80		lherz
J-982 8-2	-4.86		lherz
J-982 8-3	-4.34		lherz
J-982 8-4	-4.63		lherz
J-982 8-5	-5.04		lherz
J-982 8-6	-4.72		lherz
J-982 8-7	-4.20		lherz
J-982 8-9	-3.84		lherz
J-982 8-10	-3.68		lherz
J-982 12-1	-3.28		harz
J-982 12-2	-3.53		harz
J-982 13-2	-2.24		harz
J-982 13-3	-2.68		harz
P 037	-6.02		harz
P 101	-10.29		harz
P 155	-7.06		harz
P 136	-3.82		harz
P 146	-5.90		harz
P 137	-3.37	3.74	harz
P 152	-3.48		harz
P 095	-6.43		harz
P 045	-5.91		harz
P 131	-3.18		harz
P 099	-7.71		harz
P 102	-5.93		harz
P 034	-3.70		lherz
P 071	-2.74		lherz
P 081	-3.02		lherz
P 097	-10.02		lherz
P 108	-4.28		lherz
P 147	-3.50		lherz
P 174	-6.79		lherz
M2	-4.81		eclog
M3	-4.34		eclog
M4	-6.13		eclog
M5	-4.38		eclog

APPENDIX 4

ELECTRON MICROPROBE METHODOLOGY AND ANALYSES FOR INCLUSIONS FROM CULLINAN MINE DIAMONDS

ELECTRON MICROPROBE

The major element chemical analyses of garnet, clinopyroxene, orthopyroxene and olivine were determined using the Cameca/Camebax electron microprobe at the University of Cape Town, Department of Geological Sciences. The samples were analysed under the following instrumental conditions:

Beam current:	40nA
Accelerating voltage:	15kV
Beam size:	2-5 μm
Analysing crystals:	TLAP for Na, Mg, Si and Al
	LiF (200) for Fe, Mn and Ni
	PET for Ca, K, Ti and Cr
Detection:	Flow counters with 10% methane in Ar gas mixture

Counting times of 10 seconds were used for the peaks and background for all elements except Ni in olivine, which had counting times of 30 seconds for peaks and backgrounds and K in clinopyroxene and Na in garnet, which had counting times of 60 seconds for peaks and backgrounds. The standards used in the analyses are listed in Table 4.1 and the lower limits of detection for the various oxides are listed in Table A.4.2. The values obtained for the individual inclusions are presented in Tables A.4.3 – A.4.8.

Table A.4.1
Standards used for the mineral phases by the electron microprobe

Oxide	Garnet	Pyroxene	Olivine
SiO_2	K-P	DIOP	M-Ol
TiO_2	RUT	RUT	RUT
Al_2O_3	K-P	K-P	K-P
Cr_2O_3	CHRO	CHRO	CHRO
FeO	K-P	K-P	M-Ol
MnO	RHOD	RHOD	RHOD
MgO	K-P	DIOP	M-Ol
CaO	K-P	DIOP	K-P
Na_2O	K-H	K-H	-
K_2O	K-H	K-H	-
NiO	-	-	NISI

M-Ol: Marhilati Olivine; K-P: Kakanui Pyrope; K-H: Kakanui Hornblende; DIOP: Synthetic Diopside; RUT: Synthetic Rutile; CHRO: Chromite 52NL11; RHOD: Synthetic Rhodonite; NISI: Synthetic Ni_2SiO_4

Table A.4.2
Lower limits of detection and standard deviations for the various oxides based on counting statistics

Oxide	Garnet	Cpx	Opx	Olivine
SiO_2	0.06 ± 0.16	0.06 ± 0.16	0.06 ± 0.16	0.06 ± 0.14
TiO_2	0.04 ± 0.02	0.04 ± 0.02	0.04 ± 0.02	0.04 ± 0.02
Al_2O_3	0.06 ± 0.10	0.04 ± 0.06	0.05 ± 0.05	0.04 ± 0.01
Cr_2O_3	0.06 ± 0.04	0.05 ± 0.02	0.04 ± 0.02	0.04 ± 0.02
FeO	0.08 ± 0.17	0.10 ± 0.07	0.07 ± 0.10	0.07 ± 0.12
MnO	0.09 ± 0.07	0.06 ± 0.02	0.06 ± 0.03	0.06 ± 0.02
MgO	0.04 ± 0.11	0.04 ± 0.08	0.05 ± 0.11	0.04 ± 0.14
CaO	0.09 ± 0.07	0.03 ± 0.09	0.02 ± 0.02	0.01 ± 0.01
Na_2O	0.01 ± 0.01	0.05 ± 0.04	0.04 ± 0.01	-
K_2O	0.01 ± 0.03	0.02 ± 0.01	-	-
NiO	-	-	-	0.06 ± 0.03

Table A.4.3: Peridotitic garnet inclusion analyses

	10-1 gt	10-3 gt	10-3 gta	10-4 gt	10-4gta	10-5 gt	10-5 gta	10-6 gt	10-6 gta	10-6 gtb	10-8 gt	10-9 gt
SiO_2	43.76	39.84	42.27	43.59	41.70	42.84	42.50	43.11	41.78	41.85	40.54	42.01
TiO_2	0.25	0.21	0.27	0.31	0.57	0.88	0.88	0.29	0.35	0.32	0.34	0.35
Al_2O_3	20.78	16.07	16.31	17.13	15.43	19.70	19.78	18.65	18.56	18.22	21.63	19.58
Cr_2O_3	3.60	8.82	9.84	6.63	10.09	4.01	3.99	6.37	6.67	6.72	2.97	5.13
FeO	6.75	6.50	6.53	7.68	7.42	7.43	7.66	7.34	7.50	7.29	6.90	6.51
MnO	0.27	0.30	0.22	0.35	0.32	0.33	0.31	0.32	0.34	0.31	0.33	0.30
MgO	19.11	21.74	18.77	17.31	19.19	20.74	20.20	19.81	19.30	20.26	22.12	22.16
CaO	4.57	5.99	6.28	6.76	6.10	3.87	3.87	4.81	4.73	4.47	4.70	4.27
Na_2O	0.11	0.05	0.07	0.12	0.10	0.13	0.25	0.01	0.03	0.06	0.06	0.08
Total	**99.26**	**99.51**	**100.56**	**99.91**	**100.93**	**99.94**	**99.45**	**100.70**	**99.25**	**99.50**	**99.60**	**100.39**
Oxy	12	12	12	12	12	12	12	12	12	12	12	12
Si	3.140	2.978	3.119	3.198	3.091	3.078	3.073	3.112	3.075	3.070	2.920	3.018
Ti	0.014	0.012	0.015	0.017	0.032	0.048	0.048	0.015	0.019	0.018	0.018	0.019
Al	1.764	1.421	1.424	1.487	1.353	1.674	1.692	1.593	1.616	1.582	1.844	1.665
Cr	0.219	0.558	0.615	0.412	0.633	0.244	0.244	0.389	0.415	0.417	0.181	0.312
Fe	0.405	0.406	0.403	0.471	0.460	0.447	0.463	0.443	0.461	0.447	0.416	0.391
Mn	0.015	0.018	0.013	0.021	0.019	0.019	0.018	0.019	0.020	0.019	0.019	0.017
Mg	2.043	2.422	2.064	1.893	2.120	2.221	2.177	2.131	2.117	2.214	2.375	2.373
Ca	0.351	0.480	0.496	0.532	0.485	0.298	0.300	0.372	0.373	0.351	0.363	0.329
Na	0.015	0.007	0.010	0.017	0.014	0.019	0.035	0.002	0.004	0.009	0.008	0.012
sum	7.976	8.303	8.159	8.052	8.208	8.047	8.051	8.077	8.100	8.126	8.144	8.136
Mg-number	83.5	85.6	83.7	80.1	82.2	83.3	82.4	82.8	82.1	83.2	85.1	85.9

Table A.4.3: continued

	10-10 gt	10-11 gt	10-12 gt	10-13 gt	10-15 gt	10-16 gt	10-18 gt	10-19 gt	10-20 gt	11-1 gt	11-2 gt	11-2 gta
SiO_2	43.81	42.84	40.76	42.09	39.22	42.75	41.96	44.01	42.91	43.96	45.78	42.55
TiO_2	0.04	N.D.	0.35	0.25	N.D.	N.D.	0.26	N.D.	0.76	0.05	N.D.	N.D.
Al_2O_3	17.62	20.98	16.91	16.38	19.00	20.39	19.19	21.75	20.53	22.00	22.75	20.82
Cr_2O_3	7.99	4.05	7.63	8.97	5.64	4.69	5.13	3.58	3.39	2.59	4.21	4.42
FeO	6.32	6.48	6.19	6.81	6.29	6.22	7.06	5.90	7.77	7.29	5.92	5.84
MnO	0.27	0.25	0.35	0.25	0.28	0.21	0.32	0.21	0.37	0.26	0.22	0.19
MgO	20.12	19.72	21.48	18.18	24.93	20.94	22.24	19.53	20.49	18.35	16.53	21.83
CaO	2.97	5.83	5.29	6.07	4.61	5.26	4.02	5.43	4.01	5.11	5.13	5.10
Na_2O	0.02	0.01	0.05	N.D.	0.01	N.D.	0.08	0.08	0.13	N.D.	0.03	N.D.
Total	**99.21**	**100.19**	**99.03**	**99.00**	**100.00**	**100.48**	**100.25**	**100.49**	**100.35**	**99.68**	**100.66**	**100.79**
Oxy	12	12	12	12	12	12	12	12	12	12	12	12
Si	3.197	3.066	3.024	3.143	2.860	3.055	3.026	3.111	3.064	3.132	3.215	3.024
Ti	0.002	N.D.	0.019	0.014	N.D.	N.D.	0.014	N.D.	0.041	0.003	N.D.	N.D.
Al	1.521	1.777	1.485	1.448	1.640	1.725	1.637	1.820	1.735	1.855	1.891	1.750
Cr	0.493	0.246	0.479	0.567	0.348	0.284	0.313	0.214	0.205	0.156	0.250	0.266
Fe	0.386	0.388	0.384	0.425	0.384	0.372	0.426	0.349	0.464	0.434	0.348	0.347
Mn	0.016	0.014	0.021	0.015	0.016	0.012	0.018	0.012	0.021	0.015	0.013	0.011
Mg	2.188	2.104	2.375	2.023	2.709	2.230	2.390	2.057	2.181	1.948	1.730	2.312
Ca	0.232	0.447	0.421	0.485	0.361	0.403	0.311	0.411	0.307	0.390	0.386	0.388
Na	0.003	0.002	0.007	N.D.	0.002	N.D.	0.011	0.011	0.018	N.D.	0.003	N.D.
sum	8.047	8.045	8.220	8.120	8.320	8.082	8.147	7.985	8.036	7.943	7.848	8.102
Mg-number	85.0	84.4	86.1	82.6	87.6	85.7	84.9	85.5	82.5	81.8	83.3	87.0

Table A.4.3: continued

	11-3 gt	11-4 gt	11-5 gt	11-5 gta	11-6 gt	11-8 gt	11-8 gta	11-9 gt	11-9 gta	11-10 gt	11-10 gta	5-1 gt
SiO_2	43.50	44.89	42.83	42.60	43.56	43.69	41.88	44.05	43.52	41.58	44.13	45.54
TiO_2	N.D.	0.64	0.32	0.37	0.33	0.30	0.37	N.D.	0.79	0.26	0.28	N.D.
Al_2O_3	18.77	21.42	19.25	18.92	19.00	19.60	18.84	19.19	19.56	19.54	20.17	19.13
Cr_2O_3	7.80	4.59	6.23	6.30	5.96	5.55	5.88	7.71	5.64	4.02	4.55	8.43
FeO	6.73	6.51	6.98	7.21	7.62	6.44	6.84	6.15	6.81	7.11	6.95	4.15
MnO	0.35	0.33	0.33	0.25	0.37	0.27	0.30	0.31	0.25	0.21	0.24	0.17
MgO	17.46	17.39	19.42	19.44	18.11	18.08	21.21	19.52	18.18	22.26	18.94	21.91
CaO	5.32	5.06	4.69	4.86	5.10	6.25	4.60	3.56	4.96	4.41	4.49	0.59
Na_2O	0.01	0.11	0.07	0.01	0.03	0.12	0.10	0.01	0.13	0.05	0.07	N.D.
Total	**99.97**	**100.93**	**100.12**	**99.97**	**100.11**	**100.29**	**100.03**	**100.50**	**99.85**	**99.45**	**99.82**	**100.05**
Oxy	12	12	12	12	12	12	12	12	12	12	12	12
Si	3.171	3.173	3.101	3.096	3.157	3.145	3.040	3.166	3.143	3.011	3.162	3.230
Ti	N.D.	0.034	0.017	0.020	0.018	0.016	0.020	N.D.	0.043	0.014	0.015	N.D.
Al	1.619	1.791	1.649	1.627	1.629	1.670	1.618	1.631	1.672	1.675	1.711	1.606
Cr	0.481	0.275	0.382	0.388	0.365	0.338	0.361	0.469	0.345	0.247	0.276	0.506
Fe	0.411	0.385	0.423	0.438	0.462	0.388	0.415	0.370	0.411	0.431	0.417	0.246
Mn	0.021	0.019	0.019	0.015	0.022	0.016	0.018	0.018	0.015	0.012	0.014	0.010
Mg	1.897	1.831	2.096	2.106	1.956	1.940	2.294	2.090	1.957	2.402	2.023	2.316
Ca	0.416	0.383	0.364	0.379	0.396	0.482	0.358	0.274	0.384	0.342	0.345	0.045
Na	0.002	0.015	0.009	0.001	0.004	0.016	0.014	0.001	0.018	0.007	0.010	N.D.
sum	8.022	7.905	8.061	8.070	8.015	8.012	8.139	8.020	7.988	8.141	7.972	7.976
Mg-number	82.2	82.6	83.2	82.8	80.9	83.4	84.7	85.0	82.6	84.8	82.9	90.4

Table A.4.3: continued

	5-2 gt	5-2 gta	5-2 gtb	5-3 gt	5-3 gta	5-4 gt	5-6 gt	5-8 gt	5-9 gt	5-10 gt	5-11 gt	5-12 gt
SiO_2	42.31	41.92	41.63	43.39	41.52	41.86	42.21	42.08	41.78	42.41	42.52	44.51
TiO_2	0.04	0.09	N.D.	N.D.	0.12	0.12	0.11	N.D.	0.24	0.06	0.06	0.04
Al_2O_3	13.24	12.58	14.54	18.10	16.37	17.90	18.21	19.03	16.51	17.73	16.05	19.74
Cr_2O_3	14.90	15.22	13.91	8.71	9.46	7.09	6.88	5.57	9.53	7.45	10.77	6.22
FeO	4.92	4.70	4.60	5.97	6.35	6.02	6.38	5.79	7.77	6.41	6.23	6.43
MnO	0.21	0.25	0.14	0.22	0.17	0.27	0.25	0.25	0.39	0.29	0.33	0.31
MgO	23.91	24.65	23.43	18.70	21.13	20.62	20.38	22.98	16.63	22.32	22.20	18.83
CaO	1.37	1.25	1.27	4.59	4.61	6.08	5.43	3.87	6.65	4.11	2.46	4.57
Na_2O	0.02	0.01	0.01	N.D.	0.03	N.D.	N.D.	0.03	0.01	N.D.	0.05	0.01
Total	**100.90**	**100.73**	**99.57**	**99.70**	**99.75**	**99.97**	**99.86**	**99.63**	**99.52**	**100.77**	**100.68**	**100.65**
Oxy	12	12	12	12	12	12	12	12	12	12	12	12
Si	3.130	3.116	3.100	3.170	3.072	3.060	3.080	3.039	3.133	3.067	3.111	3.180
Ti	0.002	0.005	N.D.	N.D.	0.007	0.006	0.006	N.D.	0.014	0.003	0.003	0.002
Al	1.160	1.107	1.281	1.565	1.434	1.548	1.573	1.627	1.465	1.517	1.390	1.669
Cr	0.933	0.958	0.876	0.538	0.592	0.439	0.425	0.341	0.605	0.456	0.667	0.376
Fe	0.304	0.292	0.287	0.365	0.393	0.368	0.389	0.350	0.487	0.388	0.382	0.384
Mn	0.012	0.015	0.009	0.013	0.010	0.016	0.015	0.014	0.024	0.017	0.020	0.018
Mg	2.636	2.730	2.600	2.036	2.330	2.246	2.217	2.473	1.858	2.405	2.421	2.005
Ca	0.109	0.099	0.102	0.359	0.365	0.476	0.425	0.300	0.534	0.319	0.193	0.350
Na	0.003	0.001	0.002	N.D.	0.004	N.D.	N.D.	0.004	0.002	N.D.	0.007	0.001
sum	8.289	8.330	8.259	8.047	8.206	8.160	8.128	8.149	8.122	8.171	8.194	7.984
Mg-number	89.6	90.3	90.1	84.8	85.6	85.9	85.1	87.6	79.2	86.1	86.4	83.9

Table A.4.3: continued

	5-12 gta	5-13 gt	5-14 gt	5-15 gt	5-16 gt	5-17 gt	5-18 gt	5-19 gt	5-19 gta	5-20 gt	5-21 gt	5-21 gta
SiO_2	43.61	39.62	40.64	42.66	43.96	42.34	42.91	42.30	40.36	42.55	43.72	42.24
TiO_2	0.13	0.36	0.08	0.05	0.05	0.09	0.14	0.16	0.35	0.06	N.D.	0.04
Al_2O_3	19.38	15.34	18.92	17.63	20.60	17.71	14.71	17.04	16.14	18.15	15.65	14.52
Cr_2O_3	6.39	9.30	5.31	6.50	3.79	7.58	12.13	8.50	9.81	6.95	12.21	12.73
FeO	6.26	6.08	6.66	6.37	6.70	6.40	4.56	6.70	7.50	6.42	6.13	6.00
MnO	0.18	0.28	0.28	0.27	0.28	0.31	0.20	0.27	0.42	0.29	0.27	0.27
MgO	19.06	23.03	23.58	20.86	19.85	21.87	24.20	20.01	19.11	21.68	18.71	20.84
CaO	4.74	5.51	5.42	4.71	4.82	4.49	1.77	5.94	6.77	4.58	3.55	3.52
Na_2O	0.04	0.01	0.04	0.06	N.D.	N.D.	N.D.	0.05	0.06	N.D.	N.D.	N.D.
Total	**99.82**	**99.52**	**100.94**	**99.11**	**100.05**	**100.80**	**100.63**	**100.97**	**100.52**	**100.67**	**100.25**	**100.21**
Oxy	12	12	12	12	12	12	12	12	12	12	12	12
Si	3.150	2.964	2.933	3.123	3.134	3.067	3.133	3.089	3.016	3.074	3.227	3.144
Ti	0.007	0.020	0.005	0.003	0.003	0.005	0.008	0.009	0.020	0.003	N.D.	0.002
Al	1.656	1.358	1.616	1.527	1.738	1.518	1.271	1.472	1.427	1.551	1.367	1.279
Cr	0.391	0.589	0.324	0.403	0.229	0.465	0.750	0.526	0.620	0.425	0.763	0.802
Fe	0.378	0.381	0.402	0.390	0.399	0.388	0.278	0.409	0.469	0.388	0.378	0.374
Mn	0.011	0.017	0.016	0.016	0.016	0.018	0.012	0.016	0.025	0.017	0.016	0.016
Mg	2.051	2.568	2.536	2.276	2.109	2.361	2.633	2.178	2.128	2.335	2.058	2.312
Ca	0.367	0.442	0.419	0.370	0.368	0.349	0.138	0.465	0.542	0.354	0.280	0.281
Na	0.005	0.001	0.006	0.008	N.D.	N.D.	N.D.	0.007	0.009	N.D.	N.D.	N.D.
sum	8.020	8.338	8.257	8.115	7.995	8.170	8.223	8.170	8.256	8.147	8.090	8.217
Mg-number	84.4	87.1	86.3	85.4	84.1	85.9	90.4	84.2	82.0	85.7	84.5	86.1

Table A.4.3: continued

	5-21 gtb	5-22 gt	5-23 gt	5-24 gt	5-25 gt	6-1 gt	6-2 gt	6-3 gt	6-4 gt	12-1 gt	12-1 gta	12-2 gt
SiO_2	42.21	42.57	44.87	42.42	43.20	42.76	42.00	40.38	44.80	41.53	43.08	41.66
TiO_2	0.05	0.29	N.D.	N.D.	0.42	0.46	0.05	0.07	N.D.	0.16	0.16	0.31
Al_2O_3	14.68	17.51	19.77	17.29	18.88	18.77	18.21	18.38	17.97	19.47	19.71	19.75
Cr_2O_3	12.35	7.82	7.13	8.54	5.91	5.84	6.17	7.10	5.87	5.48	5.71	5.02
FeO	5.90	6.84	6.20	6.47	6.80	7.73	6.15	6.60	5.97	6.31	6.43	6.74
MnO	0.28	0.36	0.31	0.26	0.31	0.31	0.25	0.30	0.21	0.28	0.31	0.32
MgO	21.88	20.25	17.55	20.33	20.67	18.27	22.82	20.52	22.32	22.64	20.92	21.64
CaO	3.60	4.88	4.24	5.34	4.39	4.87	4.40	6.30	2.93	4.47	4.51	4.60
Na_2O	N.D.	0.09	N.D.	0.02	0.13	0.07	N.D.	N.D.	0.01	0.03	N.D.	0.09
Total	**100.98**	**100.61**	**100.07**	**100.70**	**100.70**	**99.13**	**100.05**	**99.66**	**100.12**	**100.37**	**100.83**	**100.14**
Oxy	12	12	12	12	12	12	12	12	12	12	12	12
Si	3.114	3.100	3.224	3.095	3.102	3.134	3.042	2.980	3.198	2.992	3.080	3.007
Ti	0.003	0.016	N.D.	N.D.	0.023	0.025	0.003	0.004	N.D.	0.009	0.008	0.017
Al	1.282	1.509	1.681	1.493	1.604	1.628	1.561	1.605	1.518	1.660	1.668	1.687
Cr	0.771	0.482	0.433	0.527	0.359	0.362	0.378	0.443	0.355	0.334	0.346	0.307
Fe	0.364	0.417	0.373	0.395	0.408	0.474	0.372	0.408	0.356	0.380	0.385	0.407
Mn	0.017	0.021	0.018	0.016	0.018	0.018	0.014	0.018	0.012	0.016	0.018	0.018
Mg	2.406	2.198	1.879	2.210	2.212	1.996	2.463	2.257	2.375	2.431	2.229	2.328
Ca	0.284	0.381	0.327	0.417	0.338	0.382	0.341	0.498	0.224	0.345	0.345	0.356
Na	N.D.	0.015	N.D.	0.003	0.017	0.016	N.D.	N.D	0.004	0.004	N.D.	0.013
sum	8.245	8.137	7.935	8.158	8.082	8.035	8.175	8.213	8.044	8.171	8.078	8.139
Mg-number	86.9	84.1	83.4	84.8	84.4	80.8	86.9	84.7	87.0	86.5	85.3	85.1

Table A.4.3: continued

	13-1 gt	13-2 gt	13-3 gt	M3	P034	P037	P045	P071	P081	P095	P097	P099
SiO_2	42.10	43.14	42.71	40.70	43.08	40.85	40.45	40.63	40.59	40.98	40.96	45.72
TiO_2	0.39	0.11	N.D.	0.82	N.D.	0.10	N.D.	0.07	N.D.	0.11	0.28	0.07
Al_2O_3	19.30	20.41	16.49	22.13	22.90	12.28	7.94	16.75	19.63	12.63	17.37	17.84
Cr_2O_3	5.47	4.69	9.36	0.08	2.37	15.17	20.14	8.60	4.55	14.70	7.31	2.59
FeO	6.82	6.15	6.68	15.11	4.85	4.27	6.22	7.14	11.99	4.15	8.74	5.92
MnO	0.33	0.29	0.33	0.28	0.21	0.19	0.30	0.29	0.50	0.14	0.35	0.24
MgO	20.64	22.33	19.14	7.91	23.86	22.43	22.10	19.11	17.02	22.79	18.92	25.00
CaO	4.47	3.38	5.79	13.87	3.78	3.31	1.90	6.60	5.28	3.16	5.49	2.62
Na_2O	0.08	N.D.	0.02	0.09	N.D.	N.D.	N.D.	N.D.	N.D.	N.D.	N.D.	0.09
Total	**99.64**	**100.50**	**100.55**	**100.99**	**101.05**	**98.60**	**99.05**	**99.19**	**99.56**	**98.66**	**99.42**	**100.09**
Oxy	12	12	12	12	12	12	12	12	12	12	12	12
Si	3.056	3.065	3.140	3.023	2.999	3.137	3.208	3.056	3.026	3.120	3.062	3.219
Ti	0.021	0.006	N.D.	0.046	N.D.	0.006	N.D.	0.004	N.D.	0.006	0.016	0.004
Al	1.658	1.716	1.434	1.945	1.879	1.112	0.742	1.485	1.725	1.149	1.531	1.481
Cr	0.336	0.282	0.582	0.005	0.282	0.274	0.413	0.449	0.748	0.266	0.546	0.349
Fe	0.414	0.366	0.411	0.938	0.012	0.012	0.020	0.018	0.032	0.013	0.022	0.014
Mn	0.019	0.017	0.020	0.017	2.476	2.567	2.612	2.142	1.891	2.596	2.108	2.623
Mg	2.233	2.364	2.097	0.876	0.282	0.272	0.161	0.532	0.422	0.262	0.440	0.198
Ca	0.348	0.257	0.456	1.103	0.000	0.000	0.000	0.000	0.000	0.000	0.000	0.012
Na	0.014	N.D.	0.003	0.013	N.D.	N.D.	N.D.	N.D.	N.D.	N.D.	N.D.	0.000
sum	8.101	8.072	8.144	7.965	8.018	7.994	7.999	8.027	8.022	8.004	8.013	7.995
Mg-number	84.4	86.6	83.6	48.3	89.8	90.3	86.4	82.7	71.7	90.7	79.4	88.3

Table A.4.3: continued

	P101	P102	P108	P131	P136	P137	P146	P147	P152	P155	P174
SiO_2	43.73	42.64	42.87	43.48	42.65	43.16	43.60	41.96	43.68	42.17	42.51
TiO_2	0.07	0.05	0.39	N.D.	N.D.	N.D.	N.D.	0.91	N.D.	0.07	0.07
Al_2O_3	20.86	21.23	18.42	21.06	18.55	20.69	21.22	18.89	20.63	16.69	18.52
Cr_2O_3	2.98	3.71	5.56	4.47	7.27	3.53	4.38	4.31	3.87	9.77	6.27
FeO	5.92	5.45	6.79	5.71	6.08	5.94	4.24	7.51	5.91	5.66	6.25
MnO	0.21	0.19	0.24	0.24	0.31	0.21	0.18	0.32	0.21	0.28	0.24
MgO	24.57	24.21	21.24	23.96	23.09	23.40	25.03	20.30	24.32	22.92	20.87
CaO	1.85	1.62	4.90	2.13	2.14	1.87	1.17	4.71	1.51	2.80	5.39
Na_2O	N.D.	N.D.	N.D.	N.D.	N.D.	N.D.	N.D.	0.18	N.D.	N.D.	N.D.
Total	**100.19**	**99.10**	**100.41**	**101.05**	**100.09**	**98.80**	**99.82**	**99.09**	**100.13**	**100.36**	**100.12**
Oxy	12	12	12	12	12	12	12	12	12	12	12
Si	3.077	3.039	3.098	3.057	3.085	3.088	3.070	3.068	3.085	3.089	3.089
Ti	0.004	0.003	0.021	N.D.	N.D.	N.D.	N.D.	0.050	N.D.	0.004	0.004
Al	1.730	1.784	1.569	1.745	1.582	1.745	1.761	1.628	1.718	1.441	1.586
Cr	0.348	0.325	0.410	0.336	0.368	0.355	0.250	0.459	0.349	0.347	0.380
Fe	0.013	0.011	0.015	0.014	0.019	0.013	0.011	0.020	0.013	0.017	0.015
Mn	2.577	2.572	2.287	2.510	2.489	2.495	2.626	2.212	2.560	2.502	2.260
Mg	0.139	0.124	0.379	0.160	0.166	0.143	0.088	0.369	0.114	0.220	0.420
Ca	0.000	0.000	0.000	0.000	0.000	0.000	0.000	0.026	0.000	0.000	0.000
Na	N.D.	N.D.	N.D.	N.D.	N.D.	N.D.	N.D.	0.000	N.D.	N.D.	N.D.
sum	7.999	7.997	7.991	7.988	7.986	7.973	7.968	7.998	7.984	7.998	7.994
Mg-number	88.1	88.8	84.8	88.2	87.1	87.5	91.3	82.8	88.0	87.8	85.6

Table A.4.4: Eclogitic garnet inclusion analyses

	M3
SiO_2	40.70
TiO_2	0.82
Al_2O_3	22.13
Cr_2O_3	0.08
FeO	15.11
MnO	0.28
MgO	7.91
CaO	13.87
Na_2O	0.09
Total	**100.99**

Oxy	12
Si	3.023
Ti	0.046
Al	1.945
Cr	0.005
Fe	0.938
Mn	0.017
Mg	0.876
Ca	1.103
Na	0.013
sum	7.965

Mg-number	48.3

Table A.4.5: Peridotitic clinopyroxene inclusion analyses

	10-1 cpx	10-2 cpx	10-3 cpx	10-4 cpx	10-5 cpx	10-5 cpxa	10-6 cpx	10-7 cpx	10-7 cpxa	10-8 cpx	10-10 cpx	10-11 cpx
SiO_2	57.14	55.06	55.24	57.29	56.92	56.71	55.96	57.49	57.08	56.68	57.28	57.34
TiO_2	0.11	N.D.	0.07	0.14	0.35	0.36	0.07	0.09	0.11	0.08	1.10	N.D.
Al_2O_3	2.39	0.93	1.56	2.05	2.85	3.40	1.72	2.06	2.45	1.55	3.27	1.33
Cr_2O_3	2.19	0.58	1.97	2.36	1.95	2.06	1.79	1.86	1.85	2.50	1.81	0.93
FeO	3.05	3.27	3.45	2.52	3.20	3.50	2.95	2.73	2.67	2.15	3.47	2.62
MnO	0.12	0.10	0.10	0.09	0.12	0.13	0.13	0.14	0.09	0.07	0.08	0.08
MgO	16.70	20.77	20.95	16.77	16.79	16.26	18.67	17.95	17.09	17.56	16.02	18.07
CaO	16.07	18.02	15.74	17.47	14.85	14.73	17.25	16.28	16.64	16.78	13.69	19.48
Na_2O	2.14	0.42	1.45	2.08	2.70	2.95	2.04	2.14	2.14	1.73	3.49	0.90
K_2O	0.04	0.05	0.04	0.07	0.06	0.07	0.05	0.05	0.04	0.06	N.D.	0.06
Total	**99.97**	**99.23**	**100.68**	**100.84**	**99.77**	**100.16**	**100.68**	**100.82**	**100.20**	**99.15**	**100.21**	**100.80**
Oxy	6	6	6	6	6	6	6	6	6	6	6	6
Si	2.048	1.993	1.979	2.041	2.040	2.029	2.005	2.041	2.039	2.048	2.040	2.038
Ti	0.003	N.D.	0.002	0.004	0.009	0.010	0.002	0.002	0.003	0.002	0.029	N.D.
Al	0.102	0.040	0.066	0.087	0.121	0.144	0.073	0.087	0.103	0.066	0.138	0.056
Cr	0.066	0.018	0.060	0.071	0.059	0.062	0.054	0.056	0.056	0.076	0.055	0.028
Fe	0.091	0.099	0.103	0.075	0.096	0.105	0.088	0.081	0.080	0.065	0.103	0.078
Mn	0.003	0.003	0.003	0.003	0.004	0.004	0.004	0.004	0.002	0.002	0.002	0.002
Mg	0.892	1.121	1.118	0.891	0.897	0.867	0.997	0.949	0.910	0.946	0.850	0.957
Ca	0.617	0.699	0.604	0.667	0.570	0.565	0.662	0.619	0.637	0.650	0.522	0.742
Na	0.148	0.029	0.101	0.143	0.188	0.205	0.142	0.148	0.148	0.121	0.241	0.062
K	0.002	0.002	0.002	0.003	0.003	0.003	0.002	0.002	0.002	0.003	N.D.	0.003
sum	3.973	4.003	4.038	3.985	3.986	3.993	4.029	3.989	3.981	3.979	3.982	3.966
CaTs	-0.051	0.007	0.019	-0.045	-0.049	-0.039	-0.007	-0.043	-0.042	-0.050	-0.070	-0.038
Jad	0.270	0.043	0.087	0.248	0.278	0.284	0.140	0.228	0.244	0.243	0.332	0.160
Acm	-0.120	-0.011	0.016	-0.101	-0.088	-0.077	0.004	-0.079	-0.094	-0.119	-0.091	-0.095
Wo	0.334	0.346	0.292	0.356	0.310	0.302	0.334	0.331	0.340	0.350	0.296	0.390
En	0.446	0.560	0.559	0.445	0.448	0.434	0.498	0.475	0.455	0.473	0.425	0.479
Fs	0.046	0.050	0.052	0.037	0.048	0.052	0.044	0.040	0.040	0.032	0.052	0.039
Mg number	90.7	91.9	91.5	92.2	90.3	89.2	91.9	92.1	91.9	93.6	89.2	92.5

Table A.4.5: continued

	10-12 cpx	10-13 cpx	10-14 cpx	10-15 cpx	10-16 cpx	10-17 cpx	10-18 cpxa	10-18 cpx	10-19 cpx	10-19 cpxb	10-19 cpxa	10-20 cpx
SiO_2	54.93	56.40	56.89	55.38	55.84	56.77	56.35	56.92	55.29	57.26	56.58	55.77
TiO_2	0.09	N.D.	N.D.	0.07	N.D.	0.22	0.06	0.04	0.12	0.12	0.13	0.11
Al_2O_3	1.73	0.69	0.63	3.10	1.08	2.43	2.46	2.19	5.71	5.94	6.69	2.09
Cr_2O_3	2.50	1.24	1.23	2.54	0.57	2.87	2.21	2.15	2.08	2.01	2.04	1.93
FeO	2.64	2.27	2.46	2.38	3.57	2.87	2.79	2.71	2.65	2.70	2.83	2.64
MnO	0.13	0.09	0.11	0.07	0.15	0.11	0.11	0.11	0.11	0.12	0.08	0.09
MgO	18.41	19.21	19.12	16.51	22.51	16.99	17.95	17.98	15.48	15.14	13.98	18.56
CaO	17.18	19.72	19.52	17.07	16.35	15.61	16.58	16.14	13.56	12.30	12.50	16.81
Na_2O	2.09	0.73	0.67	2.69	0.40	2.74	2.31	2.11	4.04	4.75	4.52	2.15
K_2O	N.D.	N.D.	0.05	N.D.	0.03	0.03	0.04	0.04	0.07	0.07	N.D.	0.04
Total	**99.81**	**100.55**	**100.80**	**99.97**	**100.57**	**100.68**	**100.88**	**100.40**	**99.11**	**100.41**	**99.42**	**100.24**
Oxy	6	6	6	6	6	6	6	6	6	6	6	6
Si	1.993	2.020	2.029	2.001	1.986	2.030	2.010	2.032	1.992	2.025	2.021	2.002
Ti	0.002	N.D.	N.D.	0.002	N.D.	0.006	0.002	0.001	0.003	0.003	0.004	0.003
Al	0.074	0.029	0.027	0.133	0.045	0.103	0.104	0.092	0.243	0.249	0.283	0.089
Cr	0.077	0.038	0.037	0.078	0.017	0.087	0.067	0.065	0.063	0.060	0.062	0.059
Fe	0.080	0.068	0.073	0.072	0.106	0.086	0.083	0.081	0.080	0.080	0.085	0.079
Mn	0.004	0.003	0.003	0.002	0.004	0.003	0.003	0.003	0.003	0.003	0.002	0.002
Mg	0.996	1.026	1.016	0.889	1.193	0.905	0.954	0.956	0.831	0.798	0.744	0.993
Ca	0.668	0.757	0.746	0.661	0.623	0.598	0.634	0.617	0.523	0.466	0.478	0.647
Na	0.147	0.051	0.046	0.188	0.028	0.190	0.160	0.146	0.282	0.326	0.313	0.150
K	N.D.	N.D.	0.002	N.D.	0.001	0.001	0.002	0.002	0.003	0.003	N.D.	0.002
sum	4.041	3.991	3.981	4.025	4.005	4.009	4.017	3.995	4.026	4.012	3.991	4.026
CaTs	0.005	-0.020	-0.030	-0.003	0.013	-0.035	-0.012	-0.033	0.004	-0.028	-0.024	-0.005
Jad	0.142	0.107	0.124	0.216	0.036	0.260	0.193	0.222	0.298	0.364	0.393	0.158
Acm	0.005	-0.056	-0.075	-0.027	-0.007	-0.069	-0.032	-0.075	-0.012	-0.036	-0.080	-0.006
Wo	0.332	0.388	0.388	0.332	0.305	0.317	0.323	0.325	0.260	0.247	0.251	0.326
En	0.498	0.513	0.508	0.445	0.597	0.453	0.477	0.478	0.416	0.399	0.372	0.496
Fs	0.040	0.034	0.037	0.036	0.053	0.043	0.042	0.040	0.040	0.040	0.042	0.040
Mg number	92.6	93.8	93.3	92.5	91.8	91.3	92.0	92.2	91.2	90.9	89.8	92.6

Table A.4.5: continued

	11-4 cpx	11-4 cpxa	11-5 cpx	11-6 cpx	11-8 cpx	11-8 cpxa	11-9 cpx	11-10 cpx	7-1 cpx	7-2 cpx	7-2 cpxa	7-3 cpx
SiO_2	54.03	55.42	56.12	56.20	55.06	55.97	56.91	56.44	55.07	60.61	56.32	56.67
TiO_2	0.13	0.23	0.06	0.07	0.11	0.11	0.91	0.07	0.82	0.03	0.04	0.28
Al_2O_3	1.47	2.95	1.42	1.38	2.24	2.23	4.50	1.92	4.08	1.78	1.71	2.89
Cr_2O_3	1.48	2.22	2.07	1.50	2.17	2.26	2.29	1.54	2.57	1.90	1.92	2.32
FeO	2.32	2.54	2.62	3.06	2.39	2.36	2.84	3.31	2.63	1.84	2.16	2.52
MnO	0.08	0.09	0.11	0.12	0.08	0.08	0.11	0.10	0.12	0.10	N.D.	0.08
MgO	19.07	15.94	18.13	18.79	17.97	17.72	14.34	18.87	15.11	13.99	16.21	15.94
CaO	19.50	17.23	17.24	17.92	17.55	17.17	14.20	15.76	14.65	19.01	19.09	17.09
Na_2O	1.14	2.46	1.53	1.45	2.30	2.34	3.74	1.91	3.94	1.17	1.31	2.58
K_2O	0.04	0.05	N.D.	0.09	0.05	N.D.	0.03	0.03	0.03	0.03	0.08	0.02
Total	**99.57**	**99.13**	**99.35**	**100.60**	**100.01**	**100.37**	**99.87**	**99.96**	**99.03**	**100.75**	**99.16**	**100.42**
Oxy	6	6	6	6	6	6	6	6	6	6	6	6
Si	1.970	2.014	2.030	2.013	1.990	2.010	2.035	2.022	2.001	2.139	2.046	2.029
Ti	0.003	0.006	0.002	0.002	0.003	0.003	0.024	0.002	0.022	0.001	0.001	0.008
Al	0.063	0.127	0.061	0.059	0.096	0.095	0.191	0.082	0.175	0.074	0.074	0.122
Cr	0.046	0.068	0.063	0.045	0.066	0.069	0.069	0.047	0.079	0.057	0.059	0.070
Fe	0.071	0.077	0.079	0.092	0.072	0.071	0.085	0.099	0.080	0.054	0.066	0.075
Mn	0.002	0.003	0.003	0.004	0.002	0.002	0.003	0.003	0.004	0.003	N.D.	0.002
Mg	1.036	0.863	0.978	1.003	0.968	0.948	0.764	1.008	0.818	0.736	0.878	0.850
Ca	0.762	0.671	0.668	0.687	0.680	0.661	0.544	0.605	0.570	0.719	0.743	0.656
Na	0.081	0.173	0.107	0.101	0.161	0.163	0.259	0.133	0.278	0.080	0.093	0.179
K	0.002	0.002	N.D.	0.004	0.002	N.D.	0.001	0.001	0.001	0.001	0.004	0.001
sum	4.036	4.005	3.991	4.009	4.041	4.021	3.976	4.002	4.029	3.864	3.964	3.992
CaTs	0.027	-0.020	-0.032	-0.015	0.007	-0.013	-0.059	-0.024	-0.023	-0.140	-0.047	-0.036
Jad	0.056	0.235	0.188	0.133	0.148	0.189	0.378	0.177	0.301	0.410	0.227	0.265
Acm	0.027	-0.059	-0.081	-0.028	0.015	-0.026	-0.118	-0.043	-0.022	-0.329	-0.131	-0.086
Wo	0.368	0.345	0.350	0.351	0.336	0.337	0.302	0.315	0.297	0.429	0.395	0.346
En	0.518	0.431	0.489	0.501	0.484	0.474	0.382	0.504	0.409	0.368	0.439	0.425
Fs	0.035	0.039	0.040	0.046	0.036	0.035	0.042	0.050	0.040	0.027	0.033	0.038
Mg number	93.6	91.8	92.5	91.6	93.1	93.1	90.0	91.0	91.1	93.1	93.0	91.9

Table A.4.5: continued

	7-4 cpx	7-5 cpx	7-7 cpx	7-7 cpxa	7-8 cpx	7-8 cpxa	7-9 cpx	7-10 cpx	7-11 cpx	7-12 cpx	7-13 cpx	7-14 cpx
SiO_2	55.38	55.99	56.12	55.97	55.74	56.10	61.62	56.80	54.77	54.98	53.31	54.31
TiO_2	N.D.	0.06	0.53	0.49	0.05	0.07	0.13	0.10	0.15	0.04	0.67	0.98
Al_2O_3	1.01	1.31	4.02	4.15	1.97	3.51	3.67	2.39	2.28	1.09	6.94	4.25
Cr_2O_3	1.93	1.67	2.79	3.11	2.86	2.91	2.97	2.05	2.62	1.41	0.09	2.24
FeO	3.52	3.35	2.51	2.49	2.11	2.40	2.02	2.93	2.82	2.85	8.04	3.18
MnO	0.10	0.12	0.15	0.09	0.12	0.10	0.09	0.13	0.13	0.15	0.09	0.07
MgO	19.92	19.40	15.29	14.27	17.05	15.46	12.28	18.09	17.31	19.59	11.98	15.33
CaO	16.07	17.10	14.94	15.63	17.08	15.61	15.40	15.76	16.23	19.18	14.18	13.84
Na_2O	0.95	0.91	3.95	3.60	2.19	3.04	2.50	2.12	2.93	1.47	4.34	5.15
K_2O	0.07	0.07	0.03	0.02	0.08	0.04	N.D.	N.D.	0.04	0.04	0.07	N.D.
Total	**99.05**	**100.06**	**100.39**	**99.89**	**99.33**	**99.32**	**100.77**	**100.40**	**99.30**	**100.88**	**99.82**	**99.41**
Oxy	6	6	6	6	6	6	6	6	6	6	6	6
Si	2.012	2.013	2.012	2.019	2.024	2.030	2.156	2.026	1.997	1.977	1.949	1.976
Ti	N.D.	0.002	0.014	0.013	0.001	0.002	0.004	0.003	0.004	0.001	0.018	0.027
Al	0.044	0.056	0.171	0.177	0.085	0.150	0.152	0.101	0.099	0.046	0.300	0.183
Cr	0.059	0.051	0.085	0.095	0.088	0.089	0.088	0.062	0.081	0.043	0.003	0.069
Fe	0.107	0.101	0.075	0.075	0.064	0.073	0.059	0.087	0.086	0.086	0.246	0.097
Mn	0.003	0.004	0.004	0.003	0.004	0.003	0.002	0.004	0.004	0.004	0.003	0.002
Mg	1.079	1.040	0.817	0.767	0.923	0.834	0.641	0.962	0.941	1.050	0.653	0.831
Ca	0.626	0.659	0.574	0.604	0.664	0.605	0.578	0.603	0.634	0.739	0.555	0.539
Na	0.067	0.064	0.275	0.251	0.154	0.213	0.169	0.147	0.207	0.102	0.308	0.364
K	0.003	0.003	0.001	0.001	0.004	0.002	N.D.	N.D.	0.002	0.002	0.003	N.D.
sum	4.000	3.991	4.027	4.005	4.011	4.001	3.849	3.994	4.054	4.051	4.038	4.087
CaTs	-0.013	-0.015	-0.026	-0.032	-0.026	-0.032	-0.160	-0.029	-0.001	0.022	0.033	-0.003
Jad	0.129	0.136	0.307	0.336	0.224	0.303	0.559	0.221	0.182	0.046	0.238	0.258
Acm	-0.059	-0.069	-0.031	-0.084	-0.066	-0.088	-0.390	-0.074	0.027	0.059	0.073	0.106
Wo	0.319	0.337	0.300	0.318	0.345	0.318	0.369	0.316	0.318	0.359	0.261	0.271
En	0.539	0.520	0.408	0.383	0.461	0.417	0.320	0.481	0.470	0.525	0.326	0.416
Fs	0.054	0.050	0.038	0.038	0.032	0.036	0.030	0.044	0.043	0.043	0.123	0.048
Mg number	91.0	91.2	91.6	91.1	93.5	92.0	91.5	91.7	91.6	92.5	72.6	89.6

Table A.4.5: continued

	7-15 cpx	7-16 cpx	7-16 cpxa	7-17 cpx	7-18 cpx	7-18 cpxa	7-19 cpx	7-20 cpx	7-20 cpxa	8-1 cpx	8-1 cpxa	8-3 cpx
SiO_2	59.64	56.11	55.47	56.34	55.69	56.60	55.95	56.04	56.52	55.84	56.60	54.09
TiO_2	N.D.	0.43	0.45	N.D.	0.18	0.21	0.06	0.46	N.D.	0.08	0.09	0.07
Al_2O_3	1.21	2.39	2.76	1.07	2.47	3.05	1.35	4.05	0.82	2.40	2.66	1.42
Cr_2O_3	1.46	2.44	2.51	1.12	2.00	1.80	2.11	2.53	1.36	2.05	2.11	2.23
FeO	2.18	2.53	2.72	2.89	3.06	3.17	3.21	2.62	2.13	2.73	2.77	2.19
MnO	0.10	0.11	0.10	0.11	0.14	0.14	0.12	0.14	0.06	0.14	0.11	0.09
MgO	15.96	16.06	17.14	20.76	17.40	16.57	19.70	15.54	17.79	17.92	16.79	16.79
CaO	19.12	16.39	16.67	16.42	16.15	15.31	16.03	14.72	20.95	16.18	16.25	18.06
Na_2O	1.02	2.56	3.05	0.79	2.45	2.30	1.29	3.81	1.00	2.42	2.29	1.71
K_2O	N.D.	N.D.	N.D.	N.D.	N.D.	N.D.	N.D.	N.D.	0.06	N.D.	N.D.	N.D.
Total	**100.78**	**99.08**	**100.92**	**99.58**	**99.60**	**99.17**	**99.97**	**99.99**	**100.99**	**99.79**	**99.71**	**99.03**
Oxy	6	6	6	6	6	6	6	6	6	6	6	6
Si	2.107	2.036	1.989	2.020	2.013	2.039	2.013	2.013	2.025	2.011	2.035	2.020
Ti	N.D.	0.012	0.012	N.D.	0.005	0.006	0.002	0.012	N.D.	0.002	0.002	0.002
Al	0.050	0.103	0.117	0.046	0.106	0.130	0.057	0.172	0.035	0.102	0.113	0.063
Cr	0.044	0.075	0.076	0.034	0.061	0.055	0.064	0.077	0.041	0.063	0.064	0.071
Fe	0.064	0.077	0.082	0.087	0.093	0.095	0.097	0.079	0.064	0.082	0.083	0.068
Mn	0.003	0.003	0.003	0.003	0.004	0.004	0.004	0.004	0.002	0.004	0.003	0.003
Mg	0.840	0.868	0.916	1.109	0.937	0.890	1.057	0.832	0.950	0.962	0.900	0.935
Ca	0.724	0.637	0.640	0.631	0.626	0.591	0.618	0.567	0.804	0.624	0.626	0.723
Na	0.070	0.180	0.212	0.055	0.171	0.161	0.090	0.265	0.070	0.169	0.160	0.124
K	N.D.	N.D.	N.D.	N.D.	N.D.	N.D.	N.D.	N.D.	0.003	N.D.	N.D.	N.D.
sum	3.903	3.991	4.047	3.985	4.015	3.971	4.002	4.021	3.994	4.020	3.986	4.008
CaTs	-0.107	-0.048	-0.001	-0.020	-0.018	-0.045	-0.015	-0.025	-0.025	-0.014	-0.037	-0.022
Jad	0.309	0.273	0.195	0.120	0.202	0.274	0.151	0.300	0.126	0.192	0.252	0.178
Acm	-0.238	-0.092	0.017	-0.065	-0.031	-0.113	-0.061	-0.035	-0.054	-0.023	-0.092	-0.054
Wo	0.416	0.343	0.321	0.326	0.322	0.318	0.317	0.296	0.415	0.319	0.331	0.373
En	0.420	0.434	0.458	0.555	0.469	0.445	0.528	0.416	0.475	0.481	0.450	0.468
Fs	0.032	0.038	0.041	0.043	0.046	0.048	0.048	0.039	0.032	0.041	0.042	0.034
Mg number	92.9	91.9	91.8	92.8	91.0	90.3	91.6	91.4	93.7	92.1	91.5	93.2

Table A.4.5: continued

	8-4 cpx	8-4 cpxa	8-5 cpx	8-5 cpxa	8-6 cpx	8-7 cpx	8-8 cpx+opx	8-9 cpx	8-10 cpx
SiO_2	58.88	56.59	56.13	55.97	55.40	58.75	56.94	55.44	56.98
TiO_2	0.04	N.D.	0.04	N.D.	0.30	N.D.	0.08	0.20	0.26
Al_2O_3	1.32	1.48	1.26	1.33	3.18	1.39	1.38	2.52	2.53
Cr_2O_3	0.98	1.07	0.88	0.90	1.89	1.31	1.70	2.05	1.35
FeO	2.60	3.31	3.45	3.65	2.51	1.72	3.20	2.52	2.96
MnO	0.10	0.12	0.13	0.13	0.10	0.07	0.10	0.11	0.07
MgO	18.01	19.08	22.02	21.56	16.18	15.21	16.11	17.14	17.58
CaO	17.89	16.82	15.47	15.87	17.07	20.40	18.78	17.18	15.70
Na_2O	0.86	1.02	0.83	0.71	2.89	0.90	1.67	2.59	2.25
K_2O	N.D.	N.D.	N.D.	N.D.	N.D.	0.06	0.05	N.D.	0.03
Total	**100.74**	**99.55**	**100.30**	**100.19**	**99.54**	**100.10**	**100.12**	**99.81**	**99.70**
Oxy	6	6	6	6	6	6	6	6	6
Si	2.077	2.033	1.999	1.998	2.004	2.098	2.053	2.003	2.038
Ti	0.001	N.D.	0.001	N.D.	0.008	N.D.	0.002	0.005	0.007
Al	0.055	0.063	0.053	0.056	0.136	0.059	0.059	0.108	0.107
Cr	0.029	0.033	0.027	0.027	0.058	0.040	0.052	0.063	0.041
Fe	0.077	0.099	0.103	0.109	0.076	0.051	0.097	0.076	0.088
Mn	0.003	0.003	0.004	0.004	0.003	0.002	0.003	0.003	0.002
Mg	0.947	1.021	1.169	1.147	0.872	0.809	0.865	0.923	0.937
Ca	0.676	0.647	0.590	0.607	0.662	0.781	0.726	0.665	0.602
Na	0.059	0.071	0.057	0.049	0.203	0.062	0.117	0.181	0.156
K	N.D.	N.D.	N.D.	N.D.	N.D.	0.003	0.002	N.D.	0.002
sum	3.924	3.971	4.002	3.998	4.021	3.905	3.975	4.028	3.980
CaTs	-0.078	-0.033	0.000	0.001	-0.012	-0.098	-0.055	-0.008	-0.045
Jad	0.240	0.162	0.079	0.081	0.218	0.295	0.221	0.188	0.238
Acm	-0.182	-0.091	-0.022	-0.032	-0.015	-0.229	-0.101	-0.006	-0.081
Wo	0.377	0.340	0.295	0.303	0.337	0.439	0.390	0.337	0.324
En	0.473	0.511	0.584	0.574	0.436	0.405	0.433	0.461	0.469
Fs	0.038	0.050	0.051	0.054	0.038	0.026	0.048	0.038	0.044
Mg number	92.5	91.1	91.9	91.3	92.0	94.0	90.0	92.4	91.4

Table A.4.6: Eclogitic clinopyroxene inclusion analyses

	M3 cpx	M4 cpx	M5 cpx
SiO_2	54.74	55.01	55.70
TiO_2	0.21	0.50	0.12
Al_2O_3	4.30	7.91	2.38
Cr_2O_3	N.D.	0.06	1.83
FeO	6.59	7.46	2.28
MnO	0.07	0.09	0.08
MgO	13.02	11.80	16.31
CaO	19.86	13.93	18.21
Na_2O	1.86	3.77	2.13
K_2O	N.D.	N.D.	N.D.
Total	**100.68**	**100.62**	**99.11**
Oxy	6	6	6
Si	1.985	1.972	2.023
Ti	0.006	0.013	0.003
Al	0.184	0.336	0.102
Cr	N.D.	0.002	0.056
Fe	0.200	0.224	0.069
Mn	0.002	0.003	0.002
Mg	0.703	0.630	0.883
Ca	0.771	0.535	0.709
Na	0.130	0.262	0.150
K	N.D.	N.D.	N.D.
sum	3.983	3.978	3.998
CaTs	0.010	0.014	-0.026
Jad	0.166	0.309	0.211
Acm	-0.035	-0.047	-0.061
Wo	0.381	0.261	0.367
En	0.352	0.315	0.441
Fs	0.100	0.112	0.035
Mg number	77.9	73.8	92.7

Table A.4.7: Olivine inclusion analyses

	10-2 ol	10-3 ol	10-13 ol	10-13 ola	10-13 olb	11-2 ol	5-11 ol	5-12 ol	5-14 ol	7-1 ol	7-11 ol	7-11 ola	8-8 ol	8-8 ola
SiO_2	42.41	41.05	40.91	41.83	43.30	43.01	41.70	43.41	41.11	42.77	41.53	43.61	40.94	43.81
TiO_2	N.D.	N.D.	N.D.	N.D.	N.D.	N.D.	N.D.	N.D.	N.D.	N.D.	N.D.	N.D.	N.D.	N.D.
Al_2O_3	N.D.	N.D.	N.D.	N.D.	N.D.	N.D.	N.D.	0.05	N.D.	N.D.	N.D.	N.D.	N.D.	N.D.
Cr_2O_3	0.08	0.12	N.D.	0.01	0.04	0.04	0.05	0.09	0.06	N.D.	0.06	0.06	0.05	0.08
FeO	8.37	8.77	7.30	7.61	7.60	7.20	6.53	8.12	8.41	6.82	7.61	7.22	8.75	8.42
MnO	0.13	0.09	0.10	0.08	0.11	0.10	0.10	0.12	0.12	0.10	0.09	0.12	0.13	0.14
MgO	48.85	49.92	50.61	50.72	49.36	48.26	50.79	47.94	50.61	49.81	50.60	49.16	50.26	47.45
CaO	0.10	0.08	0.03	0.02	0.04	0.07	0.02	0.11	0.09	0.01	0.03	0.08	0.05	0.12
NiO	0.48	0.48	0.50	0.48	0.43	0.49	0.43	0.41	0.41	0.46	0.43	0.49	0.47	0.61
Total	**100.47**	**100.52**	**99.51**	**100.76**	**100.89**	**99.19**	**99.64**	**100.25**	**100.83**	**100.01**	**100.38**	**100.78**	**100.66**	**100.68**
Oxy	4	4	4	4	4	4	4	4	4	4	4	4	4	4
Si	1.025	0.998	0.998	1.007	1.036	1.045	1.010	1.047	0.995	1.030	1.004	1.043	0.994	1.053
Ti	N.D.	N.D.	N.D.	N.D.	N.D.	N.D.	N.D.	N.D.	N.D.	N.D.	N.D.	N.D.	N.D.	N.D.
Al	N.D.	N.D.	N.D.	N.D.	N.D.	N.D.	N.D.	0.001	N.D.	N.D.	N.D.	N.D.	N.D.	N.D.
Cr	0.002	0.002	N.D.	0.000	0.001	0.001	0.001	0.002	0.001	N.D.	0.001	0.001	0.001	0.002
Fe	0.169	0.178	0.149	0.153	0.152	0.146	0.132	0.164	0.170	0.137	0.154	0.144	0.178	0.169
Mn	0.003	0.002	0.002	0.002	0.002	0.002	0.002	0.002	0.002	0.002	0.002	0.002	0.003	0.003
Mg	1.760	1.808	1.840	1.820	1.761	1.747	1.833	1.723	1.825	1.788	1.823	1.752	1.818	1.700
Ca	0.003	0.002	0.001	0.001	0.001	0.002	0.001	0.003	0.002	0.000	0.001	0.002	0.001	0.003
Ni	0.023	0.023	0.024	0.022	0.020	0.023	0.020	0.019	0.019	0.021	0.020	0.023	0.022	0.028
sum	2.986	3.013	3.014	3.004	2.973	2.967	3.000	2.962	3.015	2.980	3.006	2.968	3.017	2.960

Table A.4.8: Orthopyroxene inclusion analyses

	10-11 opx	10-11 opxa	5-8 opx	5-15 opx	5-15 opxa
SiO_2	58.88	59.89	57.94	59.29	56.12
TiO_2	N.D	N.D	N.D	N.D	N.D
Al_2O_3	0.46	0.32	0.84	0.86	1.02
Cr_2O_3	0.16	0.13	0.33	0.33	0.43
FeO	4.59	4.32	4.60	4.48	5.03
MnO	0.09	0.11	0.12	0.09	0.11
MgO	34.81	34.39	34.30	34.22	35.39
CaO	1.09	1.07	1.20	1.05	1.10
Na_2O	0.15	N.D	0.09	N.D.	0.06
Total	**100.22**	**100.21**	**99.42**	**100.32**	**99.28**
Oxy	6	6	6	6	6
Si	2.009	2.035	1.997	2.017	1.950
Ti	N.D.	N.D.	N.D.	N.D.	N.D.
Al	0.018	0.013	0.034	0.035	0.042
Cr	0.005	0.004	0.010	0.010	0.013
Fe	0.131	0.123	0.133	0.127	0.146
Mn	0.003	0.003	0.003	0.002	0.003
Mg	1.771	1.742	1.762	1.735	1.832
Ca	0.040	0.039	0.044	0.038	0.041
Na	0.010	N.D.	0.006	N.D.	0.004
sum	3.986	3.958	3.989	3.965	4.032
CaTs	-0.01	-0.04	0.00	-0.02	0.05
Jad	0.04	0.09	0.04	0.08	-0.05
Acm	-0.03	-0.09	-0.03	-0.08	0.05
Wo	0.02	0.04	0.02	0.03	0.00
En	0.89	0.87	0.88	0.87	0.92
Fs	0.07	0.06	0.07	0.06	0.07
Mg number	93.1	93.4	93.0	93.2	92.6

APPENDIX 5

LA ICP-MS METHODOLOGY FOR CULLINAN MINE DIAMONDS

The analyses were performed at the University of Cape Town using a Perkin Elmer Elan 6000 ICP-MS (inductively coupled plasma – mass spectrometer) instrument coupled to a Cetac LSX-200 laser ablation module that uses a 266nm frequency quadrupled Nd-YAG laser. A typical analysis consisted of three replicates of 100 readings each. Each replicate represented one sweep of the mass range. The counting time for one sample was typically 90 - 120 s. Every hour the argon carrier gas was analysed to establish a background. The NIST 610 and 612 glass standards were used to calibrate relative element sensitivities for the analysis of the silicate minerals. In-house standards were used for the oxide phases (ROM33, MON34 and JJG1424). The following elements were analysed: Ni, La, Ce, Nd, Sm, Eu, Gd, Dy, Er and Yb. All analyses have been normalized to the C1-chondrite composition (after Sun and Mc Donough, 1989). The preferred values for the standards are presented in Figure A.5.1 and Table A5.1. The results of the garnet peridotitic analyses are presented in Table A.5.2.

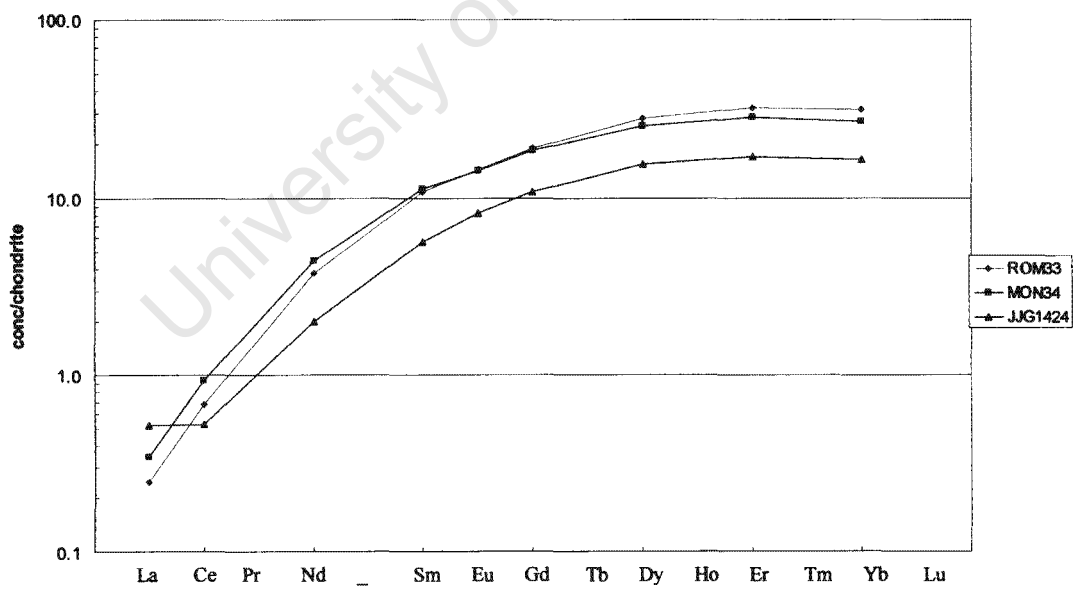

Figure A.5.1 A REE plot of the preferred values for the standards normalized to C1-chondrite.

Table A.5.1: Preferred values (ppm), relative standard deviations (%RSD) and normalised values for the standards used.

	ROM33			MON34			JJG1424		
	Ave ppm	%RSD	normalised	Ave ppm	%RSD	normalised	Ave ppm	%RSD	normalised
Ni	49.450	2.039		121.000	1.509		15.875	4.724	
La	0.058	1.562	0.246	0.081	4.394	0.342	0.122	3.902	0.515
Ce	0.418	2.293	0.682	0.575	2.245	0.940	0.320	2.552	0.523
Nd	1.763	0.851	3.774	2.080	1.039	4.454	0.938	3.185	2.007
Sm	1.653	2.723	10.801	1.735	2.376	11.340	0.870	2.968	5.686
Eu	0.838	2.462	14.440	0.828	3.178	14.267	0.480	1.701	8.276
Gd	3.910	2.968	19.027	3.790	2.914	18.443	2.220	2.728	10.803
Dy	7.083	2.607	27.884	6.415	3.016	25.256	3.948	2.553	15.541
Er	5.340	2.461	32.266	4.698	2.282	28.384	2.823	2.427	17.054
Yb	5.273	2.027	31.015	4.543	2.241	26.721	2.798	3.135	16.456

Table A5.2: giving REE (in ppm) with supplementry information on paragenesis, REE group, Cr-number, temperature (using Canil, 1999) and Ni (ppm) for the garnet inclusions.
Errors given are 1 standard deviation.

REE	10-4gt	10-4gt sp2	10-6gt sp2	10-8gt	10-11gt sp2	10-16gt	10-18gt sp2	11-5gt	11-5gt sp2
spot size (micron)	50	50	50	50	50	50	50	50	100
La	0.07	0.07	0.29	0.46	1.54	3.36	2.53	-0.11	0.07
Ce	1.19	1.32	0.70	1.09	2.95	7.19	4.69	0.41	0.52
Nd	1.93	2.42	1.33	1.40	2.05	4.08	2.44	1.42	1.38
Sm	1.05	0.90	0.36	1.05	0.72	1.58	0.73	0.54	0.78
Eu	0.31	0.49	0.33	0.55	0.43	0.33	0.30	0.34	0.32
Gd	1.26	1.30	0.85	1.50	0.81	1.05	0.70	1.38	1.10
Dy	1.34	1.71	1.02	2.56	0.85	1.34	0.43	1.27	1.24
Er	0.91	0.88	0.47	1.74	0.61	0.91	0.52	0.48	0.53
Yb	1.42	1.35	0.89	1.81	0.57	0.61	0.41	0.77	0.48
paragenesis	lherz	lherz	lherz	lherz	lherz	lherz	lherz	lherz	lherz
REE group	2	2	2	2	3	3	3	2	2
Cr-number	21.7	21.7	19.6	8.9	12.1	14.1	16.1	19.2	19.2
Ni	106.8	113.1	123.6	55.0	407.0	3.4	4.0	89.7	78.0
Temperature	1231	1246	1270	1077	n.d	1392	n.d	1188	1154

1 sd error	10-4gt	10-4gt sp2	10-6gt sp2	10-8gt	10-11gt sp2	10-16gt	10-18gt sp2	11-5gt	11-5gt sp2
La	0.0	0.1	0.2	0.5	0.3	0.0	0.2	0.1	0.0
Ce	0.1	0.1	0.1	1.2	0.3	0.3	0.4	0.2	0.1
Nd	0.3	0.7	0.3	0.7	0.3	0.5	0.2	0.5	0.4
Sm	0.2	0.2	0.4	0.4	0.5	0.3	0.3	0.4	0.2
Eu	0.1	0.1	0.1	0.2	0.2	0.2	0.2	0.3	0.1
Gd	0.6	0.4	0.4	0.2	0.4	0.5	0.4	0.7	0.4
Dy	0.6	0.5	0.5	0.8	0.7	0.6	0.1	1.0	0.4
Er	0.2	0.4	0.1	0.4	0.5	0.6	0.2	0.5	0.2
Yb	0.2	0.2	0.2	0.7	0.7	0.4	0.2	0.4	0.1
Ni	8.0	2.7	6.2	15.9	17.1	1.8	2.8	4.3	8.1

Table A5.2 continued

REE	12-2gt sp2	13-1gt sp2	13-2gt	13-2gt sp2	5-3gta sp2	5-4gt	5-9gt	5-9gta sp2	5-14gt
spot size (micron)	50	50	50	50	100	100	50	50	100
La	1.93	0.11	0.04	0.03	0.12	0.05	0.03	1.06	2.80
Ce	3.60	0.28	0.74	0.22	1.32	0.37	0.94	2.63	5.41
Nd	1.49	1.05	0.75	0.64	1.69	0.43	0.94	1.83	2.68
Sm	0.30	0.69	0.43	0.37	0.58	0.33	0.33	0.94	0.53
Eu	0.15	0.49	0.18	0.10	0.22	0.14	-0.02	0.58	0.06
Gd	0.52	1.06	0.38	0.35	0.50	0.51	0.54	1.12	0.38
Dy	0.46	1.80	0.38	0.29	0.63	0.83	0.52	1.37	0.37
Er	0.20	1.03	0.22	0.17	0.46	0.56	0.32	1.02	0.16
Yb	0.44	1.49	0.19	0.18	0.78	0.62	0.25	1.31	0.38
paragenesis	harz	harz	harz	harz	harz	lherz	lherz	lherz	lherz
REE group	3	2	1	1	1	2	2	2	3
Cr-number	15.4	16.8	14.1	14.1	29.2	22.1	29.2	29.2	16.7
Ni	4.8	104.6	86.1	80.3	157.5	140.9	107.9	66.1	1.4
Temperature	1165	1226	1161	1161	1339	1306	1254	1117	1265

1 sd error	12-2gt sp2	13-1gt sp2	13-2gt	13-2gt sp2	5-3gta sp2	5-4gt	5-9gt	5-9gta sp2	5-14gt
La	0.1	0.2	0.1	0.0	0.0	0.0	0.3	0.9	0.2
Ce	0.2	0.1	0.4	0.0	0.6	0.0	0.3	1.4	0.3
Nd	0.1	0.5	0.1	0.0	0.4	0.1	0.4	0.4	0.4
Sm	0.2	0.3	0.1	0.0	0.0	0.1	0.7	0.4	0.1
Eu	0.2	0.3	0.0	0.0	0.1	0.0	0.0	0.2	0.0
Gd	0.4	0.5	0.0	0.1	0.1	0.1	0.6	0.6	0.2
Dy	0.2	0.2	0.0	0.0	0.1	0.2	0.5	0.7	0.1
Er	0.1	0.5	0.0	0.0	0.0	0.1	0.2	0.6	0.0
Yb	0.2	0.3	0.0	0.0	0.2	0.2	0.2	0.4	0.1
Ni	1.1	13.2	2.0	1.4	1.8	2.1	10.4	32.0	0.3

Table A5.2 continued

REE	5-15gta	5-19gt	5-21gta	6-1gta sp2	6-2gt	6-2gt sp2	6-4gt
spot size (micron)	50	50	50	50	50	50	50
La	0.08	2.80	3.16	-0.17	0.01	0.04	0.15
Ce	1.48	5.31	6.44	0.43	0.04	0.12	1.31
Nd	0.93	2.40	2.98	1.21	0.34	0.33	1.46
Sm	0.47	0.99	1.03	0.38	0.41	0.31	0.66
Eu	0.23	0.41	0.45	0.26	0.15	0.17	0.19
Gd	0.46	0.87	0.73	1.12	0.33	0.46	0.45
Dy	0.45	0.89	0.79	1.13	0.35	0.35	0.27
Er	0.24	0.62	0.57	0.60	0.19	0.12	0.18
Yb	0.60	0.73	0.66	1.01	0.31	0.33	0.31
paragenesis	harz	lherz	harz	harz	harz	harz	harz
REE group	1	3	3	2	1	1	1
Cr-number	20.9	26.3	38.5	18.2	19.5	19.5	18.9
Ni	135.1	29.5	5.3	124.8	179.5	178.9	172.4
Temperature	1294	959	n.d	1273	1378	1377	1366

1 sd error	5-15gta	5-19gt	5-21gta	6-1gta sp2	6-2gt	6-2gt sp2	6-4gt
La	0.1	0.6	0.3	0.1	0.0	0.0	0.0
Ce	1.5	0.7	0.4	0.2	0.0	0.1	0.0
Nd	0.3	0.4	0.5	0.2	0.1	0.0	0.3
Sm	0.3	0.1	0.5	0.2	0.0	0.0	0.1
Eu	0.2	0.1	0.3	0.2	0.0	0.1	0.0
Gd	0.0	0.2	0.3	0.1	0.1	0.1	0.1
Dy	0.3	0.2	0.6	0.4	0.1	0.1	0.2
Er	0.3	0.1	0.5	0.2	0.1	0.1	0.1
Yb	0.5	0.1	0.5	0.4	0.1	0.0	0.0
Ni	10.1	20.4	4.2	1.5	4.5	3.1	3.1

APPENDIX 6
GEOTHERMOBAROMETRY ESTIMATES FOR THE MINERAL INCLUSIONS FROM CULLINAN

Table A.6.1: Peridotitic inclusion geothermometry estimations, using an estimated pressure of 55kbar (all results are in degrees centigrade)

Gt-cpx Fe^{2+}-Mg exchange thermometers				
		T-EG79	T-Ai94	T-KR00
10-1gt	10-1 cpx	1294	1363	1357
10-3 gt	10-3cpx	1357	1452	1444
10-4gta	10-4cpx	1172	1186	1185
10-5gt	10-5cpx	1280	1342	1343
10-6gt	10-6cpx	1186	1203	1209
10-6gta	10-6cpx	1161	1170	1176
10-8gt	10-8cpx	1130	1115	1135
10-10gt	10-10cpx	1435	1585	1573
10-11gt	10-11cpx	1234	1269	1268
10-12 gt	10-12cpx	1279	1329	1337
10-13gt	10-13cpx	1082	1060	1066
10-15gt	10-15cpx	1331	1404	1414
10-16gt	10-16cpx	1324	1401	1397
10-18gt	10-18cpxa	1230	1260	1272
10-18gt	10-18cpx	1214	1236	1250
10-19gt	10-19cpx	1379	1485	1474
10-19gt	10-19cpxa	1406	1531	1513
10-20gt	10-20cpx	1097	1077	1094
11-4gt	11-4cpx	1077	1052	1064
11-5gt	11-5cpx	1154	1156	1166
11-5gta	11-5cpx	1142	1141	1148
11-6gt	11-6cpx	1151	1160	1162
11-8gta	11-8cpx	1157	1156	1171
11-9gt	11-9cpx	1324	1507	1397
11-10gta	11-10cpx	1246	1292	1289

Crossing tie lines between gt and cpx
Anomalously high T in Fe-Mg exchange
text in red — Touching inclusions

Table A.6.1: continued

Pyroxene solvus thermometers					
	T-NT00		T-BKN		T-Cainopx
10-1 cpx	1277				
10-2cpx	1362				
10-3cpx	1358				
10-4cpx	1214				
10-5cpx	1261				
10-5cpxa	1234				
10-6cpx	1227				
10-7cpx	1282				
10-7cpxa	1254				
10-8cpx	1291				
10-10cpx	1210				
10-11cpx	1258	10-11cl	1193	10-11cl	1281
		10-11cla	1195	10-11cla	1274
10-12cpx	1213				
10-13cpx	1267				
10-14cpx	1285				
10-15cpx	1132				
10-16cpx	1427				
10-17cpx	1230				
10-18cpxa	1238				
10-18cpx	1289				
10-19cpx	1162				
10-19cpxa	1169				
10-19cpxb	1175				
10-20cpx	1237				
11-4cpx	1182				
11-4cpxa	1135				
11-5cpx	1289				
11-6cpx	1260				
11-8cpx	1155				
11-8cpxa	1193				
11-9cpxa	1154				
11-10cpx	1316				
7-1cpx	1071				
7-2 cpx	1273				
7-2cpxa	1192				
7-3cpx	1156				
7-4cpx	1379				
7-5cpx2	1352				
7-7cpx	1082				
7-7cpxa	1075				
7-8cpx	1202				
7-8cpxa	1178				
7-9 cpx	1307				
7-10cpx	1303				
7-11cpx	1133				
7-12cpx	1175				
7-13cpx	975				
7-14cpx	902				
7-15 cpx	1282				

Table A.6.1: continued

Pyroxene solvus thermometers					
	T-NT00		T-BKN		T-Cainopx
7-16cpx	1184				
7-16cpxa	1103				
7-17cpx	1403				
7-18cpx	1225				
7-18cpxa	1287				
7-19cpx	1365				
7-20cpx	1123				
7-20cpxa	1118				
8-1cpx	1239				
8-1cpxa	1252				
8-3cpx	1182				
8-4 cpx	1357				
8-4cpxa	1361				
8-5cpx	1423				
8-5cpxa	1418				
8-6cpx	1084				
8-7cpx	1197				
8-8cpx	1161				
8-9cpx	1136				
8-10cpx	1281				
				5-8cl	1315
				5-15cl	1271
				5-15cla	1291

Table A.6.1: continued

Gt-ol Fe^{2+}-Mg exchange thermometer	
	T-OW79
10-3ol	1182
10-3ola	1391
10-13ol	891
10-13ol2	926
11-2ol	1284
5-11ol	943
5-12ola	1106
5-14ola	1366

Nickel thermometers		
	T-C99	T-R96
10-1 gt	1270	1406
10-4gt	1231	1332
10-4gt sp2	1246	1360
10-5gt	1174	1226
10-6gt	1259	1385
10-6gt sp2	1270	1406
10-6gta	1267	1400
10-8gt	1077	1063
10-10gt	1278	1422
10-15gt	1172	1223
10-16gta	1392	1661
10-19gt	1218	1307
11-2gt	1246	1361
11-5gt	1188	1251
11-5gt2	1154	1192
11-10gt	1287	1441
5-2gtd	1263	1393
5-2gtd	1270	1406
5-3gt sp2	1341	1550
5-3gta sp2	1339	1546
5-4gt	1306	1479
5-6gt	1254	1376
5-6gt sp2	1267	1400
5-8gt	1364	1601
5-9gt	1234	1337
5-9gta	1048	1016
5-9gta sp2	1117	1128
5-10gt	1185	1246
5-14gt	1265	1397
5-15gta	1294	1455
5-15gta sp2	1275	1416
5-16gt	1276	1418
5-17gt	1197	1269
5-19gt	959	881
5-22gt	1341	1551
5-22gt sp2	1324	1516
6-1gta	1317	1500
6-1gta sp2	1273	1411
6-2gt	1378	1631
6-2gt sp2	1377	1629
6-3gt	1242	1353
6-4gt	1366	1604
13-1gt sp2	1226	1321
13-2gt	1161	1204
13-2gt sp2	1161	1204
13-3gt	1205	1283
12-12gta	1164	1209
13-1gt	1232	1334